Pre-Breakdown Ionization Processes and Impulsive Breakdown Characteristics of Gases

Ting Liu

This thesis is submitted for the degree of

Doctor of Philosophy

Department of Electronic and Electrical Engineering

University of Strathclyde

November 2022

DECLARATION

This thesis is the result of the author's original research. It has been composed by the author and has not been previously submitted for examination which has led to the award of a degree.

Ting Liu

November 2022

ACKNOWLEDGMENTS

I would like to express my sincerest thanks to a great number of people, who have guided and helped me throughout my PhD research, and I would have never completed this without them.

First and foremost, I appreciate significantly to my primary supervisor, Dr. Igor Timoshkin, for giving me the opportunity to pursue PhD, and I would like to express my deepest gratitude to him for his colossal support and expended patience that has kept me motivated throughout the entire duration of my research. His profound, trustworthy knowledge and keen insight have been invaluable to my research. Words cannot describe my gratitude for all the help and support he has given me. I also appreciate my second supervisor, Prof. Scott J. MacGregor. Despite his busy and hectic schedule as the Vice-Principal at the University of Strathclyde, he gave me feedback and suggestions. Words cannot describe my gratitude for all the help and support they have given me. I would only be achieved a PhD with their professional and excellent guidance.

I also greatly appreciate Dr. Mark Wilson and Dr. Martin Given, who gave me insightful comments and valuable suggestions. Moreover, I genuinely thank the workshop that helped with the test cell and all my colleagues and friends at HVT Research Group for their kindness and support throughout my research. Furthermore, I am eternally grateful to my family for their continuous support and belief in me.

From 2020 to 2022, we experienced the pandemic and lockdown. Albeit overstretched, there was all heartiness and good fellowship from my supervisor, colleagues, and friends. Your patience, support, and kindness are much appreciated.

ABSTRACT

Global warming has become a central issue in the problem of environmental protection. Sulphur hexafluoride (SF_6) has excellent insulation and recovery characteristics; however, this gas has significant Global Warming Potential ~23,900 times higher than CO_2. Therefore, to reduce negative environmental impact caused by SF_6 when this gas is released into atmosphere, the power and pulsed power industries are actively looking for alternative gases which can be used as insulating fluids in high voltage power and pulsed power systems. Therefore, there is an urgent need to establish breakdown properties and characteristics of common and environmentally friendly gases in different topologies and energisation regimes. Thus, further understanding of the transient pre-breakdown processes, dynamic properties of plasma streamers and experimental breakdown characteristics of common and environmentally friendly gases in a wide range of normalised pressures and electric fields is required.

The present thesis addresses this issue through: (i) the systematic investigation and analysis of the swarm characteristics of air, N_2, CO_2, and SF_6, (ii) the development of analytical models for investigation of fast ionization process in these gases, including drift-diffusion and kinetic models, (iii) the experimental investigation of the impulsive breakdown properties of air, N_2, CO_2 stressed with fast, sub-μs high voltage impulses with a rise time of up to ~50 ns in the pressure range from 6.5 kPa to 405 kPa, and (iv) the analysis of breakdown properties of humid air with selected relative humidity.

The present work has conducted a comprehensive analytical, computational and experimental investigation of transient events in common and environmentally friendly gases and their impulsive breakdown characteristics. The breakdown characteristics of the investigated gases have been obtained, and these data are presented as field-distance and time-field characteristics. These obtained results will help to optimize gaseous insulation for different power and pulsed power applications, the findings will contribute to a better understanding of the development of the fast pre-breakdown processes in gases. Thus, it will help to develop different gas-insulated

components for the HV power and pulsed power systems, such as fast plasma closing switches filled with environmentally friendly gases and gas-insulated systems.

CONTENTS

Chapter 1 Introduction

1.1 Objectives of research

Gas-insulated high voltage pulsed power systems such as fast plasma closing switches filled with gas and gas-insulated systems are widely used in the power and pulsed power industries. In many of these systems, sulphur hexafluoride (SF_6) is used as an insulating medium. However, SF_6 is identified as a potent greenhouse gas with the Global Warming Potential (GWP) of ~23,900; SF_6 molecules absorb substantially more infrared radiation than CO_2 molecules. The absorption of infrared radiation by SF_6 molecules is significantly higher compared to CO_2 molecules, leading to an increased amount of energy being trapped in the Earth's atmosphere. As a result, this contributes to the phenomenon of global warming [Eves, 2018].

In order to help to achieve the ambitious goals in climate protection, environmentally friendly gases should be used in newly-designed gas-filled insulation components and elements instead of SF_6; the retro-filling of existing systems can also be investigated. Also, using common and environmentally friendly gases will help to introduce new technologies in the traditional and pulsed power high voltage systems, such as plasma closing switches [Schaefer, 1990], circuit breakers [Dick, 2000] and gas-insulated systems [Haddad, 2004]. More information and an in-depth analysis and understanding of the reliability of different gas-filled electrical insulation systems are required to underpin this process. It can be achieved by analysing the transient breakdown characteristics, the effects of electrode geometry, voltage waveform, and polarity of voltage. Thus, innovative solutions in optimizing of different gaseous insulation systems and components can be achieved based on the modelling, simulation, and experiments.

The time-field breakdown characteristics are of particular importance for different practical applications because the measurements performed under DC energization do not provide information on the breakdown behaviour of the gas-insulated systems in the case of high voltage transient events [Levatter, 1980].

The breakdown Paschen curves do not provide information on the pre-breakdown time. Also, the breakdown voltage under pulsed conditions can differ significantly from the breakdown voltage provided by Paschen's law. The swarm parameters, including the effective ionization coefficient and electron mobility, are required to model and simulate the transient pre-breakdown processes. However, currently there is a lack of accurate analytical equations which describe these parameters in a wide range of electric fields. Moreover, there is a need for scaling relationships, which link the breakdown field and time to breakdown with the gas number density and inter-electrode gap. Such phenomenological scaling relationships will help in the analysis and coordination of practical gaseous insulating systems. Furthermore, the impulsive breakdown properties of the gases in sub-mm inter-electrode gaps stressed with short sub-μs high-voltage impulses are not fully understood. Therefore, further analytical and experimental investigation of the breakdown characteristics of the common gases and gases with low environmental impact is required.

This project aims to study the fast transient process and time-field breakdown characteristics in air, N_2, and CO_2 and compare these characteristics with SF_6. This analysis is conducted using the drift-diffusion and kinetic models. The breakdown characteristics for humid air are also analysed based on the streamer criterion. The main objectives of this project are:

- To investigate the swarm parameters (including the effective ionization and its corresponding critical field, and the mobility coefficient) for air, N_2, CO_2, and SF_6 in a wide range of electric fields up to ~ 10^4 Td.

- To develop a drift-diffusion model using accurate swarm parameters to model fast ionization fronts and to obtain time-field breakdown characteristics for air, N_2, CO_2, and SF_6.

- To obtain the time-field breakdown characteristics using the kinetic model based on Meek's avalanche-to-streamer criterion and to compare the obtained results for air, N_2, CO_2, and SF_6 with the results obtained by the drift-diffusion model.

- To conduct impulse breakdown experimental tests and to obtain the breakdown characteristics of air, N_2 and CO_2 in a sub-mm gap at different pressures using sub-μs HV impulses of both polarities.

- To analyse the obtained volt-time, field-distance and time-field breakdown characteristics for air, N_2 and CO_2.

- To investigate the breakdown characteristics of humid air and to establish the dependency of the swarm parameters for air on its humidity; to obtain the breakdown voltage of humid air based on the avalanche-to-streamer transition criterion.

The drift-diffusion and kinetic models were used to predict the breakdown characteristics of air, N_2, CO_2 and SF_6 and to compare these results with the data available in the literature. However, due to technical limitations, only air, N_2 and CO_2 were chosen to conduct the experimental tests in the present work.

1.2 Thesis overview

This thesis consists of 7 chapters. Chapter 1 provides an introduction to this project. Chapter 2 gives an overview of the breakdown mechanisms, the swarm parameters,

modelling approaches, pulse forming line, and Blumlein topologies for generating HV impulses. The simulation techniques and the impulse breakdown experiments available in the literature are reviewed. The knowledge gaps in the previous research are identified and discussed, and the objective of the present work is presented, accordingly.

Chapter 3 analyses the swarm parameters in gases, including the ionization and attachment coefficients, the effective ionization coefficient, the electron mobility, and the diffusion coefficient. An accurate analytical representation of the swarm parameters in air, N_2, CO_2, and SF_6 is obtained in a wide range of electric fields.

Chapter 4 focuses on simulating fast ionization fronts and breakdown characteristics using the drift-diffusion and kinetic models. Adopting the accurate analytical representation of the swarm parameters obtained in the previous chapter, the development of the ionization front in air, N_2, CO_2, and SF_6 has been investigated. The term "accurate" used in the present work is based on interpretation of the definition of “accuracy” provided in [Bevington 2003]: the accuracy of fitting by analytical equations is a measure of how close the result of this fitting is to the experimental data. The breakdown criterion has been introduced in the drift-diffusion model. The time-field breakdown characteristics for air, N_2, CO_2, and SF_6 are obtained by employing this criterion. The time-field breakdown characteristics are also obtained using the kinetic approach, and these results from the two models have been compared with the experimental measurement data from the literature.

Chapter 5 presents the experimental investigation of the impulsive breakdown voltage of air, N_2, and CO_2 in the needle-plane electrode topology with a gap of 100 µm. Positive and negative HV impulses with a rise time up to ~50 ns were used to investigate the impulsive breakdown characteristics of these gases in the pressure range from 6.5 kPa to 405 kPa. All breakdown events occurred on the leading edge of the HV impulses; thus, the time to breakdown and breakdown voltage were obtained in the overvolted regime. The volt-time, field-distance, and time-field breakdown characteristics have been plotted and analysed using different scaling relationships.

The obtained scaling relationships will help in further analysis of the breakdown characteristics of the gases used in the present research.

Chapter 6 investigates the breakdown characteristics of air with a relative humidity of 0%, 50%, and 100% at room temperature and atmospheric pressure in the uniform field. The analysis of the effective ionization coefficients of air with different levels of relative humidity as a function of the electric field is conducted. The critical field and the breakdown voltage as functions of *pd* are obtained for humid air based on the streamer criterion.

Chapter 7 concludes the results obtained using the drift-diffusion and kinetic models, the experimental results on impulsive breakdown characteristics, and the analysis of the breakdown characteristics of humid air. The main achievements of this work, its novelty, contribution to the field of study, and potential future work are discussed.

Chapter 2 Literature review

2.1 Introduction

In this chapter, the fundamental concepts and breakdown mechanisms are discussed, and the swam parameters in gases are analysed. The modelling of the gas discharge and breakdown process, including modelling approaches and numerical algorithms, is discussed. Associated with the simulation work conducted in this thesis, several analytical and computer models are presented and discussed. Following analysis of the experimental results on impulse breakdown of gases available in the literature, a detailed discussion of the experimental parameters and breakdown characteristics is presented. This literature review provides a basis for the analytical and experimental work conducted in the present research project.

2.2 Background

The study of gas discharges can be traced back to the early 19th century when arc discharge was first discovered. In order to explain this phenomenon, the fundamental gas discharge theory has been developed. In 1889, the empirical study on the breakdown voltage in the uniform field was published [Paschen, 1889]. The study introduced the scaling relationship between the breakdown voltage, gas pressure, and gap distance, known as Paschen's Law. Paschen's Law states that the breakdown voltage, U_{br}, is a function of (pd) the product of gas pressure, p, and the gap distance, d, between the electrodes. Thus, the relationship between U_{br} and pd, Paschen's breakdown law was established. At the beginning of the 20th century, Townsend [Townsend, 1901] initially discovered and analysed the electron avalanche in the

uniform electric field at low gas pressure. This type of discharge mechanism is known as the electron avalanche (Townsend discharge).

However, the Townsend theory is not applicable for longer inter-electrode distances or the case of significant space charges [Meek, 1953]. It was found experimentally that in these cases, the Townsend theory provides longer than experimentally measured pre-breakdown times, and in order to address this discrepancy, a new breakdown concept based on fast ionization waves (plasma streamers) was introduced. It was suggested that the slow-moving electron avalanche might transform into a fast ionization front (plasma streamer) if the specific avalanche-to-streamer criterion is satisfied.

Raether, Loeb, and Meek, [Meek, 1940] described the streamer breakdown mechanism and proposed the avalanche-to-streamer transition criterion postulating that the space charge in the avalanche head causes a significant increase in the electric field strength in front of the avalanche leading to its transformation into the plasma streamer. The streamer theory allows for analysis of the gas breakdown behaviour in a wider range of operating conditions, including longer distances (larger *pd* values).

Gas discharges underpin the operation of different high-voltage and pulse power systems and components, including plasma closing switches and circuit breakers. Gas discharges are also used in practical environmental, and biomedical applications [Laroussi, 2012]. Many research papers focus on gas breakdown characteristics in different electrode topologies and under different energization regimes.

With the advances in computer modelling, the numerical simulations of the transient plasma processes in gases have attracted significant interest and become a highly efficient method for analysing the pre-breakdown plasma fronts.

Knowledge of the ionization parameters and transport characteristics of electrons and ions in gases is essential for modelling and simulation of gas discharges and breakdown characteristics. The following sections will present and discuss the swarm

properties of electrons in air, nitrogen, carbon dioxide and SF_6 based on the data available in the literature. This comprehensive review and analysis of the available swarm data underpin the development of analytical and computational models of the fast pre-breakdown ionization waves in gases. That requires accurate mathematical expressions of the critical transport and ionization parameters, such as the first Townsend ionization coefficient and electron mobility. These swarm parameters are presented as analytical functions of the electric field. These analytical equations will be used in the computational model of the transient plasma fronts and in the kinetic phenomenological model, which is based on the streamer breakdown criterion.

2.3 Swarm parameters in gases

Swarm parameters play a critical role in gas discharge modelling, which requires highly accurate and reliable data. Following [Dutton, 1975] and [Carbone, 2021], it can be stated that the swarm parameters, in general, include coefficients that describe the generation and loss of charged particles, i.e., the ionization, attachment, recombination coefficients, and transport parameters, including the drift velocity, diffusion coefficient, and mobility.

The swarm parameters are generally expressed as functions of the reduced electrical field E/N or E/p (the field strength E normalized by the particle number density N or the pressure p), as the distribution function of the charged particles (electrons and ions) is governed by the electric field and by the collisions between the particles in the gas [Carbone, 2021].

The reduced electric field presented as E/N can be rearranged into E/p using the isothermal equation of state for an ideal gas, $p=NTk_B$, where k_B is the Boltzmann constant and T is the temperature. The unit of measurement of E/N is Td ($1\text{Td}=10^{21}\ \text{V}\cdot\text{m}^2$). This unit is used in transport, ionization, and breakdown analysis [Dutton, 1975]. For example, in [Dutton, 1975] and [Gallagher, 1983], the swarm

parameters were presented as functions of the reduced electric field *E/N*. In engineering practice *E/N* often is converted into *E/p*.

2.3.1 Swarm parameters

The swarm coefficients are used to describe the generation and loss of the charged particles due to collisions. These coefficients include the ionization, attachment, secondary ionization, and recombination coefficients, which strongly depend on the electric field.

The first (Townsend) ionization coefficient (α) is defined as the average number of newly created electrons per unit length. These new electrons are generated by collisional ionization processes by collisions with the neutral gas atoms or molecules during their movement in the external field. α expresses the number of new electrons (successful ionization events) produced by a single electron over a unit distance when it moves in the external electric field.

The attachment coefficient (η) is defined as the number of electrons that attach to atoms or molecules, forming negative ions when electrons travel a unit distance in an electronegative gas. As mentioned, this attachment process leads to the formation of negative ions in electronegative gases, such as SF_6, molecules of which have a high electron affinity. Air and CO_2 are weakly electronegative (attaching) gases, while N_2 is electropositive, i.e., a non-attaching gas [Farish, 2004]. The processes involved in the development of avalanches will be discussed in Section 3.2.

In order to describe the net rate of generation of electrons in the gas discharge process, the effective ionization coefficient (α_{eff}) is introduced, which is defined as the ionization coefficient (which characterizes the generation of electrons) minus the attachment coefficient (which characterizes the loss of electrons). Thus, α_{eff} provides the net rate of ionization (number of generated electrons per unit length)

$$\alpha_{eff} = \alpha - \eta \tag{2.1}$$

i.e., the net number of free electrons generated by collisional ionization in any electronegative gas.

α /*N*, η /*N*, a_{eff}/*N* for air as functions of *E/N* are shown in Figure 2.1, [Lowke, 1995]. These coefficients are used as an example to describe the relationship between the ionization and attachment coefficients and the effective ionization coefficient.

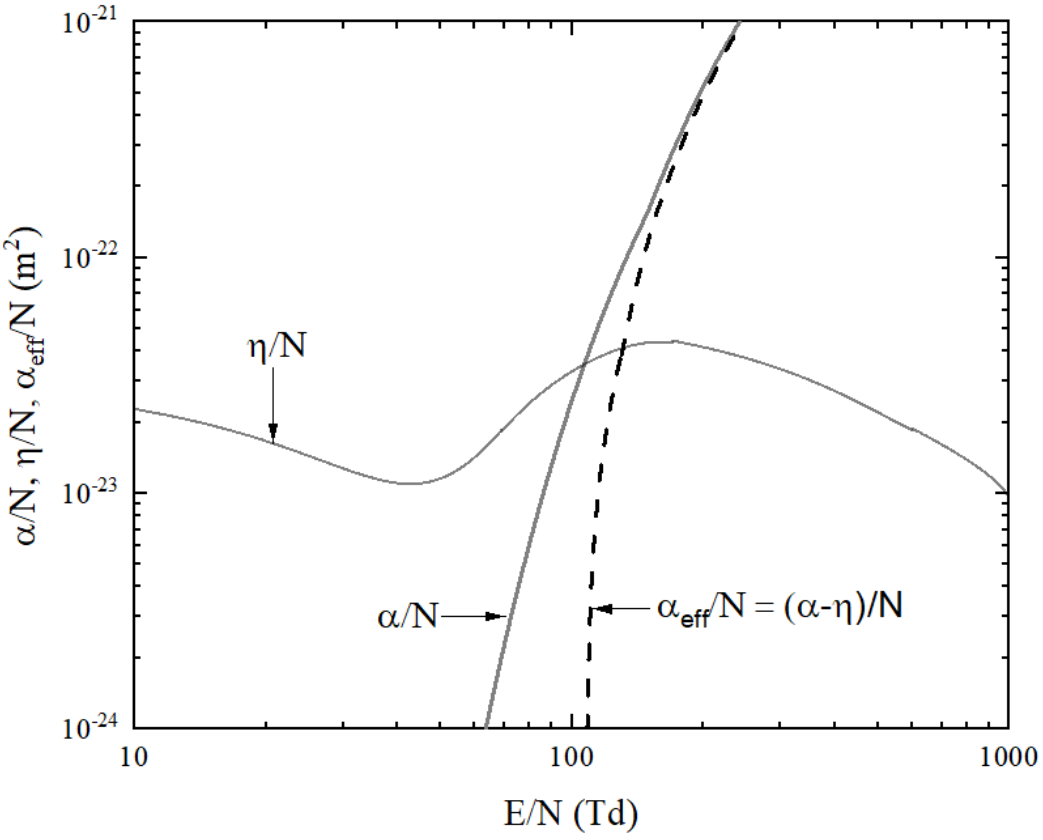

Figure 2.1 α /*N*, η /*N*, a_{eff}/*N* as function of *E/N* for air. Data adopted from [Lowke, 1995].

Figure 2.1 shows the reduced effective ionization coefficient (α_{eff}/N), which is the difference between the reduced ionization coefficients (α/N) and the reduced attachment coefficients (η/N).

It is worth noting that, as expected, at low *E/N*, the reduced ionization coefficient (α/N) is lower than the reduced attachment coefficient (η/N) as the attachment process becomes a dominant process in this field region. When *E/N* is greater than ~105 Td, the reduced ionization coefficient (α/N) becomes higher than the attachment coefficient (η/N) because the ionization process starts to intensify, resulting in the production of significant number of free electrons in the stronger electric field.

Figure 2.1 shows that the reduced ionization coefficient, (α/N), the reduced attachment coefficient, (η/N) and the reduced effective ionization coefficient, (α_{eff}/N) for air depend strongly on the reduced electric field *E/N* [Morrow, 1997].

The reduced effective ionization coefficient (a_{eff}/N) starts to grow when the reduced ionization coefficient (α/N) dominates over the reduced attachment coefficient (η/N). It means that the net ionization starts to be a dominant factor if $\alpha_{eff} > 0$, thus the net number of free electrons starts to increase. Otherwise, if the reduced attachment coefficient (η/N) is equal or greater than the ionization coefficient (α/N), the effective ionization coefficient (a_{eff}/N) is zero (or nominally less than zero), that is, if $\alpha_{eff} = 0$, there is no cumulative net ionization in the gas and discharge does not develop.

The secondary ionization coefficient (γ) is defined as the number of electrons emitted by each positive ion which strikes the cathode surface. Thus, the reciprocal value, $1/\gamma$, defines the number of positive ions which is required to produce a single secondary electron from the surface of the cathode. γ could be significantly lower than 1, i.e., multiple hits by positive ions are required to generate a single secondary electron from the cathode surface.

In addition to the attachment process mentioned above that causes the loss of electrons, the recombination process also leads to the loss of charged particles. The recombination coefficient (β) is used to describe the recombination process, including the recombination between electrons and positive ions, the recombination between positive ions and negative ions.

Although the critical field is not nominally a swarm parameter, it is an essential characteristic which is closely related to the effective ionization coefficient. It is defined as a value of the electric field at which the effective ionization coefficient is zero, $\alpha_{eff} = (\alpha - \eta) = 0$. This normalized field is known as the critical field $(E/N)_{cr}$ or $(E/p)_{cr}$, the critical field describes a threshold at which the net ionization starts to be positive and grows with an increase in the field, leading to potential development of an electron avalanche and complete breakdown.

As shown in Figure 2.2, the curves based on the results by [Morrow, 1997], [Morrow, 1986], the effective ionization coefficient for air and SF_6 $(\alpha_{eff}/N = (\alpha - \eta)/N)$ is a function of the reduced electric field, E/N. Based on these results, it is possible to identify the critical field $(E/N)_{cr}$: ~108 Td in air and ~360 Td in SF_6.

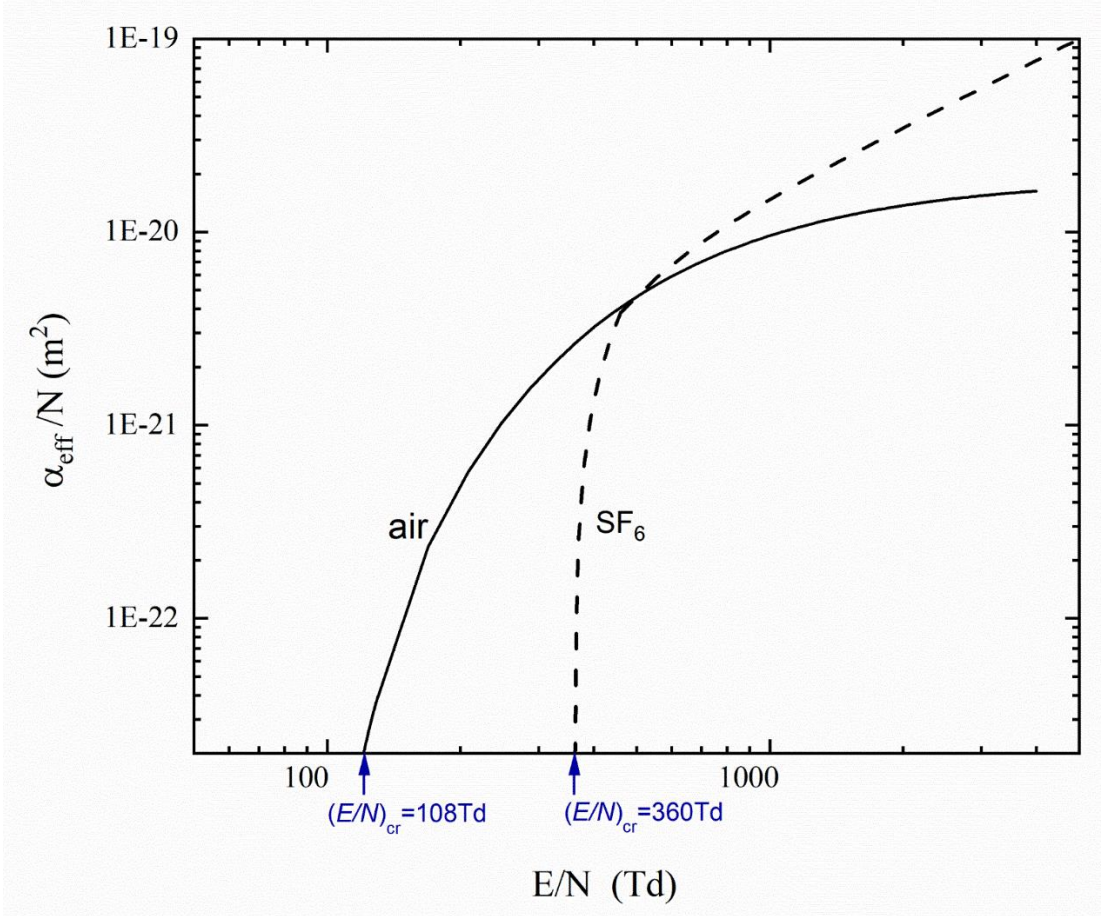

Figure 2.2 The effective ionization coefficient and critical field for air. Data adopted from [Morrow, 1997] and SF_6 [Morrow, 1986].

When the effective ionization coefficient is zero, $\alpha_{eff} = (\alpha - \eta) = 0$, the reduced critical field *E/p* for air is ~27 kV/(cm ·bar), and the reduced critical field *E*/*p* for SF_6 is ~89 kV/(cm ·bar) [Farish, 2004]. The critical field for SF_6 is significantly higher (three-fold higher) than for air. When the field is lower than the critical field, there is no net ionization in air and SF_6. Thus, the avalanches will not develop, and there will be no breakdown.

The effective ionization coefficient $(\alpha - \eta)$ as a function of the reduced field *E*/*p* for SF_6 shows a pronounced increasing tendency compared with the effective coefficient α_{eff} (*E*/*p*) in air. The critical field for air, CO_2, N_2 and SF_6 will be obtained from the literature data and analysed in Section 3.3 of this thesis.

2.3.2 Transport coefficients

The transport coefficients are used to describe the movement of charged particles, including the drift velocity, the mobility of charged particles, and the diffusion coefficient; all these parameters may strongly depend on the electric field.

Drift velocity is defined as the particle velocity when the particle is drifting under the influence of the electric field. Mobility is defined as a coefficient of proportionality between the drift velocity and the applied electric field. Equation 2.2 describes the relationship between the electron mobility, the electron drift velocity and the electric field

$$W_e = \mu E \tag{2.2}$$

where, μ is the electron mobility, W_e is the drift velocity of electrons, *E* is the electric field.

To obtain μ as a function of the reduced electric field *E/N*, Equation 2.2 can be rewritten as

$$\mu N = W_e/(\frac{E}{N}) \tag{2.3}$$

This equation will be used to model the breakdown characteristics in the present work.

The diffusion coefficient, *D*, describes the particle drift from the high-concentration area to the low-concentration area. Only the longitudinal diffusion coefficient is used in the models developed in the present work. The transverse diffusion coefficient is not considered here, as its effect is considered negligible [Tran, 2010a], [Georghiou, 2005].

2.4 Basic breakdown mechanisms

Two basic breakdown mechanisms are discussed in this section: the avalanche breakdown mechanism and the streamer breakdown mechanism.

2.4.1 Townsend avalanche

J.S. Townsend proposed the avalanche breakdown mechanism [Townsend, 1897]. Based on the concept of the electron avalanche and the secondary electron emission from the cathode surface, the process of gas discharge in the uniform field can be explained as follows.

As shown in Figure 2.3, a single electron generated by an external source of ionizing radiation (for example, gamma rays of photons) appears near the cathode; this electron gains the kinetic energy and is accelerated by the electric field, it moves towards the anode. When the energy is greater than the ionization energy of neutral atoms or

molecules, that means a threshold energy for the ionization reaction, then the ionization occurs in the gas producing more free electrons. Such a process (electron avalanche) leads to an exponential increase in the number of electrons with distance.

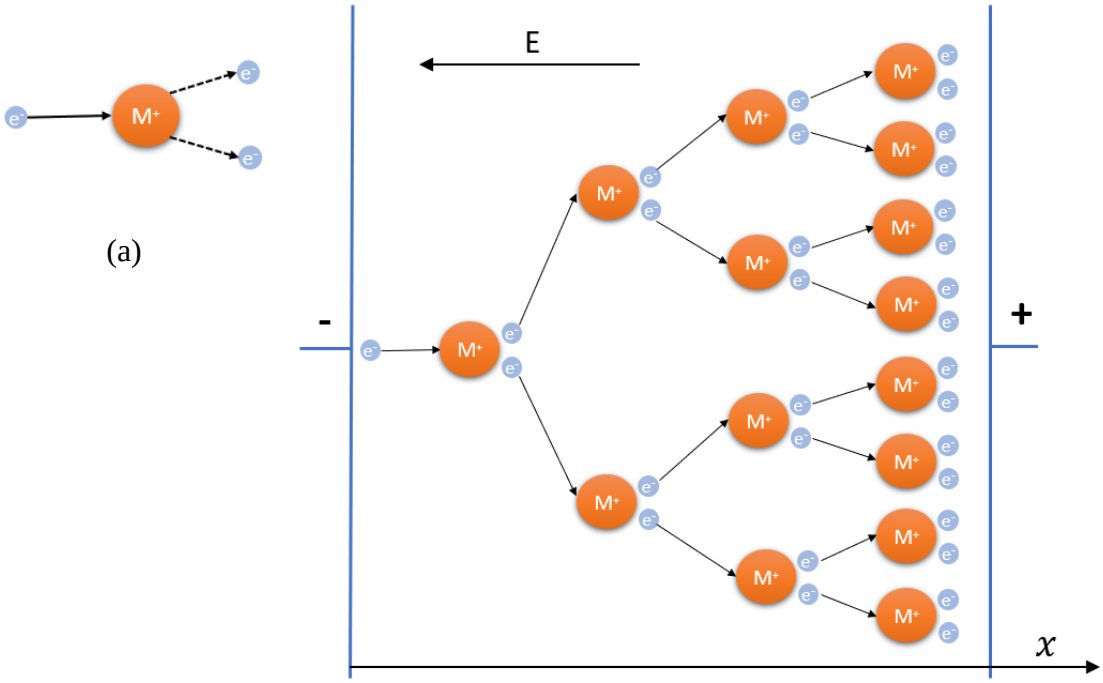

(a)

(b)

Figure 2.3 Schematic representation of the ionization avalanche in gas: (a) impact ionization [Go, 2018] (b) Avalanche breakdown mechanism [Faircloth, 2014]

Therefore, the number of electrons n in the avalanche propagating over the distance d towards the anode can be expressed as

$$n = n_0 e^{\alpha d} \tag{2.4}$$

where α is the primary ionization coefficient, d is the distance between the electrodes, n_0 is the initial number of electrons in the avalanche.

The Townsend avalanche breakdown criterion is based on the transformation of the non-self-sustained discharge into the self-sustained discharge. This transformation occurs when the following condition is met $\gamma(e^{\alpha d} - 1) = 1$. Typically γ <<1, thus $1/\gamma$ can be used to approximate $[(1+\gamma)/\gamma]$

$$\alpha d = ln\,(1/\gamma) \tag{2.5}$$

where, α is the primary ionization coefficient, d is the distance from the cathode to the anode. γ denotes the secondary ionization coefficient.

Paschen's breakdown curve describes the relationship between the breakdown voltage and the product of the gas pressure and the inter-electrode gap (*pd*). Figure 2.4 presents Paschen's curves for air, N_2, CO_2 and SF_6. It shows that for the condition of a 1 cm gap between electrodes at 1 atm, when *pd* =100 kPa·cm, the breakdown field of air is *E/p* ~32 kV/cm/atm (*E/N* ≈ 130 Td); the breakdown field of N_2 is *E/p* ~29 kV/cm/atm (*E/N* ≈ 117 Td); the breakdown field of CO_2 is *E/p* ~47 kV/cm/atm (*E/N* ≈ 190 Td); the breakdown field of SF_6 is *E/p* ~88 kV/cm/atm (*E/N* ≈ 356 Td).

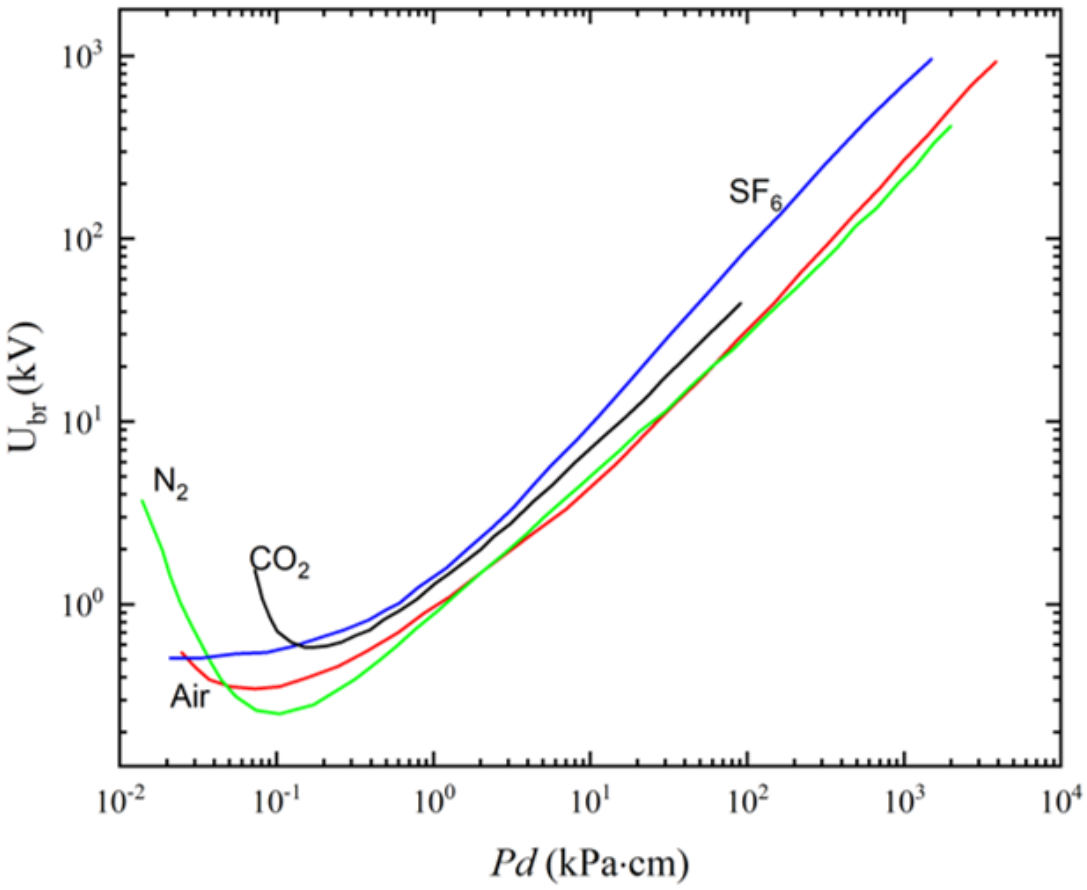

Figure 2.4 Paschen breakdown curves for common gases. Air: red line [Dakin,1974], N_2: green line [Dakin,1974], SF_6: blue line [Dakin,1974], CO_2: black line [Ollegott, 2020]

However, the Paschen scaling relationships may not be valid in the case of sub-millimeter gaps. For example, Radmilovic [Radmilovic, 2014] found that the breakdown voltage for the gaps shorter than 10 μm is lower than the breakdown voltage shown in the classic Paschen breakdown curve obtained for longer inter-electrode distances; this behaviour will be discussed in Chapter 5.

2.4.2 Streamer breakdown

The streamer breakdown mechanism was proposed by Raether, Loeb, and Meek [Meek, 1940]. This mechanism is based on transforming an avalanche (or multiple avalanches) into a fast ionization front (streamer) when the number of electrons in the

avalanche head reaches ~10^8. This condition forms the Meek criterion of the avalanche-streamer transition [Dubinova, 2016].

Figure 2.5 (a) shows that free electrons are accelerated by the external electric field E_{ex} between the electrodes. Due to the higher mobility of electrons, the surplus of fast, free electrons (initial electrons in gases may come from different sources, such as cosmic rays, UV illumination) drifts at the head of the avalanche, while the heavier positive ions are left in the tail of the avalanche.

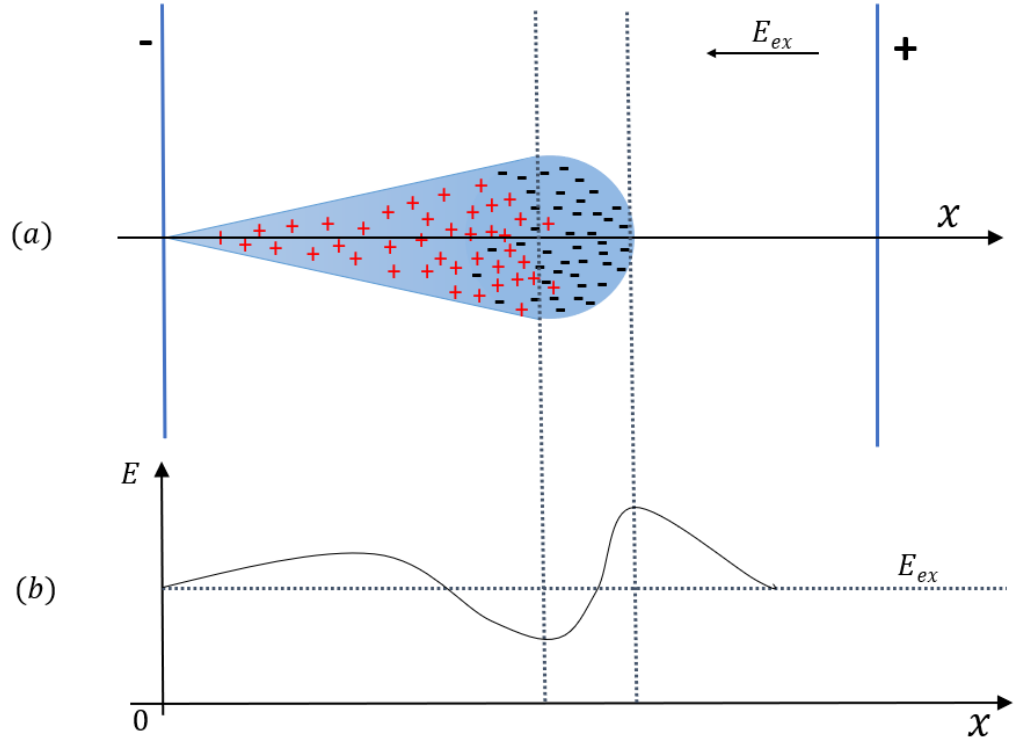

Figure 2.5 Schematic distribution of charged particles and electric field in an avalanche, E_{ex} is the external field [Faircloth, 2014]

The distribution of electrons and positive ions shows that the space charge in the avalanche creates a new local electric field. Therefore, it has been seen from Figure 2.5 (b) that the electric field is enhanced at the head of the avalanche, as a result of the intense space charge at the front of the avalanche.

Two types of streamers, a negative streamer and a positive streamer, are shown in Figure 2.6. The recombination process between electrons and positive ions leads to the emission of photons, which may cause photoionization. Thus, additional smaller avalanches can be created in front of a positive streamer.

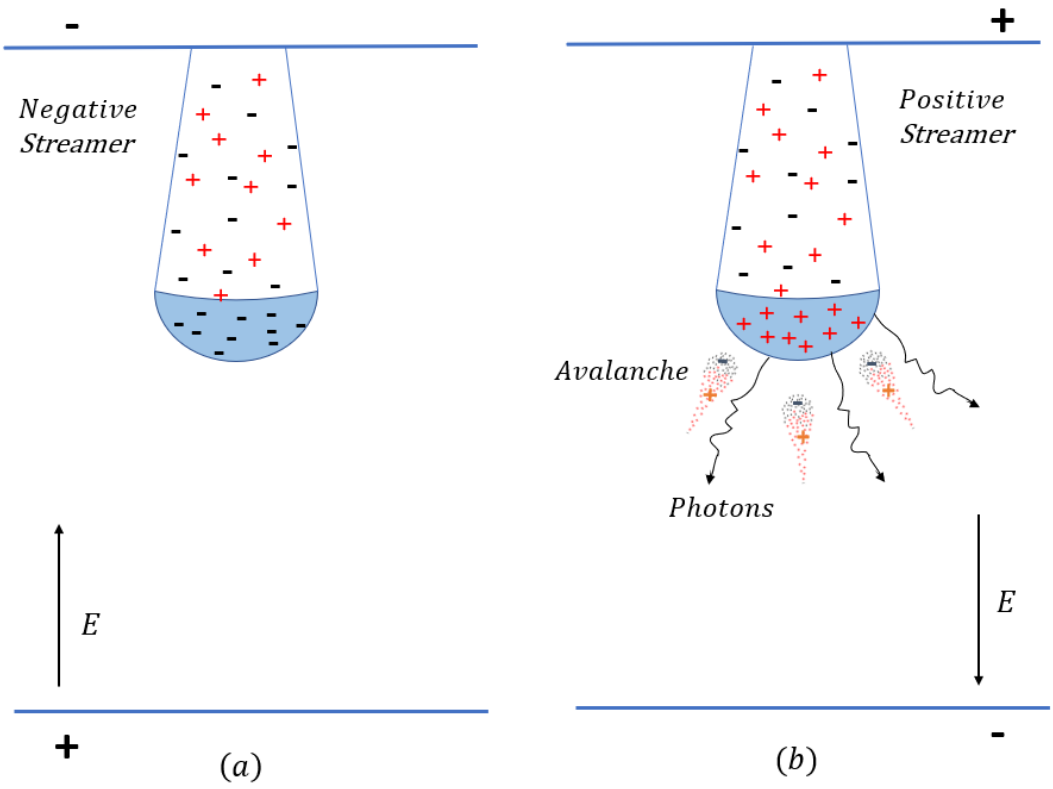

Figure 2.6 (a) Negative streamer and (b) positive streamer [Dubinova, 2016]

In the case of a negative streamer as shown in Figure 2.6 (a), the propagation direction is from the cathode to the anode, the photoionization may also occur, but only initial seed electrons support the streamer development process [Dubinova, 2016]. The breakdown eventually occurs when the streamer crosses the gap between electrodes.

Photoionization is an essential process in developing a positive streamer as shown in Figure 2.6 (b), the incoming electron avalanches generated by photons are sucked into the head of a streamer. These photons are emitted by the electron-ion recombination

process [Ollegott, 2020] and help maintain the streamer propagation towards the cathode.

The Meek criterion of avalanche-streamer transition will be used in the kinetic model (Section 4.3).

2.5 Modelling approaches

Two simulation approaches used for modelling gas discharge and breakdown processes are discussed in this section: the drift-diffusion approach and the analytical kinetic approach. These approaches will be used in the present work in Chapter 4. Also, the basic concept of numerical algorithms based on the finite element method is also presented in this section.

2.5.1 Drift-diffusion model

The equations of the drift-diffusion approach are derived from the Boltzmann equation to describe the generation and loss of the charged particles. This approach can be used to model the development of the ionization front from its formation, including its propagation through the gaseous environment.

The continuity equation contains the drift term, the diffusion term, time-dependent, the particle source term, and the particle sink term. It allows to obtain the time-dependant distribution of charged particles: the electrons, and positive and negative ions, generated by ionization and attachment process and recombination reactions. The particle distributions are coupled with Poisson's equation to consider the effect of space charge on the local electric field.

Following [Raizer, 1991], the number density of particles moving in the electric field in a gas can be expressed as

$$\frac{\partial n}{\partial t} + \nabla \cdot (\pm \vec{v} n - D \nabla n) = particle\ Source\ term - particle\ Sink\ term \quad (2.6)$$

where n is the time-dependent density of specific particles, D is the diffusion coefficient, $\vec{v}$ is the vector drift velocity, and the sign of the drift term depends on the positive and negative charges and the electric field ($\vec{v} = \mu \vec{E}$). The particle source term denotes the generation of particles, and the particle sink term describes the loss of particles.

The number density of the electrons, positive ions and negative ions can be expressed as

$$\frac{\partial n_e}{\partial t} + \nabla \cdot \left(-n_e \mu_e \vec{E} - D_e \nabla n_e\right) = n_e(\alpha - \eta)\left|\mu_e \vec{E}\right| - n_e n_p \beta_{ep} \quad (2.7)$$

$$\frac{\partial n_p}{\partial t} + \nabla \cdot \left(n_p \mu_p \vec{E} - D_p \nabla n_p\right) = n_e \alpha \left|\mu_p \vec{E}\right| - n_e n_p \beta_{ep} - n_n n_p \beta_{np} \quad (2.8)$$

$$\frac{\partial n_n}{\partial t} + \nabla \cdot \left(-n_n \mu_n \vec{E} - D_n \nabla n_n\right) = n_e \eta \left|\mu_n \vec{E}\right| - n_n n_p \beta_{np} \quad (2.9)$$

where, n_e, n_p, n_n denote the number density of the electrons, the positive ions and the negative ions respectively; t is time; α is the primary ionization coefficient; η is the attachment coefficient; β_{ep} is the recombination coefficient of the electrons and positive ions; β_{np} is the recombination coefficient of the negative ions and positive ions; D_e, D_p, D_n are the electrons diffusion, the positive ions diffusion and the negative ions diffusion respectively; μ_e, μ_p, μ_n are the mobility of the electrons, the mobility of the positive ions and the mobility of the negative ions; $\vec{E}$ is the vector of electric field.

The local field influenced by the space charge is determined by Poisson's equation

$$\nabla^2\varphi = -\frac{e\left(n_p - n_n - n_e\right)}{\varepsilon_0\varepsilon_r} \tag{2.10}$$

where φ means the electric potential, ε_0 is the vacuum permittivity, ε_r is the relative permittivity, e is the elementary charge.

The Finite element method (FEM) has become the most acceptable numerical method for solving partial differential equations (PDEs) based on weak formulation. The basic concept of the FEM is to divide the continuum domain into elements, which form a mesh. The node is the intersection of mesh lines, then approximated by the interpolation functions at nodes or the Galerkin method [Tezuka, 2011].

The elements can be curved and unstructured. Due to this choice, the essential advantage of the FEM is its ability to implement complicated geometries and different boundaries. This method also allows for higher-order accuracy to be obtained [Dick, 2009], but it is computationally expensive.

COMSOL Multiphysics software is employed to solve partial differential equations (PDEs). It is one of the most commonly used techniques for dealing with complex multi-physics problems, such as the drift-diffusion model.

The drift-diffusion model can be implemented in COMOSL to examine the charge density distribution over time and the electric field in the breakdown process, [Georghiou, 2005], [Hagelaar, 2005], [Serdyuk, 2013].

The COMSOL Multiphysics software will be used to implement the drift-diffusion model in Section 4.2.

2.5.2 Kinetic model

Typically, the time to breakdown (t_{br}) consists of two components: statistical and formative time intervals. The statistical time is generally referred to as the time interval from the moment of application of voltage to the moment when initial free electron(s) which initiates an avalanche process appear in the gap. The formative time is nominally the time interval which is required for the electron avalanche (ionisation front) to bridge the gap between the electrodes.

The kinetic approach is based on the Meek avalanche-to-streamer criterion and describes the critical transition from a slow electron avalanche to a fast plasma streamer. The time required for the avalanche to develop the critical space charge in its head (10^8 electrons) is significantly longer than the time required for the streamer to bridge the remaining space between electrodes.

Thus, this time required for the critical charge development [Raizer, 1991] is considered to be the time to breakdown in the kinetic approach. This time is a function of the ionization coefficient, frequency of ionization, mobility of electrons and the normalized electric field.

According to the Townsend model, the charge, *Q*, in the avalanche head is a function of the ionization frequency and time

$$Q \propto exp\,(\upsilon \,.\, t) \tag{2.11}$$

As indicated by the Meek breakdown criterion (transition from avalanche to streamer), the time interval required by a single electron avalanche to develop into the streamer is the time at which the number of electrons reaches specific value of ~ 10^8 [Pedersen, 1967], [Schumann, 1923], [Petcharaks, 1999]. Therefore, it can be stated

$$\upsilon_{ionis}\, t_{br} \geq 18 \tag{2.12}$$

where, υ_{ionis} is the ionization frequency in the unit of $1/s$, which is a function of the product of the ionization coefficient and the electronic drift velocity; t_{br} is the time to breakdown, which refers to the formative breakdown time.

As the statistical time has a stochastic nature it is difficult to include this time into analytical models. Thus, in the present work the total time to breakdown will be considered as the formative time only (Chapter 4).

2.6 Review of simulation techniques

Modelling is commonly used to analyse the complex streamer propagation and breakdown processes. This section presents the research work focused on the simulation of the pre-breakdown processes in gases, their breakdown behaviour is presented, and the literature data are discussed and compared.

In [Dhali, 1987], the flux-corrected transport (FCT) technique was used in a two-dimensional (2D) drift-diffusion model for simulation of the streamer development in N_2 at 760 Torr in the parallel plane electrodes with the gap separation of 5 mm. The swarm parameters used in this model are inaccurate in the high field range. The ionization coefficient as a function of *E/N* used by [Dhali,1987] shows a good agreement with the experimental data from [Bowls, 1938] in the range of *E/N* from 60 Td to 500 Td only. However, when the electric field is above 500 Td, the analytical equation for the primary ionization coefficient becomes inaccurate showing a lower value of α than the experimental data.

Kulikovsky has investigated the positive streamer in a uniform field in air at atmospheric pressure by using a 2D drift-diffusion model [Kulikovsky, 1997]. The gap separation between electrodes was 1 cm. However, the available field range for the ionization coefficient used in this model is only up to 800 Td, which means the

model does not provide information on the ionization coefficients in the high field range.

A 2D model of positive streamers in a 5 cm point-plane gap in air at atmospheric pressure has been developed in [Morrow, 1997]. The modelling results obtained by this model show that the positive streamer head develops when the applied voltage is 20 kV, but the streamer does not reach the cathode and stops at 3.5 cm from the anode; the total streamer development time was 10 μs. Although the analytical ionization coefficients are used in the whole range of electric fields in this model, they show visible deviation from the experimental values in the high field region.

Nikonov has employed the finite difference method (FDM) in the parallel-plane breakdown numerical model of streamers in a short gap (0.05 cm) in the air at atmospheric pressure [Nikonov, 2001]. This model is based on the continuity equations. [Nikonov, 2001] provided the ionization coefficients as functions of the electric field in a wide range of the field (no limitations are indicated). However, their analytical ionization coefficient significantly differs from the experimental values obtained in high electric fields .

Numerical modelling of streamers in the parallel-plate electrodes with a separation of 2 mm has been carried out by Kang [Kang, 2003]. Two-dimensional (2D) models were developed and solved by FEM. However, in the models, the ionization coefficient as a function of the electric field was used only for the fields lower than 1000 Td. The paper does not provide the ionization coefficient for higher fields.

The finite element method (FEM), in conjunction with the flux corrected transport algorithm (FCT), was used in a three-dimensional (3D) point-plane model of a streamer in air at atmospheric pressure [Georghiou, 2005]. The authors compare their computational results and demonstrate that the FEM-FCT is better than FDM-FCT when the solution was obtained using the unstructured grids. However, the ionization coefficient in the model is presented for an unspecified range of electric fields, and it shows significant deviation from the experimental values in the high field.

In [Ducasse, 2007], a two-dimensional drift-diffusion model of positive streamer in the point-plane topology in air at atmospheric pressure has been developed. The gap separation was 1 mm and the applied voltage was 3 kV. The results show similar accuracy for both the FEM-FCT (finite element method - flux corrected transport), and the FVM-MUSCL (finite volume method - monotonic upwind-centered scheme for conservation-law) algorithm, but the computational cost of the FEM-FCT scheme is twice as expensive as the FVM-MUSCL. Furthermore, the ionization coefficient is provided for electric field less than 1000 Td. No ionization coefficient for the high field is provided in this paper.

Eichwald [Eichwald, 2018] has modelled a negative streamer in a parallel wire-wire topology in air at atmospheric pressure using a fluid approach (drift-diffusion approach). The simulation domain was a two-dimensional (2D) cylindrical symmetry domain with a gap between electrodes of 1 mm. The positive applied voltage is used. However, the model used the ionization coefficients, validated for fields less than 400 Td.

[Raizer, 1991] has provided the ionization coefficients for CO_2 only in a narrow range of the fields between ~1500 Td and ~3000 Td. The work conducted by Sandia National Laboratories [Sandia, 2003] does not provide the ionization coefficients for the field above 2500 Td in air and 2000 Td in N_2. [Hagelaar, 2005] provides the ionization coefficients for SF_6 in the extensive range of electric fields, but their analytical ionization coefficients show a visible deviation from the experimental values at high fields.

Such deviation may cause significant inaccuracy when modelling transient discharges and breakdown processes, especially in the high electric field. In order to address this issue, a comprehensive analysis of the available experimental and analytical values of the ionization coefficients for different gases is required. Accurate analytical equations for the swarm parameters will underpin modelling of the fast transient processes in gases, which is required for different practical power and pulsed power applications.

In the literature, the analytical equations for the swarm parameters including the effective ionization coefficient and electron mobility are available only in the limited range of electric fields. This restriction may lead to inaccuracies in simulation results if the used model(s) will rely on this limited range parameters. Thus, accurate representation of the swarm parameters in the wide range of electric fields is required for modelling of the transient plasma events in gases, including the transient pre-breakdown processes. Chapter 3 will discuss the comparison of the literature and experimental data and will provide an analytical representation of the effective ionization coefficients for air, N_2, CO_2 and SF_6.

2.7 Review of experimental data

The breakdown results can be different for different experimental conditions, for example, for different impulse waveforms, shapes of electrodes, gap distances, the presence or absence of initial ionizing photons and the measurement methodology. The following sections will provide an overview of the experimental tests regarding the methodologies and measurements taken from the selected literature for different gases.

In [Felsenthal, 1965], Felsenthal and Proud provide the results of their experimental breakdown characteristics of air and N_2 obtained in the impulsive regime in the uniform field. HV impulses with the rise time from 0.25 ns to 1.0 ns were used. The gap separation was from 0.13 cm to 6.0 cm. The pressure range was from 1 mmHg to 760 mmHg. A source of ultraviolet light was used to illuminate the cathode. The applied voltage was from 5 kV to 30 kV for air and from 4 kV to 20 kV for N_2. However, it is noted that the time to breakdown is the formative time (t_f). The results provided in this paper include the reduced electric field (E/p) as a function of the product of the pressure and formative time to breakdown (pt_f) for air; the measured formative time is from 0.5 ns to 18 ns. For N_2, the formative time is from 0.4 ns to 25 ns. The results show the time-field breakdown characteristics in the wide range of the

field. The highest electric field used in the air tests was up to 20000 Td and up to 10000 Td in N_2.

Mankowski, Dickens, and Kristiansen [Mankowski, 1998] have presented the test methodology and breakdown results in air and N_2. A Marx-bank-driven pulse forming line was built and delivered a voltage pulse of about 750 kV, with a rise time of ~400 ps and a pulse duration of 3 ns. For air, two electrode geometries were used to investigate the breakdown characteristics, including a hemispherical electrode with a gap distance from 1 mm to 3 mm at the pressure range of 100 kPa to 5.2 MPa, and a point-plane electrode with a gap from 2 to 4 mm at the pressure of 1.38 MPa and 2.75 MPa. Both polarities were used. The results show that for the point-plane electrode system, in the range of the breakdown time from 0.5 ns to 2 ns, the breakdown field for negative polarity is higher than the breakdown field in the case of positive polarity. Hemispherical electrodes with the gap separation from 1 mm to 3 mm were used to obtain the breakdown characteristics of N_2 in the pressure range from 240 kPa to 4.1 MPa. The breakdown electric field strength (E) as a function of the breakdown time (t_{br}) was obtained for N_2 in this pressure range. It is noted that the electric field was calculated as the applied voltage divided by the gap separation (even for the point-plane geometry). The breakdown time is the total time to breakdown (t_{br}), which is defined as "the time between the arrival of the incident voltage at the gap and the collapse of the voltage across the gap" [Mankowski, 1998]. The time-field breakdown characteristics in air were obtained for the fields lower than 3000 Td.

Kawada, Shamoto, and Hosokawa [Kawada, 1988] have performed experimental measurements of the breakdown characteristics in the uniform field in air and N_2 under impulsive voltages. The HV pulses with a 10.8 ns rise time and a half peak width of 30 and 74 ns were used in their tests. The pressure was in the range from 330 Torr to 1520 Torr (~44 kPa to ~ 202 kPa), and the gap distances between electrodes were 1 cm, 2 cm, and 3 cm in these experimental tests. Ultraviolet light produced by an external source was directed to the cathode. The authors obtained the breakdown voltage as a function of the product of the pressure (p) and the gap distance (d),

for *pd* from 1 atm·cm to 2.5 atm·cm. However, the result of breakdown time was not reported by the authors.

In [Dick, 2000], the investigation of the N_2 breakdown behaviour in the electrode system formed by hemispherical electrodes at different pressures has been performed by stressing the electrodes with voltage pulses with a rising time of 55 ns and a duration of 160 ns. The gap distance between the electrodes was 0.7 mm. The relationship between the reduced breakdown field (E/p) and the pressure (p) for N_2 was plotted and showed a linear decreasing slope of breakdown field (E/p) in the pressure range from 0.1 MPa to 4.93 MPa. The authors discussed that a significantly higher breakdown voltage could be achieved for HV impulses with sub-nanosecond rising time. The breakdown time was measured to explain the relationship between the electric field and the breakdown time.

Carboni, Lackner, and Giri [Carboni, 2001] designed monocone-plate and point-plane test systems to investigate the impulsive breakdown characteristics of different gases at different pressures. The Marx generator was used to generate the high voltage pulses with a rising time of ∽300 ps and duration of 5 ns. The gap distance between electrodes was set to 0.091 cm in the monocone-plate test system and to 0.18 cm in the point-plane test system. The authors reported the following experimental results: the breakdown field as a function of the pressure and the breakdown field as a function of the stress time for air and N_2 at the pressures from 30 atm to 100 atm. But it should be noted that the effective stress time (t_{eff}), which was introduced in this work, was defined as the time interval from 89% to 100% of the breakdown voltage.

An experimental investigation of the breakdown characteristics in the parallel-plane electrodes in air at different pressures in both, single and repetitive modes under ns pulse energization has been undertaken by Shao [Shao, 2006]. The breakdown field was defined as the breakdown voltage divided by the gap distance between the electrodes. The breakdown time lag (τ) was defined as "the time interval between the initial spike and subsequent large current rise" [Shao, 2006]. In the single pulse tests, the gap length between the electrodes was set to 10 mm with an accuracy of ± 0.1 mm.

The pressures of 0.1 MPa and 0.2 MPa were used. The single voltage pulses with a magnitude of 100 kV, a rising time of ~10 ns, and a half-peak duration of (20 - 30) ns were applied to the electrode system. The result of these tests was the breakdown time lag (τ) as a function of the gas pressure (p). In the repetitive pulse tests, HV impulses with a rate of 1 pulse per second were applied to the electrode, the gap distance of 15 mm was used, and the electric field in these tests was 66.7 kV/cm. The results of these tests include the reduced breakdown field (E/p) as a function of the product of the breakdown time lag and the pressure ($p\tau$). These characteristics were obtained in the E/p range from 60 V/(cm·Torr) to 160 V/(cm·Torr) (~181 Td to ~484 Td).

In [Ivanov, 2016], the experimental tests were carried out in N_2 at pressures of 5 atm, 10 atm, 20 atm, and 40 atm in the electrode system with the adjustable gap separation from 0.25 to 3 mm (0.05 mm error) in the uniform field. The overvoltage regime was used, and HV pulses with a rise time of 250 ps were used in these tests. Ivanov and Sharypov discussed the differences and effects of varying the pressure (p) and the electrode gaps (d) on the breakdown voltage (U_{br}) and the breakdown formation time (t_{form}). The breakdown voltage (U_{br}) as a function of the product of the pressure (p) and the gap distance between electrodes (d), the reduced breakdown electric field E/p as a function of the product of the breakdown formation time t_{form} were obtained. The results show that the average breakdown field decreases with an increase in the pressure and breakdown formation time (t_{form}). It is noted that the breakdown formation time (t_{form}) was introduced and defined as "the time passed after applying voltage to the gap until amplitude value U_{br} is reached."

Kumar, Huiskamp and Pemen [Kumar, 2021] have performed the experimental measurements of the impulsive breakdown characteristics of CO_2 in the rod-plane and point-plane geometries using positive and negative polarity. The HV impulses with the total rise time of 2 μs and the fall time of 160 μs were used in these breakdown tests. The breakdown voltage (U_{br}) as a function of the gas pressure (p), and the breakdown voltage as a function of the breakdown time lag are provided for both polarities. For the rod-plane breakdown tests conducted in CO_2 at different pressures, the pressure in the range from 0.1 MPa to 0.3 MPa was used. The gap separation from

the rod electrode with a diameter of 20 mm to the plane electrode was 30 mm. The maximum electric field was calculated using COMSOL Multiphysics software. It has been observed that the breakdown field for the positive impulses is higher than that for the negative impulses at the increased gas pressure. The breakdown time lag shows a decreasing trend with an increase in the breakdown voltage. For the point-plane tests in CO_2, the gap distance between the tip of the point electrode with a diameter of 1 mm, which was attached to a sphere with a diameter of 40 mm, and the plane grounded electrode was 15 mm. The pressure in the range from 0.1 MPa to 0.5 MPa was applied. It can be seen from the experimental results that the breakdown voltage for the positive polarity impulses is much lower than that for the negative polarity impulses. It is noted that the breakdown time lag is defined as "the time duration between half the maximum amplitude of the pulse." [Kumar, 2021]. The results (time-field breakdown characteristics) were obtained for the fields up to 200 Td only.

Following this comparison of the experimental settings and breakdown characteristics, this section also discusses the original experimental results. For the purpose of finding a scaling relationship between the breakdown time, breakdown field and the particle number density, the field-time breakdown characteristics will be used in the present work. It is proposed to conduct this comprehensive analysis in order to establish the scaling relationship between the product of the time to breakdown and the particle number density and the reduced electric field for different gases in a wide range of the electric fields, E/N, in the impulsive, sub-μs breakdown regime.

It is known that both time to breakdown and breakdown electric field positively correlate with the particle number density, N. There is evidence that if N is changed by changing gas pressure or temperature, the product of the time to breakdown and the number density (tN) and the reduced electric field, E/N, are changed. Thus, it is important to assess the sensitivity of the breakdown characteristics to changes in these parameters. Also, it is of great interest to obtain the time-field breakdown characteristics for larger values of E/N.

It also has been noticed that Felsenthal and Proud used the formative time, t_f, to obtain the field-time breakdown characteristic of various gases stressed with the fast-rising pulsed voltage in the uniform field [Felsenthal,1965]. From another point of view, Carboni used the effective stress time, t_{eff}, defined as the time interval between 89% and 100% of the breakdown voltage [Carboni, 2001] to plot the field-time breakdown characteristics. Other researchers obtained the breakdown time, defined as the time interval from the moment of voltage application to the breakdown moment i.e., the voltage collapse moment. Such impulse waveforms, their rise time, duration, and fall time described above are classified as non-standard waveforms of HV impulses.

In addition, the breakdown events were obtained under different test conditions, for example with or without UV illumination. For example, [Kawada, 1988], [Felsenthal, 1965] used UV light to stimulate the development of breakdown, whereas other research papers discussed here did not. The UV illumination directly affects the statistical time, i.e., the time required for the first electron to appear in the gap. The statistical time during the breakdown process will be significantly shortened or completely eliminated in this case. Thus, it is difficult to compare the reported breakdown results directly if the test conditions are different.

As shown in Table 2.1, different conditions used in the experimental tests by different authors make it difficult to conduct a direct comparison and analysis of the obtained results. For example, different definitions of breakdown time, rise time and delay time are used by different authors. It may be problematic to discriminate the impact of each of these factors on the breakdown characteristics.

Therefore, it is essential to establish a specific methodology of investigation of the breakdown voltage and time to breakdown to examine the breakdown characteristics. This will help to evaluate and provide further understanding of the breakdown characteristics in transient regimes.

Table 2.1 Comparison of experimental conditions

	Literature	Gas	Geometry	Distance between electrodes	Rise time of waveform	Test condition	Breakdown characteristics measured
1	[Felsenthal, 1965]	Air	Parallel-plane	1.3 to 60 mm	0.25 to 1 ns	UV illumination	U_{br}, t_f
		N_2	Parallel-plane	1.3 to 60 mm	0.25 to 1 ns	UV illumination	
2	[Mankowski, 1998]	Air	Hemispherical electrodes	1 to 3 mm	400 ps		U_{br}, t_{br}
		Air	Point-plane	2 to 4 mm	400 ps		
		N_2	Hemispherical electrodes	1 to 3 mm	400 ps		
3	[Kawada, 1988]	Air	Parallel-plane	10 to 30 cm	10.8 ns	UV illumination	U_{br}
		N_2	Parallel-plane	10 to 30 cm	10.8 ns	UV illumination	
4	[Dick, 2000]	N_2	Hemispherical profile	0.7 mm	55 ns		U_b
5	[Carboni, 2001]	Air	Monocone	0.91 mm	∽300 ps		U_{br}, t_{eff}
		N_2	Monocone	0.91 mm	∽300 ps		
		N_2	Point-plane	1.8 mm	∽300 ps		
6	[Shao, 2006]	Air	Parallel-plane	10 mm	∽10 ns		U_{br}, τ
		N_2	Parallel-plane	10 mm	∽10 ns		
7	[Ivanov, 2016]	N_2	Parallel-plane	0.25 to 3 mm	250 ps		U_{br}, t_{form}
8	[Kumar, 2021]	CO_2	Rod-plane	30 mm	2 μs		U_{br}, T
		CO_2	Point-plane	15 mm	2 μs		

2.8 Pulse forming line and Blumlein topologies for generation of HV impulses

This section overviews the basic pulse power topologies used in the present work to generate defined HV impulses. This analysis underpins the development and characterization of the Blumlein power generator system, which will provide support for the experimental work in Chapter 5.

Pulsed power is a technology of increasing instantaneous power by accumulating and storing electrical energy over a comparatively long time interval and then releasing it in a much shorter time interval. This technology can be used in different pulsed power applications, such as the generation of electrical discharges in gaseous, solid and liquid dielectrics, generation of transient plasma for different practical applications, [Mesyats, 2005].

High voltage pulses can be generated by accumulating energy in a capacitor, and then releasing this energy into a load using closing switch [Mesyats, 2005]. Pulse generators generally can be categorized into two main types: the circuits based on capacitive energy storage and transmission line-type pulse generators [Glasoe, 1948]. In terms of transmission line-type pulse generators, the pulse forming line (PFL) is one of the well-known topologies used to generate defined HV impulses. The basic PFL circuit consists of a transmission line (coaxial cable) charged through a charging resistor and a closing switch connected in series to a load. A schematic diagram of the basic PFL circuit is shown in Figure 2.7.

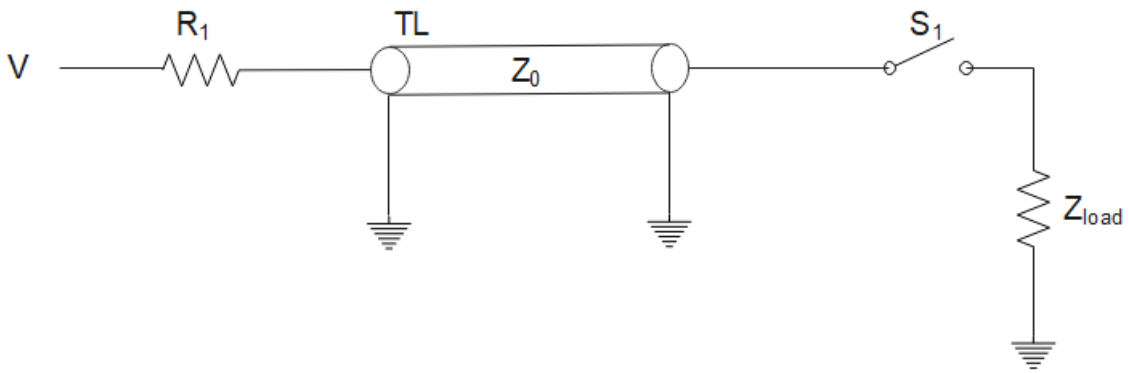

Figure.2.7 Basic PFL circuit [Wilson, 2011]

In Figure 2.7 *V* is the voltage of a DC charging source, Z_{load} represents the load impedance, R_1 is the charging resistor, *TL* is the loss-free transmission line. Z_0 is the characteristics impedance of the transmission line, defined as

$$Z_0 = \sqrt{L'/C'} \tag{2.13}$$

where *L'* and *C'* are the distributed inductance and capacitance of the transmission line.

The value of the characteristic impedance depends on the geometry of the line, relative permittivity and relative permeability of the insulating material of the coaxial cable. The velocity of propagation of impulse along the transmission line, u_p, is

$$u_p = \frac{c}{\sqrt{\mu_r \varepsilon_r}} \tag{2.14}$$

where, u_p is the velocity. c is the speed of light. μ_r is the relative magnetic permeability, and ε_r is the relative electrical permittivity.

Initially, the transmission line is charged to a source voltage *V* through the charging resistor. When switch S_1 closes, the impulse with a magnitude of half the charging

voltage and duration of two transient times is generated across the load. If the load impedance is equal to the impedance of the transmission line, there will be no reflections in the circuit and a well-defined HV impulse will appear across the load.

The Blumlein generator is another topology commonly used to generate HV impulses, this topology was proposed by Alan Blumlein in 1937. The circuit shown in Figure 2.8 is a schematic representation of the Blumlein pulse generator. This topology is used to produce HV impulses with the same magnitude as charging voltage, *V*. A fast rise time can be achieved using this Blumlein topology. A *DC* source is used to charge the transmission lines through charging resistor *R1*, and a load is connected directly between two transmission lines.

When switch S_1 is closed, the output impulse appears across the load. If the load impedance equals the impedance of the transmission line multiplied by 2, $Z_{load} = 2Z_0$, the output voltage impulse across the load will have a trapezoidal waveshape shown schematically in Figure 2.9.

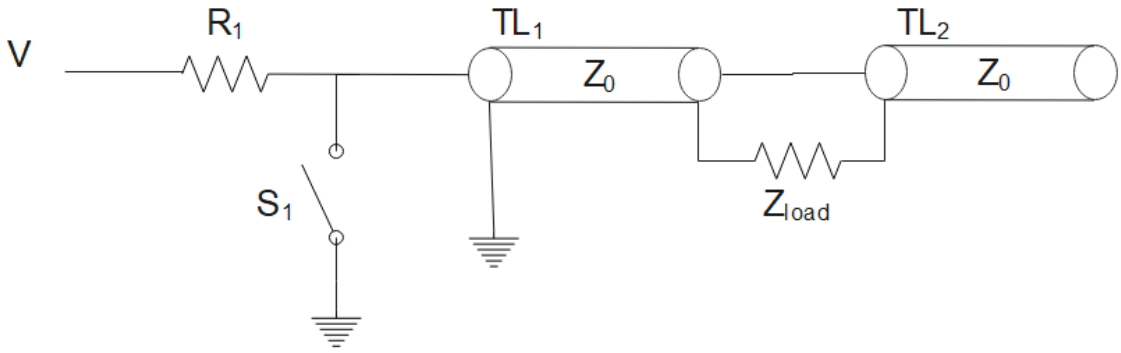

Figure. 2.8 Blumlein circuit [Wilson, 2011]

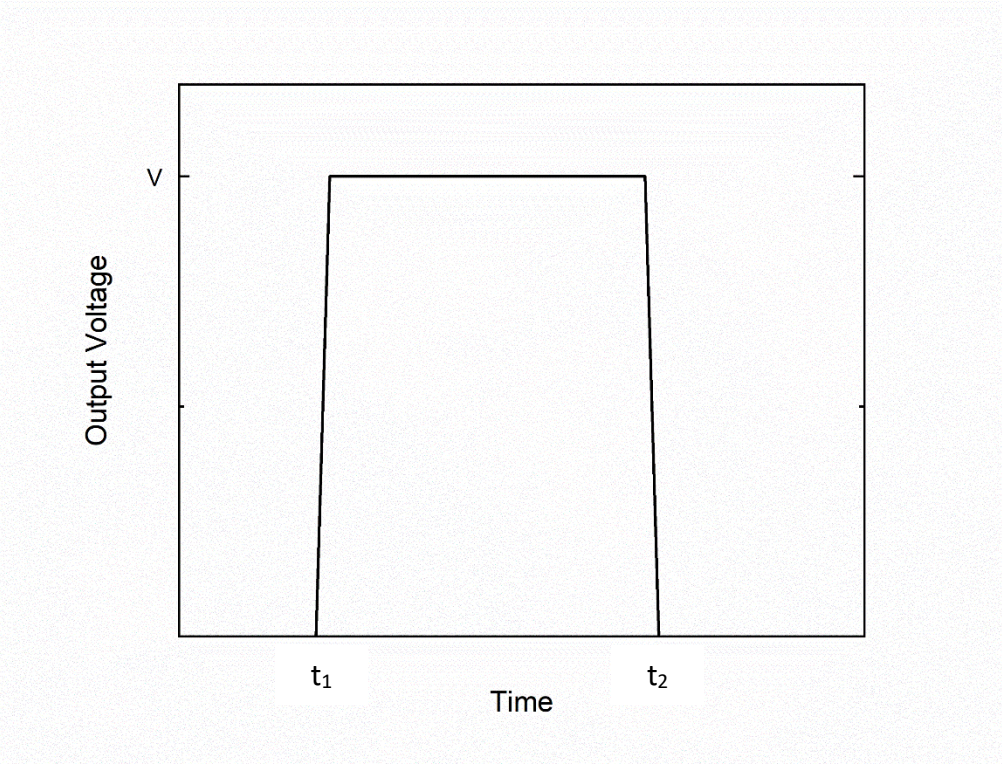

Figure. 2.9 Output voltage waveform of the Blumlein circuit across matched load

The Blumlein pulsed power topology was used in this work to produce high voltage impulses to study the breakdown characteristics of different gases. Sections 5.2-5.3 will describe and model the Blumlein pulsed power generator used in the present work.

There are two main reasons which underpin selection of the Blumlein generator for the experimental tests. This generator provides a fast rise time and high *dV/dt*, and it does not store a significant amount of energy, thus the overvolted regime is achieved and the erosion of electrodes is minimized.

2.9 Discussion and conclusion

The basic breakdown mechanisms have been discussed in the present review. In order to model the gas discharge processes and breakdown characteristics, the swarm and transport parameters of gases are required, these parameters have also been discussed in this chapter. The simulation approaches used to model fast transient plasma

processes in gases have been presented and discussed. Moreover, the experimental results on gas discharges and breakdown behaviour of different gases available in the literature have been described and analysed in this chapter.

The electron swarm parameters play an important role in modelling of fast ionisation processes in gases. The accuracy of the analysis of the pre-breakdown processes and breakdown characteristics in different gases and different electrode topologies depends on information on the swarm parameters. The research completed to date highlights the requirements for analytical representation of the swarm parameters in a wide range of electric fields. Nevertheless, in many publications these parameters are provided only for a limited range of *E/N*; for example, in the models presented by [Kulikovsky, 1997], [Serdyuk, 2013], [Eichwald, 2018] the ionization coefficients were provided only for electric fields which do not exceed 1000 Td.

However, the reduced electric fields above 1000 Td are used in different practical applications, such as gas-filled plasma closing switches. Therefore, analysis of the breakdown behaviour of different gases requires further understanding and detailed information on the swarm parameters in such high electric fields. Accurate and efficient model(s) of complex discharge processes in common and environmentally friendly gases are required for optimisation of gaseous insulation in different HV power and pulsed power applications.

These models and the obtained results will contribute to further understanding of the breakdown behaviour of gases and will help to optimise and coordinate gaseous insulation in different high voltage applications. The detailed analysis of the transport and ionization parameters in air, N_2, CO_2, and SF_6 will be examined in Chapter 3, and the analytical models will be presented and discussed in Chapter 4.

Furthermore, it is of great interest to investigate experimentally the time-field breakdown characteristics of common and environmentally friendly gases in a wider range of *E/N* in the impulsive, sub-μs breakdown regime.

As discussed in Section 2.7, the breakdown time presented in the literature is typically measured under different experimental conditions. Thus, it is often problematic to conduct direct comparison between breakdown characteristics presented in different research papers. To provide better understanding of the breakdown characteristics in impulsive breakdown regimes, it is vital to establish an accurate–measurement methodology and to examine the time-field breakdown characteristics of common and environmentally friendly gases.

Thus, the main objective of the experimental part of this work is to investigate the breakdown characteristics of air, N_2, and CO_2 stressed with sub-µs HV impulses in the electrode topology formed by the needle-plane electrodes in a wider range of electric fields. The detailed description of the experimental system used in this work and the obtained results will be presented and discussed in Chapter 5.

Chapter 3 Swarm parameters in air, N_2, CO_2 and SF_6

3.1 Introduction

The swarm parameters, including the swarm coefficients and transport parameters of electrons in different gases, have been discussed in Chapter 2, that presents an overview of the data currently available in the literature, the progress in modelling of the plasma fronts, and the limitations of current approaches. In order to improve the accuracy of modelling and to increase the range of applicability of simulation models, it is necessary to obtain accurate analytical functions of the swarm parameters in a wide range of electrical fields.

This chapter aims to examine the key swarm parameters: the main transport coefficients (the drift velocity, the mobility and the diffusion coefficient); and the parameters used in the streamer modelling: the first ionization (Townsend) coefficients, the electron attachment coefficient and the net electron production rate per unit length. These swarm parameters will be presented as functions of the reduced electric field, *E/N*.

Also, the critical field, i.e., the field at which (α-η)=0, is obtained for different gases. The comprehensive study of the experimental data available in the literature is conducted in the present chapter. The literature data on the swarm parameters in air, N_2, CO_2, and SF_6 are collected and thoroughly analysed. As a result of this study, the analytical expressions for the swarm parameters as functions of the reduced electric field are obtained by finding and fitting the most suitable analytical functions to the experimental data. This study provides analytical expressions for the swarm

parameters for the selected gases in a wide range of electric fields, that will underpin the drift-diffusion and kinetic modelling of the fast ionization fronts in these gases.

The developed analytical expressions for the effective ionization coefficients are used to determine the critical field, which aims to evaluate potential differences in the breakdown behavior of air, N_2, CO_2, and SF_6.

Following that, the products of the electron mobility and gas number density are plotted as a function of the reduced electric field for air, N_2, CO_2, and SF_6. These μN functions are fitted with analytical fitting lines for the further use in the drift-diffusion and kinetic models.

3.2 Ionization, attachment and effective ionization coefficients

A significant number of experiments have been conducted to investigate the swam parameters in gases, and their results are available in the literature. For example, Dutton [Dutton, 1975] provides experimental data on the electron swarm parameters in different gases, including their transport and ionization coefficients. Gallagher [Gallagher, 1983] reports the data on the electron swarm coefficients in the electronegative gases, including SF_6, CO_2, air, and O_2. Morrow [Morrow, 1997] provides the functional equations of the swarm parameters in air. [Dutton, 1975], [Gallagher, 1983], [Morrow, 1997] used the first ionization coefficients normalized by the particle density (α/N) as functions of the reduced electric field (E/N) to express the relationship between the ionization coefficient and the electric field. The attachment coefficient also was normalized by the particle number density (η/N) and presented as a function of the reduced electric field (E/N) to express the relationship between the attachment coefficient and the electric field. Moreover, Nikonov [Nikonov, 2001] proposes an air discharge model employing the fitting function for the ionization coefficient (α) as a function of the reduced electric field (E/p) and the attachment coefficient (η) as a function of the reduced electric field (E/p), similar

parameters used in [Novak, 1988]. Furthermore, [Sandia, 2003] presents the results of breakdown modelling in different nonuniform geometries in air and provides the effective ionization coefficient for air normalized by pressure (α_{eff}/p) as a function of the reduced electric field (*E/p*).

The ionization and attachment processes can be expressed as: the reduced first ionization coefficient (α/N *or* α/p) as a function of the reduced electric field (*E/N* or *E/p*), the reduced attachment coefficient (η/N or η/p) as a function of the reduced electric field (*E/N* or *E/p*), and the reduced effective coefficient (α_{eff}/N or α_{eff}/p) as a function of the reduced electric field (*E/N* or *E/p*).

To identify potential disagreements between different representations of the ionization and attachment coefficients, the coefficients that are expressed as the effective ionization coefficients obtained from the literature have been presented in a single graph for each gas. These coefficients have been normalized and plotted as reduced effective coefficients (α_{eff}/N) (*E/N*) in Figures 3.1.1-3.4.2.

After presenting all available experimental and analytical coefficients in a single graph, these data have been fitted with the selected analytical functions using the OrginPro graphing software.

3.2.1 Air

Table 3.1 presents the analytical equations for the ionization, the attachment and the effective ionization coefficients for air obtained through comprehensive analysis of the available literature data. The analytical equations for the coefficients are provided together with the field ranges in which they are valid.

TABLE 3.1

Analytical equations for α/N, η/N and α_{eff}/N in air

Air	Analytical equations for ionization and attachment coefficients
[Morrow,1997]	$\alpha/N(m^2) = 2 \cdot 10^{-16} \cdot \exp(-7.248 \cdot 10^{-15}/\left(\frac{E}{N}/10^{17}\right)) \cdot 10^{-4}$ $E/N > 150\text{Td}$ $= 6.619 \cdot 10^{-17} \cdot \exp(-5.593 \cdot 10^{-15}/\left(\frac{E}{N}/10^{17}\right)) \cdot 10^{-4}$ $E/N \leq 150\text{Td}$ $\frac{\eta}{N}(m^2) = (8.889 \cdot 10^{-5} \cdot \left(\frac{\frac{E}{N}}{10^{17}}\right) + 2.567 \cdot 10^{-19}) \cdot 10^{-4}$ $E/N > 150\text{Td}$ $= (6.089 \cdot 10^{-4} \cdot \left(\frac{\frac{E}{N}}{10^{17}}\right) - 2.893 \cdot 10^{-19}) \cdot 10^{-4}$ $70\text{Td} < E/N \leq 150\text{Td}$
[Kulikorsky,1997]	$\alpha/N(m^2) = 1.4 \cdot 10^{-16} \cdot \exp(-660/\left(\frac{E}{N}\right)) \cdot 10^{-4}$ $\frac{\eta}{N}(m^2) = 6 \cdot 10^{-19} \cdot \exp(-100/\left(\frac{E}{N}\right)) \cdot 10^{-4}$ $10\text{Td} < E/N < 800\text{Td}$

[Nikonov,2001]	$\alpha\ /N(m^2) = 1.18 \cdot 10^{-20} \cdot \exp\left(-701.08/\left(\frac{E}{N}\right)\right)$ $E/N < 327.24\text{Td}$ $= 4.4 \cdot 10^{-20} \cdot \exp\left(-1080.45/\left(\frac{E}{N}\right)\right)$ $E/N > 327.24\text{Td}$ $\eta/N\ (1/m) = \max\left(13.55/(E/N)/N; 4.88\right.$ $\left. \cdot 10^{-4}\left(\frac{E}{N}\right)^2/N\right)$ $E/N < 30.3\text{Td}$ $= 4.88 \cdot 10^{-4}\left(\frac{E}{N}\right)^2$ $30.3\text{Td} < E/N < 151.5\text{Td}$ $= 0.91\left(\frac{E}{N}\right)^{0.5}$/N $151.5\text{Td} < E/N < 272.7\text{Td}$ $= 81.57\left(\frac{E}{N}\right)^{0.5}$/N $E/N > 272.7\text{Td}$
[Sandia, 2003]	$\alpha_{eff}\ /\text{N}\ (m^2) = 4.55 \cdot 10^{-20} \cdot \exp\left(-1107.77/\left(\frac{E}{N}\right)\right)$ $E_s/N \leq E/N \leq 2424\text{Td}$ $= 2.36 \cdot 10^{-20} \cdot \exp\left(-749.19/\left(\frac{E}{N}\right)\right.$ $60.6\text{Td} \leq E/N \leq E_s/N$ $E_s/N = 545.4\text{Td}$
[Eichwald,2018]	$\alpha_{eff}\ /N\ (m^2) = 4.77 \cdot 10^{-4} \cdot (\frac{E}{N} - 94.7)^2 \cdot 10^{-4}$ $\cdot 10^{-18}$ $94.7\text{Td} < E/N < 400\text{Td}$

The analytical equations obtained for the reduced ionization and attachment coefficients in air are based on data by [Morrow, 1997], [Kulikovsky, 1997], and [Nikonov, 2001]. The reduced effective ionization coefficient in air is based on the results by [Eichwald, 2018], [Sandia, 2003], Table 3.1. The obtained equations for α_{eff} have been normalized by N and converted into α/N, η/N and α_{eff}/N in SI units for further use in the drift-diffusion and kinetic models.

For the purpose of comparing the coefficients in a complete picture, the reduced effective ionization coefficients in air (α_{eff}/N) presented in Tables 3.1-3.4 have been plotted as functions of the reduced electric field (*E/N*) in Figures 3.1.1-3.4.2 using OriginPro graphing software.

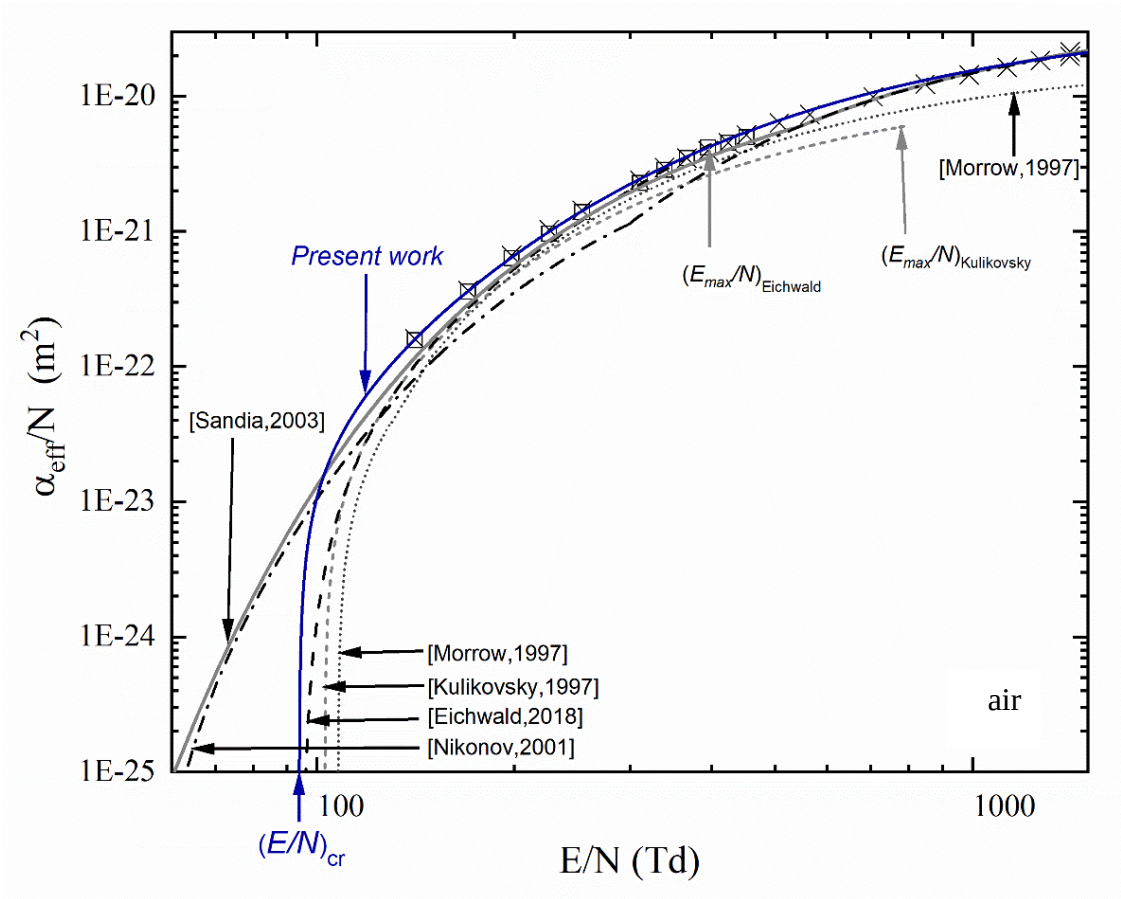

Figure 3.1.1 α_{eff}/N as a function of E/N in air. Experimental data: ☐, [Sanders, 1933]; × [Masch, 1932]. Fitting curves: dashed line, [Eichwald, 2018]; short, dashed line, [Kulikovsky, 1997]; grey short, dotted line, [Morrow, 1997]; dashed dotted line, [Nikonov, 2001]; solid grey line, [Sandia, 2003]. Fitting curve: solid blue line, the present work. E_s/N represents the transition between different fitting curves from [Sandia, 2003] and [Nikonov, 2001]; E_{max}/N represents maximum value of E/N for fitting curves [Kulikovsky, 1997] and [Eichwald, 2018]. $(E/N)_{crit}$ shows the asymptotic value of the critical normalized field

[Kulikorsky, 1997], [Sandia, 2003] and [Eichwald, 2018] provided their analytical expressions for the swarm parameters only within the limited range of electric fields in Figure 3.1.1. [Morrow, 1997] and [Nikonov, 2001] report these coefficients for a wider range of E/N. However, their analytical expressions show notable deviation from the experimental data provided in [Sanders, 1933] [Masch, 1932]. It has been found that these coefficients are lower than the experimental data in the range of fields from ~150Td to ~1500 Td, especially when the electric field is higher than 600 Td. For these high fields, the expressions given in [Kulikorsky, 1997] and [Morrow, 1997]

show significantly lower values of the ionization coefficient as compared with the experimental data by [Masch, 1932].

Therefore, it is important to address this issue of discrepancy between the analytical expressions for the ionization coefficient available in the literature and the experimental data. For accurate modelling of the fast transient processes, it is necessary to establish accurate analytical expressions for the swarm coefficients in a wider range of electric fields.

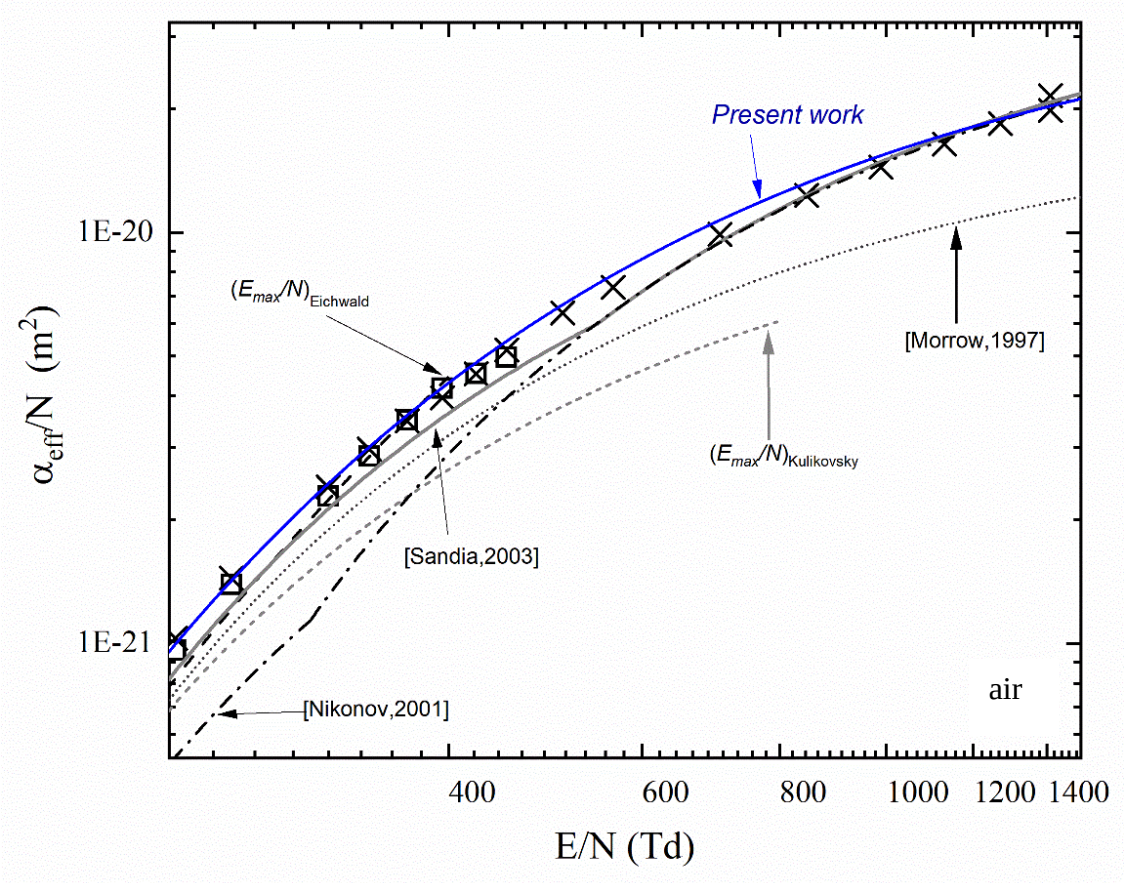

Figure 3.1.2 A zoomed view of Figure 3.1.1 in the range of the normalized electric field *E/N* from ~300 Td to ~1500 Td.

Figure 3.1.2 presents a zoomed view of a section of Figure 3.1.1. As Figure 3.1.2 shows, there is a discrepancy between different representations of the ionization coefficient available in the literature, especially in the range of the normalized electric field from ~300 Td to ~1500 Td. There are abrupt changes (kinks) in the ionization

coefficient curves obtained by [Sandia, 2003] and [Nikonov, 2001], which represent the transition between different parts of the fitting curves.

The maximum field value, E_{max}/N, represents the maximum value of E/N for each specific fitting range. For example, [Kulikovsky, 1997] and [Eichwald, 2018] provide their fittings within the limited range of electric fields for $E_{max}/N < 800$ Td.

The ionization coefficient obtained by [Nikonov, 2001] is fitted with a good accuracy in the range of high electric fields, from ~700 Td to ~1500 Td. Nevertheless, this fitting provides the ionization coefficient lower than the experimental values for lower electric fields, between ~150 Td and ~400 Td.

Furthermore, the magnitude of the ionization coefficient provided by [Morrow, 1997] and [Kulikovsky, 1997] is slightly underestimated in the range of E/N between ~150 Td to ~350 Td compared with the experimental data given in [Sanders, 1933]. However, with an increase in the electric field, the magnitude of the reduced ionization coefficient is lower than the experimental data in the range of the electric field E/N from ~600 Td to ~1500 Td.

It is worth noting that, as expected at high E/N up to 1500 Td, the reduced effective ionization coefficient is in accordance with the literature data [Sanders, 1933] and [Masch, 1932]. However, for E/N above 300 Td, the analytical fitting from [Kulikovsky, 1997] becomes lower when compared with the experimental results obtained from [Masch, 1932], as presented in Figure 3.1.2.

In the present work, a fitting curve for the reduced effective ionization coefficient in air has been constructed using the experimental data for the ionization coefficients from [Sanders, 1933] and [Masch, 1932]. The experimental data points were fitted with an exponential function using OriginPro (v.2021) graphing software, and this fitting curve is given by Equation 3.1

$$\alpha_{eff}/N = 4\cdot10^{-20} exp\,(-985/\,(E/N+43)) - 30\cdot10^{-24}\ (m^2)$$
$$94\ \text{Td} < E/N < 1500\ \text{Td} \qquad (3.1)$$

where α_{eff}/N is the reduced effective ionization coefficient in m^2, and E/N is the reduced electric field in Td.

The analytical blue solid line curve for air is shown in Figure 3.1 (referred to as "the present work"), providing a good agreement with the experimental data in a wide range of the reduced electric fields from 94 Td to 1500 Td. It has been found that this fitting line has provided a smooth fitting in the whole range of the electric fields without transition point.

The present work compares the fitting from the exponential solution and some literature measurements for the reduced effective ionization coefficient in air. A good agreement is observed between the experimental results and the proposed analytical equation.

3.2.2 N_2

As N_2 is an electropositive gas, the attachment coefficient of this gas is zero, $\eta = 0$, and the reduced effective ionization is $\frac{\alpha_{eff}}{N} = (\alpha - \eta)/N = \alpha/N$. The reduced ionization coefficient for N_2 as a function of E/N has been compared with the experimental data taken from [Bowls,1938] and the UNAM database [UNAM database, 2022]. The analytical functions of α/N have been taken from [Raizer, 1991], [Sandia, 2003], [Davies, 1978], [Dhali, 1987], [Vitello, 1994].

TABLE 3.2

Analytical equations of ionization coefficient for N_2

N_2	Analytical equations of ionization coefficient
[Dhali, 1987] [Vitello,1994] [Davies, 1971]	$\alpha/N(m^2) = 1.73 \cdot 10^{-20}(exp)^{-\frac{789.1}{E/N}}$
[Sandia, 2003]	$\alpha/N(m^2) = 3.12 \cdot 10^{-22}(exp)^{-\frac{429.33}{E/N}}$ $60.6\text{Td} \leq E/N \leq 90.9\text{Td}$ $= 2.67 \cdot 10^{-20}(exp)^{-\frac{834.62}{E/N}}$ $90.9\text{Td} \leq E/N \leq E_s/N$ $= 3.64 \cdot 10^{-20}(exp)^{-\frac{1037.96}{E/N}}$ $654.48\text{Td} \leq E/N \leq 1818\text{Td}$

As shown in Table 3.2, the analytical expressions from the literature have been converted into the unit of Td to compare the reduced effective ionization coefficient (α_{eff}/N) as a function of the reduced electric field (*E/N*) for N_2.

[Dhali, 1987] and [Sandia, 2003] provide only the reduced ionization coefficient, α/N, which is the same as the reduced effective ionization coefficient $\alpha_{eff}/N = \alpha/N$ due to the electropositive nature of N_2.

As shown in Figure 3.2, the ionization coefficient provided in [Sandia, 2003] is in a good agreement with the experimental data presented in [Bowls,1938] and in the UNAM database [UNAM database, 2022] in the field range from 60.6 Td to 1818 Td. However, no ionization coefficient for N_2 was provided for the fields above this value.

The ionization coefficient for N_2 as a function of *E/N* used by [Dhali, 1987], [Vitello, 1994] and [Davies, 1971], shows a good agreement with the experimental data of [Bowls, 1938] and UNAM database [UNAM database, 2022] in the range of *E/N* from 60 Td to 500 Td, but when the electric field increased above 500 Td, the analytical fitting for the ionization coefficient becomes lower than the experimental data.

In the present work, the reduced effective ionization coefficient for N_2, as a function of the reduced electric field *E/N*, $\frac{\alpha_{eff}}{N}(\frac{E}{N}) = \frac{\alpha}{N}(\frac{E}{N})$ has been reconstructed by fitting an analytical exponential function to the experimental data obtained from the literature.

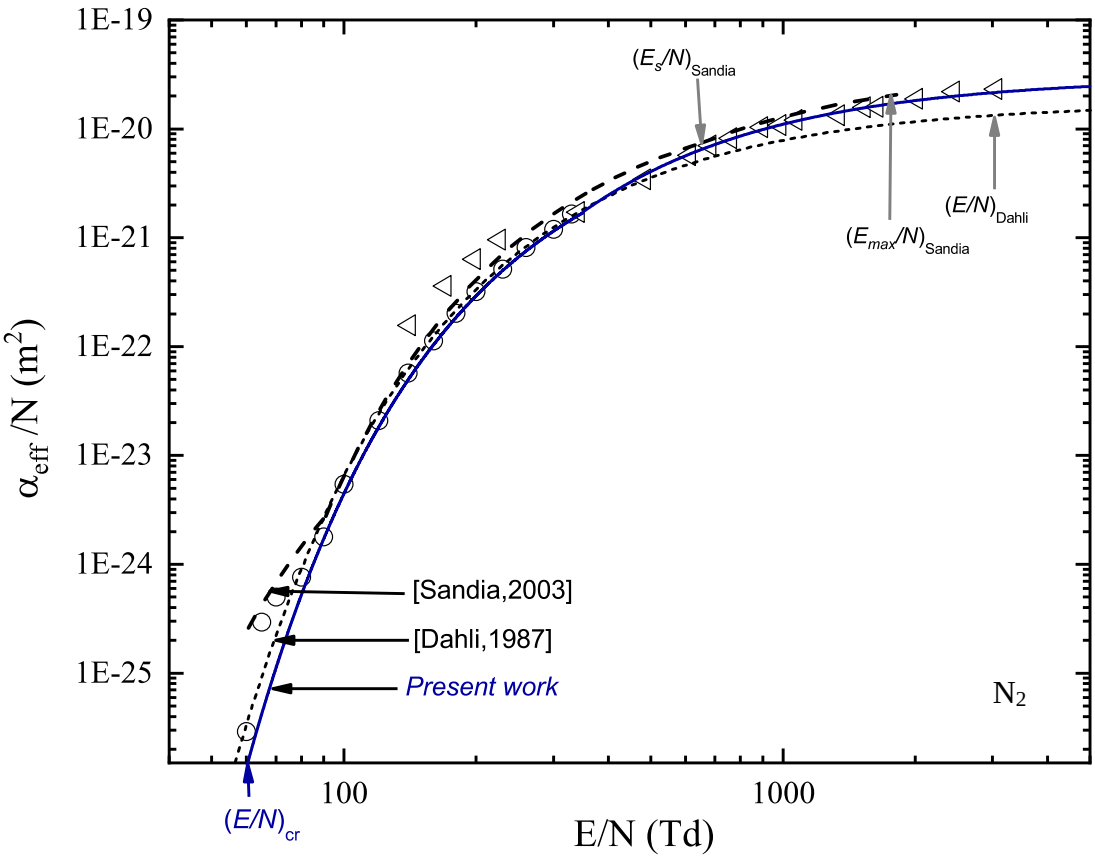

Figure 3.2.1 The effective ionization $(\alpha)/N$ in m^2 as a function of reduced electric field E/N in Td for N_2. ◅: experimental data from [Bowls, 1938];○: experimental data from [UNAM database, 2022], Dash: fitting curve from [Sandia, 2003]; dot: fitting curve from [Davies, 1978], [Dhali, 1987], [Vitello, 1994]; solid blue line: fitting curve obtained in the present work ($60\text{Td} < E/N < 5000\text{Td}$). *$(E/N)_{crit}$* shows the asymptotic value of the critical normalized field

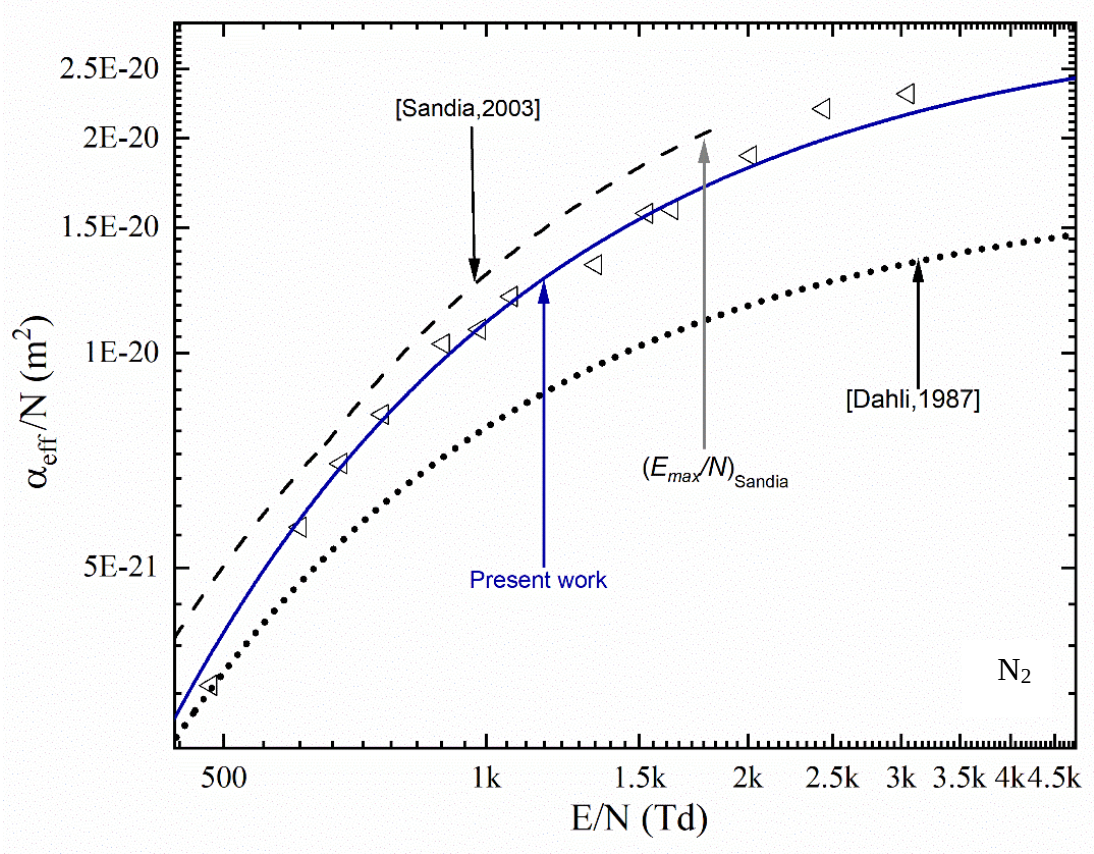

Figure 3.2.2 A zoomed view of the part of Figure 3.2.1

Figure 3.2.2, which is a zoomed view of Figure 3.2.1, provides the effective ionisation coefficient at higher values of the field. E_{max}/N used in [Sandia 2003] is ~2000 Td. The analytical function for the ionization coefficient is provided by [Dahli, 1987] in the range of the fields from 500 Td to 4500 Td. However, this function significantly underestimates the coefficient compared to the experimental data from [Bowls, 1938].

The ionization coefficient curve shown in Figure 3.2.1 has been obtained by fitting the analytical function given by Equation (3.2) to the experimental data from [Bowls, 1938] and [UNAM database, 2022] using the OriginPro (v.2021) graphing software. The following analytical fitting equations for the ionization coefficients in nitrogen have been obtained

$$\alpha/N = 1.7\cdot10^{-20} exp\ (-800/(E/N-3)) \quad (m^2)$$
$$60\ Td < E/N < 350\ Td$$
$$\alpha/N = 3\cdot10^{-20} exp\ (-1000/(E/N)) \quad (m^2) \qquad (3.2)$$
$$350\ Td < E/N < 5000\ Td$$

where, α_{eff}/N is the reduced effective ionization coefficient in the unit of m^2, and E/N is the reduced electric field in Td.

The analytical fitting, Equation (3.2), for N_2 shown in Figure 3.2.1 is in line with the experimental data from [Bowls, 1938] and [UNAM database, 2022] in a wide range of the reduced electric fields from ~60 Td to ~5000 Td.

3.2.3 CO_2

For CO_2, the experimental data for the effective ionization coefficient as a function of the reduced electric field were obtained from [UNAM database, 2022]. These data have been used in the present work to derive an analytical function for the ionization coefficient.

Together with experimental data, the functional dependencies $\alpha_{eff}/N(E/N)$ taken from [Raizer, 1991] have been used in this comparative analysis. These functions are provided in Table 3.3.

TABLE 3.3

Analytical equations for ionization coefficient for CO_2

CO_2	Analytical equations of ionization coefficient
[Raizer,1991]	$\alpha_{eff}/N(m^2) = 6.07 \cdot 10^{-20} \cdot (-1414.3/\frac{E}{N})$ $1515\ \text{Td} < \frac{E}{N} < 3030\text{Td}$

As shown in Table 3.3, [Raizer, 1991] provides the analytical expression for the reduced effective ionization coefficient as a function of the reduced field strength in a very limited field range, only from 1515 Td to 3030 Td.

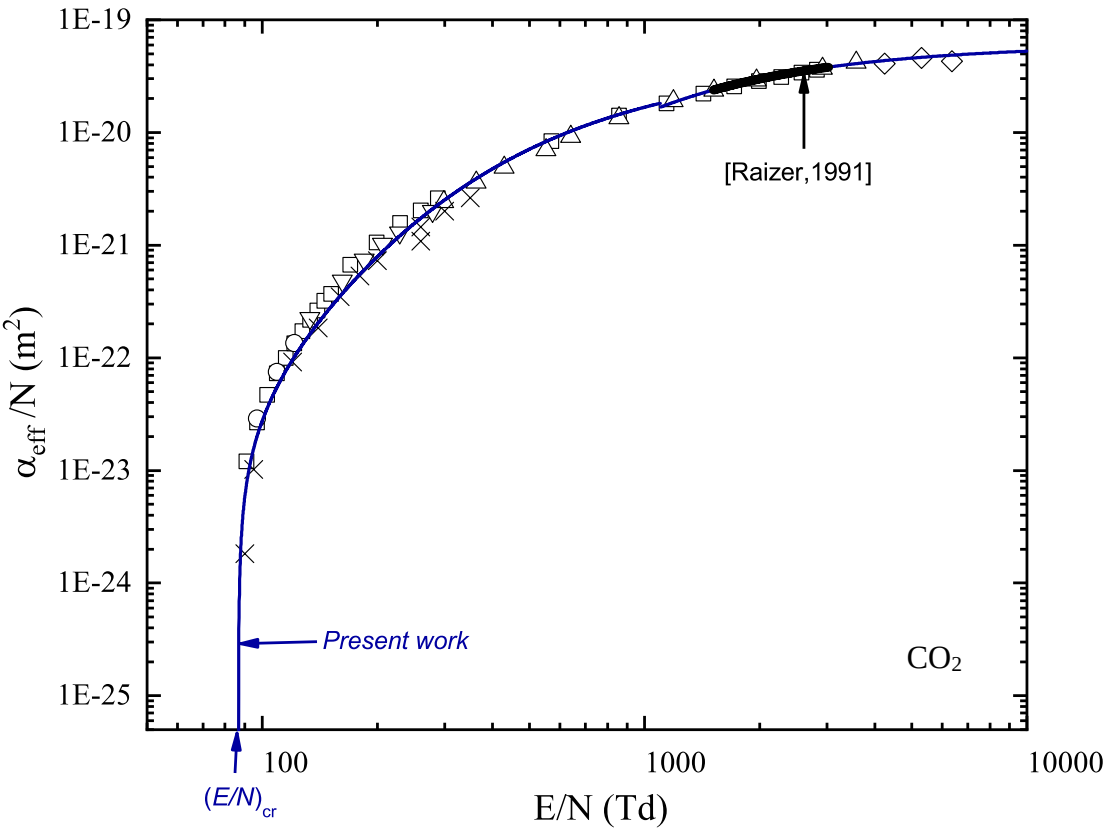

Figure 3.3.1 α_{eff}/N as a function of E/N in CO_2. Experimental data points: × [UNAM database, 2022], □, ○, ▽, △ and ◇, [Dutton database, 2022]. Fitting curves: bold solid line, [Raizer, 1991]; solid line, the present work. $(E/N)_{crit}$ shows the asymptotic value of the critical normalized field

In Figure 3.3.1, the reduced effective ionization coefficient (α_{eff}/N) for CO_2 has been plotted as a function of the reduced electric field (*E/N*) (Table 3.3) [Raizer, 1991].

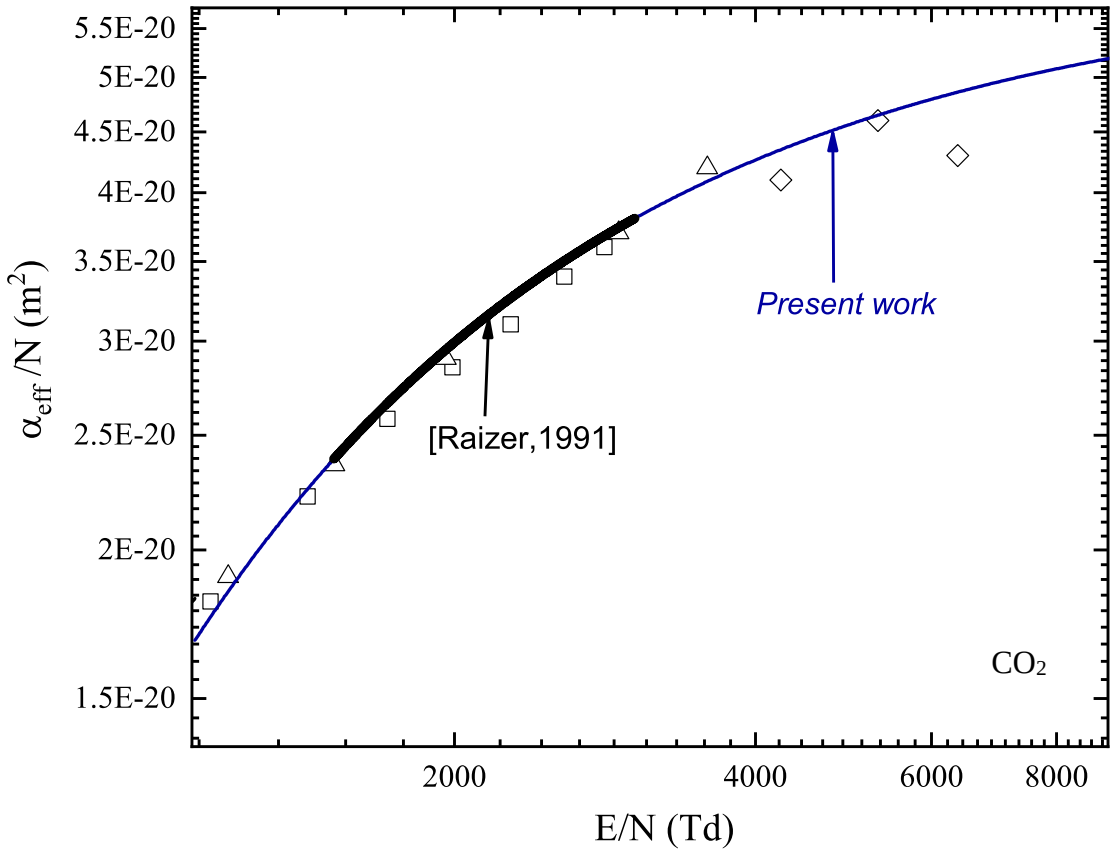

Figure 3.3.2 A zoomed view of the part of Figure 3.3.1

Figure 3.3.2 shows a zoomed view of a section of Figure 3.3.1. It can be seen that the expression of the effective ionization coefficient fits well the experimental data provided in [UNAM database, 2022] only in the limited range of the electric fields, from ~1500 Td to ~3000 Td.

In the present work, an analytical expression for the ionization coefficient for CO_2 is obtained by fitting the exponential function (3.3) to the experimental data [UNAM database, 2022] and [Dutton database, 2022] using OriginPro graphing software

$$\alpha_{eff}/N = 4.3\cdot10^{-20} exp\,(-986/\,(E/N+49)) - 30\cdot10^{-24} \quad (m^2)$$
$$86\ \text{Td} < E/N < 1100\ \text{Td}$$
$$\alpha_{eff}/N = 6.07\cdot10^{-20} exp\,(-1414/\,(E/N)) \quad (m^2) \tag{3.3}$$
$$1100\ \text{Td} < E/N < 10000\ \text{Td}$$

where, α_{eff}/N is the reduced effective ionization coefficient in the unit of m^2, and E/N is the reduced electric field in Td.

The analytic curve obtained in the present work for CO_2 is consistent with the experimental data [UNAM database, 2022] and [Dutton database, 2022] in a wide field range of electric fields from 86 Td to 10,000 Td.

3.2.4 SF_6

For SF_6, the expressions for the ionization and attachment coefficients taken from [Morrow,1986] have been normalized by N and converted into SI units. These expressions are presented in Table 3.4.

TABLE 3.4

Ionization and attachment coefficient for SF_6

SF_6	Analytical equations of ionization and attachment coefficient
[Morrow,1986]	$\alpha/N(m^2) = 3.4473 \cdot 10^{34} \cdot (\frac{E}{N}/10^{21})^{2.985}$ $E/N < 460\text{Td}$ $= 11.269 \cdot (\frac{E}{N}/10^{21})^{1.159}$ $E/N > 460\text{Td}$ $\frac{\eta}{N}(m^2) = 2.0463 \cdot 10^{-20} - 0.25379 \cdot \left(\frac{\frac{E}{N}}{10^{21}}\right)$ $+ 1.4705 \cdot 10^{18}\left(\frac{\frac{E}{N}}{10^{21}}\right)^2 - 3.0078$ $\cdot 10^{36}\left(\frac{\frac{E}{N}}{10^{21}}\right)^3$ $50\text{Td} < E/N < 200\text{Td}$ $= 7.0 \cdot 10^{-21} \cdot \exp(-2.25 \cdot 10^{18} \cdot \left(\frac{\frac{E}{N}}{10^{21}}\right))$ $E/N > 200\text{Td}$

As shown in Figure 3.4.1, Morrow [Morrow,1986] provides the reduced ionization coefficient α/N and the reduced attachment coefficient η/N, these coefficients (Table 3.4) have been used to obtain the reduced effective ionization coefficient functions $\alpha_{eff}/N = \alpha/N - \eta/N$, and α_{eff}/N has been plotted using OriginPro graphing software.

It can be seen that the expression provided by [Morrow,1986] matches well with the experimental data from [Christophorou, 2000] from 360 Td to 2500 Td. However, for a higher electric field range from 2500 Td to 7000 Td, the effective ionization coefficient is overestimated. In addition, there is a sudden change in the ionization coefficient at 200 Td (the analytical function is not smooth).

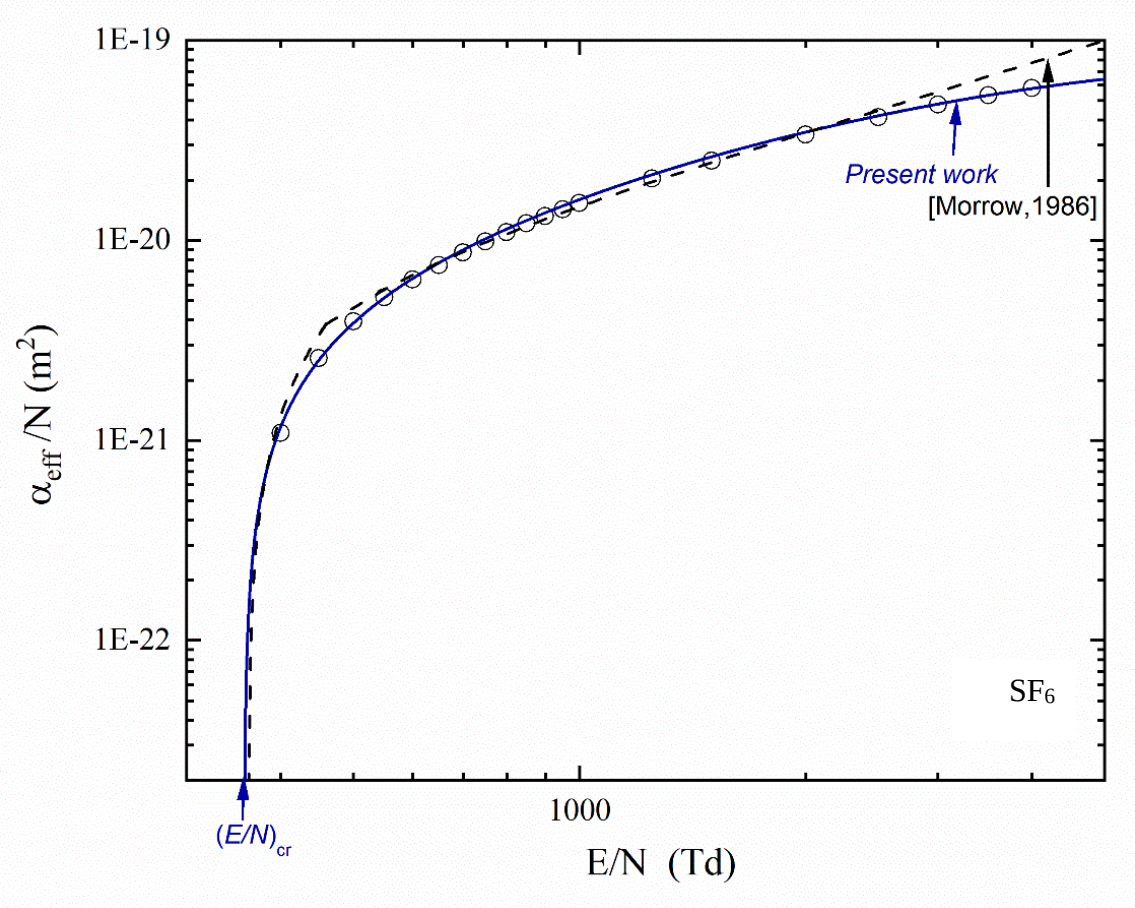

Figure 3.4.1 α_{eff}/N as a function of E/N in SF_6. Experimental data: ○ [Christophorou, 2000]. Fitting curves: dashed line, [Morrow, 1986]; solid blue line, the present work. $(E/N)_{crit}$ shows the asymptotic value of the critical normalized field

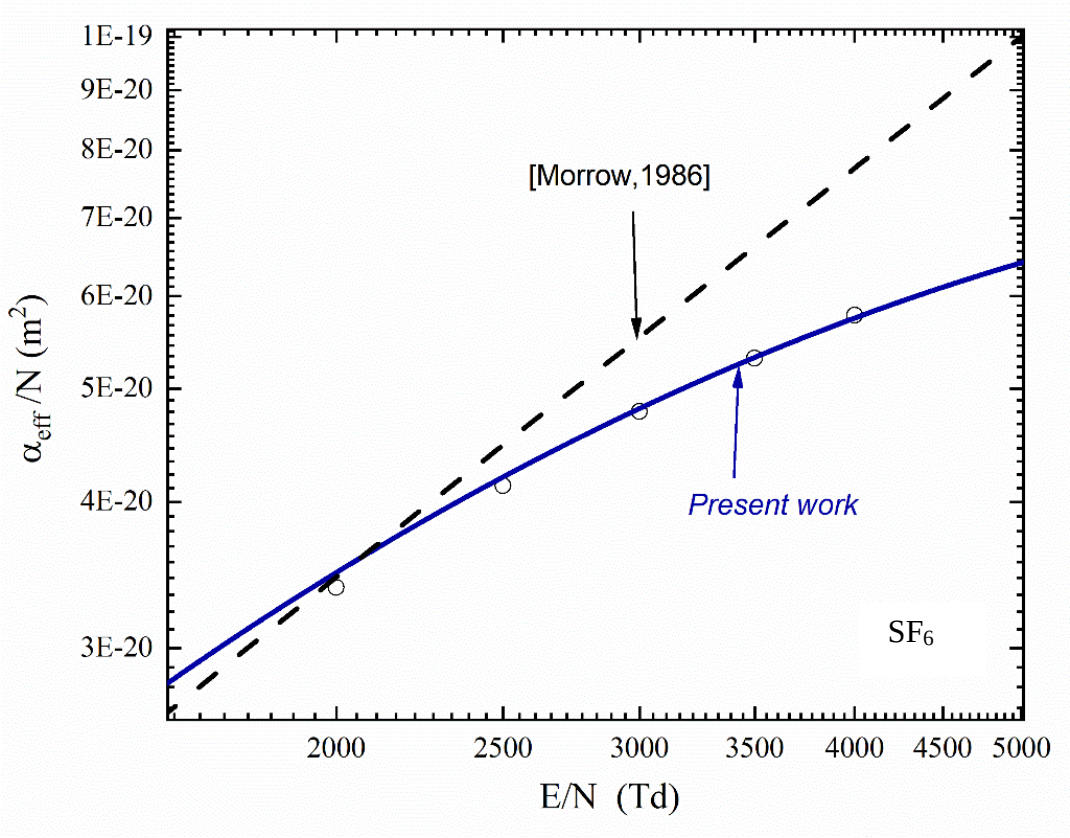

Figure 3.4.2 A zoomed view of the part of Figure 3.4.1

Figure 3.4.2, a zoomed view of a part of Figure 3.4.1, shows the reduced effective ionization coefficient reported in [Morrow, 1986], which is fitted with the analytical function in the range of *E/N* from 360 Td to 2000 Td. This analytical expression predicts values of α_{eff}/N significantly lower than the experimental data from [Christophorou, 2000] for reduced fields greater than 2500 Td.

In the present work, the reduced effective ionization coefficient in SF_6 as a function of the reduced electric field was obtained by establishing the analytical form of the fitting curve (Equation 3.4) and by obtaining the best fit to the experimental data. The experimental data from [Christophorou, 2000] were used in this fitting procedure performed in OriginPro graphing software. The obtained analytical expression for α_{eff}/N is given by Equation 3.4

$$\alpha_{eff}/N = -9.06\cdot10^{-20} exp\,(-(E/N)/2875) + 8\cdot10^{-20}\ \ (m^2)$$
$$360\ Td < E/N < 5000\ Td \qquad (3.4)$$

where, α_{eff}/N is the reduced effective ionization coefficient in the unit of m^2, and E/N is the reduced electric field in Td.

The analytical curve (3.4) plotted in Figure 3.4.1 follows the experimental data [Christophorou, 2000] in a wide range of electric fields, from 360 Td to 5000 Td.

3.3 Critical field

The electric field that the net gain of the ionization starts to become positive is the critical condition for the breakdown of gases. This field at which the effective ionization coefficient is zero is called the critical field, $(E/N)_{cr.}$

This field above the critical field shows that the net electron ionization is positive, it provides the conditions for the development of electron avalanches (ionization fronts) which may lead to the complete breakdown of gas.

The effective ionization coefficients as functions of E/N have been discussed and presented for a wide range of the reduced electric fields in Section 3.2. According to the definition of the critical field, $\frac{\alpha_{eff}}{N} = 0$ at $(E/N)_{cr}$, the critical fields for air, N_2, CO_2 and SF_6 can be obtained from Figures 3.1.1 - 3.4.1. The obtained values of the critical field for air, N_2, CO_2, and SF_6 are presented and compared with the published literature data in Table 3.5.

TABLE 3.5

Critical Field

Gas	$(E/N)_{cr}$,(Td) (The present work)	$(E/N)_{cr}$,(Td) (Data from literature)
Air	~94	94.7 [Eichwald, 2018], 99.4 [Bagheri, 2018] 98.5 [Lowke, 2003]
N_2	~60	60 [Haefliger, 2018]
CO_2	~86	86 [Wang, 2016], 82 [Davies, 1978]
SF_6	~360	359 [Itoh, 1979], 360 [Christophorou, 2000], [Hernandez-Avila, 2003], [Satoh, 1988], 361[Aschwanden, 1984] 362 [Itoh, 1988], [Kline, 1979]

Table 3.5 provides the values of the critical field for air obtained by Bagheri [Bagheri, 2018] and Lowke [Lowke, 2003], 99.4 Td and 98.5 Td, respectively. In the present work, the obtained critical field for air is ~94 Td, which is consistent with data reported in [Eichwald, 2018]. This paper reports a value of 94.7 Td, which is close to the values from [Bagheri, 2018] and [Lowke, 2003].

The critical field for N_2 reported by Haefliger $(E/N)_{cr}$ is 60 Td. The critical field for N_2 obtained in the present work from Figure 3.2.1 and by Equation 3.2 is ~60 Td, which is in a good agreement with the value reported in [Haefliger, 2018].

The critical fields for CO_2 reported by [Wang, 2016] and [Davies, 1978] are 86 Td, and 82 Td, respectively. The critical field for CO_2 obtained in the present work from

Figure 3.3.1 is ~86 Td, which is in a good agreement with the literature data [Wang, 2016] and [Davies, 1978].

Regarding SF_6, Christophorou, Hernandez, and Satoh provide the critical field value of 360 Td, Aschwanden reports a value of 361 Td, and Itoh and Kline provide the critical field of 362 Td. The critical field for SF_6 obtained in the present work through the fitting curve in Figure 3.4.4 is ~360 Td, which is in good agreement with [Christophorou, 2000], [Hernandez, 2003], [Satoh, 1988], [Aschwanden, 1984], [Itoh, 1988], [Kline, 1979].

3.4 Electron mobility

The mobility of electrons is another critical parameter required for accurate modelling of the ionization fronts in gases. The electronic mobility, μ_e, is defined as the drift velocity divided by the electric field [Gallagher, 1983].

There are a number of published papers [Chen, 2018], [Hasegawa, 1996], [Schlumbohm, 1965b], [Christophorou, 2000] in which the transport parameters in different gases have been investigated, these parameters include the electron mobility and drift velocity obtained by experimental or numerical methods.

In the present work, the literature data have been fitted with allometric functions (Equation 3.5) using OriginPro graphing software. This fitting has been conducted in the field range from 100 Td to 1000 Td. A and B are free fitting parameters

$$\mu_e N = A(E/N)^{-B} \qquad (\mathrm{m\cdot V\cdot s})^{-1} \tag{3.5}$$

In Equation 3.5, $\mu_e N$ is expressed in units of $(\mathrm{m\cdot V\cdot s})^{-1}$ and E/N is expressed in units of Td.

The numerical values of the fitting parameters, A and B for each gas, with their standard errors, obtained using OriginPro graphing software are given in Table 3.6-3.9. The standard errors allow for the estimation of the accuracy of the fitting [Originlab, 2022].

TABLE 3.6.

Parameters A and B for fitting function (Equation 3.5) for air

$\mu_e N = A(E/N)^{-B}$	
	Air
A	$3.361 \cdot 10^{24}$ ($\pm 4.164 \cdot 10^{23}$)
B	0.222 (±0.019)

TABLE 3.7

Parameters A and B for fitting function (Equation 3.5) for N_2

$\mu_e N = A(E/N)^{-B}$	
	N_2
A	$1.700 \cdot 10^{24}$ ($\pm 1.715 \cdot 10^{23}$)
B	0.09 (±0.018)

TABLE 3.8

Parameters *A* and *B* for fitting function (Equation 3.5) for CO_2

$\mu_e N = A(E/N)^{-B}$	
	CO_2
A	$8.683 \cdot 10^{24}$ ($\pm 1.284 \cdot 10^{23}$)
B	0.416 (±0.002)

TABLE 3.9

Parameters *A* and *B* for fitting function (Equation 3.5) for SF_6

$\mu_e N = A(E/N)^{-B}$	
	SF_6
A	$3.085 \cdot 10^{24}$ ($\pm 3.032 \cdot 10^{22}$)
B	0.284 (±0.002)

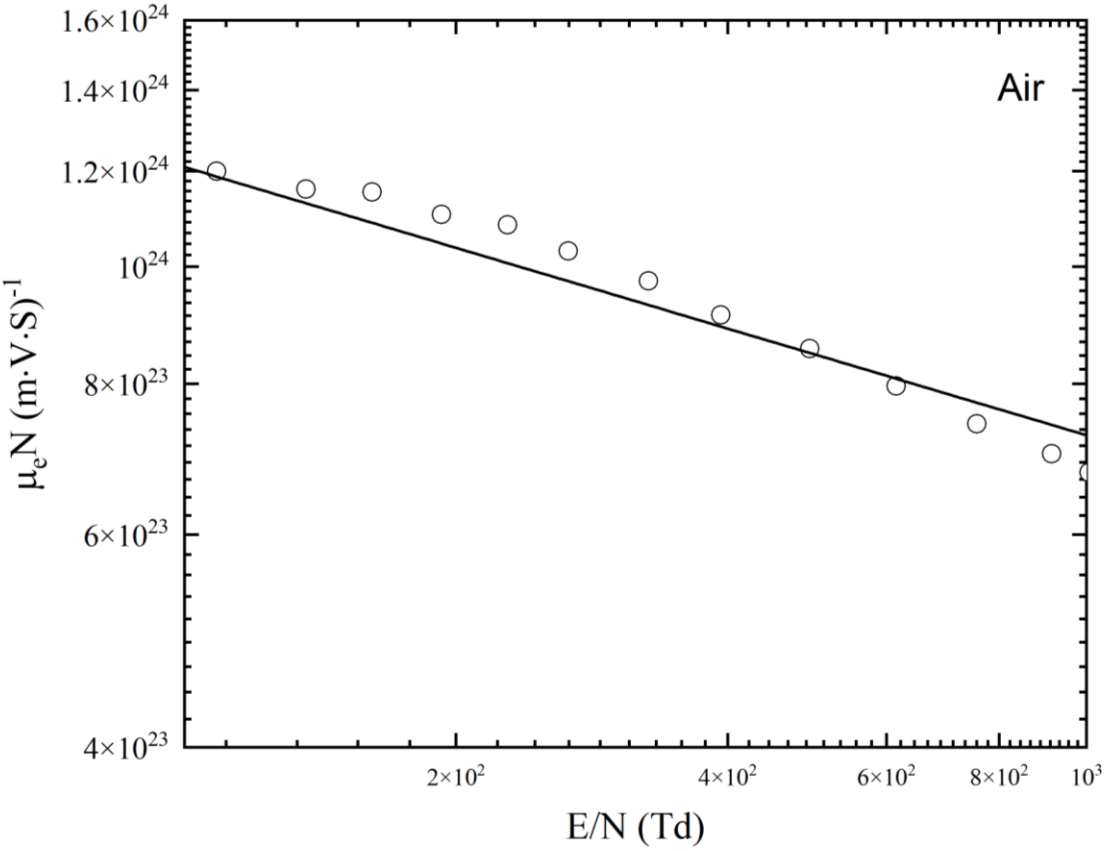

Figure 3.5 $\mu_e N$ as a function of *E/N* for air. Simulation data from literature: ○ [Chen, 2018]. Fitting curves for the present work (Table 3.6): dark line, air

As presented in Figure 3.5, the fitting curve was used to fit the data on the electron mobility, [Chen, 2018]. $\mu_e N$ as a function of *E/N* for air was obtained using Equation 3.5, $\mu_e N$ *(E/N)* will be used in the drift-diffusion and kinetic models. The obtained fitting parameters are listed in Table 3.6. It can be seen from Figure 3.5 that the fitting function provides a good agreement with the literature data [Chen, 2018] in a wide range of electric fields up to 1000 Td.

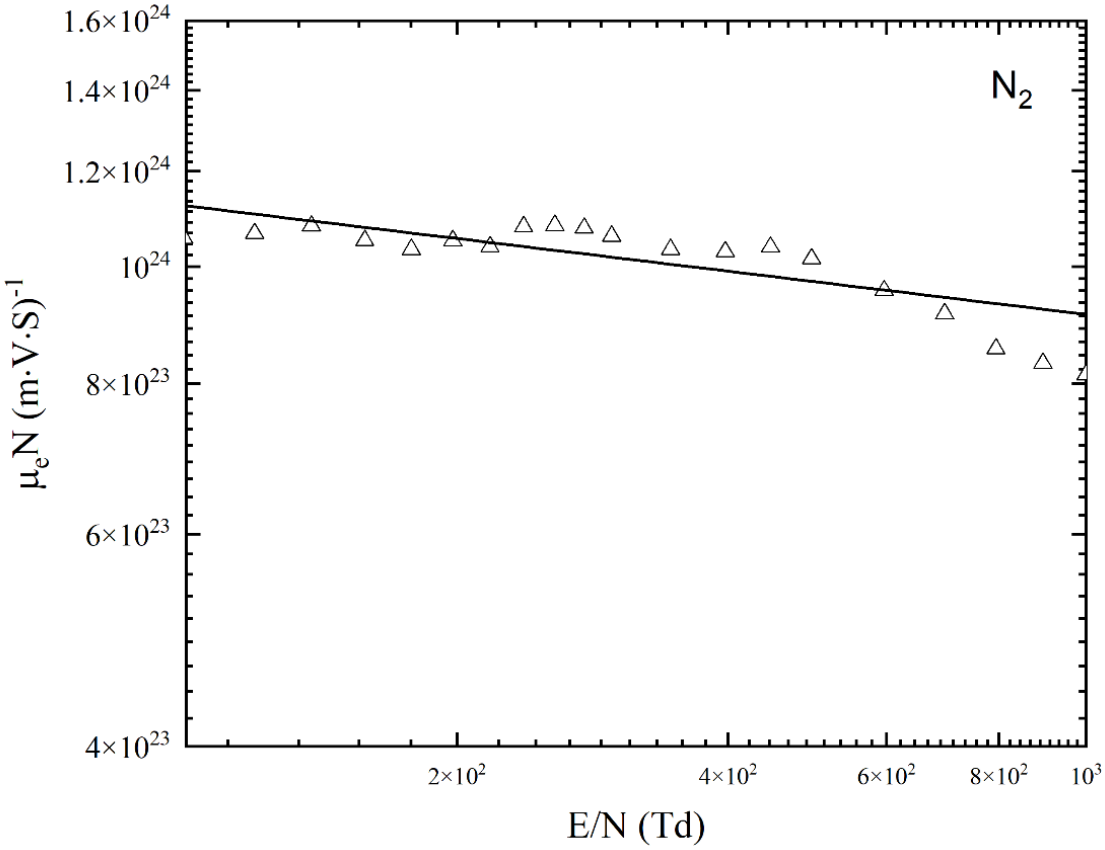

Figure 3.6 $\mu_e N$ as a function of E/N for N_2. Experimental data from literature: △, [Hasegawa, 1996]. Fitting curves for the present work (Table 3.7): dark line, N_2

As shown in Figure 3.6, Hasegawa [Hasegawa, 1996] reports the data on the drift velocity of electrons as a function of the reduced electric field in N_2 in the range from 20 Td to 1000 Td. These data are in good agreement with the experimental measurements by Nakamura (1987), Saelee (1977), and Roznerski (1984).

The experimental electron drift velocity presented in [Hasegawa, 1996] was converted into the electron mobility, and these values were fitted with an analytical function (Equation 3.5) using OriginPro software.

This fitting provides an analytical expression for $\mu_e N$ as a function of E/N for N_2. The obtained fitting parameters are specified in Table 3.7. Figure 3.6 shows that the obtained fitting is in good agreement with the literature data [Hasegawa, 1996] in a wide range of electric fields up to 1000 Td.

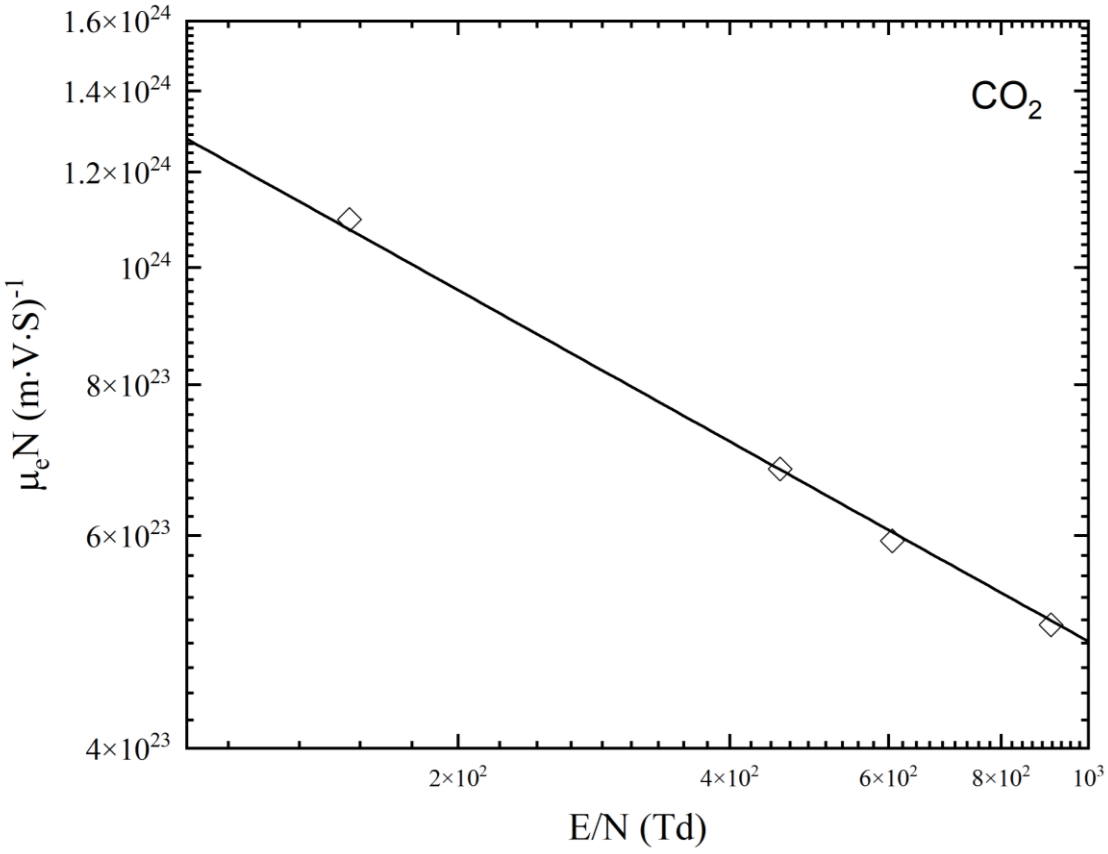

Figure 3.7 $\mu_e N$ as a function of E/N for CO_2. Experimental data from literature: ◇, [Schlumbohm, 1965b]. Fitting curves for the present work (Table 3.8): dark line, CO_2

Figure 3.7 [Schlumbohm, 1965b] shows the experimental drift velocity of electrons for CO_2 as a function of the reduced electric field up to 1000 Td. The experimental data on the electron drift velocity from [Schlumbohm, 1965b] were analysed, converted into the electron mobility and fitted with Equation 3.5 using OriginPro graphing software.

This fitting provides $\mu_e N$ as a function of E/N for CO_2 and the obtained fitting parameters are specified in Table 3.8. It can be seen from Figure 3.7, that this fitting shows a good agreement with the literature data from [Schlumbohm, 1965b] in a wide range of electric fields from 100 Td to 1000 Td.

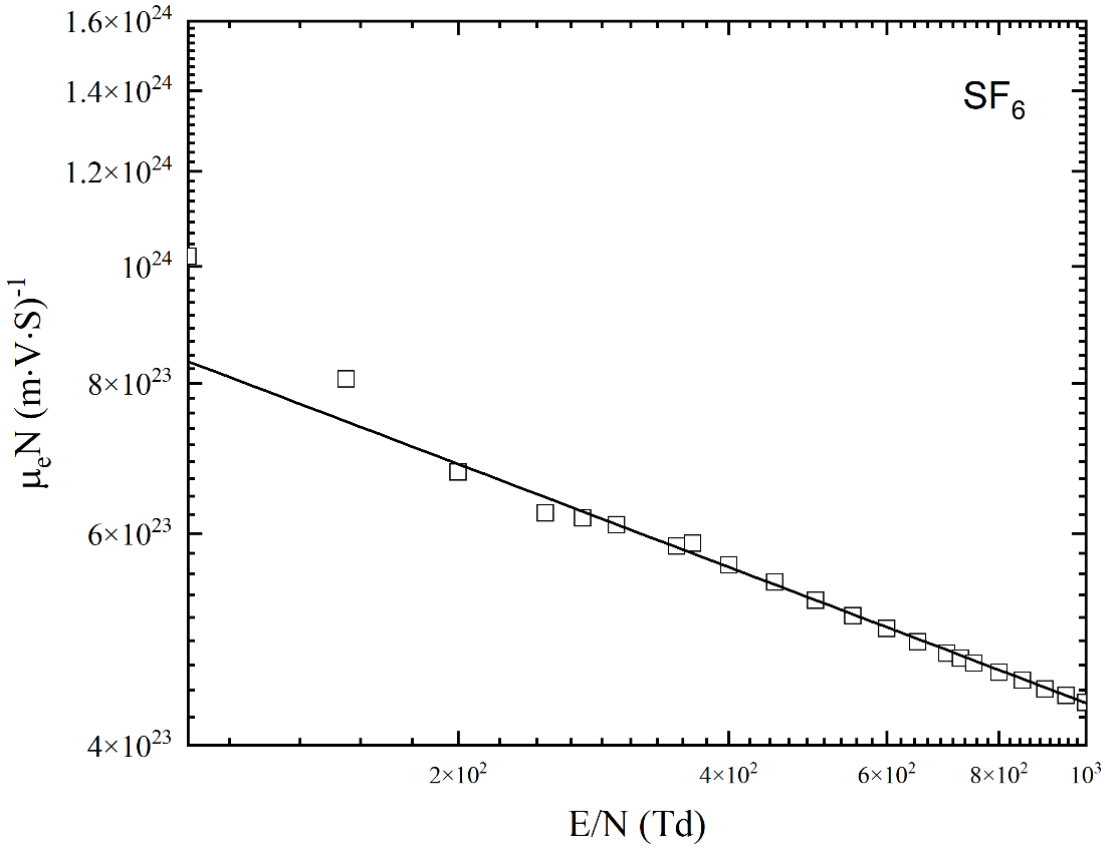

Figure 3.8 $\mu_e N$ as a function of E/N for SF_6. Simulation data from literature: □ [Christophorou, 2000]. Fitting curves for the present work (Table 3.9): dark line, SF_6

[Christophorou, 2000] reviewed the experimental data on the electron drift velocity in SF_6 and provided electron drift velocity in SF_6 depending on the reduced electric field, ranging from 100 Td to 4000 Td.

The drift velocity [Christophorou, 2000] was converted into the electron mobility and fitted with Equation 3.5. Figure 3.8 shows $\mu_e N$ as a function of E/N for SF_6. Equation 3.5 fits the experimental data from [Christophorou, 2000] in the range of the electric fields from 100 Td to 1000 Td. The obtained fitting parameters are listed in Table 3.9.

TABLE 3.10

$\mu_e N$ for different gases

Gas	$\mu_e N$, (m·V·s)$^{-1}$
Air	$3.361 \cdot 10^{24}(E/N)^{-0.222}$
N_2	$1.7 \cdot 10^{24}(E/N)^{-0.09}$
CO_2	$8.68 \cdot 10^{24}(E/N)^{-0.416}$
SF_6	$3.085 \cdot 10^{24}(E/N)^{-0.284}$

Table 3.10 shows the analytical expressions for the products of the electron mobility and particle number density, $\mu_e N$, as functions of *E/N* for air, N_2, CO_2, and SF_6. These functions were obtained by Equation 3.5 using the fitting parameters listed in Tables 3.6 - 3.9. These functions will be used in the drift-diffusion and kinetic models in Chapter 4.

3.5 Discussion

This chapter provides the systematic investigation and analysis of the key swarm parameters in a wider range of electric fields based on the experimental results available in the literature.

The swarm parameters in air, N_2, CO_2, and SF_6, including the ionization and attachment coefficients, the effective ionization coefficient, and the electron mobility have been analysed in the present work. In addition, the critical field values for these

gases have also been discussed based on the obtained analytical expressions for the effective ionization coefficients.

It has been shown that in the previous studies, [Sanders, 1933], [Masch, 1932], [Bowls,1938], [UNAM database,2022], [Dutton database, 2022], [Christophorou, 2000], the analytical functions for the reduced effective ionization coefficients α_{eff}/N for air, N_2, CO_2 and SF_6, were obtained only in the limited range of electric fields. α_{eff}/N has a noticeably lower or higher value than the experimental data at higher electric fields.

In the present work, the reduced effective ionization coefficients α_{eff}/N for air, N_2, CO_2, and SF_6 have been obtained as smooth analytical functions of the reduced electric field *E/N* in a wide range of *E/N*.

For air, the analytical fitting to α_{eff}/N has been obtained in the extended range of *E/N* up to 1500 Td (the obtained critical field is ~94 Td); for N_2, the analytical fitting to α_{eff}/N has been obtained in the extended electric field up to 60 Td to 5000 Td and obtained critical field is ~60 Td; for CO_2, the analytical fitting to α_{eff}/N has been obtained in the extended range of reduced electric fields up to 10000 Td, and the obtained critical field ~86 Td; for SF_6, the analytical fitting to α_{eff}/N has been obtained in the extended range of *E/N* up to 5000 Td, and the obtained the critical field is ~360 Td. These values are in good agreement with the experimental data available in the literature.

The accurate analytical expressions of the product of the electron mobility and the number density $\mu_e N$ for air, N_2, CO_2 and SF_6 as functions of *E/N* in a wide range of the reduced electric fields from 100 Td to 1000 Td were obtained using allometric functions (Equation 3.5) which were fitted to the experimental and analytical results available in the literature.

These accurate swarm parameters in a wide range of electric fields will be used in the drift-diffusion and kinetic models in Chapter 4.

Chapter 4 Drift-diffusion and kinetic models

4.1 Introduction

In this chapter, the drift-diffusion and kinetic models are used to simulate the development of the fast ionization fronts and breakdown characteristics in air, N_2, CO_2, and SF_6. The drift-diffusion model is developed in the COMSOL Multiphysics software. This model allows for the detailed investigation of the development of the ionization front in the spatial and temporal domains. The breakdown criterion based on the electron density established in the inter-electrode gap is introduced and used to model the field-time breakdown characteristics of different gases.

The kinetic model is another approach used in this chapter to study the breakdown characteristics of gases. This analytical model is based on the Meek avalanche-to-streamer transition criterion and does not require the solution of the drift-diffusion equations for the charged species. Thus, this approach provides a straightforward methodology for calculating breakdown voltages or fields as functions of energization time for gases with known electronic mobility and effective ionization coefficients.

The comparison between the results (the field-time breakdown characteristics) obtained using these two models is presented, and the analytical results obtained in this study are compared with the experimental data available in the literature.

This chapter also presents the analysis of the Townsend and streamer conditions for different gases to characterize the potential type of breakdown in different experimental conditions (gas pressure and gap distance) for different gases depending on the duration of the electric stress applied to the electrodes.

4.2 Drift-diffusion model

The numerical solution of the partial differential equations is used to solve different problems in science and engineering. The partial differential equations used in the drift-diffusion model allow for modelling the transient plasma discharge processes in different gases.

In this section, the drift-diffusion model is implemented in COMSOL Multiphysics software to investigate the creation and annihilation of the electrons, negative ions and positive ions in gases with the application of the electric field in time.

4.2.1 Drift-diffusion approach

The drift-diffusion model is commonly used in gas discharge and breakdown analysis. This model is based on the continuity equations for the number density of different particle species.

The drift-diffusion equations have been discussed in Chapter 2. The continuity equations for the number density of the electrons, positive ions, and negative ions can be written as

$$\frac{\partial n_e}{\partial t} + \nabla \cdot \left(-n_e \mu_e \vec{E} - D_e \nabla n_e\right) = n_e(\alpha - \eta)\left|\mu_e \vec{E}\right| - n_e n_p \beta \tag{4.1}$$

$$\frac{\partial n_p}{\partial t} + \nabla \cdot \left(n_p \mu_p \vec{E}\right) = n_e \alpha \left|\mu_p \vec{E}\right| - n_e n_p \beta - n_n n_p \beta \tag{4.2}$$

$$\frac{\partial n_n}{\partial t} + \nabla \cdot \left(-n_n \mu_n \vec{E}\right) = n_e \eta \left|\mu_n \vec{E}\right| - n_n n_p \beta \tag{4.3}$$

where, n_e, n_p, n_n are the number density of specific particles, subscripts e, p, n indicate the electrons, the positive ions and the negative ions, respectively. t is time, α is the ionization coefficient, η is the attachment coefficient, β is the recombination coefficient, D is the diffusion coefficient, μ is the mobility, E is the electric field.

The coefficient of the electron-positive ions recombination β_{ep} and the coefficients of the negative and positive ions recombination, β_{np}, are assumed to be the same and equal to β, following the work by Georghiou [Georghiou, 2001].

The diffusion coefficient of the positive ions, D_p, and the diffusion coefficient of the negative ions, D_n, are negligible as the effect of diffusion of ions is very small compared to that of electrons, following the work by Tran [Tran , 2010a], Dahli [Dahli, 1987], Hallac [Hallac, 2003], Morrow [Morrow, 1997], Georghiou [Georghiou, 2005], Ducasse [Ducasse, 2007].

The number density of specific particles determines the development of the space charge. As a result, the electric field is modified by the space charge as described by Poisson's equation [Georghiou, 2005]

$$\nabla^2 \varphi = -\frac{\rho}{\varepsilon_0 \varepsilon_r} = -\frac{e\left(n_p - n_n - n_e\right)}{\varepsilon_0 \varepsilon_r} \tag{4.4}$$

$$\vec{E} = -\nabla \varphi \tag{4.5}$$

where $\vec{E}$ is the vector field, φ means the electric potential, ε_0 is the vacuum permittivity, ε_r is the relative permittivity, e is the elementary charge. ρ is defined as the density of the total space charge.

4.2.2 Drift-diffusion model: Implementation in COMSOL

COMSOL Multiphysics software is a finite element method (FEM) software widely used in the simulations of gas discharges and investigation of ionization fronts and streamer propagation.

According to the drift-diffusion approach discussed in Section 4.1.1, the drift-diffusion model in the present work has been implemented in COMSOL Multiphysics software utilizing the partial differential equations (PDEs) interface and the electrostatics module using specific boundary conditions.

This model allows for simulation of the breakdown characteristics based on modelling the development of ionization fronts in air, N_2, CO_2, and SF_6 and postulated by Equations 4.1-4.3. The model describes the creation and annihilation of the electrons, negative ions, and positive ions with time in the externally applied electric field.

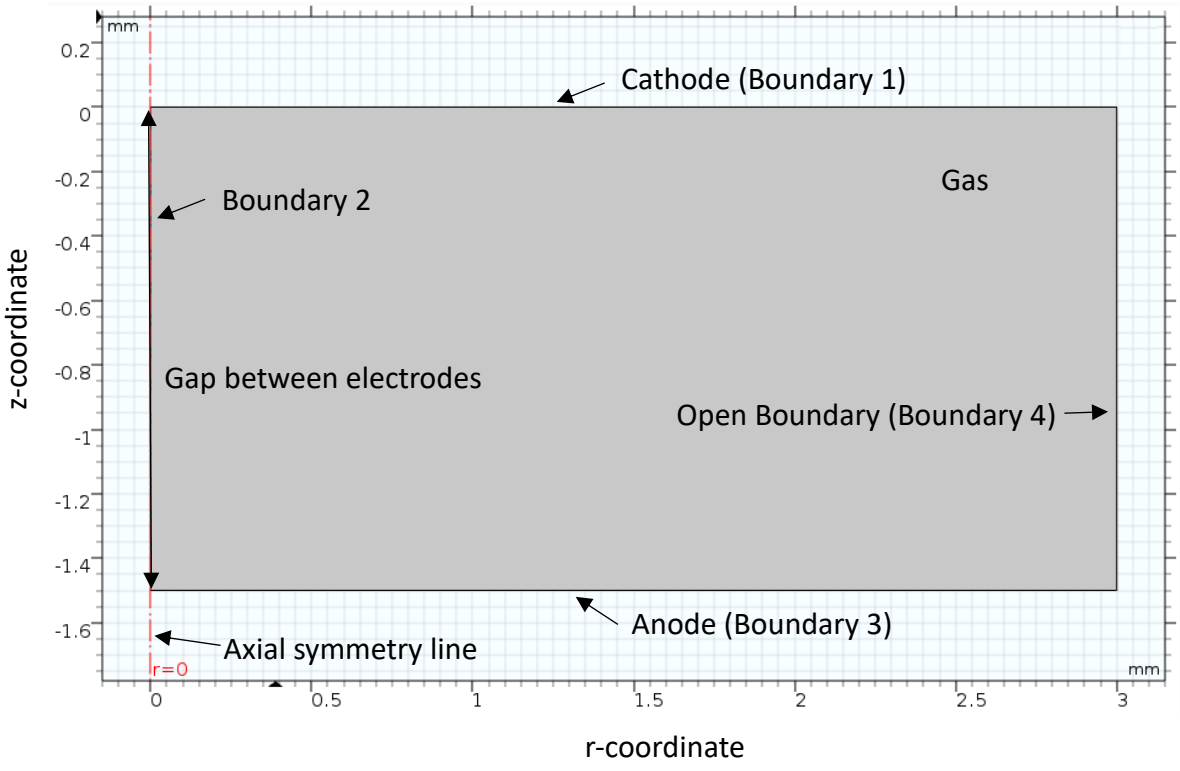

Figure 4.1. Computational domain of the drift-diffusion model

As shown in Figure 4.1, a symmetrical geometry of the model is established in the cylindrical coordinate system with the inter-electrode gap of 1.5 mm and the radius of the plane electrode of 3 mm. A negative high voltage is applied to a plane electrode, and the lower Ground electrode is at zero potential.

The drift-diffusion model includes a set of PDE continuity equations for the electrons and positive and negative ions. The boundary conditions at the electrodes and the physical interfaces must be specified to solve these PDE equations.

Two types of boundary conditions are used in the model. The Dirichlet boundary condition is applied to specify a fixed value for the independent variables at the boundary, such as voltage. As the cathode (negatively stressed electrode) is a source of secondary electrons, i.e., the secondary ionization process occurs at the cathode /gas interface, the Neumann boundary condition is used at this interface to represent the effect of the secondary ionization process.

The simulation domain has a rectangular shape of 1.5 mm by 3 mm filled with investigated gas kept at atmospheric pressure and room temperature. This domain includes four boundaries: boundary 1 is the cathode (made of copper) at the top of the domain, and the secondary ionization process occurs at this interface (boundary); boundary 2 is the axis of symmetry; boundary 3 represents the anode (ground) electrode made of copper, and the potential of this electrode is equal to zero; boundary 4 is an open boundary.

The present model emphasizes the formative time and field of the breakdown characteristics. In order to simulate the process appearance of initial electrons generated by radiation, cosmic rays, radioactivity or UV photons, the seed electrons and the positive ions comprising a neural initial local space charge with the Gaussian distribution were placed at the center of the cathode. It is known that such seed particles do not significantly change the characteristics of the ionization front [Georghiou, 2000]. The distribution of the seed electrons and positive ions is expressed as

$$n_{e0}(r,z) = n_{max} e^{-\frac{(r-r_0)^2}{2\sigma_r^2} - \frac{(z-z_0)^2}{2\sigma_z^2}} \quad (4.6)$$

$$n_{p0}(r,z) = n_{max} e^{-\frac{(r-r_0)^2}{2\sigma_r^2} - \frac{(z-z_0)^2}{2\sigma_z^2}} \quad (4.7)$$

where n_{e0} is the electrons density of seed, n_{p0} is the positive ions density, n_{max} is the maximum number density (10^{12} m^{-3}). r-coordinate is $r_0 = 0$ and z -coordinate is $z_0 = 0$. The spatial spread of the seed particles is characterised by $\sigma_r = \sigma_z = 0.025$ mm, [Tran, 2010b].

The main swarm parameters used in this model include the effective ionization coefficient, and the electron mobility coefficient. These characteristics for air, N_2, CO_2 and SF_6 have been discussed in Chapter 3.

The following additional assumption should be taken into account in the drift-diffusion model: following the models by [Bourdon, 2010], [Luque, 2008], [Gupta, 2000], [Yurgelenas, 2006], and [Tran, 2010a], the background ionization is neglected in the present work.

The secondary electron emission process is required to sustain the development of the ionization front. The secondary electrons are generated by positive ions colliding with the cathode. The models developed by [Sandia, 2003], [Ducasse, 2007], [Lowke, 2003], [Luque, 2008], [Tran, 2010b] state that the secondary ionization coefficients are in the range from 10^{-2} to 10^{-4}. Thus, the secondary ionization coefficient based on these literature data is in order of $\gamma \sim 10^{-3}$. In the present work, the constant value of the secondary ionization coefficient, $\gamma = 0.004$ is used in the drift-diffusion model, following the work by Tran [Tran, 2010b].

TABLE 4.1

Swarm parameters used in the drift-diffusion model for air

Parameter	Value/function used in the present paper	References
$D(\frac{\mathrm{m}^2}{\mathrm{s}})$	0.18	[Kulikovsky, 1997] [Kang, 2003]
$\mu_e\ (\frac{\mathrm{m}^2}{\mathrm{V}\cdot\mathrm{s}})$	$3.361\cdot 10^{24}(E/N)^{-0.222}/N$ $10\ \mathrm{Td} \le E/N \le 1000\ \mathrm{Td}$	Obtained in Chapter 3
$\mu_p\ (\frac{\mathrm{m}^2}{\mathrm{V}\cdot\mathrm{s}})$	$2.34\cdot 10^{-4}$	[Morrow, 1997] [Chen, 2017]
$\mu_n\ (\frac{\mathrm{m}^2}{\mathrm{V}\cdot\mathrm{s}})$	$2.7\cdot 10^{-4}$ $E/N > 50\ \mathrm{Td}$ $1.86\cdot 10^{-4}$ $E/N < 50\mathrm{Td}$	[Morrow, 1997] [Chen, 2017]
$\beta\ (\frac{\mathrm{m}^3}{\mathrm{s}})$	$2\cdot 10^{-13}$	[Morrow, 1997] [Georghiou, 2005] [Hallac, 2003]
$\frac{\alpha_{eff}}{N}(\mathrm{m}^2)$	$4\cdot 10^{-20}\cdot exp^{-985/((\frac{E}{N})+43)} - (30\cdot 10^{-24})$ $94\ \mathrm{Td} < E/N < 1500\mathrm{Td}$	Obtained in Chapter 3

For air, as shown in Table 4.1, the diffusion coefficient is 0.18 m^2/s [Kulikovsky, 1997] [Kang, 2003]. This value has been employed in the present model.

The mobility of positive and negative ions provided in [Morrow, 1997] has been used in the present work. These values were also adopted in Chen's model [Chen, 2017]. The recombination coefficient β of the electrons and positive ions of $2 \cdot 10^{-13}\,\frac{\mathrm{m}^3}{\mathrm{s}}$ presented in [Morrow, 1997] has been used in the present model, which also was used in [Georghiou, 2005], [Hallac, 2003].

TABLE 4.2

Swarm parameters used in the drift-diffusion model for N_2

Parameter	Value/function used in the present paper	References
$D(\frac{\mathrm{m}^2}{\mathrm{s}})$	0.18	[Vitello, 1994]
$\mu_e\ (\frac{\mathrm{m}^2}{\mathrm{V}\cdot\mathrm{s}})$	$1.7 \cdot 10^{24}(E/N)^{-0.09}/N$ $50\mathrm{Td} \le E/N \le 1000\mathrm{Td}$	Obtained in Chapter 3
$\mu_p\ (\frac{\mathrm{m}^2}{\mathrm{V}\cdot\mathrm{s}})$	$2.5 \cdot 10^{-4}$	[Davies, 1966], [McDaniel, 1973]
$\beta\ (\frac{\mathrm{m}^3}{\mathrm{s}})$	$\sim 1 \cdot 10^{-13}$	[Douglas, 1973]
$\frac{\alpha_{eff}}{N}(\mathrm{m}^2) = \frac{\alpha}{N}$	$1.7 \cdot 10^{-20} \cdot exp^{-800/((\frac{E}{N})-3)}$ $60\mathrm{Td} < E/N < 350\mathrm{Td}$ $3 \cdot 10^{-20} \cdot e^{-1000/(\frac{E}{N})}$ $350\mathrm{Td} < E/N < 5000\ \mathrm{Td}$	Obtained in Chapter 3

Table 4.2 presents the swarm parameters used in the drift-diffusion model for N_2. Their numerical values are as follows: the diffusion coefficient of 0.18 (m^2/s) is proposed by Vitello [Vitello, 1994]; the mobility of positive ions is provided by Davies [Davies, 1966] and McDaniel [McDaniel, 1973]; the recombination coefficient $\beta \sim 10^{-13}\ \frac{m^3}{s}$ is presented by Douglas [Douglas, 1973]; the attachment coefficient is $\eta = 0$ as N_2 is an electropositive gas [Vitello, 1994], [Davies, 1971], [Kulikovsky, 1994].

The swarm parameters used in the drift-diffusion model for SF_6 have been obtained by the expressions shown in Table 4.3. The diffusion coefficient and the mobilities of the positive and the negative ions were taken from [Morrow, 1986]. The recombination coefficient $\beta \sim 10^{-13}$ is in line with [Jungblut, 1989].

Table 4.4 presents the swarm coefficients and transport coefficients used in the drift-diffusion model for CO_2. The diffusion coefficient of 0.1 m^2/s was obtained from the analysis presented in [Schlumbohm, 1965a]. The recombination coefficient $\beta \sim 10^{-13}\ \frac{m^3}{s}$ is consistent with the data obtained in [Ponduri, 2016]. The fitting equation for the mobilities of positive and negative ions is based on the data obtained from [Viehland, 1995] and has been analysed in the present work.

Tables 4.1-4.4 provide the effective ionization coefficient and the electron mobility for air, N_2, CO_2, and SF_6 obtained from Section 3.2. These coefficients are given as functions of the electric field and will be discussed further and used in Section 4.3.

The breakdown criterion has been introduced and used in the drift-diffusion model to obtain the breakdown voltage and time to breakdown for all investigated gases. The computational procedure is illustrated in Figure 4.2.

TABLE 4.3

Swarm parameters used in the drift-diffusion model for SF_6

Parameter	Value/function used in the present paper	References
$D(\frac{\mathrm{m}^2}{\mathrm{s}})$	$3.553 \cdot 10^{-2} \cdot (E/N)^{0.2424}$ $E/N < 650\mathrm{Td}$	[Morrow, 1986]
$\mu_e\ (\frac{\mathrm{m}^2}{\mathrm{V} \cdot \mathrm{s}})$	$3.085 \cdot 10^{24} \cdot (E/N)^{-0.284}/N$ $25\mathrm{Td} \leq E/N \leq 4000\mathrm{Td}$	Obtained in Chapter 3
$\mu_p\ (\frac{\mathrm{m}^2}{\mathrm{V} \cdot \mathrm{s}})$	$6.0 \cdot 10^{-5}$ $E/N < 120\mathrm{Td}$ $1.216 \cdot 10^{-5} \ln\left(\frac{E}{N}\right) + 0.01 \cdot 10^{-4}$ $120\mathrm{Td} < E/N < 350\mathrm{Td}$ $-1.897 \cdot 10^{-5} \ln\left(\frac{E}{N}\right) + 1.83 \cdot 10^{-4}$ $E/N > 335\mathrm{Td}$	[Morrow, 1986]
$\mu_n\ (\frac{\mathrm{m}^2}{\mathrm{V} \cdot \mathrm{s}})$	$1.69 \cdot 10^{-10}\ (E/N)^2 + 0.53 \cdot 10^{-4}$ $E/N < 500\mathrm{Td}$	[Morrow, 1986]
$\beta\ (\frac{\mathrm{m}^3}{\mathrm{s}})$	$\sim 10 \cdot 10^{-13}$	[Jungblut, 1989]
$\frac{\alpha_{eff}}{N}(\mathrm{m}^2)$	$-9.06 \cdot 10^{-20} \cdot exp^{-(\frac{E}{N})/2875} + (8 \cdot 10^{-20})$ $360\mathrm{Td} < E/N < 5000\mathrm{Td}$	Obtained in Chapter 3

TABLE 4.4

Swarm parameters used in drift-diffusion model for CO_2

Parameter	Value/function used in the present paper	References
$D(\frac{\mathrm{m}^2}{\mathrm{s}})$	~ 0.1	[Schlumbohm, 1965a]
$\mu_e\ (\frac{\mathrm{m}^2}{\mathrm{V}\cdot\mathrm{s}})$	$8.68\cdot 10^{24}\cdot (E/N)^{-0.416}/N$ $151\mathrm{Td} \le E/N \le 6062\mathrm{Td}$	Obtained in Chapter 3
$\mu_p\ (\frac{\mathrm{m}^2}{\mathrm{V}\cdot\mathrm{s}})$	$6.52\cdot 10^{-5}\cdot e^{(-(\frac{E}{N})/399)} + (6.96\cdot 10^{-5})$ $50\mathrm{Td} \le E/N \le 1200\mathrm{Td}$	Data from [Viehland, 1995], Fitting equation from the present work
$\mu_n\ (\frac{\mathrm{m}^2}{\mathrm{V}\cdot\mathrm{s}})$	$6.47\cdot 10^{-6}\cdot e^{((((\frac{E}{N})-7.4)/86.7)} + (1.22\cdot 10^{-4})$ $5\mathrm{Td} \le E/N \le 150\ \mathrm{Td}$	Data from [Viehland, 1995], Fitting equation from the present work
$\beta\ (\frac{\mathrm{m}^3}{\mathrm{s}})$	$\sim 1\cdot 10^{-13}$	[Ponduri, 2016]
$\frac{\alpha_{eff}}{N}(\mathrm{m}^2)$	$4.3\cdot 10^{-20}\cdot exp^{-986/((E/N)+49)} - (30\cdot 10^{-24})$ $86\mathrm{Td} < E/N < 1100\mathrm{Td}$ $6.07\cdot 10^{-20}\cdot exp^{-1414/(E/N)}$ $1100\mathrm{Td} < E/N < 10000\mathrm{Td}$	Obtained in Chapter 3

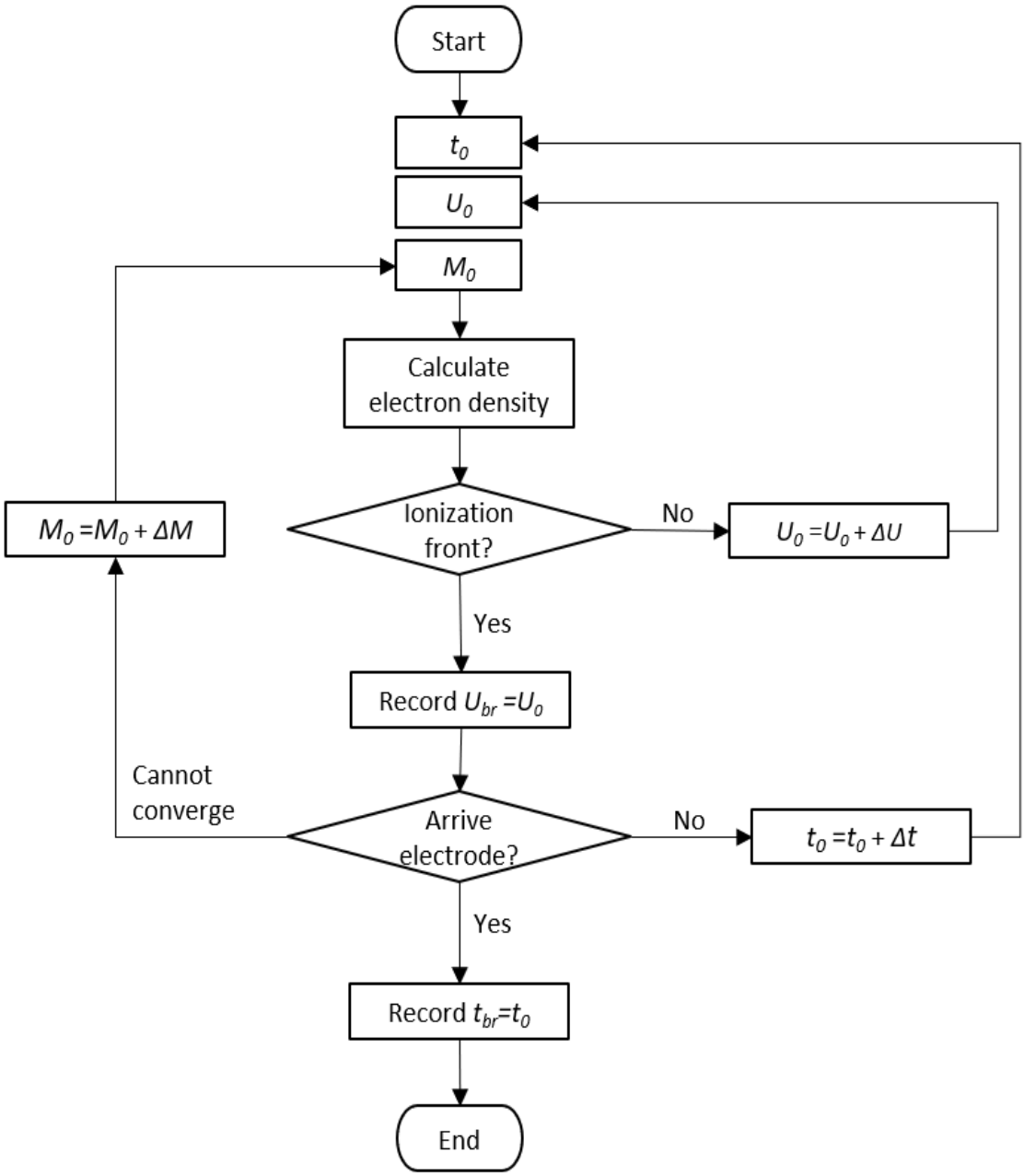

Figure 4.2 Flow chart illustrating calculation procedure for the breakdown voltage U_{br} and time to breakdown t_{br}

As shown in Figure 4.2, the computation starts at time zero, t_0, at this time the voltage is set as U_0 and the initial value of the mesh, M_0, is chosen. Then the electron density is calculated.

When the electron density associated with the ionization front (streamer) has a uniform distribution in the developing streamer (discharge) channel in the gap, the breakdown criterion is satisfied. Then the voltage U_0 is recorded as the breakdown voltage U_{br}.

If the electron distribution in the discharge channel is not uniform, the voltage is increased by ΔU (ΔU is the voltage increment). This voltage step is added to the initial voltage, U_0, for the next round of calculations. After several voltage increments (computational steps), the ionization front (streamer) develops and reaches the ground electrode.

Thus, the breakdown voltage is achieved (associated with the uniform distribution of the electronic density in the gap) and recorded. At this moment, time is recorded as the time to breakdown, t_{br}.

Otherwise, if the simulation algorithm cannot converge, the mesh parameter becomes $M_0 + \Delta M$, and then run the simulation model. If the ionization front cannot arrive at the ground electrode, the time becomes $t_0 + \Delta t$, and then run the model until they satisfy the breakdown criterion. Then the breakdown voltage U_{br} and time to breakdown t_{br} are obtained.

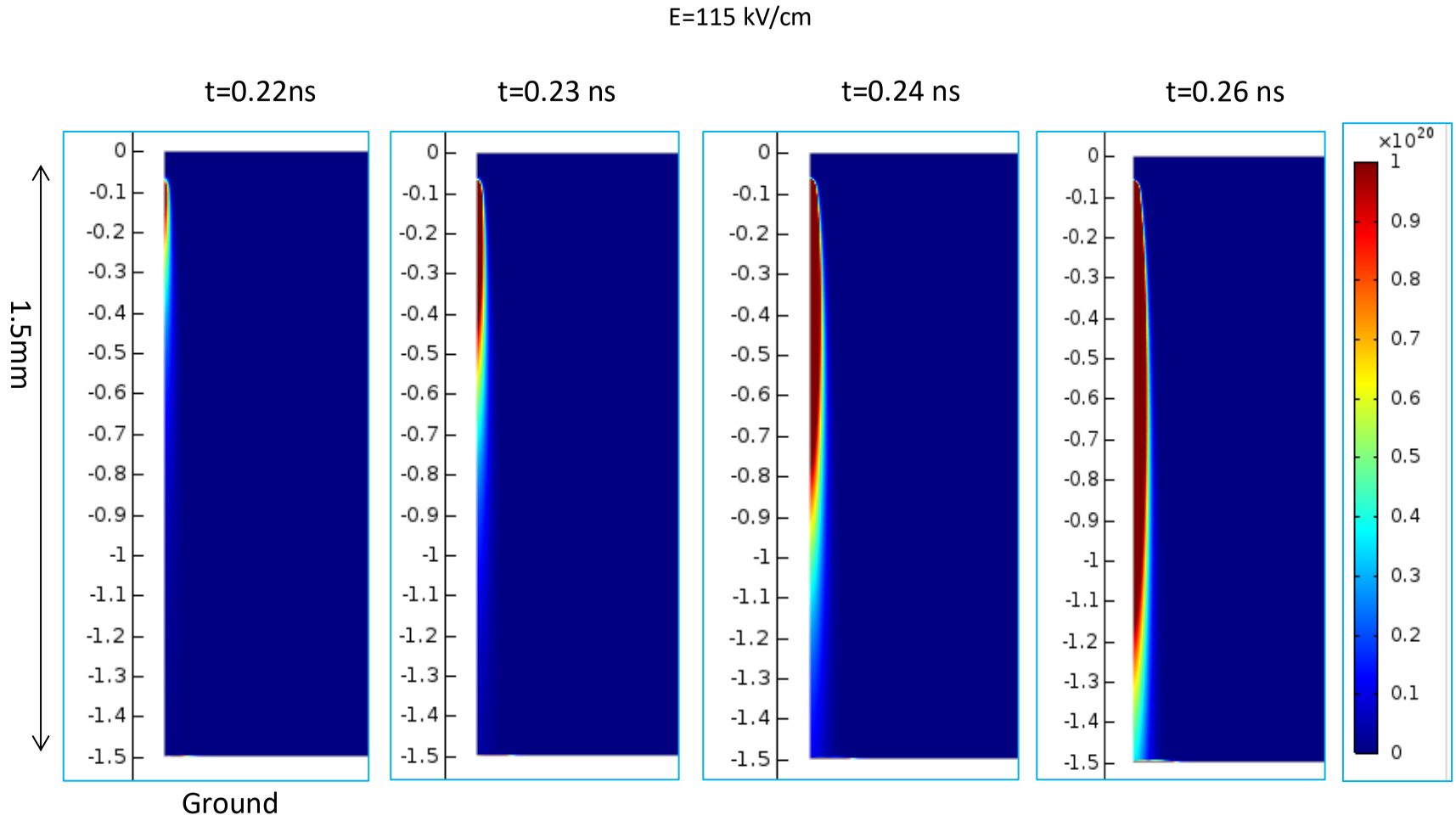

Figure 4.3 Distribution of electron density in air (E=115kV/cm, 1atm)

Using this calculation procedure, the development of negative ionization front in gas at atmospheric pressure has been modelled.

For example, Figure 4.3 shows the development of the ionisation front in air at the pressure of 1 atm in the parallel-plane geometry with a gap of 1.5 mm; the applied negative voltage is 17.3 kV. The ionization front is presented at different time instances: the ionization front propagates from the cathode towards the anode (snapshot at 0.22 ns) and bridges the gap at 0.26 ns. When the ionization fronts reach the anode, the breakdown criterion is satisfied, thus the breakdown field of 115 kV/cm and the time to breakdown t_{br} of 0.26 ns are obtained.

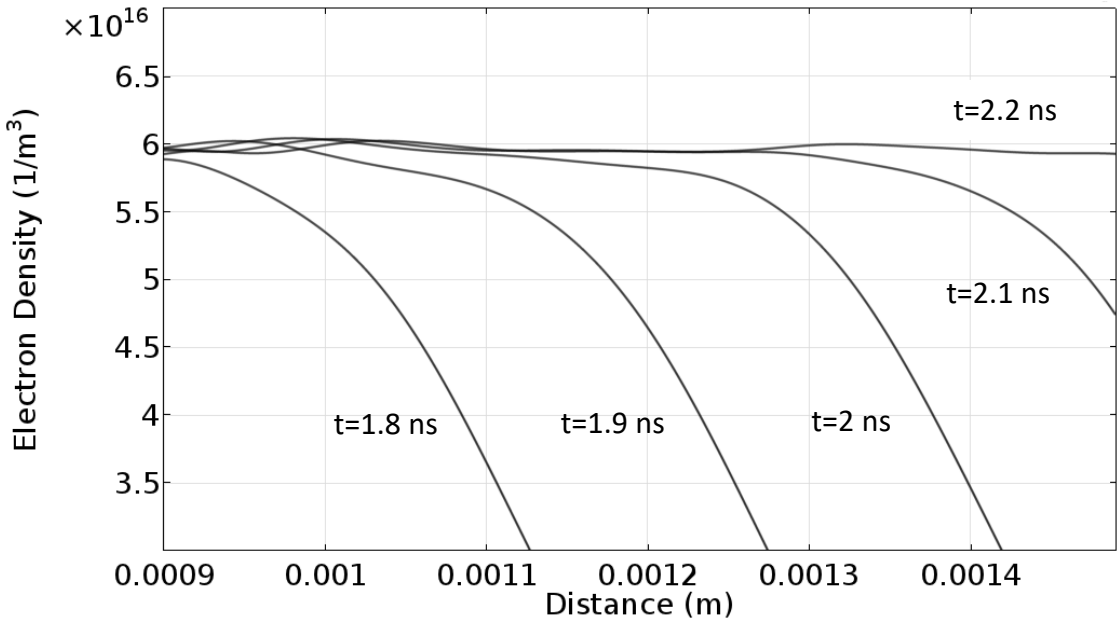

Figure 4.4 Distribution of electron density in in air (E=60 kV/cm)

Another example, as shown in Figure 4.4, in air, at the pressure of 1atm, the electric field of 60 kV/cm corresponds to a negative voltage of - 9 kV applied to the cathode. The results of the simulation of the electron density distribution in the parallel-plane geometry with a gap of 1.5 mm are presented at different times.

As shown in Figure 4.4, by the time the electrons with the density of $6 \cdot 10^{16}$ $1/m^3$ approached the anode, the electron density in the gap is almost uniform. The breakdown criterion is met at the time to breakdown t_{br} = 2.2 ns and the breakdown field E_{br} =60 kV/cm.

Similar breakdown criterion has also been used by Levko [Levko, 2019] in their computational study of the fast plasma fronts in gases. The breakdown in their model occurs when the electric field behind the plasma front collapses, due to the formation of conductive plasma.

4.3 Kinetic model

The kinetic approach is an analytical model which is based on the avalanche-to-streamer transition criterion. It is used here to obtain the time to breakdown and the reduced breakdown field for air, N_2, CO_2, and SF_6 over a wide range of electrical fields.

4.3.1 Kinetic model and field-time characteristics of gases

According to the Townsend model of an electron avalanche, the charge, *Q*, in the avalanche head is a function of the ionization frequency and time

$$Q \propto exp\,(\upsilon \,.\, t) \tag{4.8}$$

According to the Meek criterion, the avalanche is transformed into a streamer (streamer breakdown event) when the number of electrons reaches ~10^8. Therefore, it can be derived as

$$\upsilon_{ionis}\, t_{br} \geq 18 \tag{4.9}$$

where υ_{ionis} is the ionization frequency in the unit of 1/s. t_{br} is the time to breakdown. As a result, the breakdown criterion can be written as

$$t_{br} \geq \frac{18}{\upsilon_{ionis}} = \frac{18}{p\left(\upsilon_{ionis}/p\right)} \tag{4.10}$$

Then, we can get

$$t_{br}p = \frac{18}{\left(\upsilon_{ionis}/p\right)} \tag{4.11}$$

where p is gas pressure in unit of Pa.

The ionization frequency in gas is a function of the product of the ionization coefficient and electronic drift velocity

$$\upsilon_{ionis} = \alpha\, v_d \tag{4.12}$$

where, α is the ionization coefficient and v_d is the electron drift velocity. The electron drift velocity is

$$v_d = \mu E \tag{4.13}$$

$$\frac{v_d}{p} = \mu \frac{E}{p} \tag{4.14}$$

where μ is the mobility. The ionization coefficient and the mobility are functions of the electric field, E/p. Thus

$$\frac{v_{ionis}}{p} = \frac{\alpha\, v_d}{p} = \alpha\, \mu \left(\frac{E}{p}\right) \tag{4.15}$$

Therefore, the time to breakdown multiplied by the gas pressure is

$$t\, p = \frac{18}{\frac{v_{ionis}}{p}} = \frac{18}{\alpha\, \mu \left(\frac{E}{p}\right)} \tag{4.16}$$

Equation (4.16) can be re-written in terms of pressure by using $p = Nk_BT$, (k_B is the Boltzmann constant, T is the temperature, and N is the particle number density)

$$t\, N = \frac{18}{\alpha\, \mu\, (E/N)} \tag{4.17}$$

where, t is the time to breakdown.

The reduced effective ionization coefficient is

$$\alpha' = \alpha_{eff}\ /N \tag{4.18}$$

Therefore, the time to breakdown, t_{br}, for each type of gas can be obtained as a function of the reduced field in the framework of the kinetic approach. The corresponding kinetic equation is

$$t_{br}\, N = \frac{18 \cdot 10^{21}}{\alpha'\, N\ \mu\, (E/N)} \tag{4.19}$$

where α' is the reduced effective ionization coefficient in m^2. $t_{br}N$ is the product of the time to breakdown and gas density, s/m^3, E/N is the reduced field in the units of Td,

μ is electron mobility in the units of $\mathrm{m}^2/(\mathrm{V}\cdot\mathrm{s})$. The gas number density, N is $\sim 2.5\cdot 10^{25}(1/\mathrm{m}^3)$ at 1 atm and 20°C.

The effective ionization coefficient, α_{eff}, and the mobility, μ, provided in Chapter 3 are used in Equation 4.19. The analytical curves $Nt_{br}(E/N)_{br}$ obtained by the kinetic model, Equation 4.19, for air, N_2, CO_2 and SF_6 are shown in Figures 4.5-4.8.

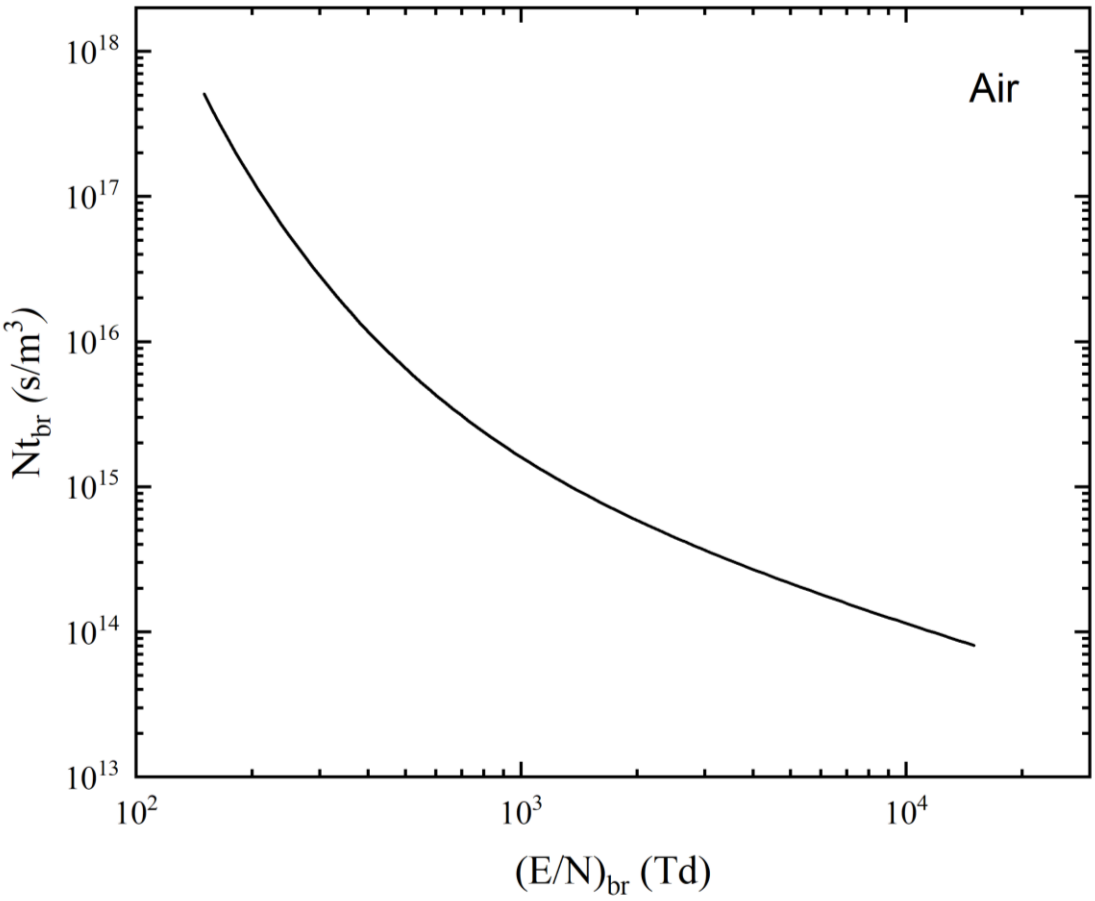

Figure 4.5 Nt_{br} as function of E/N for air obtained by Equation 4.19

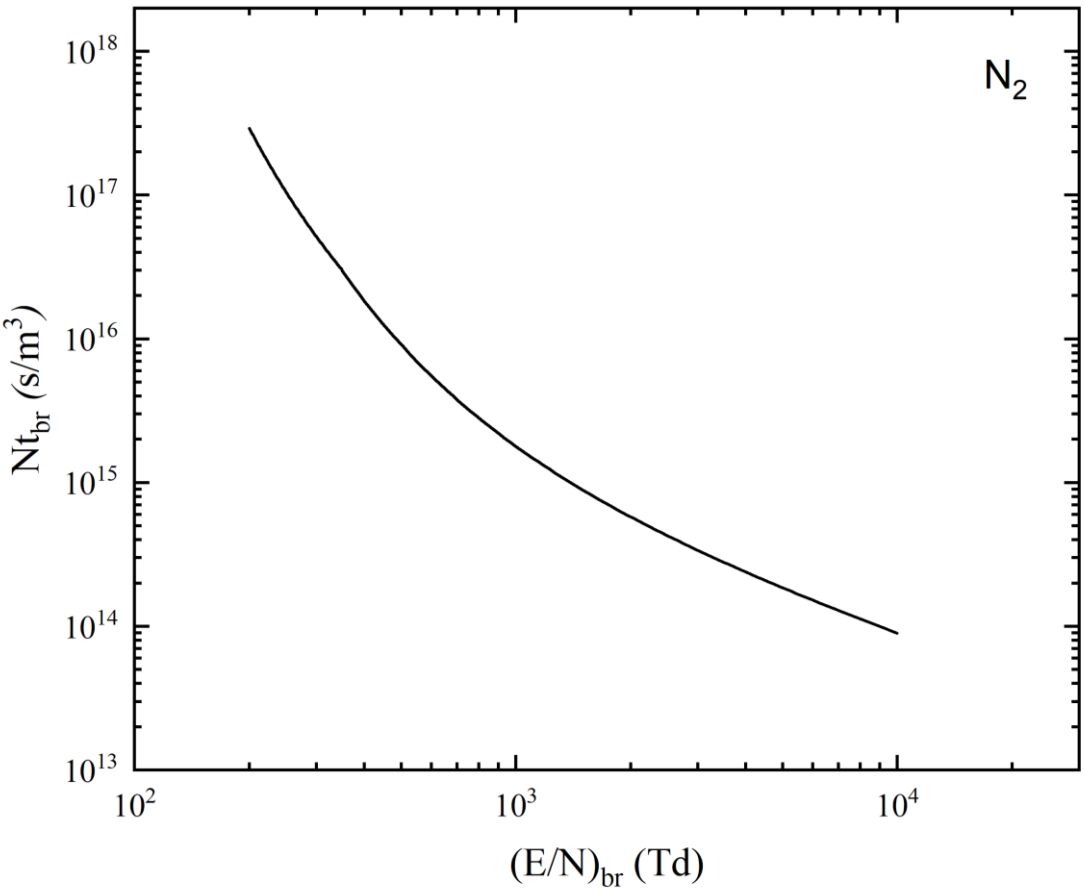

Figure 4.6 Nt_{br} as function of E/N for N_2 obtained by Equation 4.19

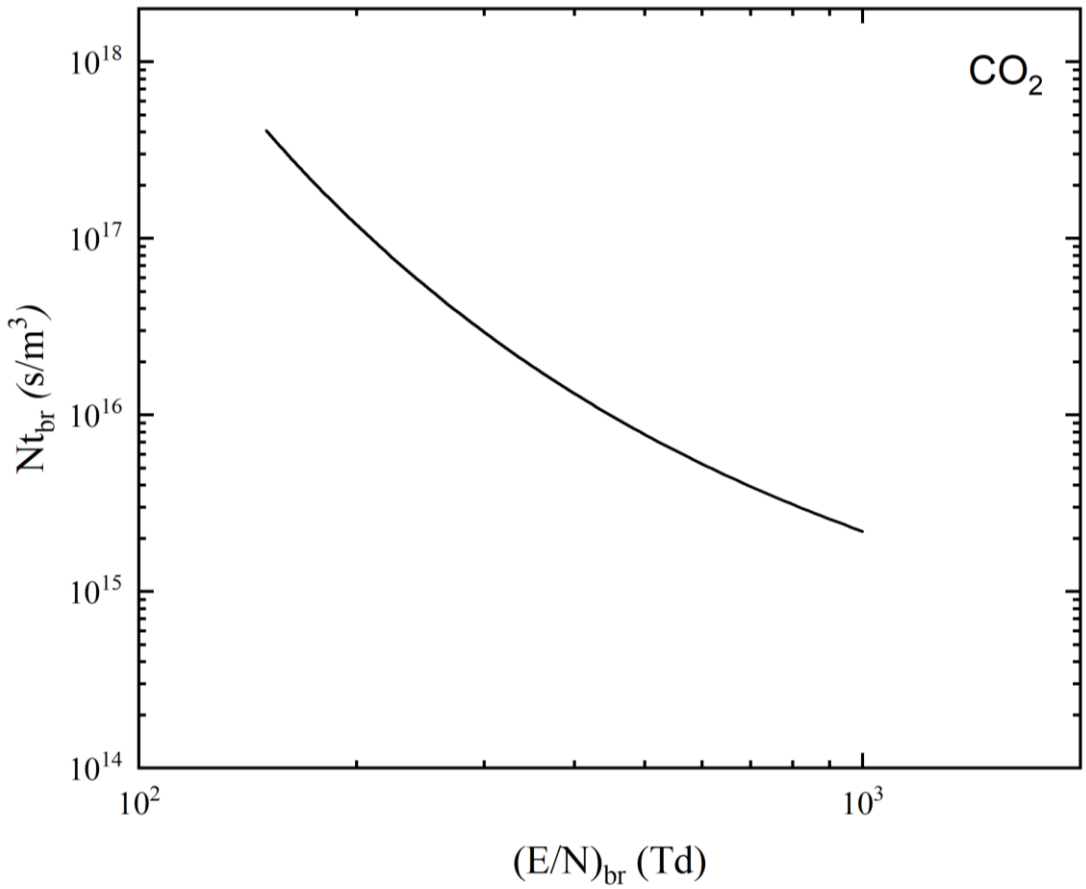

Figure 4.7 Nt_{br} as function of E/N for CO_2 obtained by Equation 4.19

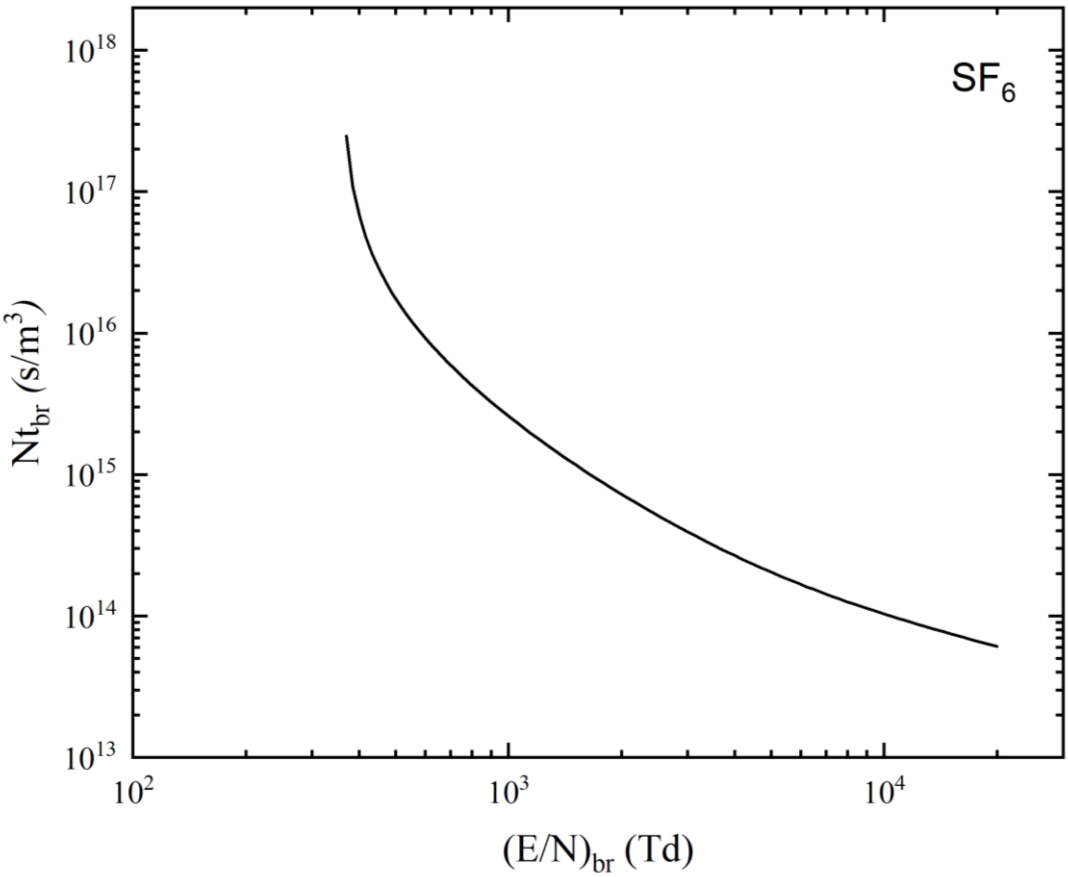

Figure 4.8. Nt_{br} as function of E/N for SF_6 obtained by Equation 4.19

Figures 4.5 - 4.8 demonstrate a decrease in the product of the particle density and the time to breakdown (Nt_{br}) with an increase in the reduced breakdown field $(E/N)_{br}$ for all investigated gases.

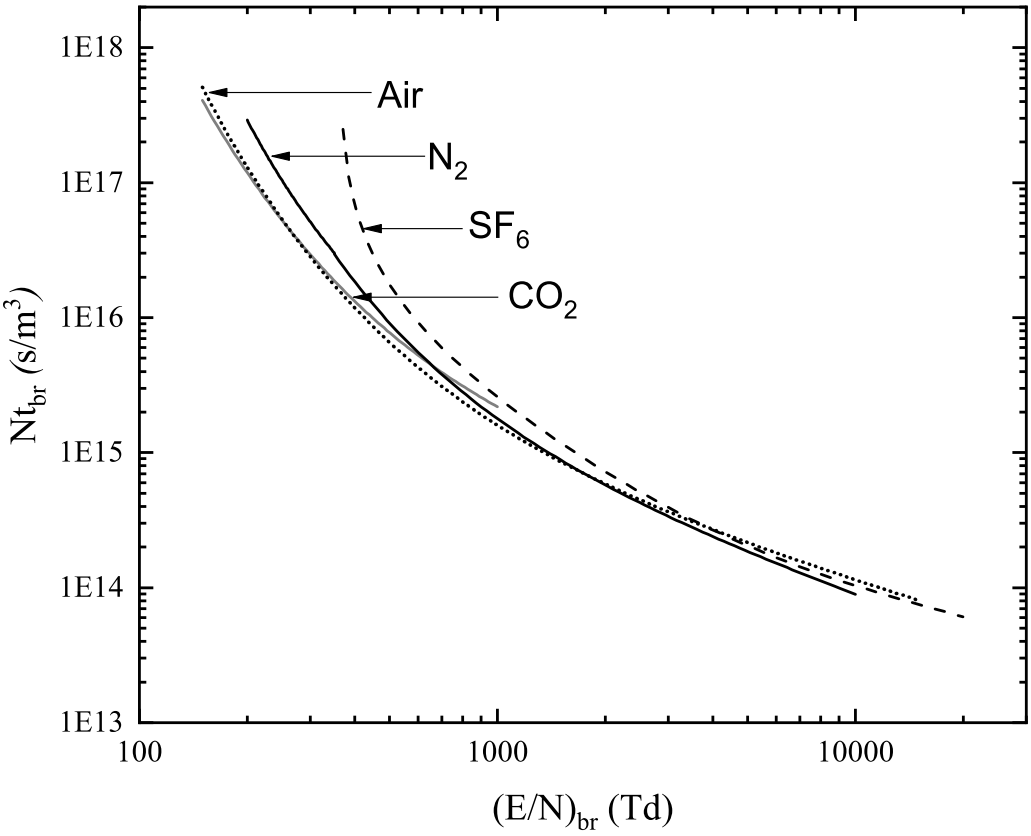

Figure 4.9 Nt_{br} as function of $(E/N)_{br}$, obtained by equation 4.19. Dotted line: air; solid dark line: N_2; solid grey line: CO_2; dashed line: SF_6

As shown in Figure 4.9, air and CO_2 show similar functional behaviour, i.e. the functional dependency Nt_{br} (E/N), for fields smaller than 10^3 Td. It is also noted that N_2 has slightly higher values of Nt_{br} than air and CO_2 in the field range from ~110 Td to ~10^3 Td, but lower values of Nt_{br} than for SF_6. Interestingly, the time to breakdown (Nt_{br}) in air for the field of ~$3 \cdot 10^3$ Td becomes higher than that in N_2, and starts to converge with that for SF_6.

4.3.2 Analysis of the discharge modes in the *Nt*(*Nd*) diagram

For the Townsend discharge mechanism, based on Equation 2.5, the relationship between (α/N) and Nd has been obtained

$$(\alpha/N) \cdot Nd = ln\,(1/\gamma) \tag{4.20}$$

where α is the ionization coefficient, d is the inter-electrode gap, γ is the second ionization coefficient, N is the gas number density.

Then, taking into account that the reduced ionization coefficient (α/N) is inversely proportional to the product of the gap separation and particle number density (Nd), it can be obtained that

$$\alpha/N \sim 1/Nd \tag{4.21}$$

Moreover, the ionization coefficient (α/N) is a function of E/N, thus

$$E/N \sim 1/Nd \tag{4.22}$$

In the Townsend discharge process, the secondary electrons are produced by the bombardment of the cathode surface by positive ions. This process is characterized by the second ionization coefficient (γ). These secondary electrons are required for the self- sustained development of the Townsend discharge.

Therefore, the minimum time required for the development of the Townsend discharge is defined by the time required for positive ions to return to the cathode.

The following condition for the Townsend discharge has been obtained [Atrazhev, 2012]

$$Nt \geq Nd/v_p \tag{4.23}$$

where t is the time and N is the gas number density, d is the gap separation between electrodes, v_p is the drift velocity of positive ions.

The drift velocity of the positive ions as a function of E/N can be expressed as

$$v_p = \mu_p N(\frac{E}{N}) \tag{4.24}$$

where v_p is the drift velocity of positive ions, μ_p is the mobility coefficient of the positive ions, E is the electric field and N is the gas number density.

The drift velocity of the positive ions in air, N_2, CO_2 and SF_6 have been obtained by Equation 4.24, and listed in Table 4.5, where the mobilities of the positive ions are obtained from Section 4.2.2 (Table 4.1-4.4).

TABLE 4.5

Drift velocity of positive ions, v_p

Gas	Drift velocity of positive ions v_p (m/s)
Air	$v_p = 2.34 \cdot 10^{-4} \cdot N \cdot \left(\frac{E}{N}\right) \cdot 10^{-21}$
N_2	$v_p = 2.5 \cdot 10^{-4} \cdot N \cdot \left(\frac{E}{N}\right) \cdot 10^{-21}$
CO_2	$v_p = [6.52 \cdot 10^{-5} \cdot exp^{\left(-\frac{\left(\frac{E}{N}\right)}{399}\right)} + (6.96 \cdot 10^{-5})] \cdot N \cdot \left(\frac{E}{N}\right) \cdot 10^{-21}$
SF_6	$v_p = 6.0 \cdot 10^{-5} \cdot N \cdot \left(\frac{E}{N}\right) \cdot 10^{-21}$

As shown in Table 4.5, v_p is the drift velocity of positive ions in m/s, *E/N* is the reduced electric field in the unit of Td, *N* is the gas number density, $1/m^3$.

In the present work, the critical avalanche time, $(Nt)_{avalanche,}$ is defined as a product of the minimal time required for the development of the Townsend discharge and the gas number density, *Nt*. This time can be obtained as a function of *Nd* by Equations 4.23 - 4.24, $Nt = Nd/v_p$, when the electric field, *E/N* , is equal to the breakdown field, $(E/N)_{br}$.

If the values of *Nt* are greater than the critical avalanche time, $Nt \geq (Nt)_{avalanche}$, the secondary electrons produced at the cathode will sustain the development of the Townsend avalanche(s). Thus, $Nt \geq (Nt)_{avalanche}$ defines the Townsend avalanche boundary condition for *Nt*.

As shown in Table 4.6, the Townsend avalanche boundary condition, $Nt \geq (Nt)_{avalanche}$, is based on Equations 4.23 - 4.24. The values required to calculate the the Townsend avalanche boundary condition for the air, N_2, CO_2 and SF_6 have been obtained using the breakdown field, $(E/N)_{br}$, presented in Section 2.4.1.

TABLE 4.6

Avalanche boundary condition

Gas	$(E/N)_{br}$ Td from Paschen curves	Avalanche boundary for $Nt \geq Nd/v_p$ (s/m^3)
Air	130	$Nt \geq Nd/758$
N_2	117	$Nt \geq Nd/734$
CO_2	190	$Nt \geq Nd/524$
SF_6	356	$Nt \geq Nd/535$

From another point of view, the streamer mechanism can be used to characterize the development of the ionization front when it reaches its critical size. At this moment, which is determined by the drift velocity of electrons, v_e, the avalanche transforms into a streamer.

The time required for this transition should be shorter than the time required for an electron to cross the gap if this electron moves with its drift velocity, v_e. Thus, the following condition could be written for the time required for the avalanche to be transformed into the streamer (streamer discharge) [Atrazhev, 2012]

$$Nt \leq Nd/v_e \tag{4.25}$$

where t is the time, N is the gas number density, d is the gap length between electrode, v_e is the drift velocity of the electrons.

Using the expression for the drift velocity as a function of the normalized electric field, *E/N*, $v_e = \mu_e E$, the following boundary condition for the streamer breakdown can be obtained

$$v_e = \mu_e N(\frac{E}{N}) \tag{4.26}$$

where v_e is the drift velocity of the electrons, μ_e is the electron mobility, E is the electric field and N is the gas number density. The drift velocities of electrons in air, N_2, CO_2 and SF_6 have been obtained by Equation 4.26 and provided in Table 4.7.

TABLE 4.7

Drift velocity of electrons

Gas	v_e (m/s)
Air	$v_e = \left(3.361 \cdot 10^{24} \left(\frac{E}{N}\right)^{-0.222}\right) \cdot \left(\frac{E}{N}\right) \cdot 10^{-21}$
N_2	$v_e = (1.7 \cdot 10^{24} (E/N)^{-0.09} \cdot \left(\frac{E}{N}\right) \cdot 10^{-21}$
CO_2	$v_e = (8.68 \cdot 10^{24} (E/N)^{-0.416} \cdot \left(\frac{E}{N}\right) \cdot 10^{-21}$
SF_6	$v_e = (3.085 \cdot 10^{24} (E/N)^{-0.284} \cdot \left(\frac{E}{N}\right) \cdot 10^{-21}$

Table 4.7 shows the drift velocity of electrons, v_e, in the unit of m/s as a function of *E/N*, these values have been obtained by using the mobility of electrons, μ_e, in the unit of $(\frac{\mathrm{m}^2}{\mathrm{V \cdot s}})$, as discussed in Section 3.4 (Table 3.10). *E/N* is the reduced electric field in the unit of Td.

In the present work, the critical streamer time, $(Nt)_{streamer}$, is defined as the product of the time required for the avalanche to reach its critical size and to transform into a streamer. The gas number density, *Nt*, as a function of *Nd* is obtained by Equations 4.25 - 4.26, $Nt = Nd/v_e$, when the electric field *E/N* is equal to the breakdown field, $(E/N)_{br}$.

Therefore, the streamer boundary condition for $(Nt)_{streamer}$ is based on Equations 4.25-4.26 and the critical electrical field, $(E/N)_{br}$, obtained in Section 2.4.1 have been calculated for air, N_2, CO_2 and SF_6, and presented in Table 4.8.

TABLE 4.8

Streamer boundary condition for *Nt*

Gas	(E/N_{br}) Td from Section 2.4.1	Streamer boundary condition, $Nt \leq Nd/v_p$ (s/m^3)
Air	130	$Nt \leq Nd/147936$
N_2	117	$Nt \leq Nd/130021$
CO_2	190	$Nt \leq Nd/186114$
SF_6	356	$Nt \leq Nd/207225$

The avalanche boundary condition and the streamer boundary condition *Nt* (*Nd*), for air, N_2, CO_2 and SF_6 are presented in Figure 4.10, where the avalanche boundary condition, $(Nt)_{avalanche}$, is defined by the Townsend mechanism, and the streamer boundary condition, $(Nt)_{streamer}$, is based on the streamer mechanism.

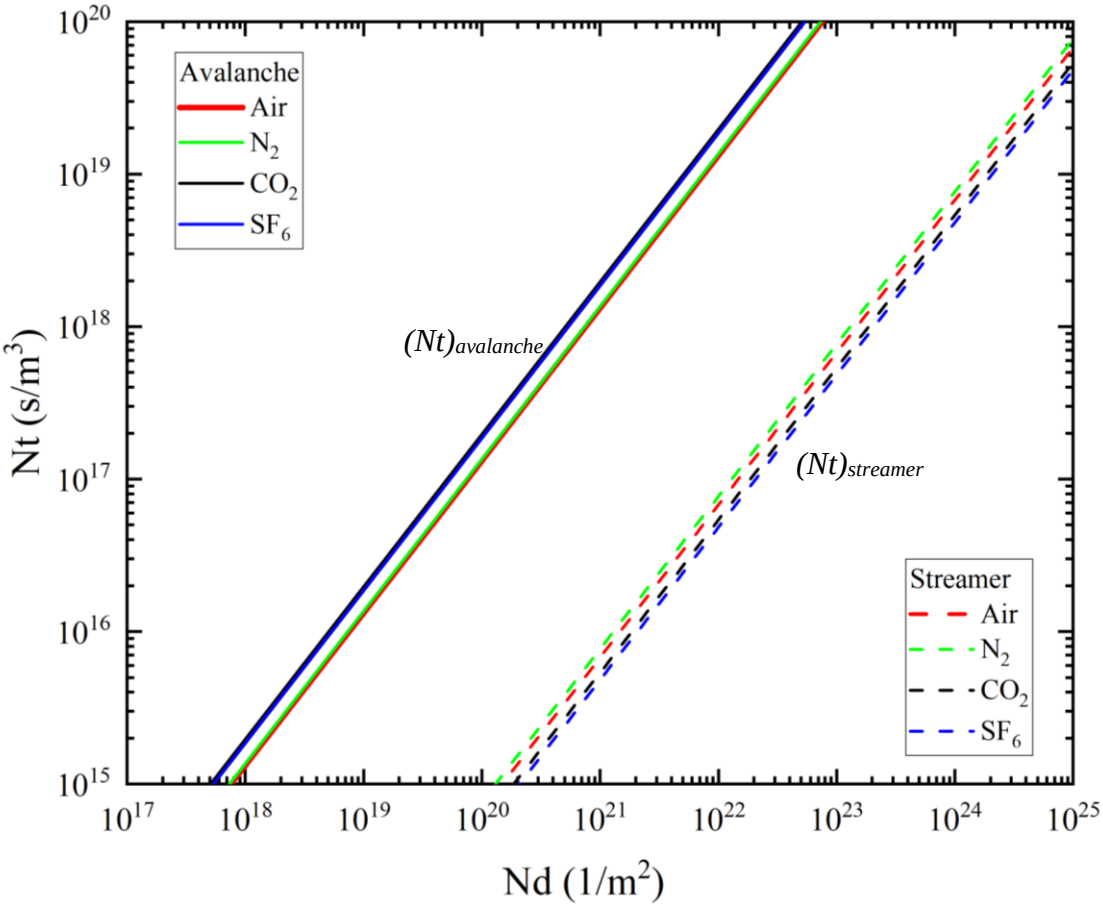

Figure 4.10 Avalanche and streamer conditions for air, N_2, CO_2 and SF_6

It can be seen from Figure 4.10 that the critical avalanche time, $(Nt)_{avalanche}$, which defines the threshold conditions for the self-sustained development of the Townsend avalanches, divides this graph into two regions: non-Townsend discharges and Townsend discharges.

When the value of Nt is greater than the critical avalanche time, $Nt \geq (Nt)_{avalanche}$, these conditions satisfy the Townsend discharge conditions and it can be stated that the discharges with such parameters are Townsend discharges. However, when the value of Nt is less than the critical avalanche time, $Nt < (Nt)_{avalanche}$, the Townsend avalanche requirements are not met.

When the value of *Nt* is lower than the critical streamer time, $Nt \leq (Nt)_{streamer}$, the conditions for the streamer discharge are achieved. When the value of *Nt* is greater than the critical streamer time, $Nt > (Nt)_{streamer}$, the streamer breakdown conditions are not met and streamers will not develop in such conditions.

When the value of *Nt* is between the critical avalanche and the critical streamer time $(Nt)_{avalanche} \leq Nt \leq (Nt)_{streamer}$, this region satisfies neither Townsend nor streamer conditions and as stated in [Atrazhev, 2012], the breakdown mechanism for such conditions is not well defined. As discussed in [Atrazhev, 2012], the equations which define the Townsend breakdown and streamer breakdown provide the limiting cases (boundaries) of a complex process, which depends upon the gap between electrodes, gas pressure and the duration of the voltage impulse.

Therefore, further experimental and analytical investigation is required to establish exact discharge and breakdown mechanisms in this region of the *Nt(Nd)* diagram.

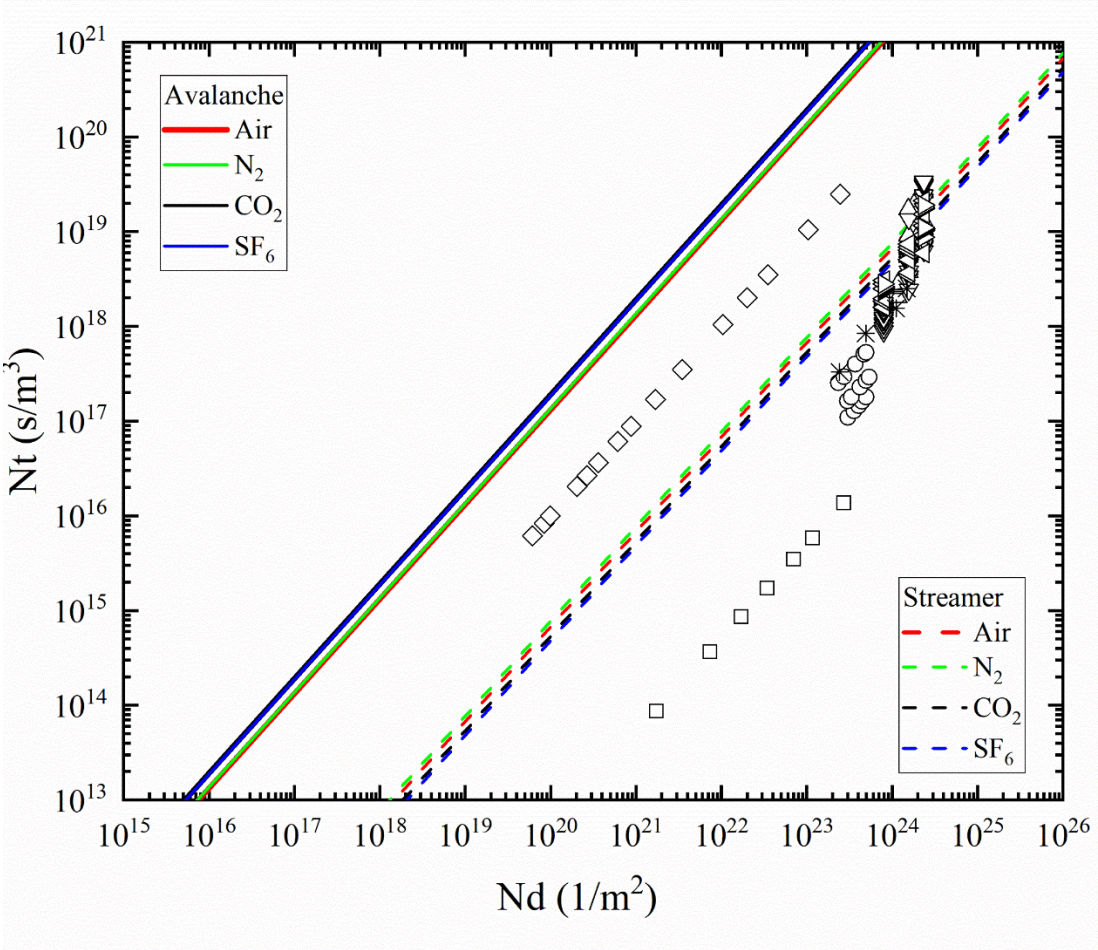

Figure 4.11 Comparison of the experimental and analytical data from the literature. □ air, rising time of 0.5 ns [Babich, 2016]; △ air negative polarity (monocone) [Carboni, 2001]; ▽ air positive polarity (monocone) [Carboni, 2001]; ◁ N_2 negative polarity (monocone) [Carboni, 2001]; ▷ N_2 positive polarity (monocone) [Carboni, 2001]; ◇ air, rising time of 1μs [Babich, 2016]; ○ air [Kawada, 1988]; * air [Shao, 2006]

The experimental and analytical data collected from the literature, [Carboni, 2001], [Shao, 2006], [Babich, 2016], [Kawada, 1988], have been used to classify the discharge mechanism based on the established boundary conditions, Figure 4.11.

Carboni [Carboni, 2001] provides the experimental data for the time to breakdown in air and N_2 in the pressure ranges from ∽30 atm to 100 atm (within the range of *E/N* up to ~ 300 Td) for both positive and negative polarities in the monocone electrode topology with the gap length of 0.091cm. The experimental *Nt* values show that in the region $Nt \leq (Nt)_{\text{streamer}}$, they satisfy the streamer breakdown boundary condition. In

the region of $(Nt)_{avalanche} \leq Nt \leq (Nt)_{streamer}$, the values do not satisfy either the Townsend or the streamer boundary condition.

Shao [Shao, 2006] presents the experimental breakdown characteristics obtained in the parallel-plane electrode topology with a gap of 1cm in air at pressures of 0.1 and 0.2 MPa, stressed with impulsive voltage with a rising time of ∽10 ns. The experimental *Nt* values are located in the region $Nt \leq (Nt)_{streamer}$ and satisfy the streamer breakdown boundary condition.

Kawada investigated the impulsive breakdown behaviour of air in the uniform field in 1cm to 3 cm gaps at the pressure range from 330 Torr to 1520 Torr (~44 kPa to ~ 202 kPa), the applied voltage impulses had the rising time of 10.8 ns. The experimental *Nt* values obtained in [Kawada, 1988] are located in the region $Nt \leq (Nt)_{streamer}$ and satisfy the streamer breakdown boundary condition.

Babich [Babich, 2016] provides the analytical breakdown voltage and breakdown time in the overvolted conditions when air at pressures less than 1 bar was stressed with short HV impulses with the rising times of 0.5 ns and 1μs in the rod-plane geometry. The experimentally obtained values of *Nt* are located in the region $Nt \leq (Nt)_{streamer}$ and satisfy the streamer breakdown boundary condition. However, the *Nt* values obtained for HV impulses with the rise time of 1μs are located in the region between the critical avalanche and the critical streamer times, $(Nt)_{avalanche} \leq Nt \leq (Nt)_{streamer}$, and therefore they do not satisfy either of the boundary conditions.

4.4 Drift-diffusion and kinetic models: results and their analysis

This section focuses on the discussion, analysis, and comparisons of the modelling results - the relationship between the breakdown field and time to breakdown obtained by the drift-diffusion and kinetic models. The nominal average velocity of the ionization fronts as a function of the applied electric field is obtained. Then, the time to breakdown as a function of the electric breakdown field for air, N_2, CO_2, and SF_6 is presented and analysed.

4.4.1 Average velocity of ionization front

The average velocity of the ionization front, v_{front}, is an important parameter of the streamer propagation. It is defined as the gap length divided by the time required for the ionization front to cross the gap between the electrodes

$$\bar{v}_{front}(\ell)=\ell/t_{br} \tag{4.27}$$

where ℓ is the length of the gap separation between electrodes, t_{br} is the time to breakdown, which is the time required for this ionization front to propagate over this distance, ℓ.

The time to breakdown and breakdown voltage has been obtained for air, N_2, CO_2, and SF_6 using the drift-diffusion model Equation 4.27. These values were used to calculate the average velocities of ionization fronts for different applied field. The nominal average velocities of the ionization front, $\bar{v}_{front}$, as a function of *E/N* for the investigated gases, are plotted in Figure 4.12.

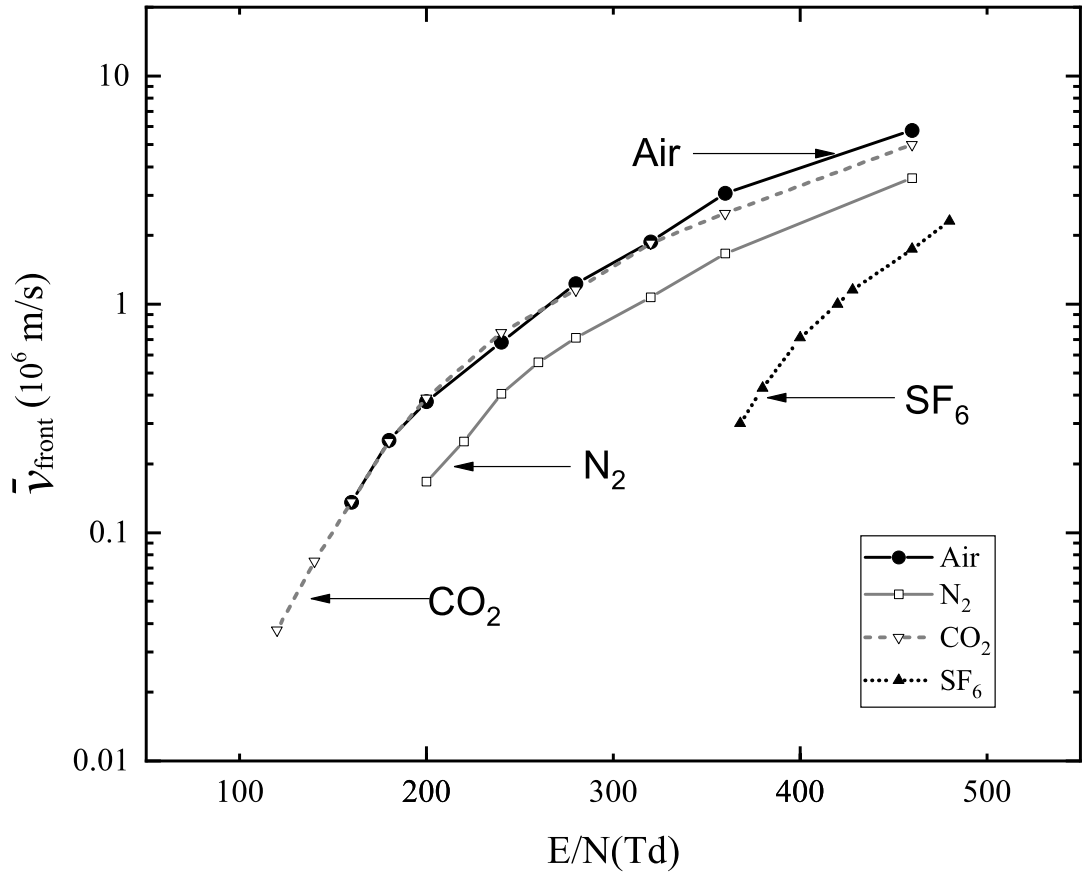

Figure 4.12 Nominal average velocity of the ionization front, $\bar{v}_{front}$, as a function of E/N. ● air; □ N_2; ▽ CO_2; ▲ SF_6. Connecting lines are given for visual guidance only

Figure 4.12 shows a gradual increase in the value of the ionization front velocity in the range of fields from ~100 Td to ~500 Td. It can be seen that the lowest velocity of the ionization front was obtained for SF_6 as compared with other gases in the range of the electric fields of ~360 to 500Td. Furthermore, it has been found that the ionization fronts have similar velocities in CO_2 and air, which agrees with the data from [Seeger, 2017].

The velocity of the ionization front in N_2 is lower than that in air and CO_2, which is confirmed by [Won, 2002] [van Veldhuizen, 2003], which provides the average velocities of the ionization fronts of ~10^5 m/s and ~10^4 m/s in N_2.

4.4.2 Time-field characteristics

The breakdown characteristics obtained by the drift-diffusion model and kinetic model are presented in this section. The time-field breakdown characteristic is the relationship between the time to breakdown (Nt_{br}) (the product of the breakdown time and the gas number density) and the reduced breakdown field $(E/N)_{br}$ for air, N_2, CO_2, and SF_6.

These characteristics have been obtained using both models to analyse and compare with the experimental results [Felsenthal, 1965], [Carboni, 2001], [Kumar, 2021], as shown in Figures 4.13-4.17.

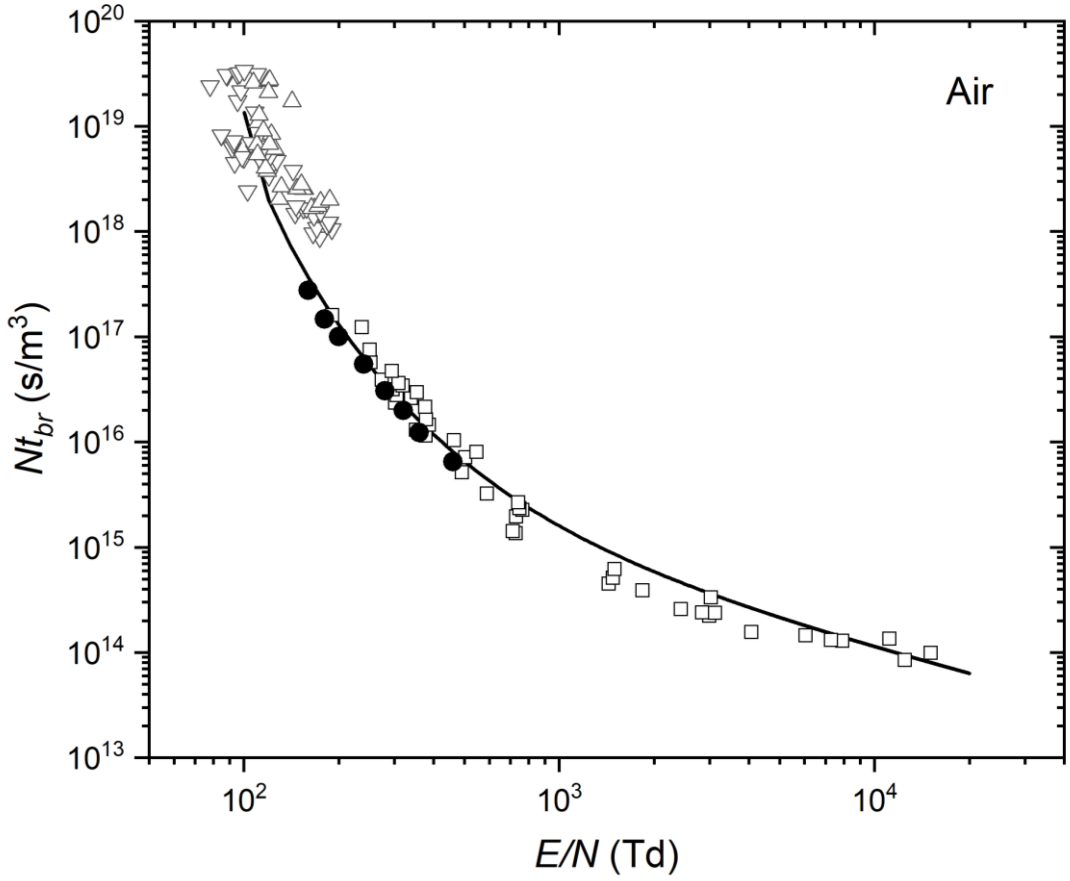

Figure 4.13 Nt_{br} as a function of $(E/N)_{br}$ in air. • Experimental data, □ [Felsenthal, 1965]; △ negative polarity (monocone) [Carboni, 2001]; ▽ positive polarity (monocone) [Carboni, 2001]; ● Drift-diffusion model, Equation 4.1 - 4.5; — Kinetic approach, Equation 4.19

Figure 4.13 shows *Nt* as a function of *E/N* for air from 100 Td to 500 Td obtained from the drift-diffusion and kinetic models. The results obtained by the kinetic model for air in the present work provide a good agreement with the experimental measurements [Felsenthal, 1965] in this range from 200 Td to $2 \cdot 10^4$ Td.

The result obtained using the kinetic model for air also shows a good agreement with the experimental data from [Carboni, 2001] in the range of the reduced electric fields from 10^2 Td to $2 \cdot 10^2$ Td.

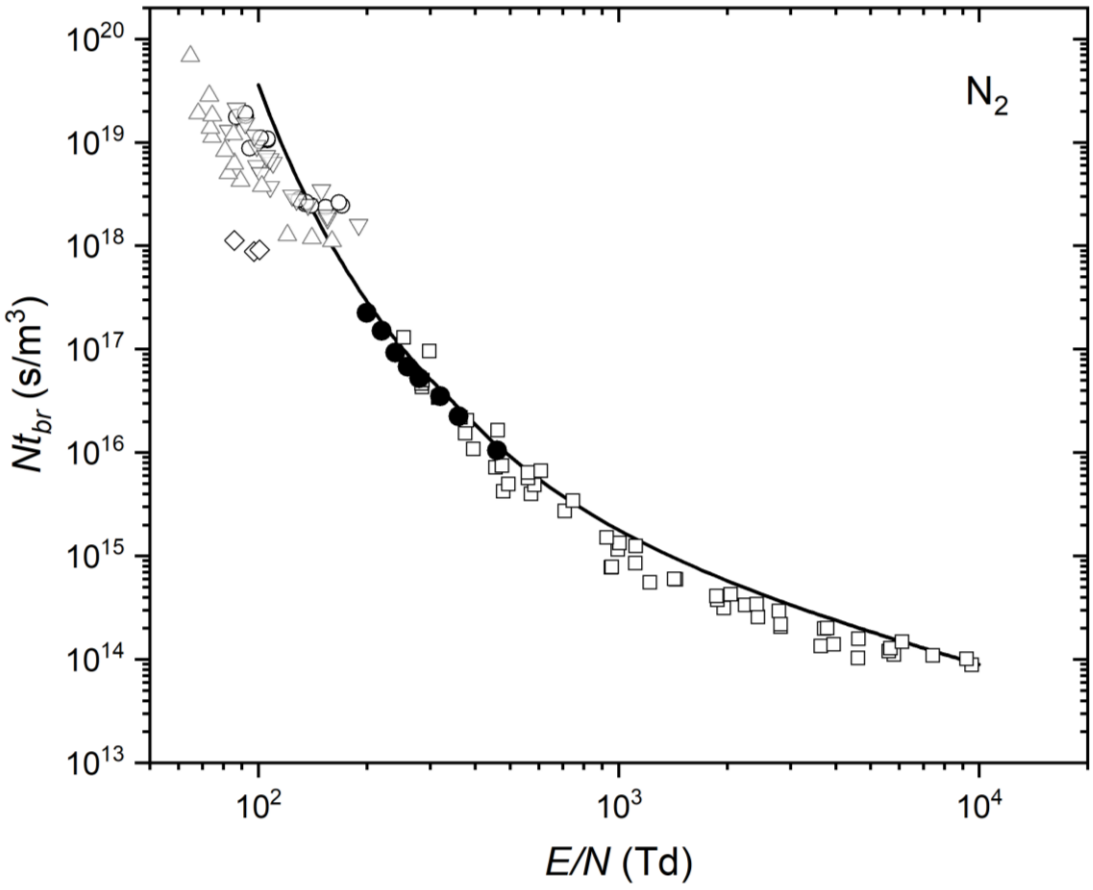

Figure 4.14 Nt_{br} as a function of $(E/N)_{br}$ in N_2. Experimental data: □ [Felsenthal, 1965]; △negative polarity (pointplane), ▽ negative polarity (monocone) [Carboni, 2001]; ◇positive polarity (pointplane), ○ positive polarity (monocone) [Carboni, 2001]; ● Drift-diffusion model, Equation 4.1 - 4.5; — Kinetic approach, Equation 4.19

Figure 4.14 shows Nt_{br} as a function of $(E/N)_{br}$ for N_2. The simulation results (shown as closed points in Figure 4.14) obtained by the drift-diffusion model agree well with the kinetic modelling line, which presents Nt as a function of E/N in the range from ~200 Td to ~500 Td.

The results from the kinetic model for N_2 provide a good agreement with the experimental measurements of the formative breakdown time [Felsenthal, 1965] in the E/N range from 200 Td to 10^4 Td. It also agrees with the experimental data on the effective breakdown time [Carboni, 2001] for the reduced electric fields from 10^2 Td to $2 \cdot 10^2$ Td.

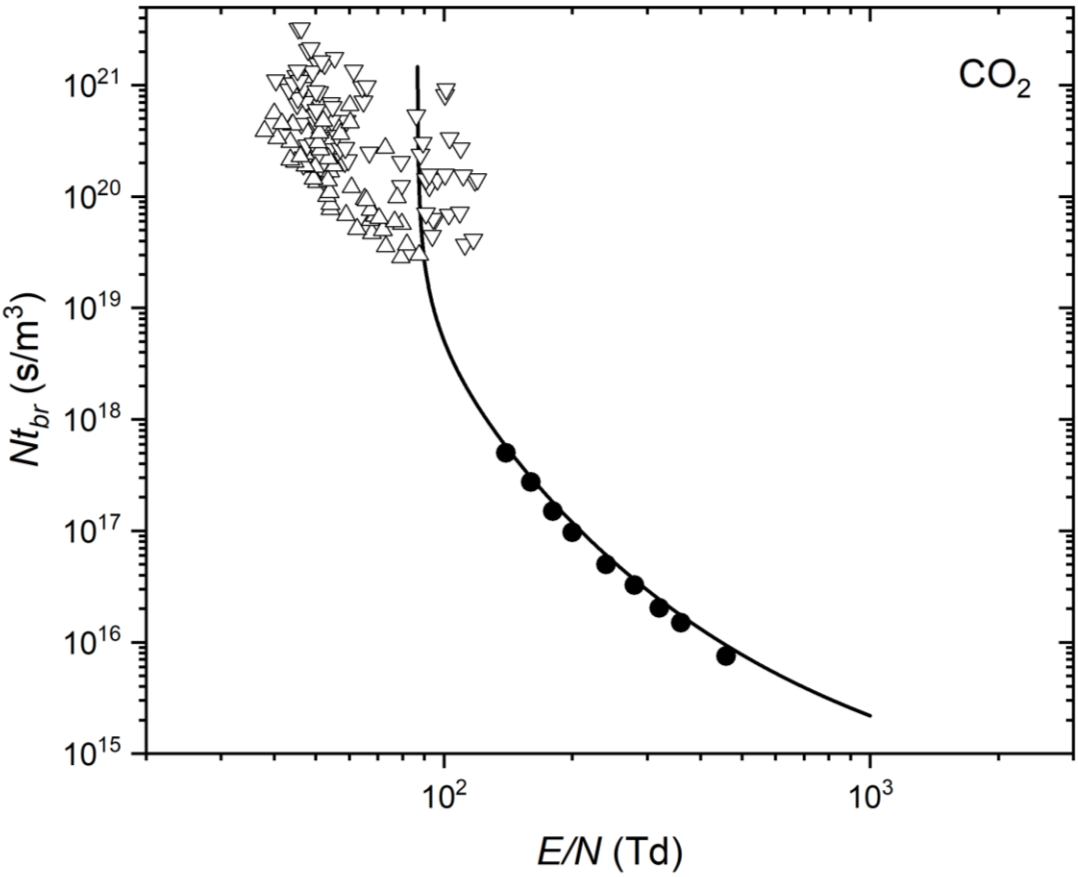

Figure 4.15 Nt_{br} as a function of $(E/N)_{br}$ in CO_2. Experimental data: △negative polarity [Kumar, 2021]; ▽positive polarity [Kumar, 2021]; ● Drift-diffusion model, Equation 4.1 - 4.5; — Kinetic approach, Equation 4.19

Figure 4.15 shows Nt_{br} as a function of $(E/N)_{br}$ for CO_2. The simulation results of Nt obtained from the drift-diffusion model are in accordance with the analytical line of Nt as a function of E/N from the kinetic model in the range from ~100 Td to ~500 Td.

The results from the kinetic model for CO_2 obtained in the present work provide a reasonable agreement with the experimental measurements [Kumar, 2021] in the reduced electric field range of up to ~100 Td.

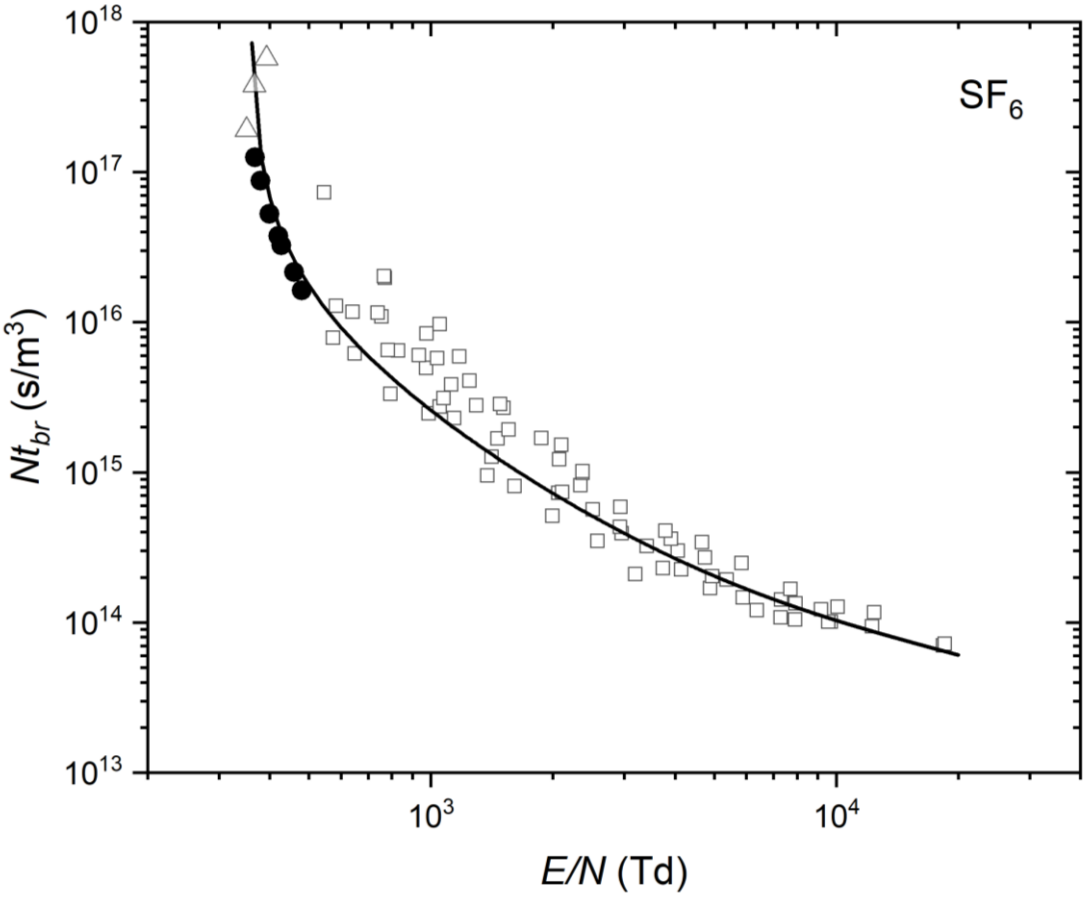

Figure 4.16 Nt_{br} as a function of $(E/N)_{br}$ in SF_6. Experimental data, □ [Felsenthal, 1965]; △ [Carboni, 2001]. ● Drift-diffusion model, Equation 4.1 - 4.5; — Kinetic approach, Equation 4.19

Figure 4.16 presents the Nt obtained from the drift-diffusion model for SF_6, (closed points). These results are in good agreement with the analytical values of Nt (E/N) obtained by the kinetic model in the range of E/N from ~360 Td to ~500 Td.

The results from the kinetic model for SF_6 obtained in the present work provide a good agreement with the experimental measurements of the formative breakdown time [Felsenthal, 1965] in the *E/N* range from 500 Td to $2 \cdot 10^4$ Td.

The result from the kinetic model for SF_6 also shows an agreement with the experimental data on the effective breakdown time [Carboni, 2001] in the reduced electric field range up to ~400 Td.

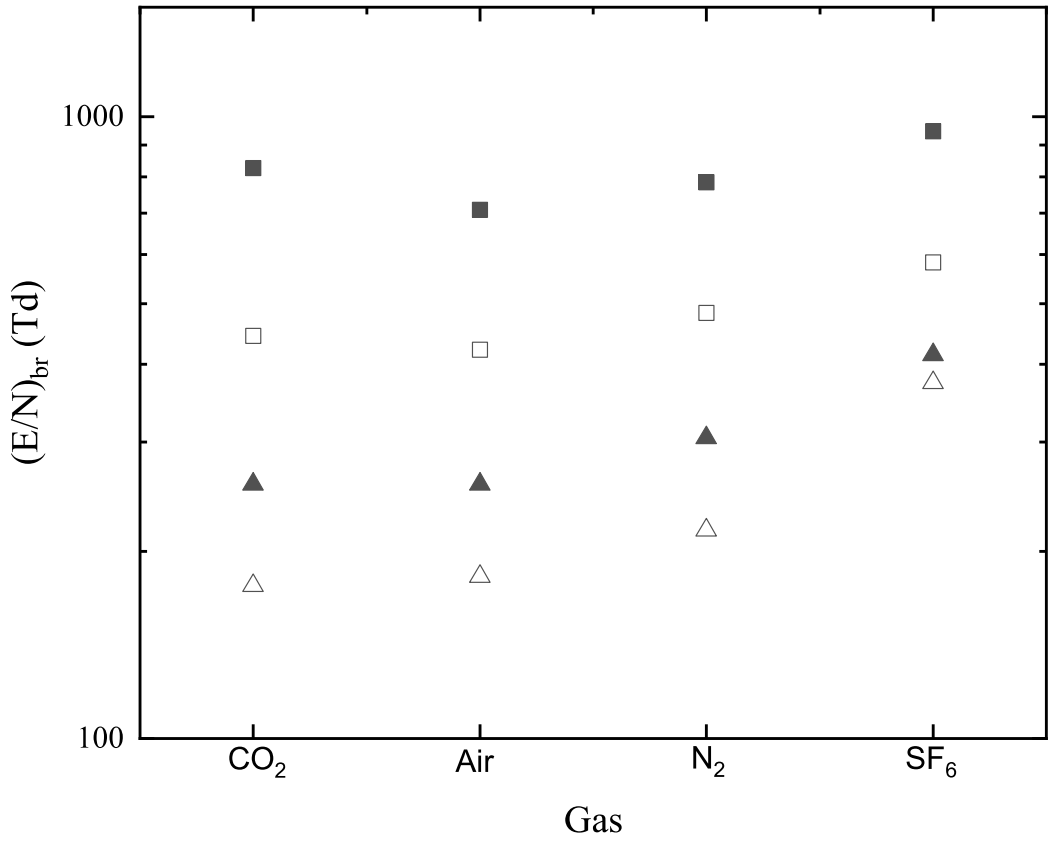

Figure 4.17 $(E/N)_{br}$ for investigated gases for specific values of Nt_{br}. △$2 \cdot 10^{17}$ (s/m^3); ▲ $5 \cdot 10^{16}$ (s/m^3); □ $1 \cdot 10^{16}$ (s/m^3); ■ $3 \cdot 10^{15}$ (s/m^3)

Figure 4.17 summarizes obtained specific values of Nt_{br} for air, N_2, CO_2 and SF_6. When $Nt_{br} = 2 \cdot 10^{17}$ s/m^3, SF_6 has the highest level of the reduced breakdown electric field compared with other gases, while CO_2 and air have similar levels of E/N. N_2 has a higher level of E/N compared with air and CO_2 at this value of Nt_{br}.

However, when $Nt_{br} = 1 \cdot 10^{16}$ s/m^3, the breakdown field for air, N_2, and CO_2 start to be close to that of SF_6. Interestingly, when Nt_{br} reaches $1 \cdot 10^{16}$ s/m^3, the E/N for CO_2 becomes higher than that for air and is almost the same as for N_2. When Nt_{br} reaches $3 \cdot 10^{16}$ s/m^3, the E/N for CO_2 is almost the same as for SF_6. This behaviour will be discussed in Section 4.5.

Overall, the simulation data obtained by the drift-diffusion model and the kinetic models, Nt_{br} $(E/N)_{br}$ for air, N_2, CO_2 and SF_6 show that the product of the time to breakdown and the gas number density (Nt_{br}) decreases with an increased reduced breakdown field (E/N). The kinetic and drift-diffusion models also provide agree well with the experimental results.

4.5 Discussion

In this chapter, the drift-diffusion and kinetic models have been developed to obtain the time-field breakdown characteristics for air, N_2, CO_2 and SF_6 in a wide range of electric fields.

The drift-diffusion model has been implemented using COMSOL Multiphysics software, an FEA computational simulation tool. The computational domain for the parallel plane geometry electrode with a gap length of 1.5 mm for air, N_2, CO_2, and SF_6 at atmospheric pressure has been established to examine the development of the ionization front. The breakdown criterion based on the establishing (almost) uniform electronic density in the channel behind the ionization front when it crossed the gas-filled gap has been introduced and used to obtain the breakdown voltage.

The simulations of the plasma fronts using the drift-diffusion model were restricted to a maximum value of the reduced electric field of 500 Td and to a plane-plane electrode topology by the limiting computational capabilities.

The model developed in this Chapter adopts the self-consistent numerical solution of the continuity equations for the electrons and positive and negative ions. These equations are coupled with the Poisson equation for the electric field. The electron swarm coefficients obtained in Chapter 3, and additional transport properties, discussed in Section 4.2.2, have been used to obtain the time-field breakdown characteristics.

The kinetic model based on the avalanche-to-streamer transition criterion has been used to calculate the time to breakdown, and to obtain the field-time breakdown characteristics using the effective ionization coefficient and the electron mobility for air, N_2, CO_2 and SF_6 presented in Chapter 3.

The results obtained by the drift-diffusion and kinetic models have been analysed and compared. The analytical breakdown characteristics obtained in the present work with the time-field breakdown experimental characteristics for air, N_2, CO_2, and SF_6 have been compared.

The analytical characteristics have been plotted and compared with the experimental data from literature, [Felsenthal, 1965], [Feltcher, 1949], [Gould, 1956]. The results obtained by the drift-diffusion and kinetic models agree with each other. The obtained results also demonstrate a good agreement with the experimental relationships between the product of the particle density and the time to breakdown, Nt_{br}, and the reduced electric field, $(E/N)_{br}$.

It has been shown that these two models can be used to predict the breakdown behaviour of different gases by modelling their time-field breakdown characteristics in a wide range of electric fields. In the case of N_2 and CO_2, further experimental work is required to provide more detailed information on the breakdown characteristics in

the lower range of normalised electric fields (E/N < 100 Td), as the experimental data available in the literature and used in this study show noticeable variations in the breakdown parameters in this field range.

Furthermore, the avalanche boundary condition based on the Townsend mechanism and the streamer boundary condition based on the streamer mechanism have been discussed and used for air, N_2, CO_2 and SF_6. The critical avalanche time $(Nt)_{avalanche}$ and the critical streamer time $(Nt)_{streamer}$ have been introduced to classify discharges according to the Townsend avalanche and streamer breakdown criteria.

Chapter 5 Impulsive breakdown of air, N_2 and CO_2: experimental results and scaling relationships

5.1 Introduction

This chapter investigates the impulsive breakdown characteristics of air, N_2, and CO_2 in the needle-plane electrode geometry with a gap length of 0.1 mm. The breakdown tests were performed at the pressure range from 6.5 kPa to 405 kPa using the HV impulses of both positive and negative polarities.

The high voltage pulsed power generator was utilized to provide voltage impulses to the needle HV electrode in the needle-plane test cell. The HV generator, high voltage and current diagnostic systems, and the test cell have been discussed in detail in Sections 2.6 and 2.8. These sections also provided the test methodology used in the present work.

The computer simulations allow for predicting pulse waveforms and optimizing the pulse generation circuit. The *RLC* lumped-element model is commonly used to represent the distributed characteristic of transmission lines.

Prior to the experimental tests, the simulation of the pulse parameters using the *RLC* lumped-element equivalent circuit was conducted. This *RLC* model implemented in PSpice was used to obtain the circuit parameters for optimization for the HV impulses generated by the Blumlein pulsed power system.

This chapter also presents the electrostatic field simulation in the needle-plane test cell using QuickField software. The Laplacian electrostatic field distribution is obtained using the experimental parameters of the HV and ground electrodes. Finally, the experimental results: the breakdown voltage, and the time to breakdown obtained for all investigated gases, are presented and analysed.

5.2 Experimental set-up to study HV impulsive breakdown behaviour of gases

This section describes the experimental system designed and developed for measurements of the HV impulsive breakdown characteristics. This system consists of four main parts: (1) the test cell with the needle-plane electrode topology; (2) the gas handling equipment; (3) the HV impulsive power supply based on the Blumlein pulse generator; and (4) the diagnostics and measurement system.

5.2.1 Needle-plane test cell

A test cell with the needle-plane electrode geometry and 0.1 mm inter-electrode distance was chosen for these tests. The design of the test cell allows for evaluation of the breakdown characteristics of gases in a divergent electric field at a sub-μs timescale. These experimental conditions are relevant to the conditions found in different micro-electromechanical devices and systems such as microplasma “lab on chip” devices [Becker, 2006], [Luo, 2012], micro-hollow cathode discharge systems [Jovović, 2014], dielectric barrier discharge devices [Niu, 2020] and other systems in which discharges may occur in short, sub-mm, gas-filled gaps.

As shown in Figure 5.1, the needle-plane test cell consists of a HV needle electrode, a plane ground electrode, a mechanical micrometer, a shaft, a sealed cylindrical container, a gas inlet/outlet port, and a test cell base.

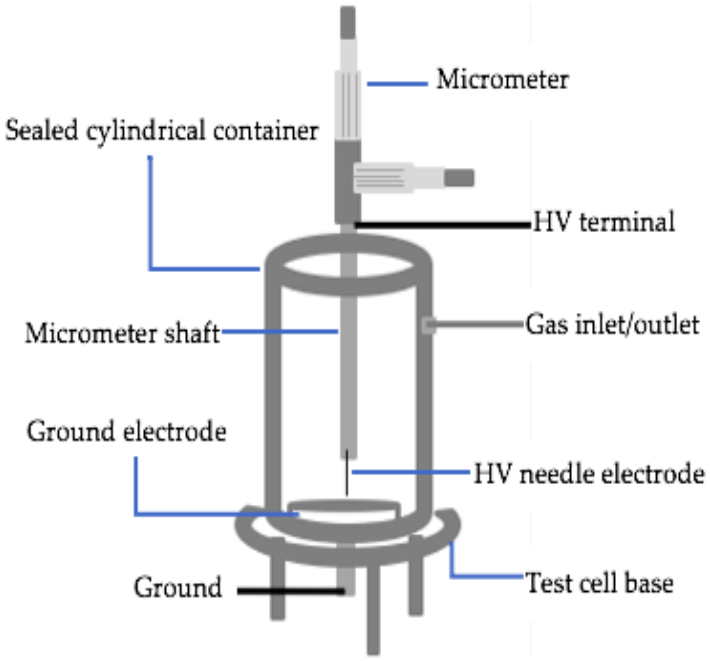

Figure 5.1 Schematic diagram of the test cell (not to scale) with the needle-plane electrode configuration

Gramophone needles with a tip radius of ~80 µm were used as HV electrodes. A needle was attached to the micrometer's shaft, controlled by the micrometer's screw gauge. Figure 5.2 shows the gramophone needle with a tip radius of ~ 80 µm photographed using an optical microscope equipped with a digital camera.

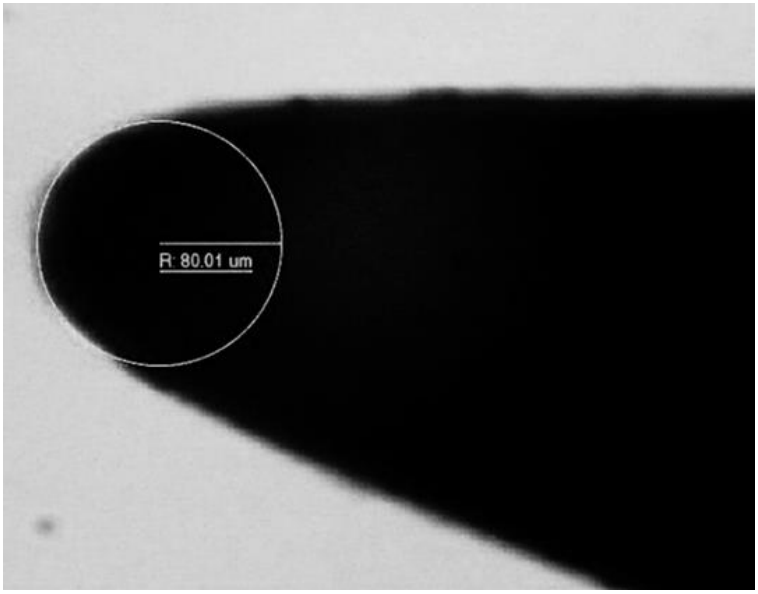

Figure 5.2 Photograph of the gramophone needle tip with ~80 μm radius under microscope

The micrometer's screw was used to enable the gap length between the HV needle electrode and the plane ground electrode to be set to 100 μm with an accuracy of ± 5.89 μm (detailed analysis of uncertainties is presented in Section 5.4).

The polished stainless-steel plane ground electrode was located at the bottom of the sealed container. This sealed cylindrical container was made of glass-reinforced nylon, it was filled with air, N_2 or CO_2, and the gas pressure was in the range of 6.5 kPa to 405 kPa. The HV electrode was energized with the HV impulsive voltage of both polarities.

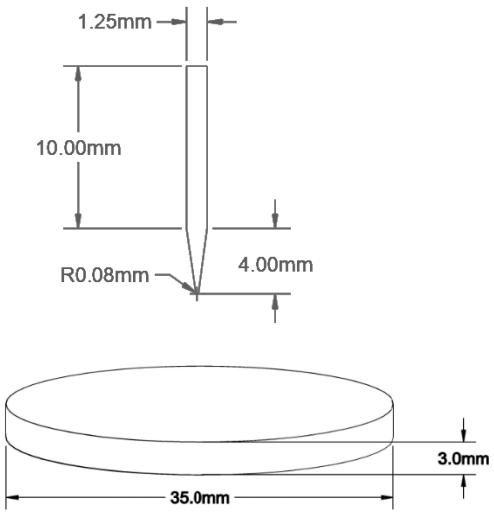

Figure 5.3 Size of needle and plane

Figure 5.3 shows the schematic dimensions of the needle and plane electrodes. The apex part of the tip of the needle was ~ 4 mm long, and the tip radius was ~ 0.08 mm. The straight part of the needle was ~10 mm long and had a 1.25 mm diameter. The grounded disc electrode has a diameter of ~35 mm and is ~3 mm thick. This disc was made of stainless steel.

In the present work, the inter-electrode gap length of 100 ± 5.89 μm was used throughout the experimental tests to ensure that each breakdown happens consistently on the leading edge of the stressed HV pulse. Thus, a direct comparison between the breakdown voltage and time to breakdown for all tested gases at different pressures was made in the case of positive and negative polarities of the HV impulses.

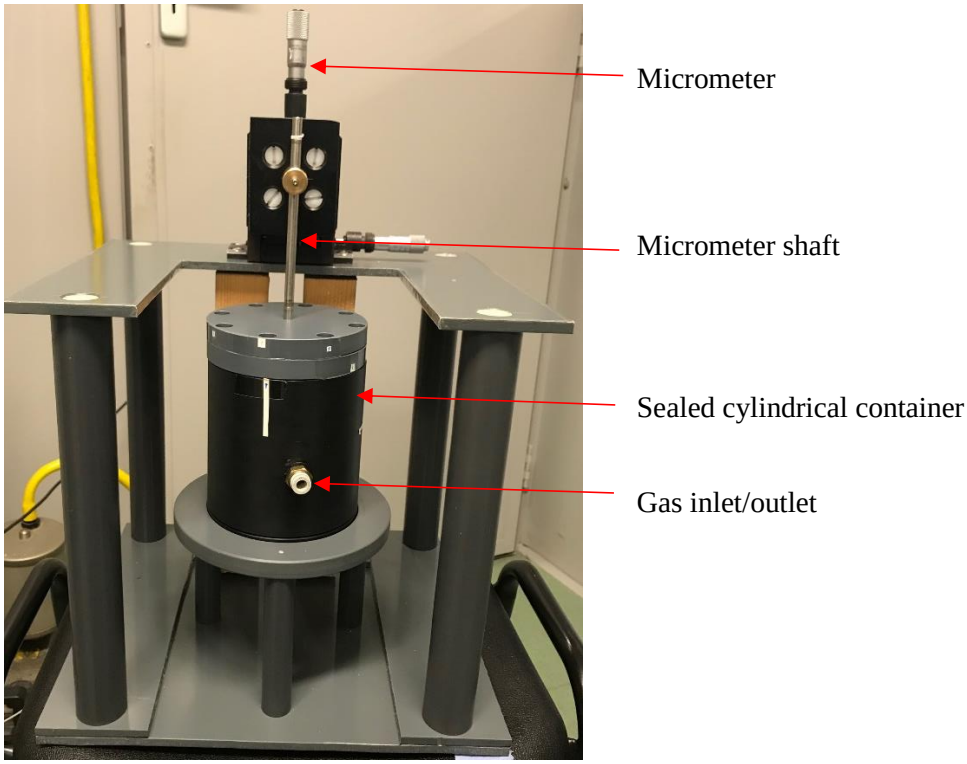

Figure 5.4 Photograph of the needle plane test cell

Figure 5.4 shows a photograph of the needle-plane test cell. The test cell was placed inside a larger grounded Faraday cage to avoid potential electromagnetic interference. The investigated gases were delivered into the test cell through the gas inlet/outlet port fitted to the test cell using the gas control and distribution board.

5.2.2 Gas control and distribution system

A gas control and distribution system was developed to change the gas within the test cell and to keep the required pressure. It consists of a custom-built gas control and distribution board, the botted gases, and a rotary vacuum pump.

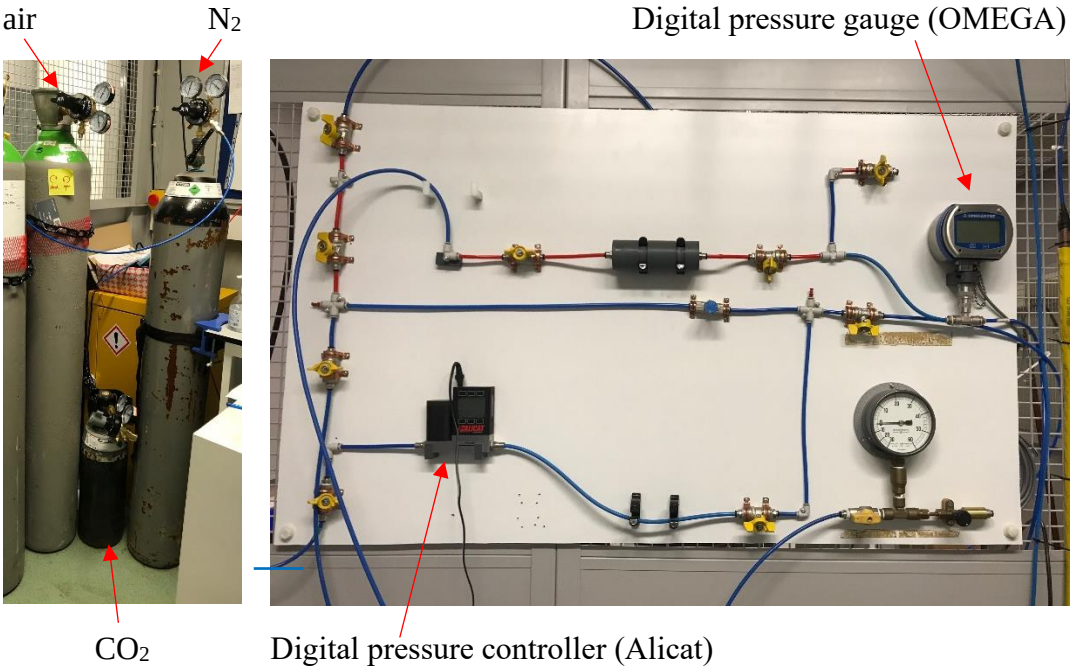

Figure 5.5 Gas control and distribution board and bottled gasses

As illustrated in Figure 5.5, gas bottles are located in the control room of the lab. These gas bottles filled with air, N_2 and CO_2 were purchased from BOC Ltd., Surrey, UK (a member of the Linde Group).

As shown in the specifications provided by BOC, the bottled air is "Zero grade" air which is the 79%/21% N_2/O_2 mixture (N_2 has a purity of 99.998%, O_2 has a purity of 99.6%); the bottled N_2 has a purity of 99.998%; the bottled CO_2 has a purity of 99.8%.

For the custom-built gas control and distribution board, a digital pressure controller purchased from Alicat Scientific Inc, Tucson, AZ, USA (Alicat PC-1500PSIG-D) was used to set and control the pressure inside the sealed test cell. The rotary vacuum pump (Edwards BS.2212) was used to evacuate the gas from the sealed test cell. A digital pressure gauge purchased from Omega Engineering Ltd., Manchester, UK (OMEGA DPGM409-010BG) was used to monitor the pressure in the spark-gap switch of the HV Blumlein pulse generator.

5.2.3 HV pulse generator and diagnostics devices

In order to study the transient breakdown characteristics under the condition of the HV impulses, it is important to have a pulsed power supply system capable of generating the impulsive waveform with the required rising time and amplitude.

The custom-built HV pulse generator based on the Blumlein line circuit was used throughout the tests to deliver the required voltage impulse to the test cell. The schematic diagram for the experimental test configuration incorporating the HV pulse generator, the test cell, and the diagnostic instruments is illustrated in Figure 5.6 [Liu, 2021].

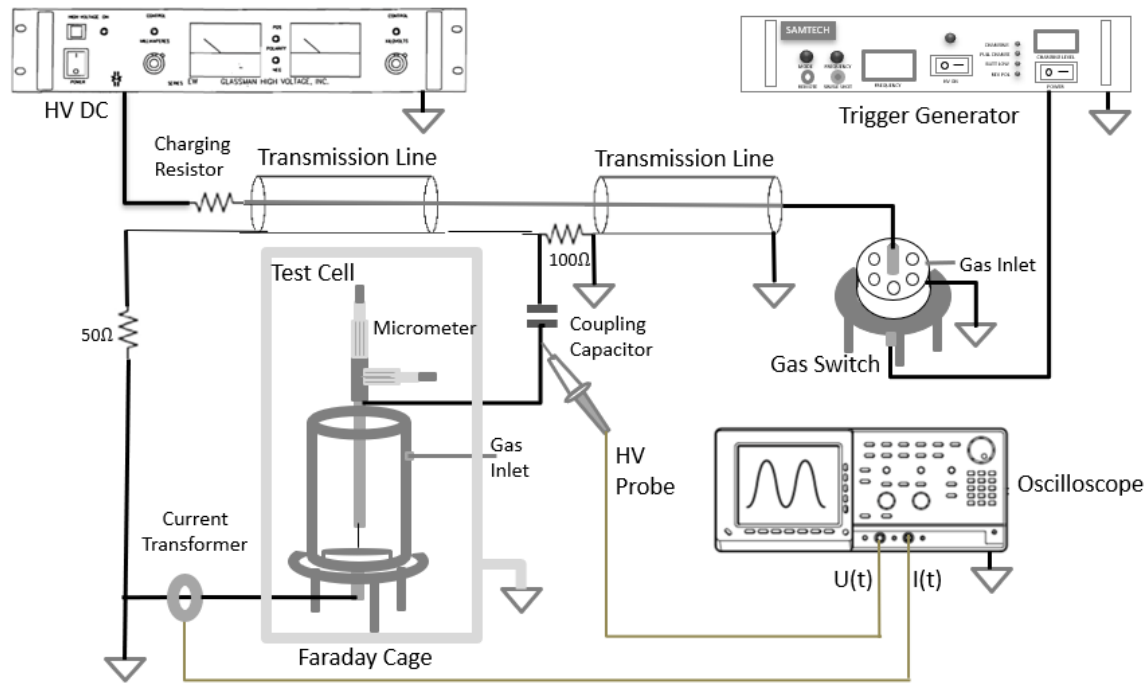

Figure 5.6 Experimental arrangement incorporating Blumlein-based HV pulse generator, test cell and diagnostic instruments

As shown in Figure 5.6, the HV pulse generator comprises seven main components, including a DC voltage power supply, a trigger generator, two transmission lines, a self-closing spark-gap switch, the charging resistor, the coupling capacitor, and the matching resistors.

The DC power supply (Glassman HV DC EH50P2) is capable of supplying a voltage of up to 50kVdc, and a current of up to 2mA, and its output ripple of less than 0.03% at full load was used to charge the two cable lines “transmission lines” (URM67 coaxial cable, each 25 m long) through the charging resistor of 100 kΩ. These characteristics are detailed in Section 5.3.1.

The spark-gap switch (air-filled trigatron) was triggered by the trigger generator (Samtech TG-01) produced by SAMTECH Ltd., Glasgow, Scotland, using the voltage up to ~37 kV. The coupling capacitor of ~245 pF is composed of eleven capacitors in series (TYPE 09000/062, 2700 pF ± 20%, 30 kV DC). This combined capacitor was placed between the output of the Blumlein generator and the needle electrode of the test cell. The matching resistors of 50 Ω and 100 Ω were used to provide the HV impulsive waveform with the required rising time, duration and amplitude.

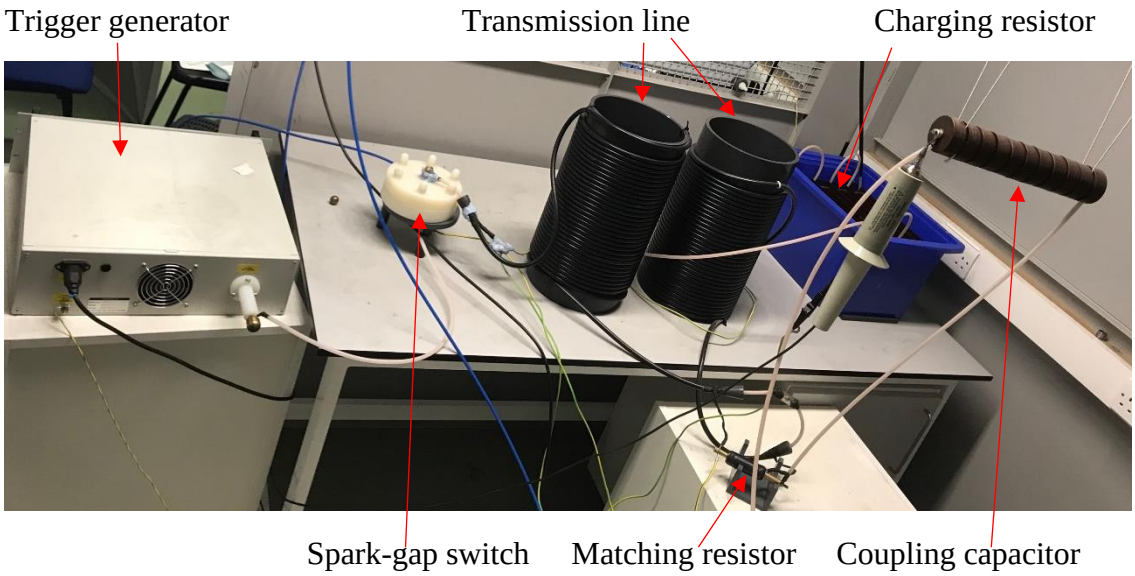

Figure 5.7 Arrangement of Blumlein circuit

As shown in Figure 5.7, the Blumlein-based HV pulse generator was used to produce a rectangular HV waveform pulse with a rising time of up to ~ 50 ns and a duration of ~ 250 ns. The voltage waveform is shown later in Section 5.3.1.

In order to measure the breakdown voltage and time to breakdown the current and voltage waveforms were obtained using the following , diagnostic devices: a digitising oscilloscope, a high voltage probe, and a current transformer.

The high voltage probe with the bandwidth of 75 MHz (Tektronix P6015A, bandwidth, 100 MΩ input resistance, 3 pF input capacitance) produced by Tektronix Inc, Beaverton, OR, USA was used to measure the breakdown voltage, this probe was connected to the HV needle electrode of the test cell. The current transformer with the bandwidth of 250 MHz (Pearson 6585) was used to obtain the current waveform.

The digitising oscilloscope with the bandwidth of 500 MHz (TDS5034B, 5 GS/s sampling rate) produced by Tektronix Inc, Beaverton, OR, USA was used to register voltage and current waveforms and to measure the breakdown voltage and pre-breakdown time for each breakdown event.

Figure 5.8 illustrates the typical voltage and current waveforms for the negative breakdown event in air at the pressure of 304 kPa. The breakdown voltage $U_{br\text{-}ch}$ and corresponding pre-breakdown time t_{br} are indicated in this figure.

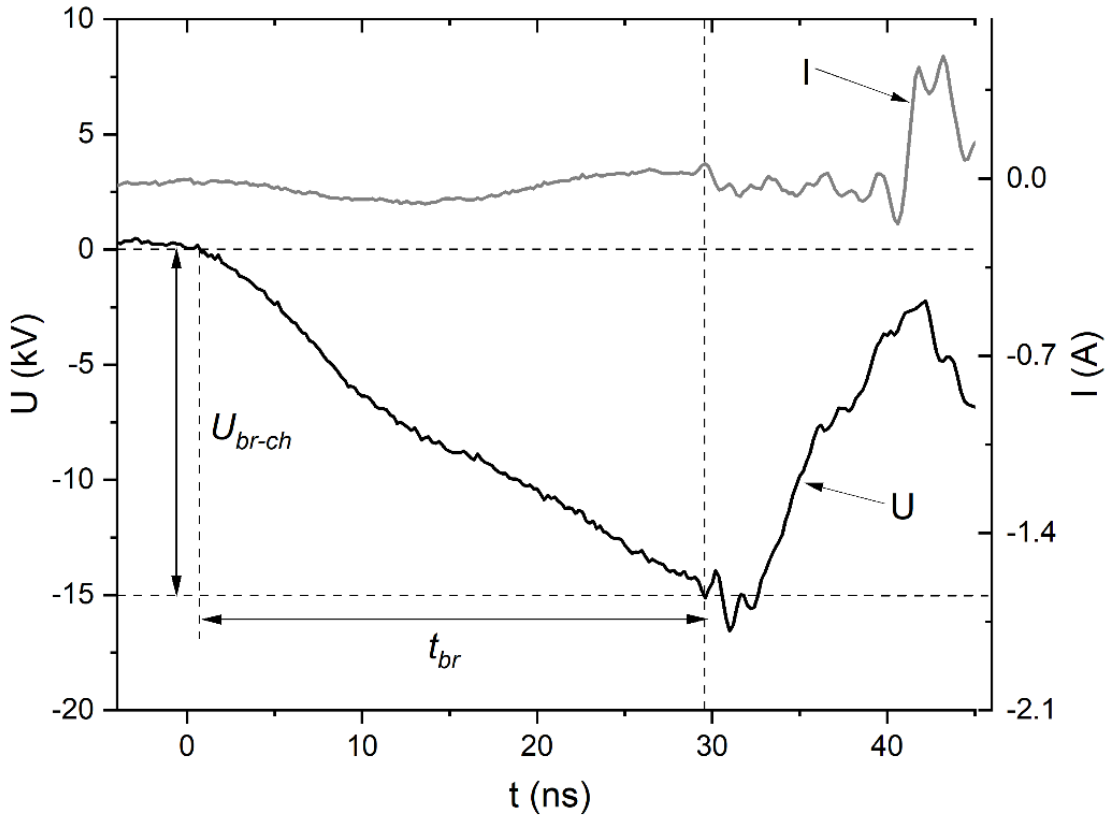

Figure 5.8 Voltage and current waveform for breakdown event in air (304 kPa). $U_{br\text{-}ch}$ and t_{br} are shown in this Figure

The breakdown voltage $U_{br\text{-}ch}$ was measured at the time when the first significant transient pre-breakdown disturbance (spike) appears in the current waveform. The pre-breakdown time, t_{br}, was obtained as the time interval between the start of the voltage impulse and the first significant transient disturbance in the current waveform.

The initial body of the breakdown plasma channel forms during the development of the main streamer that propagates to the point of breakdown, which may be after initial pre-breakdown streamers have crossed the gap, or when a cathode-directed streamer meets an anode-directed streamer together in the gap [Laity, 2011]. As a result, the current disturbances are observed in the current waveform [Beloplotov, 2018], [Rep'ev, 2006].

$U_{br\text{-}ch}$ is the voltage at which the initial breakdown channel across the gap is formed. The noticeable current disturbance (spike) in the current waveform corresponds to the

main streamer after the initial streamer(s), which starts to develop through this channel and leads to plasma heating and the formation of a highly conductive plasma-filled ch7annel between the needle and plane electrode. Consequently, the current rises sharply, and the voltage collapses when the thermalized plasma channel is formed.

It has been found that under the conditions of the present experiment, the same time interval, ~(11–12) ns, from the first significant current spike to the moment of the sharp rise in the current, has been observed for all tested gases and gas pressures. Thus, it is believed that this time is determined by the parameters of the HV impulses circuit used in the experimental tests rather than by the properties of gases.

Since no significant noise has been observed at the initial part of the HV waveform produced by the Blumlein generator, the breakdown voltage $U_{br\text{-}ch}$ is readily obtained.

However, the measured pre-breakdown time is distorted because of the rise time of the Tektronix HV P6015A probe. Therefore, the degradation in the measured pre-breakdown time should be taken into account.

The bandwidth of the Tektronix HV P6015A probe is ~ 75 MHz. Thus, the corresponding rise time of the probe t_{rise} can be obtained by Equation 5.1 [Mankowski, 1998]

$$t_{rise} = \frac{0.35}{\mathrm{f}_{Bandwidth}} = \frac{0.35}{75MHz} \approx 5ns \tag{5.1}$$

where t_{rise} is the rise time of probe, $f_{Bandwidth}$ is the bandwidth of the Tektronix HV P6015A probe.

In order to compensate for the inaccuracy in time to breakdown, the compensated time to breakdown, t_{br}, was used, this compensated time was obtained by taking the square root of the difference of squares of the measured breakdown time and the probe rise time [Dorf, 1993].

$$t_{br} = \sqrt{{t_1}^2 - {t_2}^2} \tag{5.2}$$

where t_1 is the pre-breakdown time measured from the experimental test, t_2 is the rise time of the Tektronix HV P6015A probe, $t_2 \sim 5$ ns.

The compensated time to breakdown, t_{br}, Equation 5.2, has been used in the presented analysis.

5.3 Modelling of the HV impulses and electric field in the test cell

In order to achieve the required pulse waveshape and to optimize parameters of the HV pulse generator circuit, an equivalent *RLC* circuit of the Blumlein-based HV pulse generator was developed using PSpice software (OrCAD v.16.6).

In this section, the simulation of the Laplacian electrostatic field distribution using QuickField (v.6.5) electrostatic software is also described to investigate the breakdown characteristics in the needle-plane topology test cell. The values of the electric field at the needle electrode obtained in these simulations will be used to plot the field-time breakdown characteristics of different gases in Section 5.5.

5.3.1 *RLC* lumped-element equivalent circuit of the HV Blumlein-based pulse system

The Blumlein generator can generate nanosecond HV impulses with the same amplitude as the magnitude of the charging voltage when the load resistance is twice higher than the impedance of the transmission line, [Haddad, 2004].

In this work, the *RLC* lumped-element equivalent circuit of the HV Blumlein pulsed system has been developed using PSpice software, as shown in Figure 5.9. Two transmission lines, *T1* and *T2*, used the URM67 coaxial cable (each 25 m long).

According to the specification of the URM67 coaxial cable, the nominal inductance of this cable is 250 nH/m, the nominal capacitance of the cable is 100 pF/m, and the characteristic impedance of the cable is 50 Ω.

Polyethylene is used as an insulating material between the inner core and the outer braid of the URM67 cable. Thus, the propagation velocity, u_p, of the pulse travelling along the URM67 coaxial cable is

$$u_p = \frac{c}{\sqrt{\mu_r \cdot \varepsilon_r}} = \frac{c}{\sqrt{1 \cdot 2.2}} \approx 0.67\ c \tag{5.3}$$

where u_p is the velocity, c is the light speed in vacuum of ~$3 \cdot 10^8$(m/s), μ_r is the relative magnetic permeability of $\mu_r \sim 1$, and ε_r is the relative electrical permittivity of $\varepsilon_r \sim 2.2$, [Wilson, 2011]. Therefore, the propagation velocity, u_p, of the pulse in the URM67 cable is $0.67 \cdot c = 2 \cdot 10^8$ m/s.

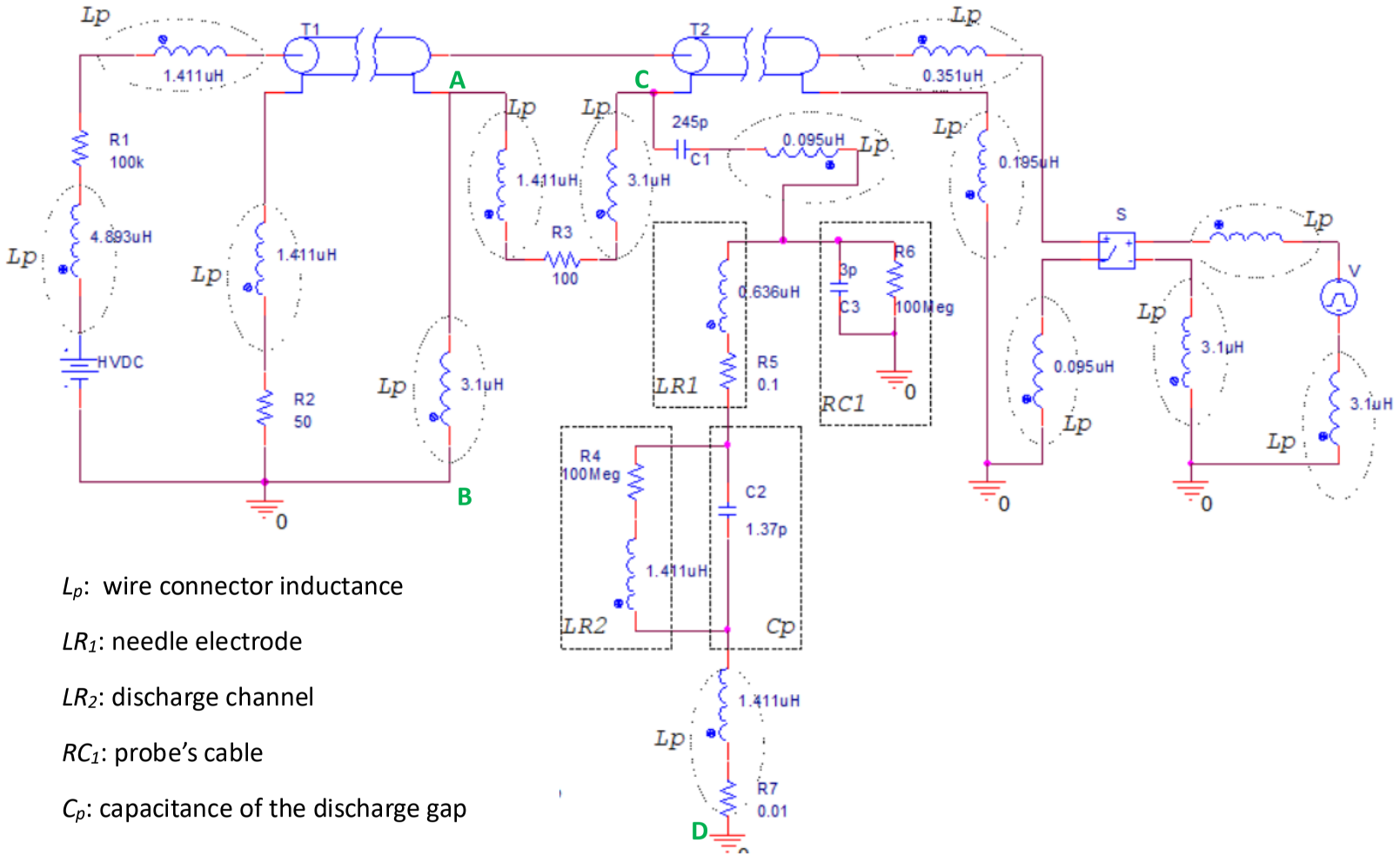

L_p: wire connector inductance

LR_1: needle electrode

LR_2: discharge channel

RC_1: probe's cable

C_p: capacitance of the discharge gap

Figure 5.9. *RLC* Lumped-element circuit of the HV pulse generator and the test cell

The matching resistance *R3* is 100 Ω (which is two times higher than the characteristics impedance of the URM67 cable, 50 Ω). Thus, the pulse amplitude across the load is nominally the same as the charging voltage provided by the HV DC power supply.

As shown in Figure 5.9, the transmission lines *T1* and *T2* are charged via the charging resistor, *R1* (100 KΩ). When the switch, *S2*, is triggered, a voltage wave starts to propagate along *T1*. This wave reaches the load (the test cell) via the coupling capacitor *C1*. The rise and fall times of the HV impulse are affected by the inductance of the circuit and the stray capacitance in the circuit [Haddad, 2004].

Using the propagation velocity of the wave, the duration of the HV impulses generated by this Blumlein circuit can be obtained

$$t_{width} = \frac{2l_{cable}}{u_p} = \frac{2 \cdot 25\ m}{2 \cdot 10^8\ m/s} \approx 250\ ns \qquad (5.4)$$

where t_{width} is the pulse width, l_{cable} is the cable length, *T1* and *T2* , (25 m), u_p is the propagation velocity of the pulse along the URM67 cable (~ $2 \cdot 10^8$ m/s).

As shown in Figure 5.9, the proposed equivalent circuit of the test systems includes not only the HV pulse generator, but also the lumped *RLC* circuit for the HV probe and the test cell. The needle electrode of the test cell is represented by an inductor and resistor connected in series, shown as segment *LR1* in Figure 5.9.

Segment *LR2* in Figure 5.9 represents the discharge channel, this segment consists of C_p - the capacitance of the gap between electrodes, and C_2 ~ 1.37 pF, the capacitance of the needle-plane test cell obtained by modelling this tests cell in the QuickField software.

An HV Tektronix P6015A probe is represented by a 100 MΩ resistor and a 3 pF capacitor connected in parallel [Merciris, 2020], shown as segment *RC1* in Figure 5.9.

In all practical pulsed power systems, parasitic inductances are unavoidable. The parasitic inductances associated with conductors, L_p are included in the equivalent circuit of the HV pulse generator shown in Figure 5.9.

The parasitic inductances of the connection cable(s) with a length of l and radius of r can be calculated using the equation for inductance of a straight conductor [Grover, 1946]

$$L_p = 0.002l\left[\ln\left(\frac{2l}{r}\right) - \frac{3}{4}\right] \tag{5.5}$$

where, L_p is the inductance in unit of μH, l is the wire length in cm, r is the wire radius in cm.

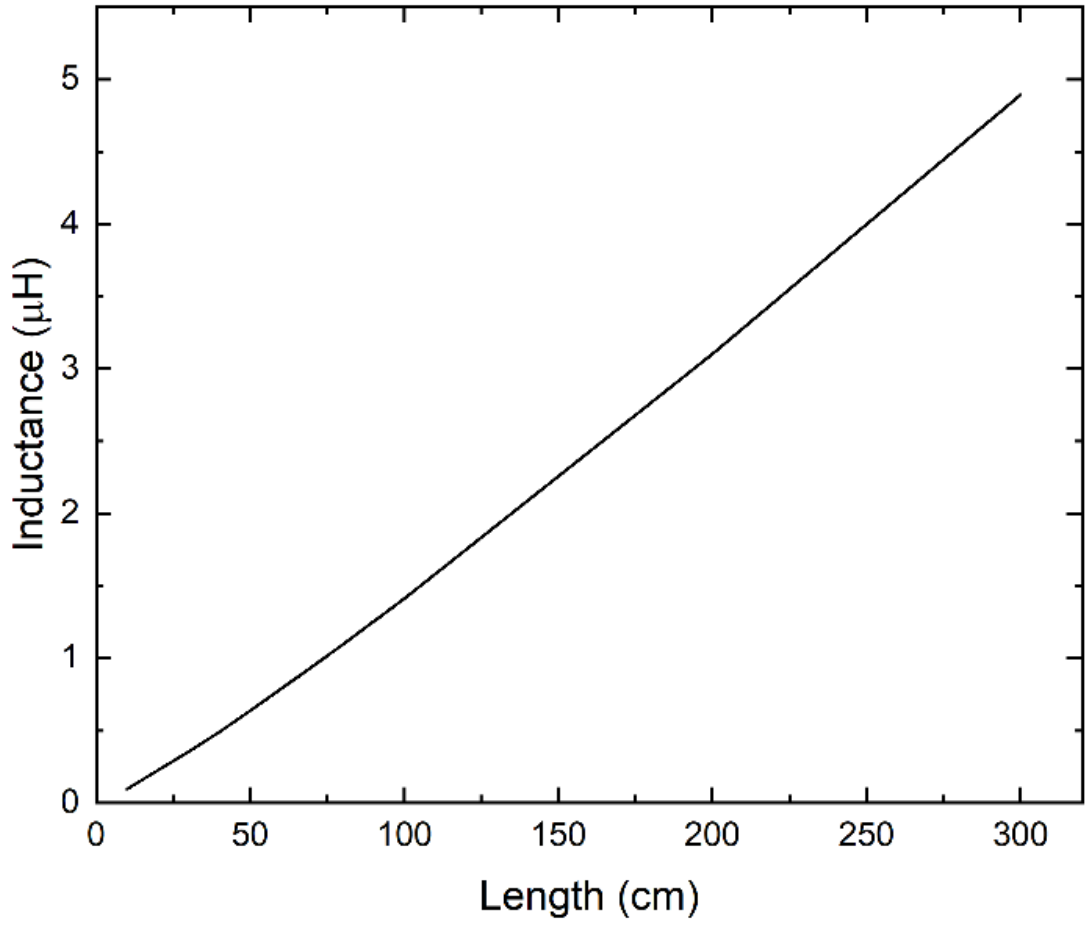

Figure 5.10 Calculated inductance values for a wire with ~1.6 mm diameter (Equation 5.5) as a function of wire length

Using Equation 5.5, the inductance of the wires with a diameter of ~1.6 mm was obtained and shown in Figure 5.10. The diameter used in this analysis represents the diameter of the conductors used in the practical system. [Grover, 1946] also provides an equation for inductance of a straight conductor at higher frequencies, however the difference between these two equations for the practical case considered in this study is only 3-4%.

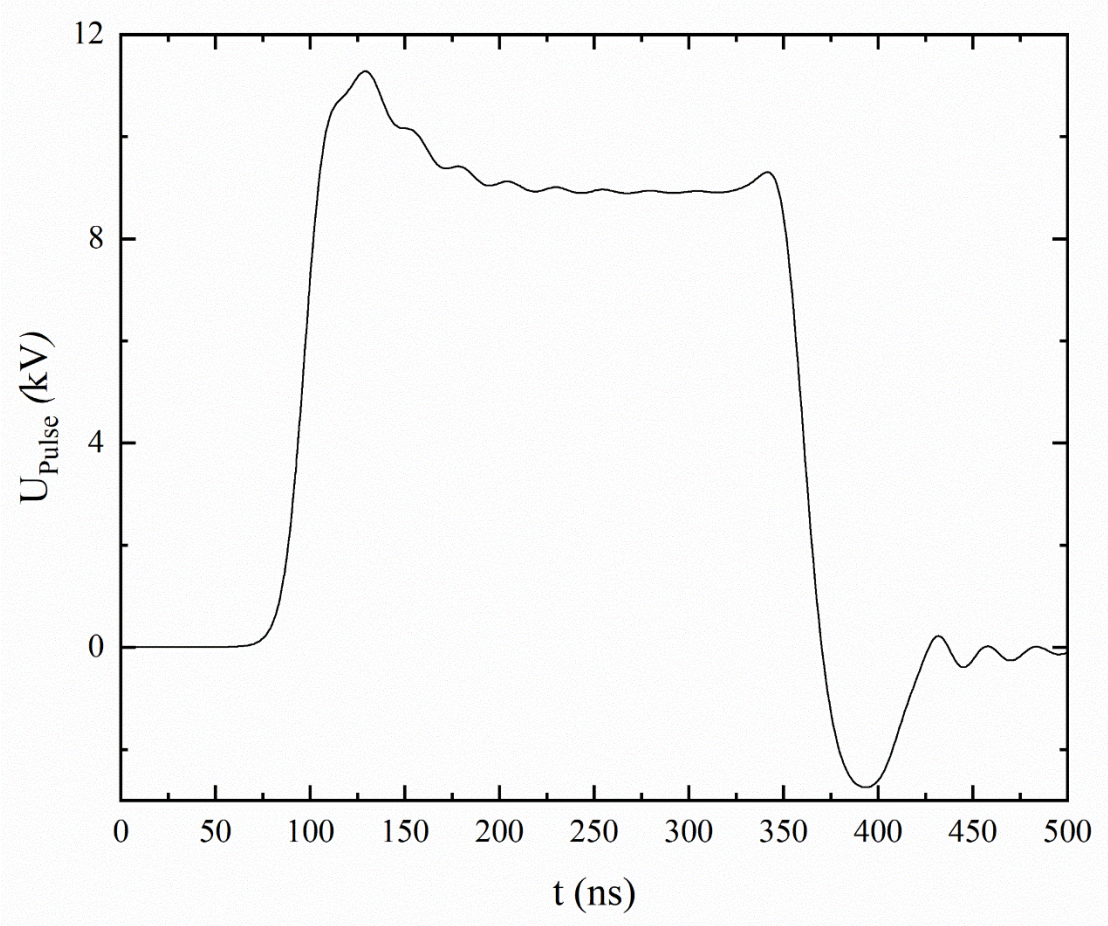

Figure 5.11. A positive impulse voltage waveform across the needle-plane test cell, obtained by the PSpice model shown in Figure 5.9 at the condition of the charging voltage of 10 kV was applied

As illustrated in Figure 5.11, the PSpice model provides a positive rectangular impulse with a rising time of ~50 ns and duration of ~250 ns. The output pulse has the same polarity and magnitude as the charging voltage.

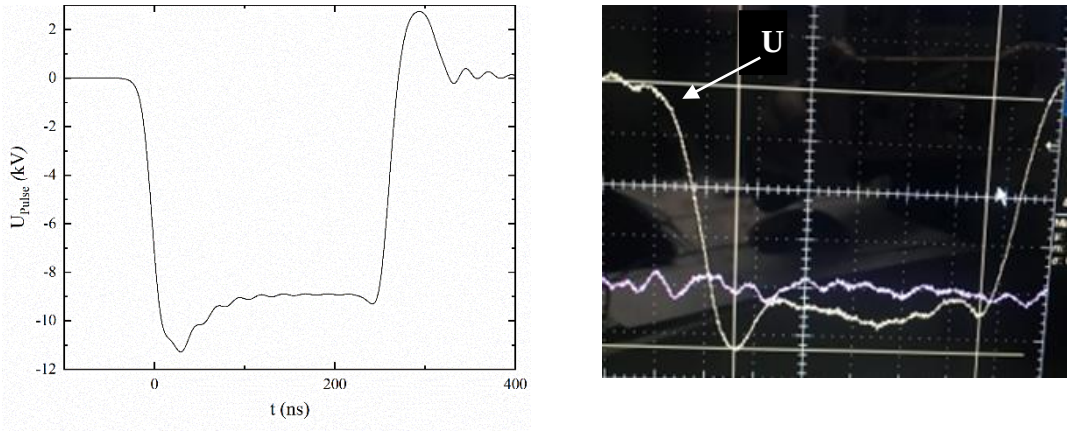

(a) (b)

Figure 5.12. (a) A negative impulse voltage waveform across the needle-plane test cell, obtained by the PSpice model shown in Figure 5.9 at the condition of interchanging A-B to C-D and the charging voltage of 10 kV was applied. (b) Practical waveforms provided by the HV pulse generator, time and voltage scales are: Horizontal axis, 40 ns/division; Vertical axis, 2 kV/division.

In order to obtain a negative impulse without changing the polarity of the HV DC source, we can reverse the load connections to the matching resistor R_3. As shown in Figure 5.9, by interchanging A-B to C-D, the polarity of outputs impulses will be reversed.

As illustrated in Figure 5.12, the PSpice model provides a negative rectangular impulse with a rising time of ~50 ns and duration of ~250 ns. The observed overshoot in both simulated waveform and practical HV impulse is due to stray elements (inductance in particular) in the Blumlein circuit.

The output pulse has an opposite polarity to the charging voltage provided the HV DC power supply. The practical waveforms provided by the HV pulse generator are in good agreement with the simulation results obtained by the *RLC* lumped-element equivalent circuit.

Therefore, this Blumlein impulse generator has been employed to provide high voltage rectangular impulses of both polarities with a ~250 ns duration and with a rise time of ~50 ns. This generator was used to investigate the breakdown characteristics of air, N_2 and CO_2 at different pressures in the sub-mm gap.

5.3.2 Modelling of electric field distribution in test cell

A test cell with the needle plane topology has been simulated using QuickField software. The needle plane topology with a 100 µm gap between the HV needle electrode and the ground plane electrode is shown in Figure 5.13.

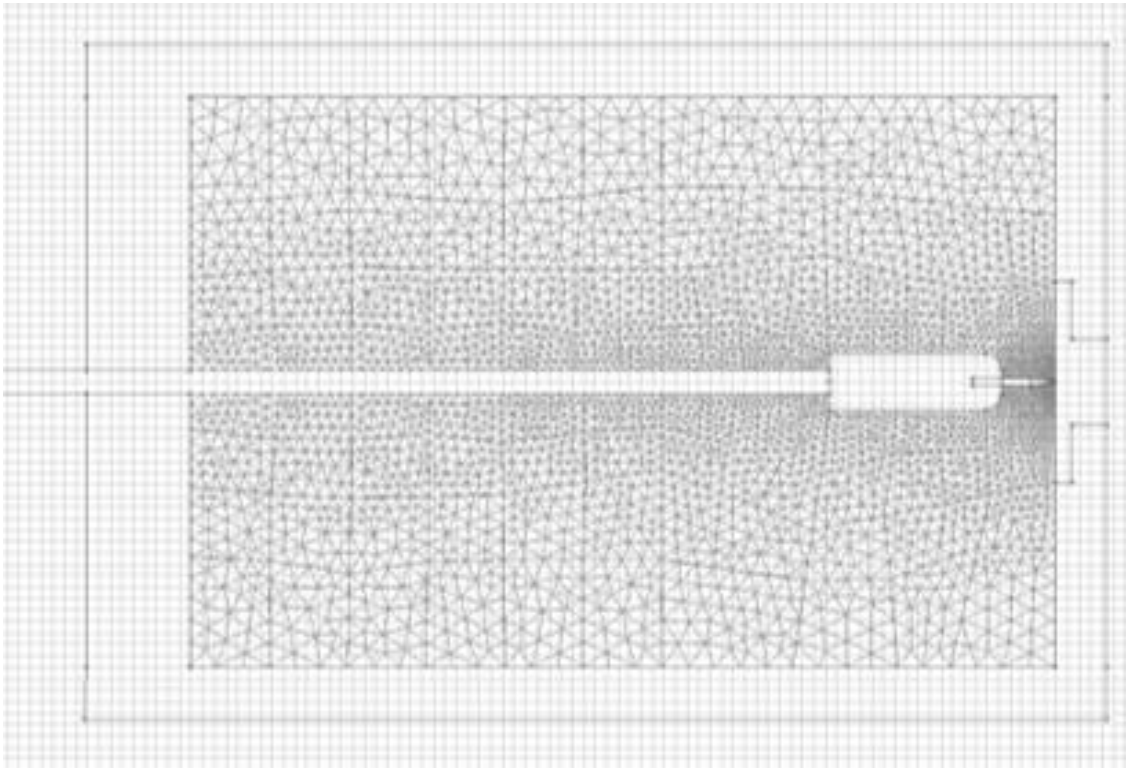

Figure 5.13. Configuration of the needle plane topology simulation in QuickField software

The charging voltage is applied to the needle electrode with a tip radius of 80 µm, and the plane is set as the ground electrode.

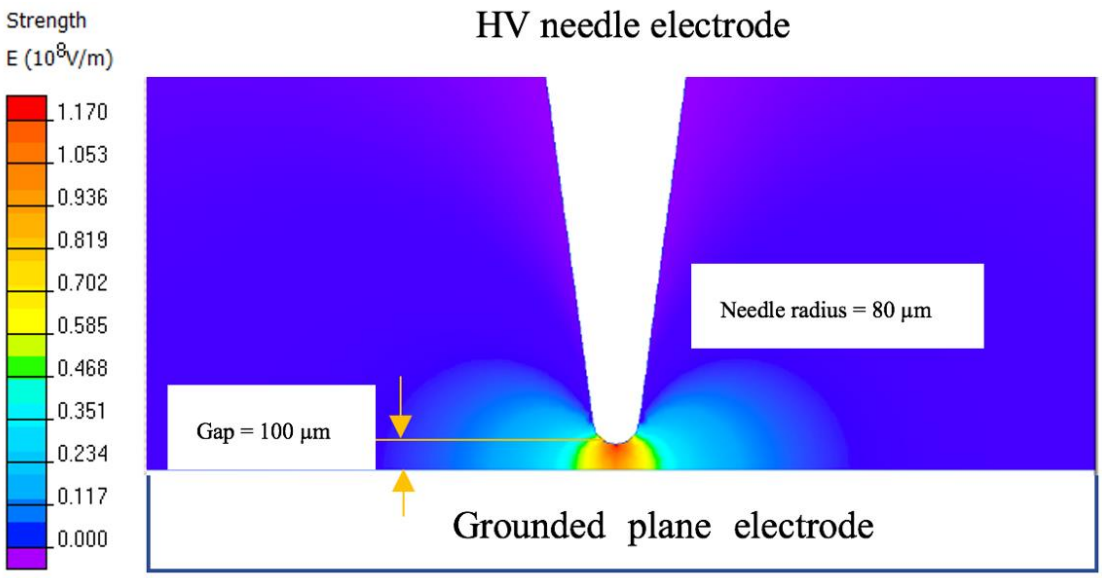

Figure 5.14 The 2D distribution of the electric field in the needle-plane topology by QuickField software

As shown in Figure 5.14, the 2D electric field distribution has been obtained between the needle and plane electrodes. It can be seen that the maximum electric field, E_{tip}, of ~$1.16 \cdot 10^3$ kV/cm is achieved at the tip of the needle electrode, when the needle is stressed with 10 kV. E_{tip} values obtained for specific values of the breakdown voltages will be used in Section 5.5 to plot the field-time breakdown characteristics for different gases, in order to compare the obtained experimental results with the literature data and modelling results performed in a uniform electric field.

5.4 Analysis of uncertainties in experimental measurements

Uncertainty exists in any measurements, it arises from different sources such as not well defined or known measurement errors, sampling issues, environmental factors, and operator skill [Bell, 2001]. In the present work, the uncertainty in the measurements has been considered to assess the quality of the experimental results.

There are two main approaches to the evaluation of uncertainty: Type A evaluation (the uncertainty is evaluated by statistical analysis using data obtained from a series of observations) and type B evaluation (evaluation of the uncertainties caused by unknown or not well-known fixed measurement errors, this evaluation is typically based on the scientific judgment which takes into account all specific details and relevant information). These two approaches were used to estimate the uncertainties in the measurements of the gap between electrodes, the breakdown voltage, the time to breakdown, the reduced electric field, and the product of the gas number density and the time to breakdown. This analysis has been conducted in accordance with "The Expression of Uncertainty and Confidence in Measurement" guide [UKAS, 2012].

Table 5.1 provides the components of the uncertainty in the gap between electrodes obtained using type B evaluation. Type B evaluation of uncertainties is typically used to obtain individual components with fixed but not well-known errors. Therefore, the uncertainties in the micrometer measurements and the electrode surface damage or erosion have been evaluated using Type B procedures. The upper and lower limits of the uncertainty in the measurement of the gap between electrodes have been obtained.

The interval between the two nearest divisions was considered to estimate the uncertainty in measurements performed by the micrometer. This interval is 10 µm, and thus it results in an error of no more than 5 µm. The micrometer readings are assigned a rectangular distribution, leading to the standard uncertainty of $5\mu m/\sqrt{3}$ = 2.887 µm.

For estimation of the uncertainty in the inter-electrode gap caused by the damage or erosion of the electrode surface, it was assumed that this variation does not exceed 1%, leading to a possible error of ±1 μm. A rectangular probability distribution is assumed. Thus, the standard uncertainty is 0.577 μm (i.e., $1\mu m/\sqrt{3} = 0.577$ μm).

The combined standard uncertainty is the square root of the sum of squares of each individual standard uncertainties

$$u_c = \sqrt{\sum u_i^2} \tag{5.6}$$

where u_c is the combined standard uncertainty, u_i is the individual standard uncertainty. Thus, the combined standard uncertainty in the gap between the electrodes, as listed in Table 5.1, is $\sqrt{2.887^2 + 0.577^2} = 2.944$ μm.

The expanded uncertainty is calculated by multiplying the combined standard uncertainty by a coverage factor *k*

$$\text{Expanded uncertainty} = k\, u_c \tag{5.7}$$

where *k* is a coverage factor. Different values of the coverage factor correspond to different confidence levels. Some commonly used coverage factors for uncertainties in normally distributed values are: $k = 1$ for a confidence level of ~ 68%; $k = 2$ for a confidence level of ~ 95%; $k = 3$ for a confidence level of ~99.7%. In the present work, the coverage factor $k = 2$ was used to evaluate the expanded uncertainty. It provides ~95% confidence level. Thus, the expanded uncertainty in the gap between the electrodes is the combined standard uncertainty multiplied by $k = 2$: $2 \cdot 2.944$ μm $=$ 5.888 μm.

TABLE 5.1

Analysis of the uncertainty in the gap between electrodes

Source of uncertainty	Value ±	Probability distribution	Divisor	Standard uncertainty
Micrometer scale	5 μm	Rectangular	√3	2.887 μm
Damage or erosion effect of surface	1 μm	Rectangular	√3	0.577 μm
Combined standard uncertainty		Assumed Normal		2.944 μm
Expanded uncertainty in the inter-electrode gap	5.888 μm coverage probability of approximately 95 %			

The expanded uncertainty in the inter-electrode gap obtained by equation (5.7) is 100.00 μm ±5.89 μm at the confidence level of ~95%.

Table 5.2 presents the uncertainty in measurements of the positive breakdown voltage in air at 101 kPa. In this case, the evaluations of both types A and B are used. Type A evaluation is typically used to obtain the repeatability uncertainty (for repeated readings that are normally distributed). In this case, the estimated standard uncertainty can be calculated as

$$u_r = s/\sqrt{n} \tag{5.8}$$

where u_r is the estimated standard uncertainty, s, is the estimated standard deviation, *n* is the number of measurements.

In the present experimental work, the positive breakdown voltage for air at 101kPa was obtained as an average value of 60 measurements, *n* = 60, with an estimated standard deviation of 0.43 kV. Thus, the estimated standard repeatability uncertainty in the breakdown voltage is $\frac{0.43\text{kV}}{\sqrt{60}} = 0.056$ kV (Table 5.2).

Other components in the combined uncertainty in the breakdown voltage can be evaluated using the Type B procedure, as these uncertainties are associated with the breakdown voltage and equipment settings. The average positive breakdown voltage for air at 101kPa obtained in the present work is 7.65 kV. An error of less than 5% is assumed in each measurement when a voltage reading is taken from the oscilloscope (i.e., ±0.383 kV, which is 5% of 7.65 kV). It is also assumed that the quantities in question are distributed normally. Thus, the standard uncertainty in the breakdown voltage is 0.383 kV/2 = 0.192 kV (Table 5.2). A limited variation of 1% is considered as the error in settings (i.e., ± 0.077 kV which is 1 % of 7.65 kV). The rectangular distribution is assigned to the quantity in question. Thus, the standard uncertainty in the equipment settings is 0.077 kV/$\sqrt{3}$ = 0.044 kV (Table 5.2).

TABLE 5.2

Uncertainty in the positive breakdown voltage of air at 101kPa

Source of uncertainty	Value ±	Probability distribution	Divisor	Standard uncertainty
Breakdown voltage	0.383 kV	Normal	2	0.192 kV
Repeated readings	0.056 kV	Normal	1	0.056 kV
Equipment Settings	0.077 kV	Rectangular	√3	0.044 kV
Combined standard uncertainty in breakdown voltage		Assumed Normal		0.205 kV
Expanded uncertainty in breakdown voltage	0.410 kV coverage probability of approximately 95 %			

The combined standard uncertainty and the expanded uncertainty can be obtained by Equations 5.6-5.7. The combined standard uncertainty in the positive breakdown voltage for air at 101 kPa is $\sqrt{0.192^2 + 0.056^2 + 0.044^2} = 0.205$ kV; and the expanded uncertainty is $2 \cdot 0.205 = 0.410$ kV (Table 5.2)

Therefore, it can be stated that the positive breakdown voltage of air at 101 kPa is 7.65 kV ±0.41 kV at the confidence level of ~95%. Using this approach, we can obtain the

uncertainty in the breakdown voltage for both positive and negative polarities at different pressures for all investigated gases.

Table 5.3 provides the uncertainty in the time to breakdown in air at 101 kPa for positive polarity. The same methodology as in the case of the combined expanded uncertainty in the breakdown voltage described above was used. The experimentally obtained average time to breakdown is 27.58 ns, and its estimated standard deviation is 1.61 ns.

Thus, the estimated standard repeatability uncertainty in the time to breakdown obtained by Equation 5.8 is $\frac{1.61ns}{\sqrt{60}} = 0.208$ ns (Table 5.3). The error in the time to breakdown is assumed to be less than 5% (i.e., ± 1.379 ns which is 5% of 27.58 ns and it is also assumed that t_{br} values are normally distributed.

It is assumed that the error in the equipment settings is less than 1% (± 0.276 ns, which is 1% of 27.58 ns) and the quantity in question is rectangular distributed. Thus, the standard uncertainty in the time to breakdown is 1.379 ns/2 = 0.690 ns, Table 5.3. The standard uncertainty in the settings is 0.276 kV/$\sqrt{3}$ = 0.159 kV.

TABLE 5.3

Analysis of uncertainty in the time to breakdown in air at 101kPa for positive polarity

Source of uncertainty	Value ±	Probability distribution	Divisor	Standard uncertainty
Time to breakdown	1.379 ns	Normal	2	0.690 ns
Repeated readings	0.208 ns	Normal	1	0.208 ns
Settings	0.276 ns	Rectangular	√3	0.159 ns
Combined standard uncertainty in time to breakdown		Assumed Normal		0.738 ns
Expanded uncertainty in t_{br}	1.476 ns coverage probability of approximately 95 %			

The combined standard uncertainty in the positive breakdown voltage of air at 101 kPa is obtained by Equation 5.6, and it is $\sqrt{0.690^2 + 0.208^2 + 0.159^2} = 0.738$ ns (Table 5.2) The expanded uncertainty obtained by Equation 5.7 is $2 \cdot 0.738 = 1.476$ ns.

As a result of this analysis, it can be stated that the time to breakdown in air at 101 *kPa* for positive polarity is 27.58 ns ±1.48 ns at the level of confidence of ~95%. Using this approach, we can obtain the uncertainty in the time to breakdown for both positive and negative polarities at different pressure in all investigated gases.

Table 5.4 presents uncertainty analysis in the measurements of the reduced breakdown electric field, *E/N*, in air at 101 kPa for positive polarity; Type A and Type B evaluations were used in this procedure. Each individual component of the uncertainty has been presented in Tables 5.1-5.3. The uncertainty in the measurements of pressure is evaluated by the Type B procedure. An error of 10% (i.e., ±10.1 kPa, which is 10% of 101 kPa) is assumed in the pressure readings, and the quantity in question is rectangular distributed.

In complex cases, which include multiplication and division of different quantities the relative or fractional uncertainties can be used. The relative standard uncertainty is a dimensionless parameter obtained by division of the standard uncertainty in the quantity in question, u_i, by this quantity, i: $\frac{u_i}{i}$. Thus, the relative combined standard uncertainty is the square root of the sum of squares of the individual relative standard uncertainties

$$\frac{u_z}{z} = \sqrt{\sum \left(\frac{u_i}{i}\right)^2} \tag{5.9}$$

where $\frac{u_z}{z}$ is the relative combined standard uncertainty of quantity z; $\frac{u_i}{i}$ is individual relative standard uncertainties.

The combined uncertainty in the time to breakdown in air at 101 kPa for positive polarity includes the following components:

the relative standard uncertainty in the pressure gauge, $\frac{5.831\text{kPa}}{101\text{kPa}} = 58$ ppt;

the relative standard uncertainty in the gap between electrodes, $\frac{2.887\mu m}{100\mu m} = 29$ ppt;

the relative standard uncertainty in the damage or erosion effect, $\frac{0.577\mu m}{100\mu m} = 6$ ppt;

the relative reading uncertainty in the breakdown voltage, $\frac{0.192\text{kV}}{7.65\text{kV}} = 25$ ppt;

the relative uncertainty in repeatable measurements of the breakdown voltage, $\frac{0.056\text{kV}}{7.65\text{kV}} = 7$ ppt;

the relative uncertainty in the equipment setting, $\frac{0.044\text{kV}}{7.65\text{kV}} = 6$ ppt.

TABLE 5.4

Uncertainty in f *E/N* in air at 101kPa for positive polarity

Source of uncertainty	Value ±	Probability distribution	Divisor	Relative standard uncertainty
Micrometer scale	5 μm	Rectangular	√3	29 ppt
Damage or erosion effect of gap	1 μm	Rectangular	√3	6 ppt
Pressure gauge uncertainty	10.1kPa	Rectangular	√3	58 ppt
Breakdown voltage	0.383 kV	Normal	2	25 ppt
Repeated reading of breakdown voltage	0.056 kV	Normal	1	7 ppt
Settings	0.077 kV	Rectangular	√3	6 ppt
Relative combined standard uncertainty		Assumed Normal		70 ppt
Expanded uncertainty in *E/N*	140 ppt / 501.2 Td coverage probability of approximately 95 %			

The relative combined standard uncertainty and the expanded uncertainty can be calculated by Equations 5.9 and 5.7. The relative combined standard uncertainty in *E/N* in air at 101 kPa for positive polarity is presented in Table 5.4. It is $\sqrt{29^2 + 6^2 + 58^2 + 25^2 + 7^2 + 6^2} = 70$ ppt. The expanded uncertainty is 140 ppt (501.2 Td).

Therefore, it can be stated that the reduced breakdown electric field *E/N* in air at 101 *kPa* for positive polarity is 3580.0 Td ±501.2 Td, with ~95% confidence level. Using this approach, we can obtain the uncertainty in the reduced breakdown electric field for positive and negative polarities at different pressures in all investigated gases.

Table 5.5 presents the uncertainty in the product of the number density of the gas, *N*, and the time to breakdown, t_{br}, Nt_{br}, for positive polarity at 101 kPa in air. The individual components of the uncertainty in the gap between electrodes and the time to breakdown have been analysed in Tables 5.1 and 5.3.

The relative standard uncertainty can be obtained using Equation 5.9. In Table 5.5, the relative standard uncertainty in the pressure gauge is $\frac{5.831\text{kPa}}{101\text{kPa}} = 58$ ppt. The relative reading uncertainty in the time to breakdown is $\frac{0.690\mu s}{27.58\mu s} = 25$ ppt. The relative standard uncertainty in repeated reading is $\frac{0.208ns}{27.58ns} = 8$ ppt. The relative standard uncertainty in the settings is $\frac{0.159ns}{27.58ns} = 6$ ppt. Thus, the relative combined standard uncertainty in Nt_{br} for positive polarity at 101 kPa in air presented in Table 5.5 is $\sqrt{58^2 + 25^2 + 8^2 + 6^2} = 64$ ppt. The expanded uncertainty is 128 ppt ($8.806 \cdot 10^{16}$ s/m^3).

TABLE 5.5

Uncertainty analysis of Nt_{br} for positive polarity at 101 kPa in air

Source of uncertainty	Value ±	Probability distribution	Divisor	Relative standard uncertainty
Pressure gauge	10.1 kPa	Rectangular	√3	58 ppt
Time to breakdown	1.379 ns	Normal	2	25 ppt
Repeatable readings	0.208 ns	Normal	1	8 ppt
Settings	0.276 ns	Rectangular	√3	6 ppt
Relative combined standard uncertainty		Assumed Normal		64 ppt
Expanded uncertainty in Nt_{br}	128 ppt / 0. $88 \cdot 10^{17}$ s/m^3 coverage probability of approximately 95 %			

As a result, it can be stated that the product of the number density of gas and the time to breakdown, Nt_{br}, for positive polarity at 101 kPa in air is: $6.88 \cdot 10^{17}$ s/m^3 $\pm 0.88 \cdot 10^{17}$ s/m^3 at the level of confidence of ~95%. Using this approach, we can obtain the uncertainty in Nt_{br} for both positive and negative polarities at different pressure in all investigated gases.

5.5 Impulsive breakdown of air, N_2 and CO_2: experimental results

The experimental results are divided into three groups to discuss the breakdown characteristics of the investigated gases in the HV needle-plane topology. First, the volt-time characteristics have been obtained for each gas, pressure, and impulse polarity. Then, the field-distance characteristics were plotted using the electric field at the tip of the needle obtained from the QuickField model. Finally, the time-field characteristics have been plotted and examined to compare the results obtained in this chapter with the literature data and simulation results obtained in Chapter 4.

5.5.1 Volt-time characteristics

The breakdown tests in air, N_2 and CO_2 have been performed using HV impulses with positive and negative polarities at pressures from 6.5 kPa to 405 kPa. The breakdown voltage, $U_{br\text{-}ch}$, and the pre-breakdown time, t_{br}, have been obtained for each gas based on 60 breakdown events (3 series of tests, each series consists of 20 breakdowns) in total. These 60 values of $U_{br\text{-}ch}$ and t_{br} have been obtained for each specified charging voltage and gas pressure using a procedure similar to what was used in [Krile, 2005] (series of 20 breakdowns were performed) to determine the pre-breakdown delay time.

In order to keep the same conditions for each series of breakdown tests, a sample preparation procedure was developed and used. Before each series of breakdown tests, a new needle electrode was installed into the test cell and the ground electrode was polished and cleaned with ethanol. The test cell was then evacuated and filled with a fresh portion of gas using the gas control and distribution system described in Section 5.2.2.

In the experimental results on the breakdown voltage, $U_{br\text{-}ch}$, no obvious functional variation has been observed in the relationship between the breakdown voltage and the breakdown number. It was shown that the value of the breakdown voltage, $U_{br\text{-}ch}$,

demonstrates random variation when plotted against the breakdown test number (for 60 breakdown events), as shown in Figure 5.15.

It demonstrates that the experimental data are not apparently affected by potential variation in test conditions. Therefore, the obtained data were used to determine the average values of the breakdown voltage and the time to breakdown. The charging voltage provided by the HV DC power supply was increased from 10 kV to 35 kV with an increase in the gas pressure in the test cell to ensure the occurrence of breakdown.

A list of the charging voltages used at each gas pressure is: For air and N_2, the charging voltage was 10 kV for 6.5 kPa, 15 kV for 67.4 kPa and 101 kPa, 20 kV for 203 kPa, 25 kV for 304 kPa and 30 kV for 405 kPa. For CO_2, the charging voltage for pressures up to the atmospheric pressure (6.5 kPa, 15 kV for 67.4 kPa and 101 kPa) was 10 kV. Because of the higher breakdown strength of CO_2 at higher pressures, from 203 kPa to 405 kPa, different charging voltages were used for these pressures; 25 kV for 203 kPa, 30 kV for 304 kPa and 35 kV for 405 kPa.

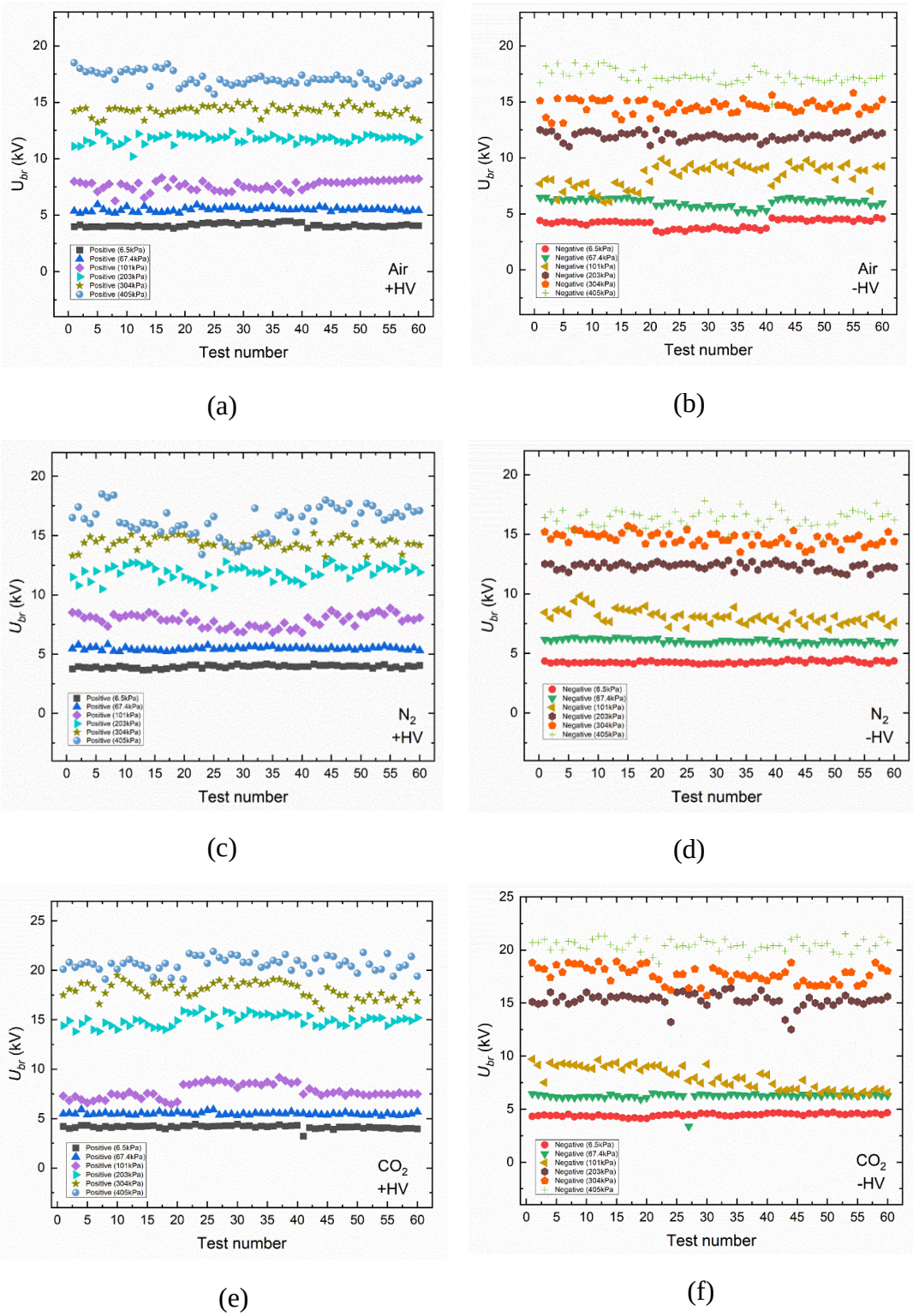

Figure 5.15 Breakdown voltage against the breakdown test number for all tested gases. (a) Positive polarity (6.5 kPa ~ 405 kPa) - breakdown voltage for air. (b) Negative polarity (6.5 kPa ~ 405 kPa) - breakdown voltage for air. (c) Positive polarity (6.5 kPa ~ 405 kPa) - breakdown voltage for N_2. (d) Negative polarity (6.5 kPa ~ 405 kPa) - breakdown voltage for N_2. (e) Positive polarity (6.5 kPa ~ 405 kPa) - breakdown voltage for CO_2. (f) Negative polarity (6.5 kPa ~ 405 kPa) - breakdown voltage for CO_2

The experimental tests were conducted using both positive and negative impulses; the diagnostics devices described in Section 5.2.3 were used to measure the breakdown voltage and the time to breakdown.

Figures 5.15 -5.16 show the breakdown voltage, $U_{br\text{-}ch}$, as a function of t_{br}, for the positive and negative impulse for air, N_2 and CO_2. Each point represents the mean value obtained from 60 breakdown events. The error bars represent the 95% confidence intervals in the breakdown voltage and time to breakdown, calculated by the approach discussed in Section 5.4.

In these graphs, a non-linear allometric function, Equation 5.10, was used to fit the experimental data by OriginPro (v.2021) graphing software.

$$U_{br\text{-}ch} = A \cdot (t_{br})^{-B} \quad \text{(kV)} \tag{5.10}$$

where $U_{br\text{-}ch}$ is the breakdown voltage in kV, t_{br} is the time to breakdown in ns; A and B are free fitting parameters. The value of A and B for both positive and negative impulses for air, N_2 and CO_2 are given in Table 5.6.

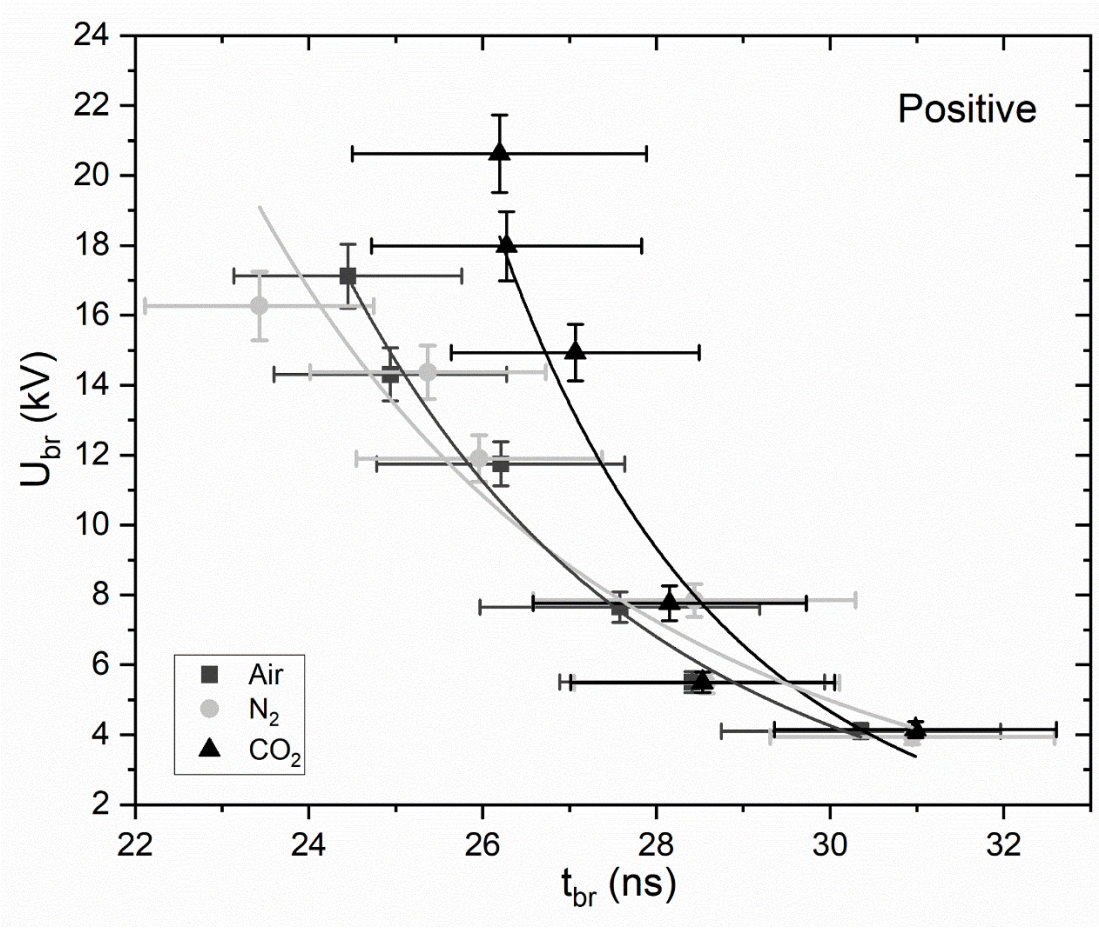

Figure 5.16 The breakdown voltage, $U_{br\text{-}ch}$, as function of t_{br}, positive polarity: ■ air; ● N_2; ▲ CO_2. Solid lines show fitting curves for each gas obtained by Equation 5.10. The error bars show the 95% confidence interval in the breakdown voltage and time to breakdown

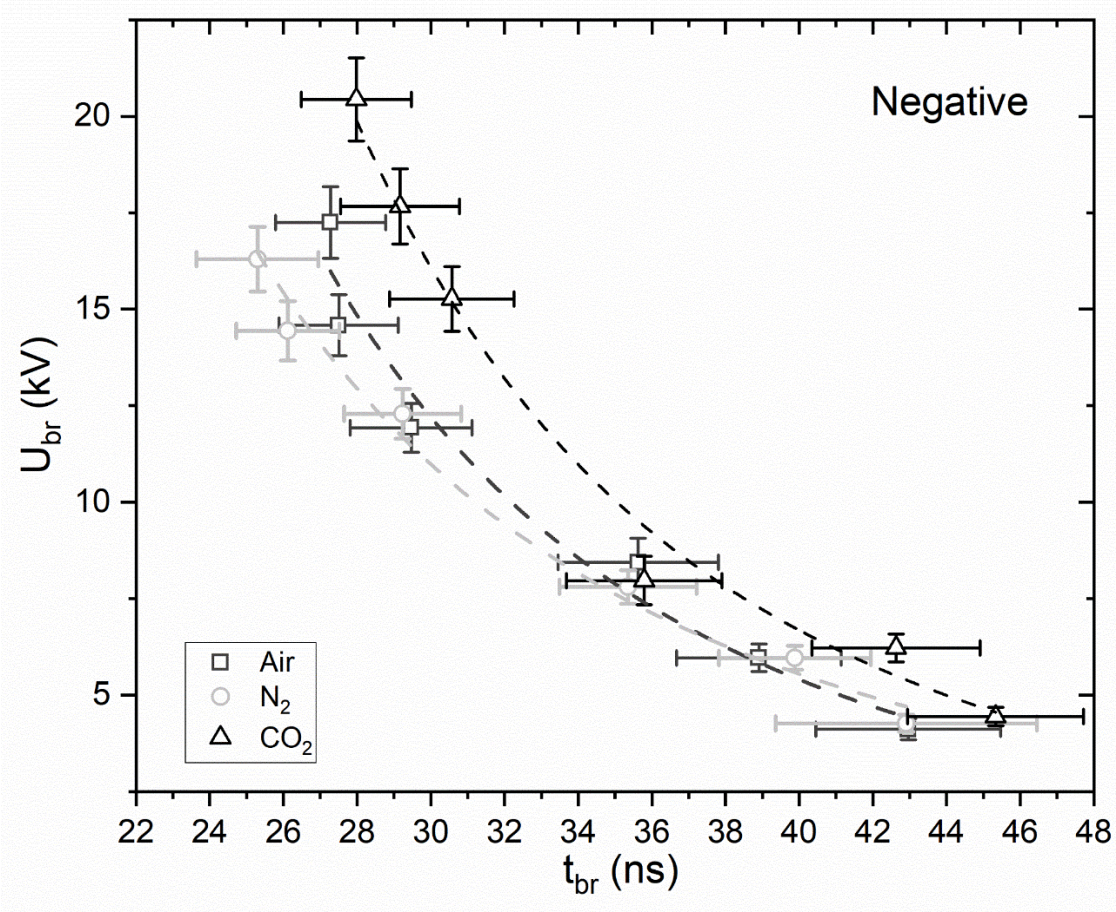

Figure 5.17 The breakdown voltage, $U_{br\text{-}ch}$, as function of t_{br}, negative polarity: □ air; ○ N_2; △ CO_2. Dashed lines show fitting curves for each gas obtained by Equation 5.10. The error bars show the 95% confidence interval in the breakdown voltage and time to breakdown

TABLE 5.6

Parameters A and B for Equation 5.10 for air, N_2 and CO_2

$$U_{br\text{-}ch}=A \cdot (t_{br})^{-B}$$

Negative polarity	Air	N_2	CO_2
A	$1.87 \cdot 10^5$	$3.53 \cdot 10^4$	$5.22 \cdot 10^5$
B	2.83	2.37	3.05
Positive polarity	**Air**	**N_2**	**CO_2**
A	$4.54 \cdot 10^{10}$	$5.29 \cdot 10^8$	$3.18 \cdot 10^{15}$
B	6.79	5.43	10.04

As shown in Table 5.6 higher values of A and B have been obtained for CO_2 as compared to that for air and N_2. It also can be observed that CO_2 has a higher breakdown voltage than the other two gases in the present electrode topology and energisation conditions.

However, for CO_2 the breakdown voltage as a function of time to breakdown decreases faster than that for air and N_2 and becomes comparable with the breakdown voltages for these gases at ~ 29 ns for positive impulses and at ~ 46 ns for negative impulses.

With regards to the polarity effects, it has been found that the value of breakdown voltage in the case of the negative energization is higher than that for the positive energization at the same time to breakdown in all three gasses. The higher breakdown voltage for negative energization could be due to the development of a negative space charge that reduces the electric field in the gap.

5.5.2 Field-distance characteristics

To obtain the field-distance breakdown characteristics, the average values of the breakdown voltage was used in the Quickfield model of the test cell to obtain the maximum field at the tip of the needle electrode at the breakdown moment, E_{tip}, for each gas and gas pressure.

The obtained normalized electric field at the tip of the needle electrode at the moment of breakdown, E_{tip}/N has been plotted in Figures 5.17-5.19 as a function of the product of the particle number density and the gap between electrodes Nd for air, N_2 and CO_2.

An allometric function (5.11) was fitted to the experimental data to obtain the functional behavior E_{tip}/N (Nd). This fitting procedure was implements using OriginPro graphing software (v.2021)

$$E_{tip}/N = C\,(Nd)^{-D} \quad \text{(Td)} \tag{5.11}$$

where, C and D are the free fitting parameters. Nd is the product of the gas number density and the gap separation between electrodes in units of $1/m^2$ and E_{tip}/N is the normalized electric field at the tip of the needle in units of Td. C and D for the investigated gases are given in Table 5.7.

TABLE 5.7

Fitting parameters C and D, Equation 5.11, for air, N_2 and CO_2

$E_{tip}/N=C\cdot(Nd)^{-D}$			
	Air	N_2	CO_2
C	$4.5\cdot10^{15}$	$1.0\cdot10^{17}$	$5.1\cdot10^{16}$
D	0.56	0.63	0.61

Figures 5.17-5.19 provide the relationship between the normalized breakdown field at the tip of the needle, E_{tip}/N, and Nd for air, N_2, and CO_2, these values are compared with the experimental data available in the literature.

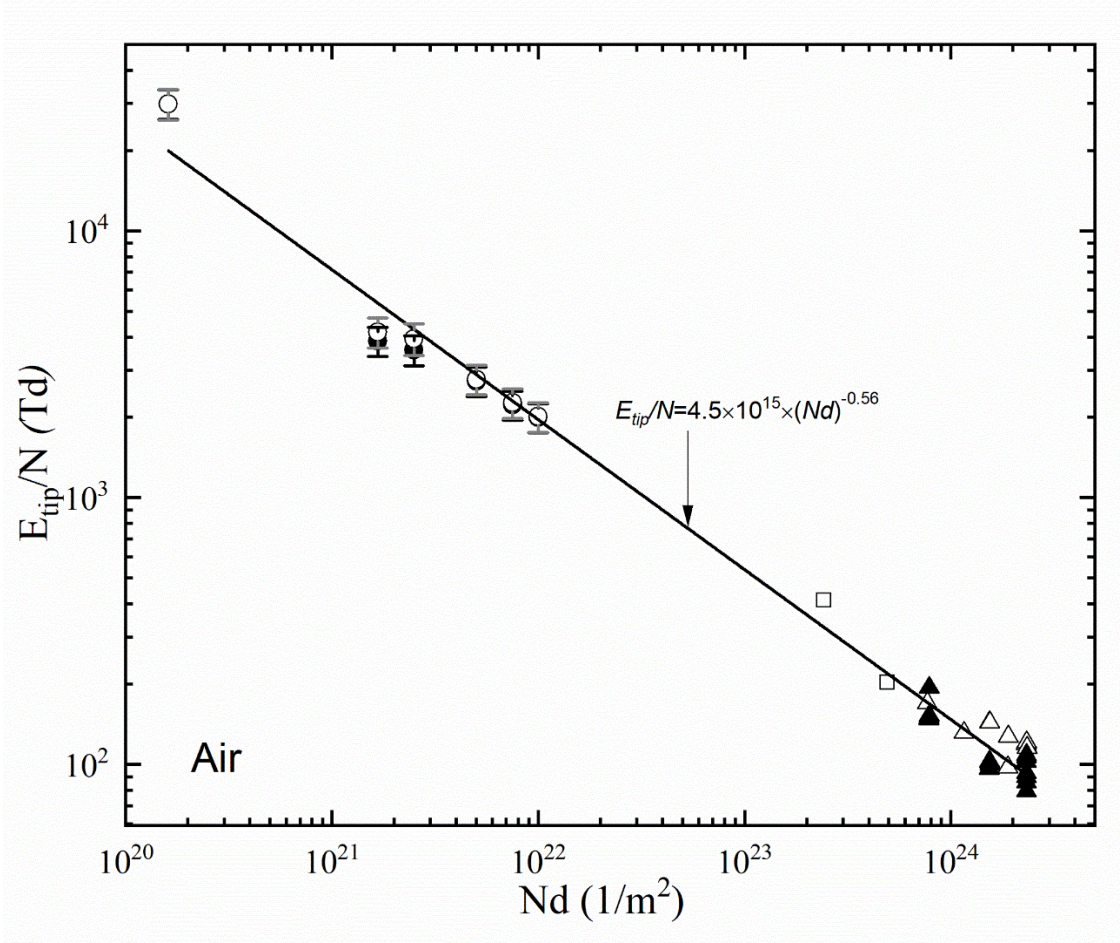

Figure 5.18 E_{tip}/N as a function of Nd in air. Experimental data: ○, negative polarity (the present work); ●, positive polarity (the present work); △, negative polarity (monocone) [Carboni, 2001]; ▲, positive polarity (monocone) [Carboni, 2001]; □, [Shao, 2006]. Solid line, fitting curve, Equation 5.11

Figure 5.18 shows the normalized electric field E_{tip}/N as a function of Nd for air for positive and negative energization. The reduced electric field at the needle tip E_{tip}/N obtained from the present work is located in the range of Nd from ~ $2\cdot10^{20}$ 1/m^2 to ~ 10^{22} 1/m^2. E_{tip}/N declines with an increase in Nd. The error bars show the 95% confidence intervals for the mean values of E_{tip}/N.

It can be found that the fitting function, Equation 5.11, is in line with the experimental data by [Carboni, 2001] and [Shao, 2006] in the range of Nd from ~ $2\cdot10^{23}$ 1/m^2 to ~ $2.5\cdot10^{24}$ 1/m^2.

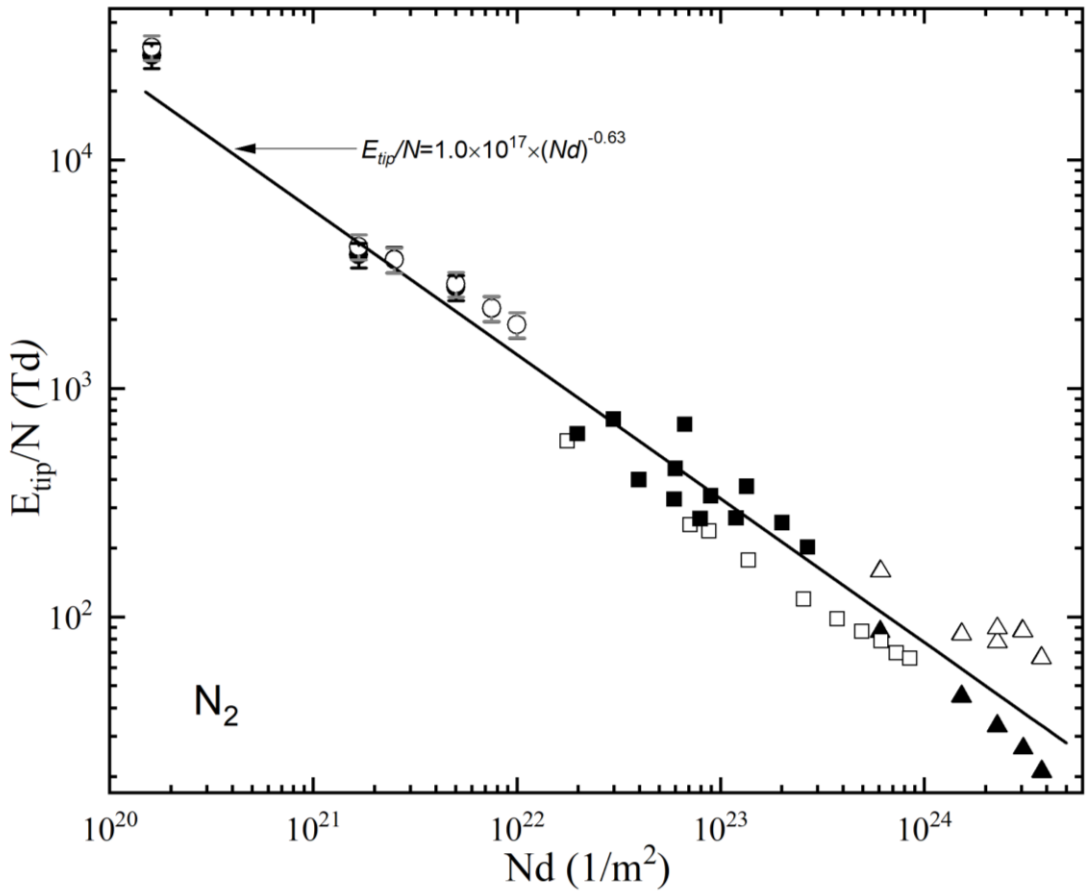

Figure 5.19 E_{tip}/N as a function of Nd in N_2. Experimental data: ○, negative polarity (the present work); ●, positive polarity (the present work); △, negative polarity (pointplane) [Carboni, 2001]; ▲, positive polarity (point-plane) [Carboni, 2001]; ■, [Cai, 2010]; □, [Dick, 2000]. Solid line, fitting curve Equation 5.11

Figure 5.19 provides the relationship between the normalized electric field E_{tip}/N and Nd for N_2 for both polarities: E_{tip}/N for negative and positive polarities (with the 95% confidence intervals) is presented as open dots and the solid dots, respectively, in the Nd range from ~ $2\cdot10^{20}$ $1/m^2$ to ~ 10^{22} $1/m^2$.

The fitting curve (Equation 5.11) for the field E_{tip}/N steadily declines with Nd. The fitting curve in the range of ~ $2\cdot10^{22}$ $1/m^2$ to ~ $4\cdot10^{24}$ $1/m^2$ shows a good agreement with the data from [Carboni, 2001], [Cai, 2010] and [Dick, 2000].

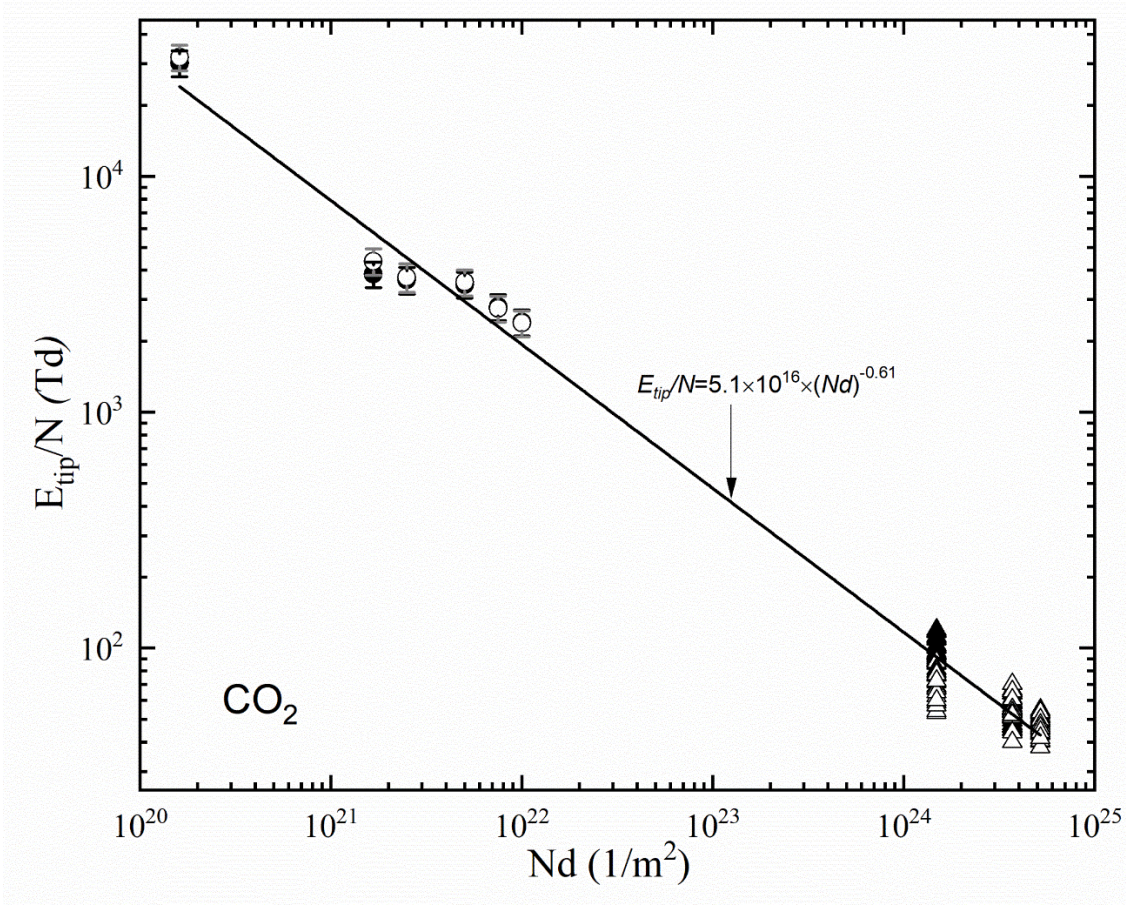

Figure 5.20 E_{tip}/N as a function of Nd in CO_2. Experimental data, the present work: ○, negative polarity; ● positive polarity. Experimental data [Kumar, 2021]: △, negative polarity; ▲, positive polarity. Solid line, fitting curve Equation 5.11

Figure 5.20 presents E_{tip}/N as a function of Nd for CO_2 for both polarities. The field at the needle tip E_{tip}/N with error bars (95% confidence intervals) obtained in the present experimental work is in the Nd range from ~ $2\cdot10^{20}$ 1/m^2 to ~ 10^{22} 1/m^2; the data by Kumar [Kumar, 2021] were obtained in the Nd range from ~ 10^{24} 1/m^2 to ~ $5\cdot10^{24}$ 1/m^2.

Comparing the fitting curve of E_{tip}/N as presented in Equation 5.11 with Kumar's data [Kumar, 2021], it can be found that Equation 5.11 is consistent with data by [Kumar, 2021] in the range of Nd from ~ 10^{24} 1/m^2 to ~ $5\cdot10^{24}$ 1/m^2. In this range, there is a clear trend of decreasing E_{tip}/N with Nd.

5.5.3 Time-field characteristics

To obtain the time-field breakdown characteristics of air, N_2 and CO_2, the average values of the time to breakdown (Section 5.5.1) were used to calculate the product of the particle number density and the total time to breakdown, Nt_{br} for each gas and gas pressure.

Typically, it is postulated that the total time to breakdown, t_{br}, equals the sum of the statistical time, t_s, and the formative time, t_f

$$t_{br} = t_s + t_f \tag{5.12}$$

In the present work the drift-diffusion and kinetic models provide the formative time only. The total time to breakdown can be obtained from the experiments. Thus, if t_{br} and t_f are known, the statistical time can be calculated.

Figure 5.21 shows the product of the formative time and gas number density, Nt_f as a function of the normalized electric field E/N obtained by Equation 4.19 for air, N_2, CO_2, and SF_6.

It also shows the total time to breakdown t_{br} multiplied by the gas particle density N as a function of the normalized electric field E_{tip}/N obtained experimentally in the present work for air, N_2 and CO_2.

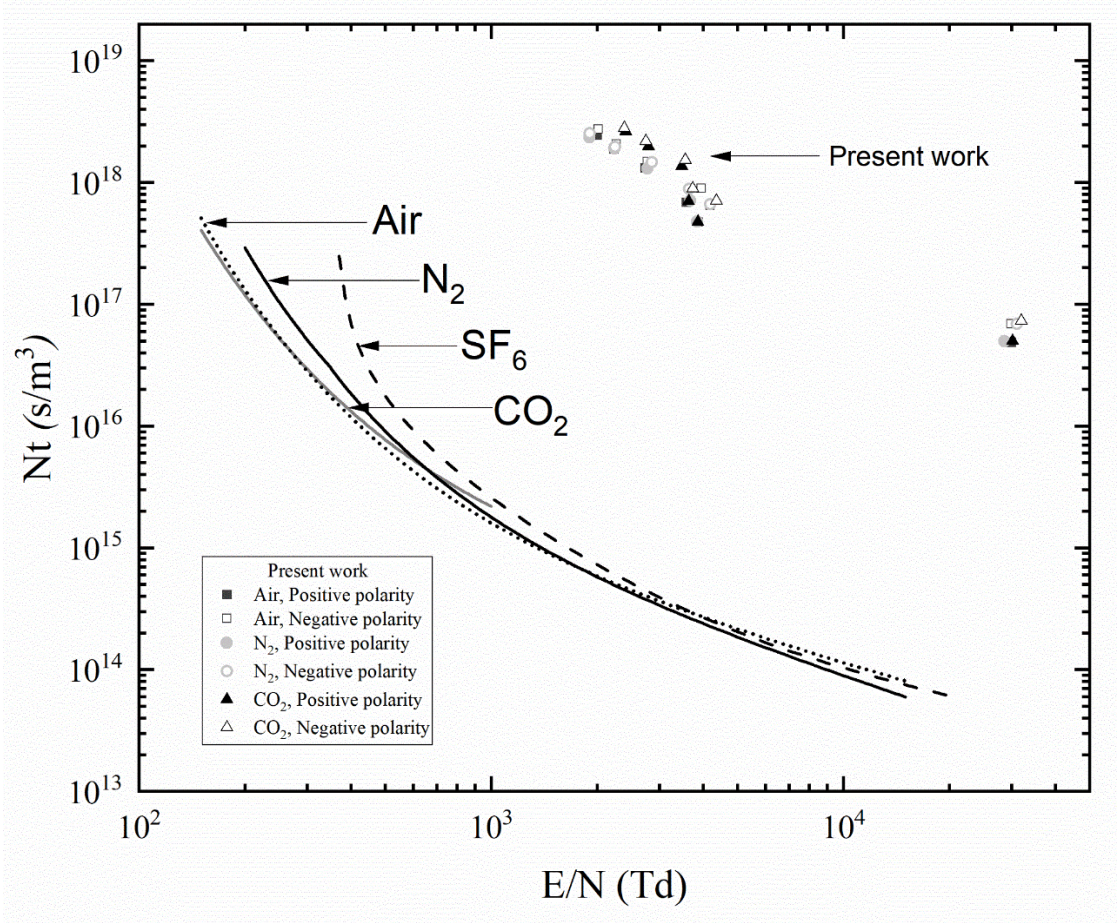

Figure 5.21 Time-field breakdown characteristic for different gases. Kinetic model, Equation 4.19, Nt_f as a function of E/N: air, dotted line; N_2, solid dark line; CO_2, solid gray line; SF_6, dashed line. Experimental results obtained in the present work, Nt_{br} as a function of E_{tip}/N: air, □negative polarity, ■positive polarity; N_2, ○negative polarity, ●positive polarity; CO_2, △negative polarity; ▲positive polarity

It can be found that the experimentally obtained time to breakdown t_{br} for the field in the range from ~$2 \cdot 10^3$ Td to ~$2 \cdot 10^4$ Td is ~ 1000 times longer than the analytical formative time t_f .

The experimental results have been fitted with the analytical allometric fitting curves using OriginPro graphing software (v.2021) in the field range from ~$2 \cdot 10^3$ Td to ~$2 \cdot 10^4$ Td

$$Nt_{br} = K\,(E_{tip}/N)^{-M} \quad (\mathrm{s/m^3}) \tag{5.13}$$

where E_{tip}/N is the normalized electric field at the needle tip in the unit of Td, and Nt_{br} is the product of the gas number density and the time to breakdown in the unit of s/m^3. K and M are the free fitting parameters, their values for air, N_2 and CO_2 are listed in Table 5.8.

TABLE 5.8

Fitting parameters K and M, Equation 5.13, for air, N_2 and CO_2

$$Nt_{br} = K \cdot (E_{tip}/E)^{-M}$$

	Air	N_2	CO_2
K	$5.8 \cdot 10^{22}$	$8.1 \cdot 10^{22}$	$1.6 \cdot 10^{23}$
M	1.35	1.38	1.44

Nt as a function of the reduced electric field E/N is presented in Figures 5.21 - 5.23, for air, N_2, and CO_2. These figures include the experimental results, the results obtained by the kinetic model discussed in Section 4.3.1, and the literature data.

An empirical equation "ρt as a function of E/ρ" has been proposed by Martin [Martin, 1991]

$$\rho t = 97800 \cdot (E/\rho)^{-3.44} \tag{5.14}$$

where ρ denotes the density of gas in the unit of g/cm^3, t is the time to breakdown in the unit of s, E expresses the average electric field in the unit of kV/cm. Equation 5.14

is based on the values of the specific gas constant [Snider, 1986], these values for air, N_2 and CO_2 are listed in Table 5.9.

TABLE 5.9

Gas constant for air, N_2 and CO_2, [Snider, 1986]

Gas	R_{gas} J/(kg·K)
Air	287.058
N_2	296.8
CO_2	188.9

The gas density is obtained by

$$\rho = p/(R_{gas} \cdot T) \tag{5.15}$$

where ρ is gas density in kg/m^3 (1 g/cm^3=1000 kg/m^3), T is the temperature in the unit of K.

Using the following link between the pressure and number density, $p=NTk_B$, we can rewrite

$$\rho\,(\frac{gm}{cc}) \cdot t(s) \cdot 10^3 \cdot R_{gas} \cdot T = p(Pa) \cdot t(\mathrm{s}) \tag{5.16}$$

$$E(\frac{\mathrm{kV}}{\mathrm{cm}})/\rho\,(\frac{\mathrm{gm}}{\mathrm{cc}}) \cdot 10^3 \cdot 1/(R_{gas} \cdot T) = E(\mathrm{kV/cm})/p(\mathrm{Pa}) \tag{5.17}$$

$$p(\text{Pa}) \cdot t(\text{s})/(Tk_B) = Nt(\text{s/m}^3) \tag{5.18}$$

$$E(\frac{\text{kV}}{\text{cm}})/p\ (\text{Pa}) \cdot 10^5 \cdot Tk_B \cdot 10^{21} = (E/N)_{\text{Td}} \tag{5.19}$$

$$Nt(\text{s/m}^3) = \frac{\rho(\frac{\text{gm}}{\text{cc}}) \cdot t(s) \cdot 10^3 \cdot R_{gas} \cdot T}{Tk_B} \tag{5.20}$$

$$(E/N)_{\text{Td}} = \frac{E(\frac{\text{kV}}{\text{cm}})}{\rho\ (\frac{\text{gm}}{\text{cc}})} \cdot 10^5 \cdot 10^3 \cdot \frac{Tk_B}{R_{gas} \cdot T} \cdot 10^{21} \tag{5.21}$$

$$\rho t(\text{s} \cdot \text{gm/cc}) = Nt(\text{s/m}^3) \cdot (\frac{k_B}{R_{gas}}) \cdot 10^{-3} \tag{5.22}$$

$$\frac{E}{\rho}\left(\frac{\text{kV/cm}}{\text{gm/cc}}\right) = (E/N)_{\text{Td}} \cdot \frac{R_{gas}}{k_B} \cdot 10^{-23} \tag{5.23}$$

Therefore, *Nt* for air, N_2 and CO_2 can be obtained and these values are shown in Table 5.10.

TABLE 5.10

Nt for air, N_2 and CO_2, [Martin, 1991]

Gas	*Nt* (s/m^3) as function of *E/N* (Td)
Air	$Nt = 2.16 \cdot 10^{25} \cdot (E/N)^{-3.44}$
N_2	$Nt = 1.99 \cdot 10^{25} \cdot (E/N)^{-3.44}$
CO_2	$Nt = 5.99 \cdot 10^{25} \cdot (E/N)^{-3.44}$

Based on these calculations, the equations provided in Table 5.10 for air, N_2 and CO_2 were used to plot *Nt* as a function of *E/N* in the field range from 100 Td to 1000 Td, *Nt* (*E/N*) are shown in Figures 5.21-5.23.

Figures 5.21-5.23 provide *Nt* as a function of the reduced breakdown field, *E/N*, for in air, N_2, and CO_2 for both positive and negative polarities. *Nt(E/N)* relationships obtained in the present work, are compared with the data from the literature obtained in various experimental conditions.

Each original experimental point in Figures 5.21-5.23 represents the average value obtained using 60 breakdown measurements. The error bars show the 95% confidence interval values. Some error bar intervals are small and not clearly seen in these figures. Analytical lines and literature experimental data points shown in Figures 5.21-5.23 have no error bars.

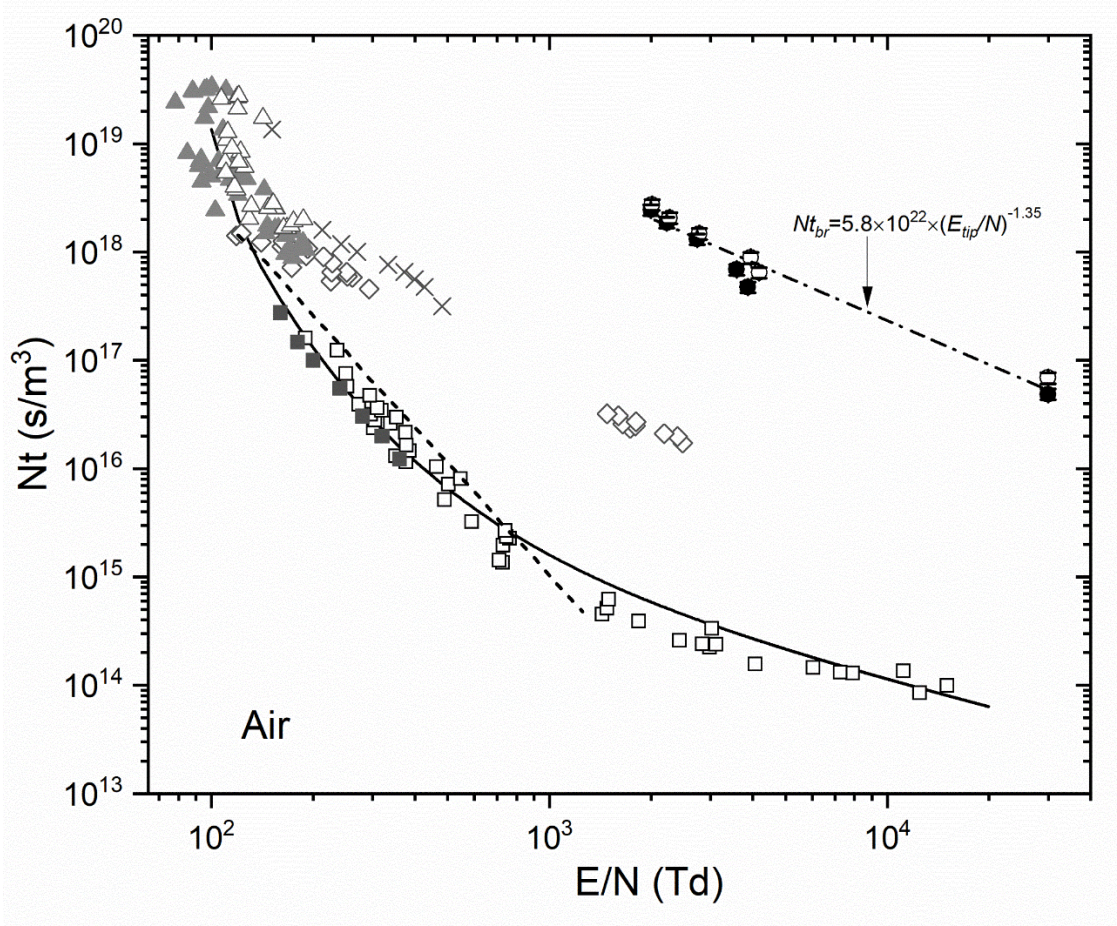

Figure 5.22 Time-field breakdown characteristic for air. Experimental data from the present work, Nt_{br} as a function of E_{tip}/N: ○ negative polarity; ● positive polarity. Fitting curves obtained in the present work: dash dotted line, fitting curve Equation 5.13. Experimental data and analytical data from the literature: △ negative polarity (monocone) [Carboni, 2001]; ▲positive polarity (monocone) [Carboni, 2001]; × [Shao, 2006]; ◇ [Mankowski, 1998]; □, [Felsenthal, 1965]; dashed line [Martin, 1991]; ■Drift-diffusion model; solid dark line, Kinetic model Equation 4.19, Nt_f as a function of E/N

Figure 5.22 shows Nt (the product of the gas number density and the breakdown time) as a function of the reduced electric field E/N for air. Nt_{br} as a function of E_{tip}/N (the total time to breakdown t_{br}, the electric field E_{tip} of the needle tip) was obtained in the present experimental work for both polarities. Nt_f as a function of E/N (the formative time t_f) for air was obtained using the drift-diffusion model and the kinetic model (Equation 4.19); for comparison the experimental results were taken from [Felsenthal, 1965], [Martin, 1991], [Mankowski, 1998], [Carboni, 2001], [Shao, 2006].

Felsenthal [Felsenthal, 1965] provides the formative time t_f for air obtained in the breakdown tests performed in the uniform field using HV pulses with the rising times from 0.25 ns to 1.0 ns, the field range was from ~ 100 Td to ~ $2 \cdot 10^4$ Td. The ultraviolet light was used to stimulate electron production at the cathode.

The analytical breakdown curve for air was plotted using data from Table 5.10, [Martin, 1991]. The total time to breakdown t_{br} obtained in the point-plane topology in air in the field range from ~ 10^2 Td to ~ $2.5 \cdot 10^3$ Td was taken from [Mankowski, 1998]. Shao [Shao, 2006] provides the total time to breakdown t_{br} in the field range from ~ 150 Td to ~ 480 Td for the uniform electrode topology.

The effective stress time, t_{eff} , was obtained in the experimental measurements using the monocone electrode [Carboni, 2001], this time was obtained in the field range from ~ 80 Td to 200 Td and is defined as the time interval between the 89% and 100% of the breakdown voltage.

It has been found that the results obtained by the drift-diffusion and kinetic models are in line with the experimental results [Felsenthal, 1965] and show a trend similar to what was obtained by [Martin, 1991], [Carboni, 2001], [Mankowski, 1998], and [Shao, 2006].

It can be seen that Nt_{br} obtained in the present work are located in the range of E/N from ~ $2 \cdot 10^3$ Td to ~ $3 \cdot 10^4$ Td. The corresponding Nt_{br} range is from ~ $2.7 \cdot 10^{18}$ s/m^3 to ~ $4.8 \cdot 10^{16}$ s/m^3. Whereas, in the same range of E/N, the data and results from [Felsenthal, 1965], [Mankowski, 1998], and the kinetic model show a significantly lower value of Nt_{br}, in Figure 5.22.

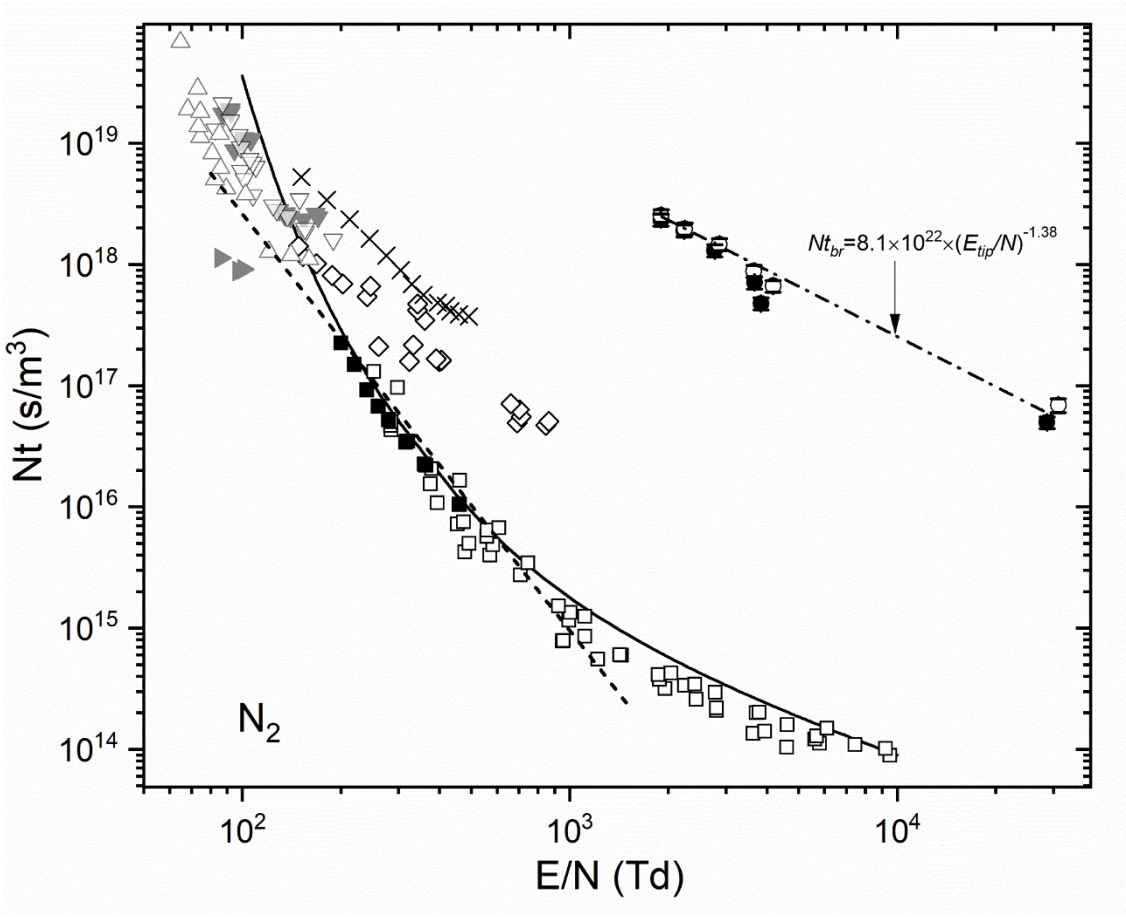

Figure 5.23 Time-field breakdown characteristic for N_2. Experimental data from the present work, Nt_{br} as a function of E_{tip}/N: ○ negative polarity; ● positive polarity. Fitting curves for the present work: dash dotted line, fitting curves from the Equation 5.13. Experimental data and analytical data from literature: △, negative polarity (point-plane) [Carboni, 2001]; ▽, negative polarity (monocone) [Carboni, 2001]; +, positive polarity (point-plane) [Carboni, 2001]; ▼, positive polarity (monocone) [Carboni, 2001]; × [Shao, 2006]; ◇ [Mankowski, 1998]; □ [Felsenthal, 1965]; dashed line [Martin, 1991]; ■ Drift-diffusion model; solid dark line, Kinetic model Equation 4.19, Nt_f as a function of E/N

Figure 5.23 shows the field-time breakdown characteristics (Nt as a function of E/N) for N_2. This figure includes the data obtained in the present experimental work with the error bars (95% confidence intervals); the simulation results obtained by the drift-diffusion model and the kinetic model (Equation 4.19); and the results from other research work obtained by [Felsenthal, 1965], [Martin, 1991], [Mankowski, 1998], [Carboni, 2001], [Shao, 2006].

The formative breakdown time for N_2, t_f , was obtained by [Felsenthal, 1965] from breakdown events stimulated by ultraviolet light, in the wide field range, up to ~ 10^4 Td. The analytical curve was plotted using data from Table 5.10, [Martin, 1991].

Mankowski [Mankowski, 1998] investigates the total time to breakdown t_{br} for N_2 in the field range from ~ 150 Td to ~ 860 Td. Carboni [Carboni, 2001] provides the experimental measurements for the effective stress time t_{eff} for N_2 in the field range from ~ 65 Td to ~ 190 Td. Shao [Shao, 2006] presents the total time to breakdown t_{br} in the field range from ~ 150 Td to ~ 500 Td .

Figure 5.23 shows the results obtained by the present models (Chapter 4), these results are in good agreement with [Felsenthal, 1965]. As can be seen from Figure 5.23, Nt demonstrates a decreasing trend with the increasing field. Higher values for Nt_{br} have been obtained in the present work (Nt_{br} is in the range from ~ $2.5 \cdot 10^{18}$ s/m^3 to ~ $4.9 \cdot 10^{16}$ s/m^3), as compared with the values provided by [Felsenthal, 1965] and by the kinetic model. This discrepancy can be attributed to the fact that the total breakdown time consists of the statistical time and the formative time, the statistical time is significantly longer than the nominal formative time provided by [Felsenthal, 1965] and both models used in the present study.

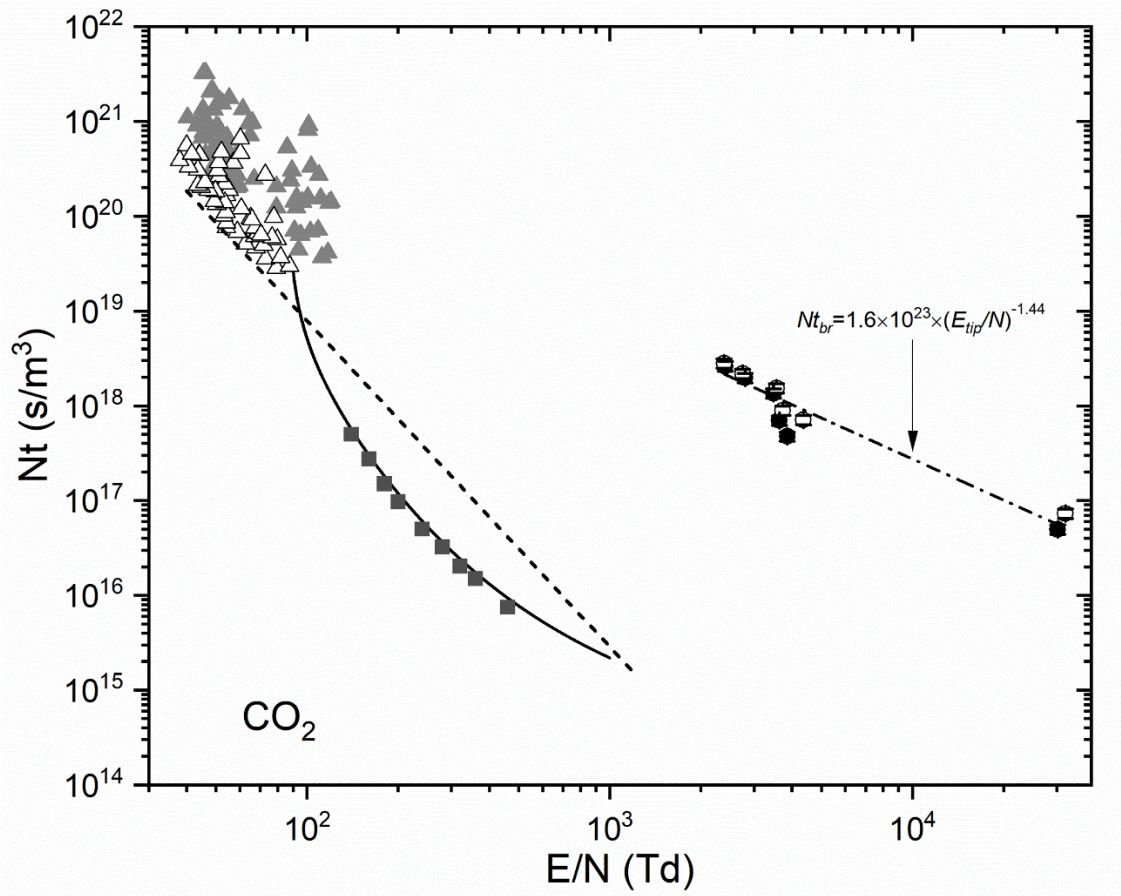

Figure 5.24 Time-field breakdown characteristic for CO_2. Experimental data from the present work, Nt_{br} as a function of E_{tip}/N: ○ negative polarity; ● positive polarity. Fitting curves for the present work: dash dotted line, fitting curves from the Equation 5.13. Experimental and analytical data from literature: △negative polarity (rod-plane) [Kumar, 2021]; ▽positive polarity (rod-plane) [Kumar, 2021]; dashed line [Marin, 1991]; ■ Drift-diffusion model; solid dark line, Kinetic model Equation 4.19, Nt_f as a function of E/N

Figure 5.24 shows Nt as a function of E/N for CO_2. The experimental data obtained using HV impulses of both polarities which provided E/N in the range from ~ $2 \cdot 10^3$ Td to ~ $3 \cdot 10^4$ Td. The values of Nt_{br} obtained in the present work are in the range from ~ $2.8 \cdot 10^{18}$ s/m^3 to ~ $4.9 \cdot 10^{16}$ s/m^3. The analytical breakdown curve for CO_2 [Martin, 1991] has been analysed in Section 5.5.3 (Table 5.10).

The data from [Kumar, 2021] were obtained using the fields in the range from ~ 40 Td to ~ 100 Td. The breakdown time, defined by the authors as "the time duration

between half the maximum amplitude of the pulse" was measured in the rod-plane electrode topology.

As shown in Figure 5.24, the experimental measurements obtained in the present work demonstrate a decreasing trend of Nt with the field, and E/N is ~10 times higher than the analytical data obtained by the drift-diffusion and kinetic models and data from [Martin, 1991] (at the same values of Nt_{br}).

Thus, the obtained experimental Nt_{br} values presented in Figures 5.21-5.23 are larger than the literature data and Nt_{br} values obtained by the kinetic model. This discrepancy could be attributed to the short, ns, rising time of the applied impulsive voltage. It also could be explained by the difference in the electrode topology, gap separation and gas pressure used in the present tests and in the experiments described in the literature.

5.6 Discussion

This chapter is focused on the experimental measurements of the breakdown characteristics of different gases in the needle-plane electrode topology with a gap of 100 μm and a needle radius of ~80 μm. Positive and negative HV impulses with the rising time up to ~50 ns were used in these tests. The impulsive breakdown characteristics have been obtained for air, N_2 and CO_2, for gas pressures ranging from 6.5 kPa to 405 kPa.

The breakdown process in the needle-plane electrode topology can be described as follows: when HV pulse is applied to the needle electrode, the electric field is established across the gap between electrodes. The ionization process starts to develop in the area close to the tip of the HV needle electrode where the field magnitude is strongest, causing the exponential growth of free electrons.

However, due to significant rate of voltage rise, dV/dt, of the applied impulse, significant overvoltage can be achieved before the complete breakdown in the gap.

Therefore, the breakdown voltage obtained in the present experimental work is higher than the (static) DC breakdown voltage for all tested gases. These results are important for analysis of fast, sub-μs transient (pre) breakdown processes because the measurements performed under DC energization are not applicable in the case of short HV impulses. Thus, the time-field characteristics should be used to characterize the breakdown behavior of gases in such case, [Levatter, 1980].

The methodology used in the present experimental work to obtain the impulsive breakdown voltages is in line with the methodology proposed by [Krile, 2006] and [Levko, 2019], where all breakdown events were registered on the leading edge of the applied HV impulses. The leading slope (the rate of voltage rise) of the voltage impulse determines the impulsive breakdown volt-time characteristics. These characteristics provide further insight into the dynamics of (pre-) breakdown processes governed by the field-dependent electron transport parameters, such as the effective ionization coefficient and mobility of charged species.

The experimental values of the breakdown voltage were used to obtain the breakdown field, E_{tip}/N, at the tip of the needle in the range from ~10^3 Td to ~10^4 Td. Therefore, the field-distance characteristics (E_{tip}/N as a function of Nd) and the time-field characteristics (Nt_{br} as a function of E_{tip}/N) for air, N_2, and CO_2 have been established and compared with the literature data.

The obtained field-distance characteristics have been fitted with the allometric functions, $E_{tip}/N=C(Nd)^{-D}$, where C and D are fitting parameters specific for each gas. It was found that these functions agree well with the literature data for the higher values of Nd. Thus these scaling relationships can be used to provide a link between the breakdown field, the gas number density and the gap between electrodes in the gases. The time-field characteristics obtained in the present work (Nt_{br} as a function of E_{tip}/N) provide the Nt_{br} values for each tested gas which are significantly higher than the analytical Nt_{br} values obtained by the kinetic model. This discrepancy can be attributed to the fact that the total breakdown time consists of the statistical time and the formative time, the statistical time is significantly longer than the nominal formative time provided by both models used in the present study. Further

experimental investigation of the transient development of plasma streamers in different gases, their initiation and propagation characteristics will help in characterisation of the statistical, formative and thermalisation time intervals. This future study could utilise fast optical diagnostic systems, which will provide visualisation of streamers and will help in developing a more detailed understanding and discrimination between different gas breakdown phases in the case of fast HV impulsive stresses. However, this work is beyond the scope of the present project.

The breakdown results obtained in the present work are important for practical pulsed power applications, for example they can be used in the development and optimization of the operational characteristics of miniature plasma closing switches and other gas-filled pulsed power components and systems.

Chapter 6 Analysis of swarm parameters and breakdown characteristics of air with different humidity levels

6.1 Introduction

In many practical high voltage and pulsed power applications, the breakdown characteristics of humid air are required. Information on the breakdown behaviour of humid air is an essential factor in optimization and coordination of air-based insulation of different high voltage systems that may operate in challenging environmental conditions, including in air with elevated humidity, such as air-insulated equipment in substations [Byrne, 2014].

Since the 1960s, the effect of humidity on the gas breakdown characteristics has been investigated. For example, the experimental work by Prasad and Graggs [Prasad, 1960] was aimed at the investigation of the ionization and attachment coefficients for humid air and water vapour in the field range from ~ 90 Td to ~ 150 Td.

Ryzko [Ryzko, 1965] has conducted experimental measurements to obtain the drift velocity of electrons in humid air and water vapour in the fields up to 300 Td.

Verhaart and Lann [Verhaart, 1984] have performed an experimental study to investigate the influence of water vapour on the breakdown properties of air and obtained the effective ionization coefficient of humid air in the low fields. They state that the critical field for humid air is $(E/N)_{cr}$ = 104 Td. Stout and Dawson [Stout, 1978] have conducted experimental measurements and of the effective ionization coefficient for humid air in fields up to ~ 300 Td.

The experimental analysis of the effective ionization coefficient of the water vapour in the high field and the critical field for the water vapour have been presented by Risbud [Risbud, 1979]; Hasegawa [Hasegawa, 2007]; and Sivoš [Sivoš, 2015].

However, detailed information on how humidity impacts the gas breakdown characteristics is still lacking due to different temperatures and pressures used in the experiments described in the literature. Thus, further analysis is required to predict breakdown characteristics of air with different levels of humidity.

In this chapter, the swarm parameters and critical field of air with different levels of humidity are investigated analytically. The effective ionization coefficients for air with a relative humidity of 0%, 50%, and 100% are obtained. And the effect of humidity on the breakdown characteristics of air is analysed using the streamer breakdown criterion.

6.2 Effective ionization and critical field for air with different relative humidity

The swarm coefficients can be calculated by the Boltzmann equation (BE). In the present work, BOLSIG+ solver [Bolsig+, 2022], a free online program, is used to solve the Boltzmann equation for different gases. It has been utilized to analyse the effect of humidity on the swarm parameters in air based on the molar fraction for each species at room temperature and atmospheric pressure.

A three-species (N_2, O_2, and H_2O) gas composition was used in the BOLSIG+ solver to obtain the effective ionization coefficients and the critical field for air with 0%, 50%, 100% RH.

As there are different molar fractions of different species for air with different relative

humidity levels, the following section starts with presenting the relationship between the relative humidity and the molar fractions of each species, including the definition of the total pressure of the gas, the partial pressure of the gas, the relative humidity and the molar fractions.

The total pressure of the gas (humid air) is obtained as a sum of the partial pressures of gas components: dry air and water vapour [Chen, 2018]

$$P_{tol} = P_{da} + P_w \tag{6.1}$$

where P_{da} represents the partial pressure of the dry air, P_w denotes the partial pressure of the water vapour, P_{tol} is the total pressure of humid air.

Relative humidity is a measure of the water vapour content in air. It is defined as the ratio of the partial pressure of water vapour to the saturated pressure with water vapour at given temperature

$$RH = \frac{P_w}{P_{sat}} \cdot 100\% \tag{6.2}$$

where P_w is the actual pressure of water vapour, and P_{sat} is the saturated pressure, RH represents the relative humidity.

The total pressure of air, P_{tol}, at temperatures of 20℃ (293.15K) and 26.85℃ (300K), is 101.3 kPa. Thus, using the saturation pressure of water vapour (P_{sat}), for these two temperatures, 2.34 kPa and 3.54 kPa respectively, [Irvine, 1984], the equation for the pressure can be re-written as

$$P_w = P_{sat} \cdot RH \tag{6.3}$$

where P_w is the actual pressure of water vapour, and P_{sat} is the saturated pressure, RH represents the relative humidity.

TABLE 6.1

Partial pressure of air with 50% RH and 100% RH

(300 K, 101.3 kPa)

Temperature (K)	Relative Humidity (%)	P_w (kPa)	P_{da} (kPa)
293.15	0	0	101.3
	50	1.17	100.13
	100	2.34	98.96
300	0	0	101.3
	50	1.77	99.53
	100	3.54	97.76

The partial pressure of water vapour, P_w, and the partial pressure of dry air, P_{da}, at relative humidities of 0%, 50%, 100% were obtained by Equation 6.3 and 6.1, and these values are shown in Table 6.1. The values of the partial pressure of air with 50% and 100% RH at 20°C agree with the literature data [Chen, 2018].

The molar fraction of dry air, χ_{da}, and water vapour, χ_w, can be calculated by the ideal gas law, which is an equivalent to the fraction of partial pressure equation

$$\chi_{da} = \frac{P_{da}}{P_{tol}} \tag{6.4}$$

$$\chi_w = \frac{P_w}{P_{tol}} \tag{6.5}$$

where P_w is the actual pressure of water vapour, and P_{tol} is the total pressure, χ_{da} is the molar fraction of dry air, and water vapour, χ_w is the molar fraction of water vapour.

TABLE 6.2

Molar fractions of different species in air

(300K, 101.3 kPa)

Relative Humidity (%)	Species	Molar Fraction (%)
Dry air, RH=0%	N_2	79
	O_2	21
Air, RH=50%	N_2	77.62
	O_2	20.63
	H_2O	1.75
Air, RH=100%	N_2	76.24
	O_2	20.27
	H_2O	3.49

The species and their molar fractions in air at different relative humidifies of 0%, 50%, and 100% at a temperature of 300K and pressure of 101.3 kPa were obtained by Equations 6.4 and 6.5. These values are shown in Table 6.2. These calculated molar fractions were then used in the BOLSIG+ solver to obtain the effective ionization coefficients for air with 0%, 50%, and 100% RH.

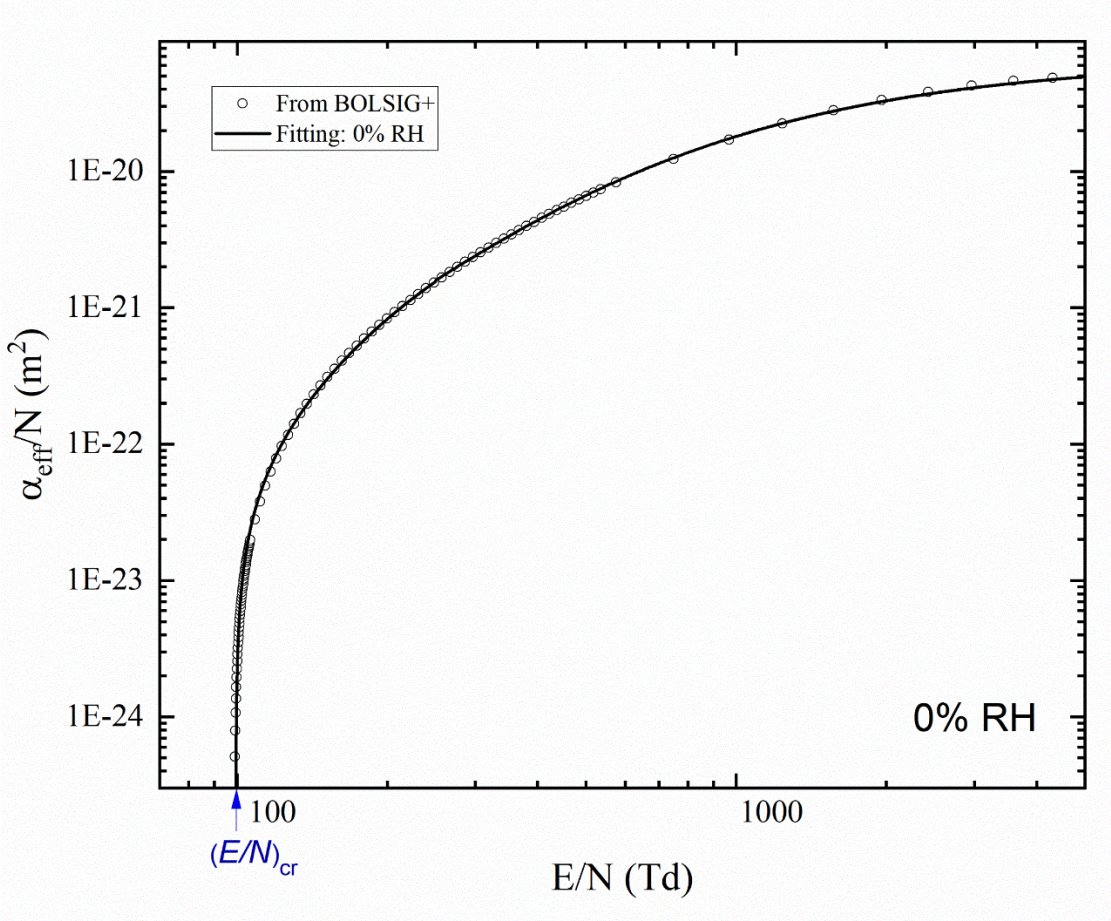

Figure 6.1 (α-η)/N as a function of E/N in air with relative humidity of 0% at 300K, 101.3kPa. Data from BOLSIG+ solver [Morgan database]

Figure 6.1 shows the reduced effective ionization coefficient for air with a relative humidity of 0% at 300K and 101.3 kPa calculated by using BOLSIG+ solver based on the Morgan database, the molar fractions of N_2 and O_2 are 79% and 21% respectively.

In the present work, a fitting curve for the reduced effective ionization coefficient for air with the relative humidity of 0% in the field range from ~ 100 Td to ~ 5000 Td was obtained using OriginPro (v.2021) graphing software. The exponential functions given by Equation 6.6 were used to fit the ionization coefficient of the humid air

$$\alpha_{eff}/N = 2.7\cdot10^{-20} exp\ (-800/(E/N+35)) - 70\cdot10^{-24} \quad 98.96\ \text{Td} < E/N < 250\text{Td}$$
$$\alpha_{eff}/N = 6.6\cdot10^{-20} exp\ (-1490/(E/N+150)) \quad 250\ \text{Td} < E/N < 5000\text{Td} \qquad (6.6)$$

where α_{eff}/N is the reduced effective ionization coefficient in the unit of m^2, and E/N is the reduced electric field in Td.

It was found that the critical field of the humid air is ~98.96 Td, which is in close agreement with the value of the critical field (~94 Td) obtained for air in Chapter 3.

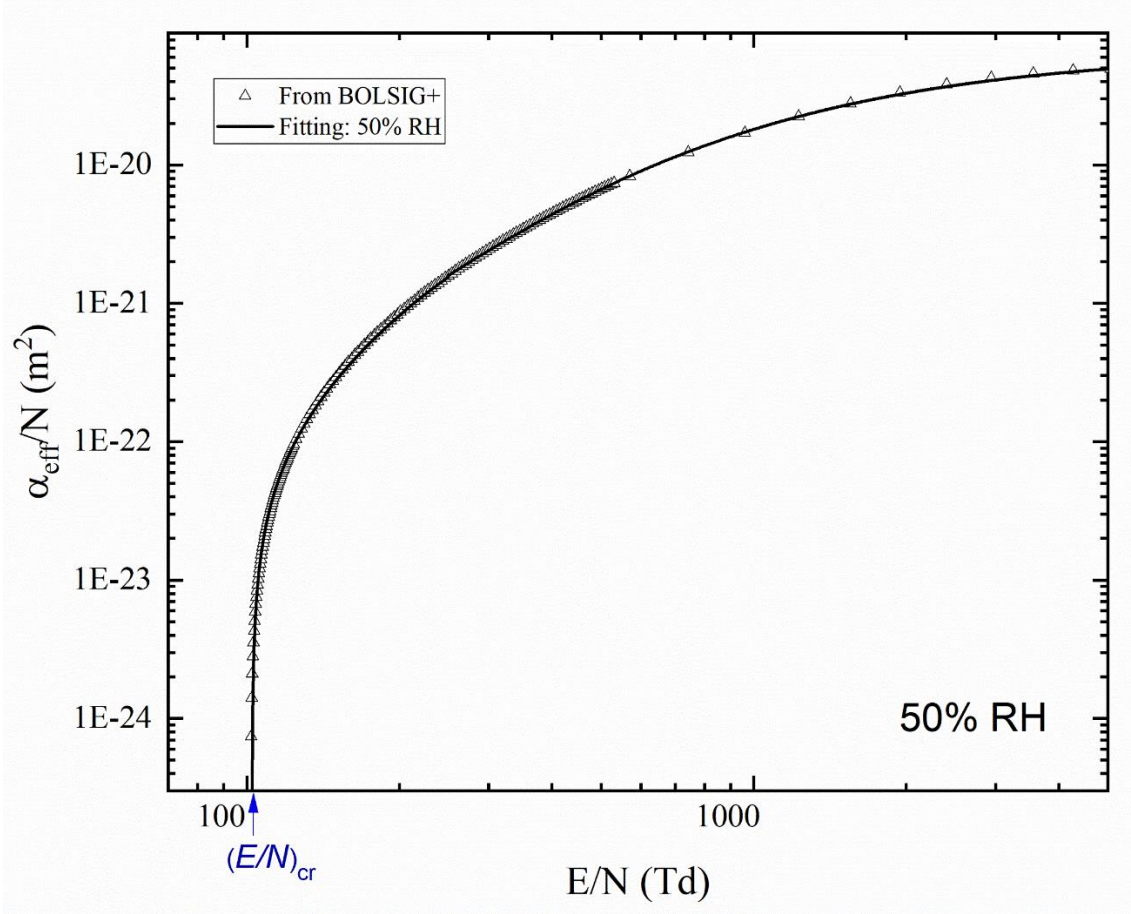

Figure 6.2 (α-η)/N as a function of E/N in air with relative humidity of 50% at 300K, 101.3kPa. Data from BOLSIG+ solver [Morgan database]

Figure 6.2 shows the reduced effective ionization coefficient as a function of the field *E/N* for air with a relative humidity of 50% was obtained using BOLSIG+ solver. The analytical curve was fitted with the exponential functions in the field range from ~ 100 Td to ~ 5000 Td using OriginPro (v.2021) graphing software. These exponential analytical functions are given by Equation 6.7

$$\begin{aligned} \alpha_{eff}/N &= 2.7\cdot10^{-20} exp\ (-800/(E/N+35)) - 80\cdot10^{-24} \quad && 101.7\text{Td} < E/N < 250\text{Td} \\ \alpha_{eff}/N &= 6.6\cdot10^{-20} exp\ (-1490/(E/N+150)) && 250\text{Td} < E/N < 5000\ \text{Td} \end{aligned} \tag{6.7}$$

It also can be seen that the critical field obtained for air with a relative humidity of 50% is ~ 101.7 Td.

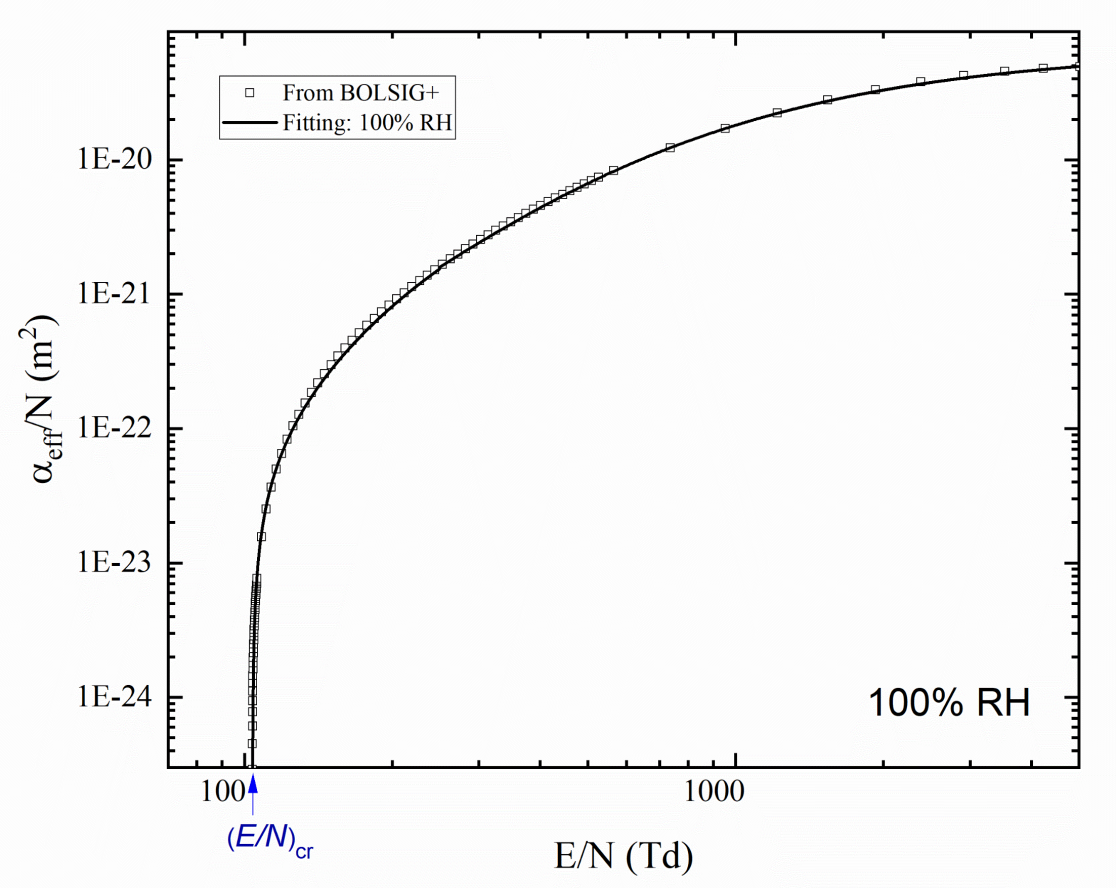

Figure 6.3 (α-η)/*N* as a function of *E/N* in air with relative humidity of 100% at 300K, 101.3kPa. Data from BOLSIG+ solver [Morgan database]

Figure 6.3 shows the reduced effective ionization coefficient as a function of the electric field for air with 100% RH (solid line) obtained by the BOLSIG+ solver. The field ranges from ~ 100 Td to ~ 5000 Td. The molar fractions (76.24% N_2, 20.27% O_2 and 3.49% H_2O) were obtained from the Morgan database for 300K and 101.3 kPa, as shown in Table 6.2.

An analytical curve fit to the reduced effective ionization coefficient for air with a relative humidity of 100% in the field range from ~ 100 Td to ~ 5000 Td was obtained using the exponential functions in OriginPro (v.2021) graphing software

$$\begin{aligned} \alpha_{eff}/N &= 2.7\cdot10^{-20} exp\ (-800/(E/N+35)) - 85\cdot10^{-24} \quad && 103.8\text{Td} < E/N < 250\ \text{Td} \\ \alpha_{eff}/N &= 6.6\cdot10^{-20} exp\ (-1490/(E/N+150)) && 250\ \text{Td} < E/N < 5000\ \text{Td} \end{aligned} \tag{6.8}$$

It was found that the critical field for air with a relative humidity of 100% is ~ 103.8 Td, which is consistent with [Verhaart,1984].

TABLE 6.3

Critical field $(E/N)_{CR}$ for air with different RH

Thermodynamic conditions	Relative humidity	$(E/N)_{cr}$,(Td)
300K 101.3kPa	0%	98.96
	50%	101.7
	100%	103.8

The critical field, $(E/N)_{cr}$, for air with a relative humidity of 0%, 50%, and 100% was obtained from the effective ionization coefficients at the condition when the effective ionization coefficient equals zero. The critical fields obtained for air with different

relative humidities is summarised in Table 6.3. It can be seen that the higher humidity has a higher critical field at the temperature of 300K and pressure of 101.3 kPa (discussed in Section 6.4).

6.3 Breakdown Voltage for air with different relative humidity

The avalanche-to-streamer transition criterion is used to obtain the value of breakdown voltage for air with a relative humidity of 0%, 50%, and 100% in the uniform electric field. This breakdown criterion is given by Equation 6.11

$$\alpha_{eff} \cdot d = K^* \tag{6.9}$$

$$\alpha_{eff} \cdot d/N = K^*/N \tag{6.10}$$

$$\alpha_{eff}/N = K^*/(N \cdot d) \tag{6.11}$$

where *d* is the minimum distance, the avalanche should travel to accumulate sufficient charge to complete its transition into the streamer, α_{eff} is the effective ionization coefficient, K^* is the changeable constant parameters (in the present work, K^*=8, K^*=12, K^*=18 were used, separately), N is the number density of the gas.

Based on the streamer breakdown criterion, the breakdown voltage, U_{br}, in the uniform field can be calculated by

$$U_{br} = E \cdot d = \left(\frac{E}{N}\right) \cdot N \cdot d \tag{6.12}$$

where U_{br} is the breakdown voltage, E is the electric field, d is the gap between electrodes, and E/N is the reduced electric field.

To obtain the reduced electric field E/N for air with the relative humidity of 0%, 50%, and 100%, Equations 6.6-6.8 for the reduced ionization coefficient were re-written for the reduced electric field, i.e., E/N as a function of α_{eff}, for each relative humidity

0%RH	E/N=-800/ln(($\frac{\alpha_{eff}}{N}$+70·10^{-24})/2.7·10^{-20}) -35	$0 < \frac{\alpha_{eff}}{N} < 1.5\cdot10^{-21}$ m^2	(6.13)
	E/N=-1490/ln($\frac{\alpha_{eff}}{N}$/6.6·10^{-20}) -150	$1.5\cdot10^{-21}$ m^2< $\frac{\alpha_{eff}}{N}$< $4.9\cdot10^{-20}$ m^2	
50%RH	E/N=-800/ln(($\frac{\alpha_{eff}}{N}$+80·10^{-24})/2.7·10^{-20}) -35	$0 < \frac{\alpha_{eff}}{N} < 1.5\cdot10^{-21}$ m^2	(6.14)
	E/N=-1490/ln($\frac{\alpha_{eff}}{N}$ /6.6·10^{-20}) -150	$1.5\cdot10^{-21}$ m^2< $\frac{\alpha_{eff}}{N}$< $4.9\cdot10^{-20}$ m^2	
100%RH	E/N=-800/ln(($\frac{\alpha_{eff}}{N}$+85·10^{-24})/2.7·10^{-20}) -35	$0< \frac{\alpha_{eff}}{N} < 1.5\cdot10^{-21}$ m^2	(6.15)
	E/N=-1490/ln($\frac{\alpha_{eff}}{N}$/6.6·10^{-20}) -150	$1.5\cdot10^{-21}$ m^2< $\frac{\alpha_{eff}}{N}$< $4.9\cdot10^{-20}$ m^2	

where E/N is the reduced electric field in Td, α_{eff}/N is the reduced effective ionization coefficient in the unit of m^2 calculated by Equation 6.11 depending on different K^* (K^*=8, K^*=12 and K^*=18 are used in the present work). Two different ranges of $\frac{\alpha_{eff}}{N}$ were used to provide more accurate fit of the normalised electric field, E/N, to the available experimental data.

Therefore, at a temperature of 300K and pressure of 101.3 kPa, the relationship between the breakdown voltage and the product of the pressure and the gap between electrodes for air with a relative humidity of 0%, 50%, and 100% was obtained using Equations 6.11 and 6.12.

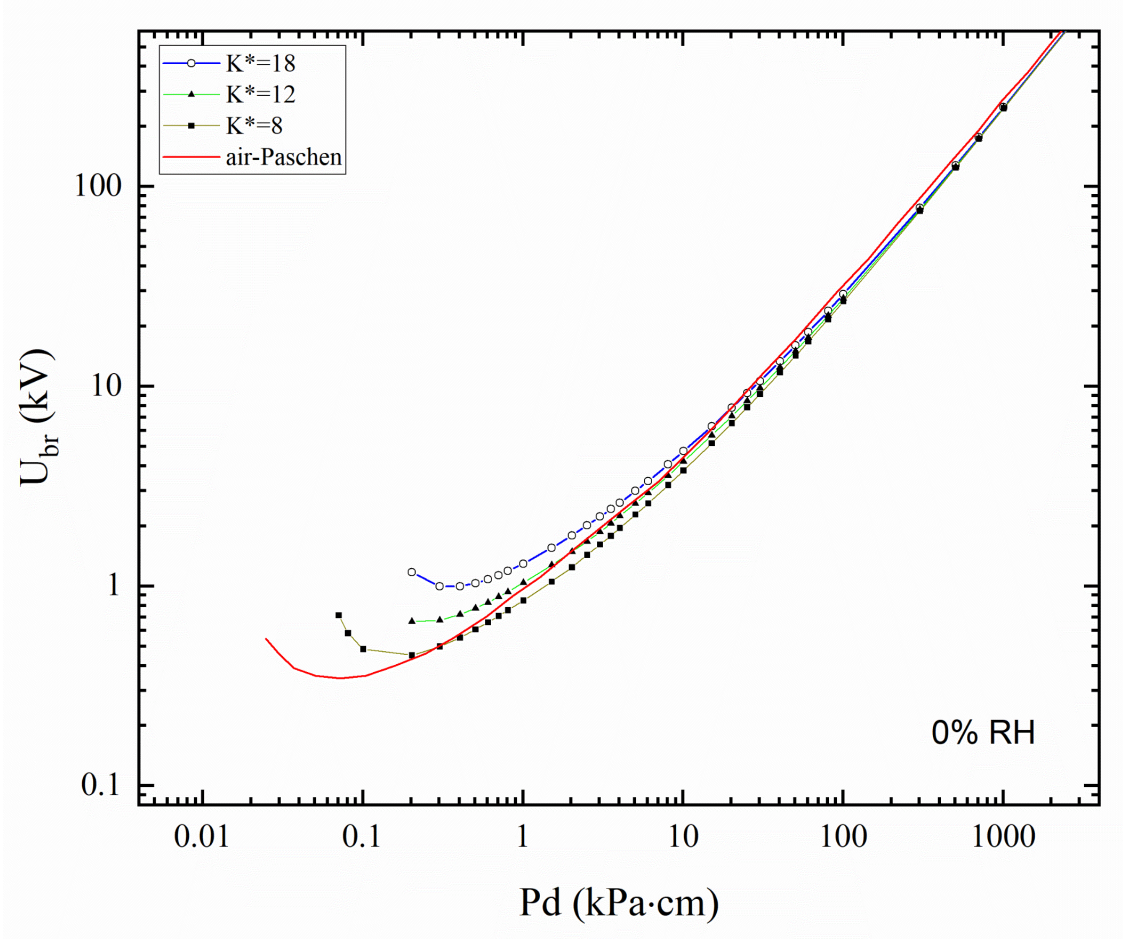

Figure. 6.4 Breakdown voltage U_{br} as a function of *pd* for air with 0%RH. Paschen curve for air [Dakin,1974]: solid red line

The breakdown voltage, U_{br} , as a function of *pd* for air with different relative humidity values is plotted in Figure 6.4, providing the comparison between U_{br} obtained for K^*=8, K^*=12 and K^*=18. For comparison, the Paschen curve for air obtained from [Dakin,1974] is also shown in Figure 6.4.

It was found that at the room temperature and atmospheric pressure, the minimum breakdown voltage of air with 0%RH, for *pd* ~ 10 kPa·cm, and K^*=8 is ~ 3.78 kV; the minimum breakdown voltage for K^*=12 is ~ 4.19 kV, and the minimum breakdown voltage for K^*=18 is ~ 4.72 kV.

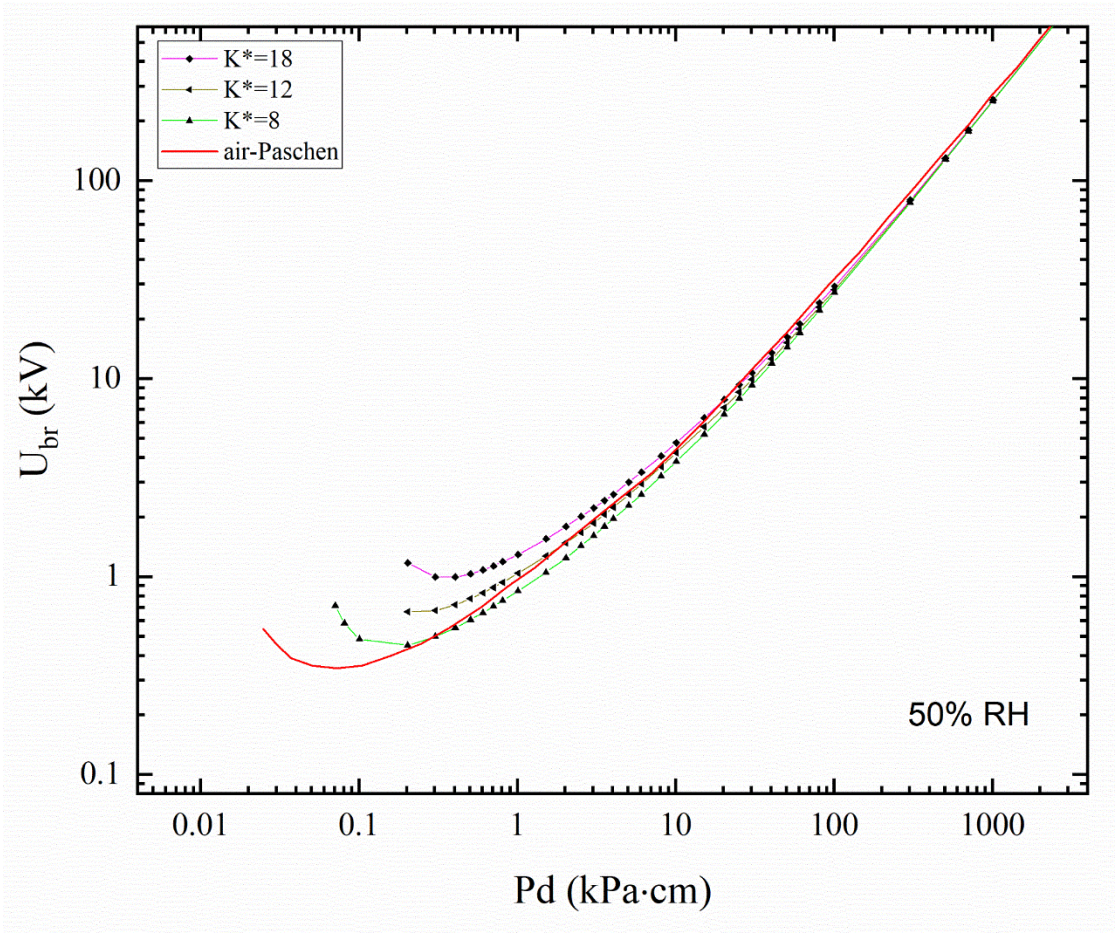

Figure 6.5 U_{br} as a function of *pd* for air with 50% RH. solid red line: the Paschen curve for air from [Dakin,1974]

The breakdown voltage U_{br} as a function of *pd* in the uniform field (the Paschen curve for air from [Dakin,1974]) was plotted in Figure 6.5 and compared with the breakdown voltage obtained for different values of K^* for air with the relative humidity of 50% RH at room temperature and atmospheric pressure.

It can be seen that at room temperature and atmospheric pressure, the breakdown voltage for 50% RH air, for *pd* ~ 10 kPa·cm, and K^*=8 is ~ 3.81 kV, the lowest breakdown voltage for K^*=12 is ~ 4.22 kV, the lowest breakdown voltage for K^*=18 is ~ 4.74 kV.

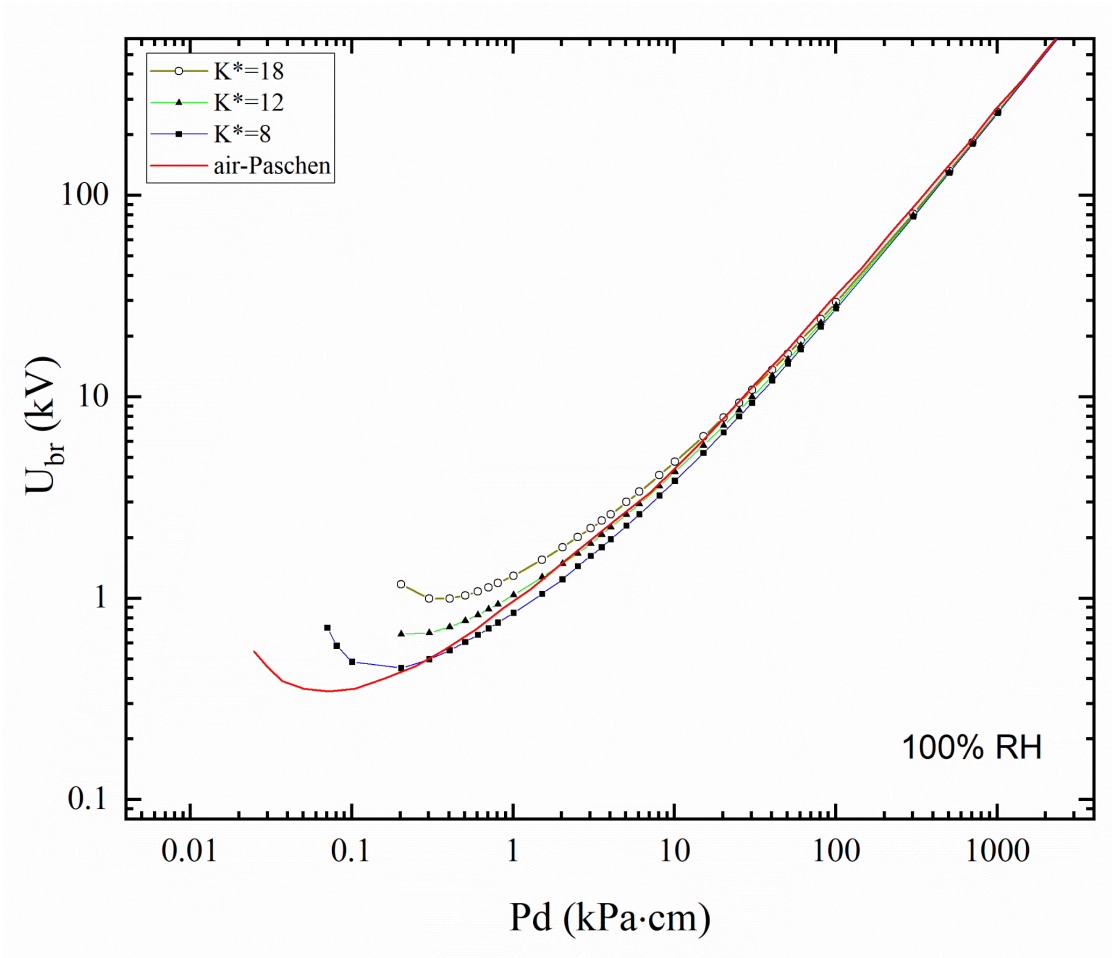

Figure 6.6 U_{br} as a function of *pd* for 100%RH air. Solid red line: the Paschen breakdown curve, [Dakin,1974]

Figure 6.6 shows the breakdown voltage U_{br} for air with the relative humidity of 100%RH obtained for different value of K^* (K^*=8, K^*=12 and K^*=18) and compared with the Paschen curve [Dakin,1974].

There is a clear trend of increasing U_{br} with *pd* in the range of above ~1 kPa·cm. The values of U_{br} at *pd* ~10 kPa·cm for different value of K^* are: ~ 3.82 kV for K^*=8; ~ 4.23 kV for K=12; ~ 4.75 kV for K^*=18.

TABLE 6.4

Breakdown voltages for specific values of *pd* for air with different RH based on Equation 6.12

U_{br}		*pd*				
		0.203 kPa·cm	1.01 kPa·cm	10.1 kPa·cm	101 kPa·cm	1010 kPa·cm
RH= 0%	K^*=8	0.449 kV	0.846 kV	3.78 kV	26.6 kV	246 kV
	K^*=12	0.663 kV	1.04 kV	4.19 kV	27.5 kV	247 kV
	K^*=18	1.17 kV	1.29 kV	4.72 kV	28.8 kV	249 kV
RH= 50%	K^*=8	0.449 kV	0.846 kV	3.81 kV	27.2 kV	253 kV
	K^*=12	0.663 kV	1.04 kV	4.22 kV	28.1 kV	254 kV
	K^*=18	1.17 kV	1.29 kV	4.74 kV	29.3 kV	256 kV
RH= 100%	K^*=8	0.449 kV	0.846 kV	3.82 kV	27.4 kV	256 kV
	K^*=12	0.663 kV	1.04 kV	4.23 kV	28.3 kV	257 kV
	K^*=18	1.17 kV	1.29 kV	4.75 kV	29.5 kV	259 kV

To compare U_{br} for specific values of *pd* at room temperature and atmospheric pressure for humid air, the breakdown voltage values were obtained by Equation 6.12 (Table 6.4). For *pd* values of 0.203 kPa·cm and 1.01 kPa·cm, the obtained breakdown voltages are almost the same for air with 0% RH, 50% RH and 100% RH. For *pd of*

10.1 kPa·cm, 101 kPa·cm and 1010 kPa·cm, the values of U_{br} slightly increase with the increasing relative humidity.

U_{br} for specific values of K^* is given in Table 6.4, when *pd* ranges from ~0.2 kPa·cm to ~10 kPa·cm. The breakdown voltage for different values of K^* varies; however, when *pd* ranges from ~100 kPa·cm to ~1000 kPa·cm, it becomes similar for different value of K^*.

It can be found that at the room temperature and atmospheric pressure for all investigated RH values, the minimum breakdown voltage for K^*=8 is ~ 0.4 kV at *pd* ~ 0.2 kPa·cm, the minimum breakdown voltage for K^*=12 is ~ 0.6 kV at ~0.2 kPa·cm, and the minimum breakdown voltage for K^*=18 is ~ 1 kV at ~0.3 kPa·cm.

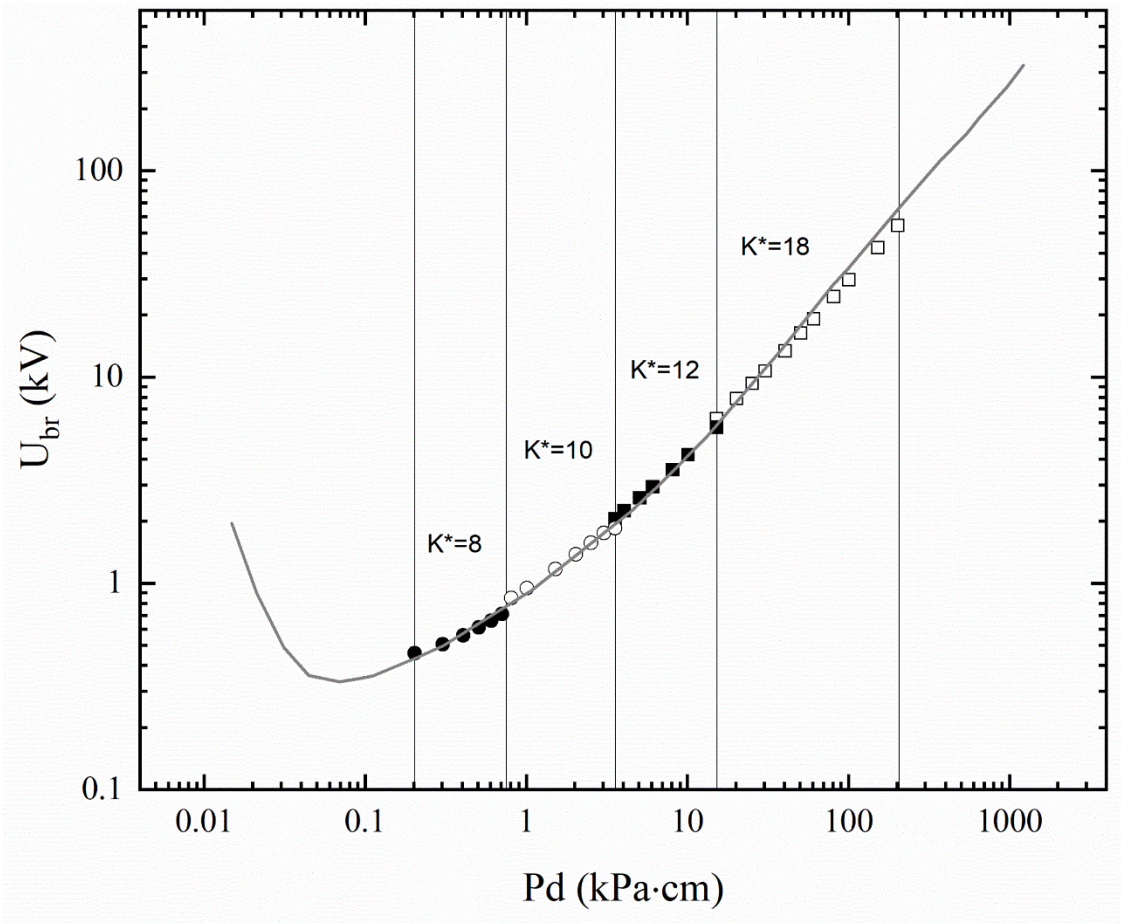

Figure 6.7 U_{br} as a function of *pd* for dry air. Paschen curves for air [Dakin,1974]: solid red line. Points were obtained by Equation 6.11 and 6.12 for K^*=8, K^*=10, K^*=12, K^*=18

U_{br} as a function of *pd* for dry air is shown in Figure 6.7. The points (U_{br}) were obtained by Equations 6.11 and 6.12 for K^*=8, K^*=10, K^*=12, K^*=18. As compared with the Paschen curves for air obtained from [Dakin,1974], it can be seen that the breakdown voltage values obtained for K^*=8 are in line with the Paschen curve for the *pd* in the range from ~ 0.2 kPa·cm to ~ 0.7 kPa·cm. U_{br} for K^*=10 agrees with the Paschen curve for *pd* in the range from ~ 0.7 kPa·cm to ~ 3.6 kPa·cm; U_{br} for K^*=12 is matching the Paschen curve for *pd* in the range from ~ 3.6 kPa·cm to ~ 15 kPa·cm. U_{br} for K^*=18 is close to the Paschen curve for *pd* in the range from ~ 15 kPa·cm to ~ 207 kPa·cm.

6.4 Discussion

This chapter analyses the breakdown characteristics of air with different relative humidity levels, 0%, 50%, and 100% in the uniform field, at room temperature and atmospheric pressure. The effective ionization coefficient for humid air was obtained as a function of the reduced electric field. Also, the critical field obtained for air with different humidity levels and the breakdown voltage as a function of the product of the pressure and the gap between electrodes was obtained based on the streamer breakdown criterion.

The effective ionization coefficient for humid air as a function of the reduced field was obtained using the BOLSIG+ solver based on the molar fraction of each species (N_2, O_2 and H_2O) in air with relative humidifies of 0%, 50% and 100%. The obtained results have been fitted with the analytical fitting curves (exponential functions) using OriginPro (v.2021) graphing software in the field range from ~ 100 Td to ~ 5000 Td.

The critical field, E/N_{cr}, was obtained from the effective ionization coefficient curves : this is the field at which the effective ionization coefficient equals zero. It was established that higher humidity leads to a higher critical field (at 300K and 101.3 kPa). It can be attributed to the fact that when the molar fraction of water vapour in air increases, the probability of collision of electrons with water molecules also

increases, which leads to the formation of negative ions, causing the reduction in the number of free electrons. Hence, a higher field must be applied to meet the conditions of breakdown.

The breakdown voltage for air with the relative humidity of 0%, 50% and 100% as a function of *pd* in the range from ~0.1 kPa·cm to ~2000 kPa·cm was obtained based on the streamer breakdown criteria. It has been found that the breakdown voltage has almost the same value for all investigated values RH, 0%, 50% and 100% for the same K^* (in the present work K^*=8, K^*=12 and K^*=18 were used).

It is also shown that the breakdown voltage increases with increasing in value of K^* for *pd* in the range from ~0.2 kPa·cm to ~10 kPa·cm. A significant difference in U_{br} is observed for different values of K^* in this range of *pd*. However, the obtained breakdown voltage becomes comparable with the breakdown voltage provided by the Paschen curve for *pd* in the range from ~100 kPa·cm to ~1000 kPa·cm.

The results obtained in this chapter show the limitation of modelling of the breakdown voltage based on the streamer breakdown criterion when the dependent value in Equation 6.12 changes only slightly. That may be due to the fact that the streamer breakdown criterion includes only the basic swarm parameters (the effective ionization coefficient), and does not include other swarm parameters, such as the mobility and the diffusion coefficient. Thus, further investigation of the breakdown characteristics of humid air is required to obtain accurate description of the breakdown voltage.

Chapter 7 Conclusions and future work

7.1 Introduction

This chapter provides the main conclusions based on the work presented in this thesis: the simulation results obtained using the drift-diffusion and kinetic models, the experimental results on HV impulsive breakdown, and the analysis of the breakdown characteristics for air with different relative humidity. The main achievements of this research project are summarized, and potential future work is proposed.

7.2 Conclusions on the presented work

7.2.1 Analytical breakdown characteristics of air, N_2, CO_2 and SF_6

The present research was aimed at further understanding the pre-breakdown processes and time-field breakdown characteristics of different gases (air, N_2, CO_2 and SF_6). The simulation results obtained by the drift-diffusion and kinetic models demonstrated a good agreement with the experiment data available in the literature in the wide range of electric fields, from ~10^2 Td up to ~$2 \cdot 10^4$ Td.

The accurate analytical representation of the swarm parameters for air, N_2, CO_2, and SF_6 in the wide range of electric fields has been obtained and analysed in Chapter 3. These parameters include the ionization coefficient, the attachment coefficient, the effective ionization coefficient, the critical field, and the mobility of electrons. The analytical expressions for the reduced effective ionization coefficient α_{eff}/N (E/N) have been obtained for all studied gases. For the first time, the analytical expressions

for the swarm parameters have been obtained for the fields up to ~ 10^4 Td. These analytical expressions can be used in the drift-diffusion and kinetic models to obtain the breakdown parameters of the investigated gases.

The critical field then has been obtained at the condition when the α_{eff}/N =0, the obtained values are: ~94 Td for air, ~60 Td for N_2, ~86 Td for CO_2, and ~360 Td for SF_6. These values of E/N_{cr} show a good agreement with the experimental data available in the literature.

The validity ranges of the effective ionization coefficients for different gases have been extended up to: 1500 Td for air, ~5000 Td for N_2, 10000 Td for CO_2, and 5000 Td for SF_6 in Section 3.2.

Moreover, the accurate analytical functions of the product of the electron mobility and the number density, $\mu_e N$, for all investigated gases were obtained for the fields in the range from 100 Td to 1000 Td. These functions are based on the experimental measurements and simulation results reported in the literature.

The obtained swarm parameters were used in the simulations presented in Chapter 4: in the drift-diffusion model and kinetic models. These two models have been employed because they can compare different approaches and allow for the breakdown process to be investigated over time. Thus, the time-field breakdown characteristics for air, N_2, CO_2, and SF_6 have been obtained.

The drift-diffusion model has been developed in COMSOL Multiphysics software in which the partial differential equations describing the transport of the charge species in plasma have been constructed and solved. These continuity equations were solved for the electrons and positive and negative ions. Then the number densities of the charged species were used to solve the Poisson equation for the electric field, which is modified by the space charge determined by the number density of specific particles.

The development of the fast plasma ionization fronts in air, N_2, CO_2 and SF_6 at atmospheric pressure and room temperature in the parallel-plane electrodes has been modelled. This model was used to investigate the development of negative ionization fronts (streamers) in these gases. Additionally, a new breakdown criterion based on the (almost) uniform electron distribution along the gap behind the ionization front has been introduced to identify the breakdown voltage and formative time to breakdown. It has been found that the simulation results obtained by the drift-diffusion model show that the velocity of the ionization front increases with an increase in the distance over which the ionization front propagates. These velocities increase with an increase in the applied electric field. The fast ionization front in CO_2 has a velocity similar to that in air; the ionization front in N_2 has a lower velocity than that in air and CO_2; the ionization front in SF_6 has the lowest velocity as compared with other gases (at ~360Td).

The kinetic model based on the streamer breakdown criterion has been used to obtain the breakdown characteristics of the studied gases air, N_2, CO_2 and SF_6 using the analytical effective ionization coefficients and the mobilities obtained from Chapter 3.

In this model, the time-field characteristics have been obtained based on the streamer breakdown criterion. In order to classify the breakdown/discharge process based on their physical mechanisms, a new approach has been developed, which takes into account the Townsend breakdown criterion and the streamer breakdown criterion.

These discharge/breakdown criteria were used to classify the nature of discharges in the *Nt(Nd)* diagram. Depending on the Townsend discharge and streamer breakdown conditions, the critical avalanche time $(Nt)_{avalanche}$ and the critical streamer time $(Nt)_{streamer}$ for air, N_2, CO_2 and SF_6 were obtained.

These conditions provide a relationship between *Nt* and *Nd* for different breakdown mechanisms. It has been found that if $Nt \geq (Nt)_{avalanche}$, it satisfies the Townsend discharge condition; if $Nt < (Nt)_{avalanche}$, the Townsend avalanche requirements are not met; if $Nt \leq (Nt)_{streamer}$, the condition for the streamer breakdown can be achieved.

If $Nt > (Nt)_{streamer}$, streamers will not be formed; if *Nt* is in the range of $(Nt)_{avalanche} \leq Nt \leq (Nt)_{streamer}$ neither Townsend discharge nor streamer breakdown criteria will be satisfied. This specific range of *Nt* requires further analysis and investigation.

The drift-diffusion and kinetic models provide the time-field breakdown characteristics for air, N_2, CO_2 and SF_6 in the wide range of electric fields, from ~10^2 Td up to ~$2 \cdot 10^4$ Td.

A good agreement has been observed between these analytically obtained characteristics and the experimental data available in the literature, including [Felsenthal, 1965], [Fletcher, 1949], [Gould, 1956]. These results confirm that the proposed simulation models can be used to obtain reliable results on the evolution of the pre-breakdown ionization fronts in different gases.

7.2.2 Experimental Impulsive breakdown characteristics of air, N_2 and CO_2

The experimental part of the thesis was aimed at a systematic investigation of the time-field breakdown characteristics of the selected gases in a point-plane electrode configuration.

The breakdown characteristics have been obtained using short sub-μs impulses of both polarities. The obtained experimental data were compared with the analytical time-field characteristics obtained by the kinetic model.

The experimental work, which presented in Chapter 5, was focused on the impulsive breakdown characteristics of air, N_2, and CO_2 in the divergent electric field at sub-μs timescale. The test cell of point-plane electrode geometry used a needle with the radius of the tip electrode of ~80 μm and a gap separation of 0.1 mm was used. The pressure was in the range of 6.5 kPa to 405 kPa, and the HV impulses with a rising time of ~50 ns of both polarities were applied to stress the point electrode.

The model of the pulse generator circuit, including parasitic capacitances and inductances, has been developed in the PSpice software package. This model demonstrated that this pulsed power generator is capable of producing HV impulses with a rising time of ~ 50 ns and duration of ~250 ns. Based on the PSpice model, the practical Blumlen pulsed power system was configured to generate ~250 ns impulses used in the breakdown tests.

In the present tests, the breakdown events were registered on the leading edge of the applied HV impulses, in line with the methodology described in [Krile, 2006] and [Levko, 2019]. These impulses were used to obtain the breakdown voltage $U_{br\text{-}ch}$ and the pre-breakdown time t_{br} for all tested gases.

It was established that these breakdown parameters were determined by the rising slope, dV/dt, of the impulses. This dependency is reflected in the obtained impulsive volt-time characteristics.

It was also found that the breakdown voltage, $U_{br\text{-}ch}$, obtained in the present experimental conditions is several tens of times higher than the static DC breakdown voltage for air, N_2 and CO_2; the combination of high dV/dt and short gap result in significant overvoltage achieved in this topology, when stressed with HV pulses with a rise time shorter than ~50 ns.

Analysis of the obtained experimental data required the uncertainty budget which was completed in the present work. A confidence level of 95% was used in the statistical analysis of the obtained breakdown data.

The time-varying field characteristics obtained under impulsive energization differ from the parameters obtained under DC energization [Levatter, 1980]. Thus, the results obtained in the present work are of particular importance for further understanding of the fast, sub-μs transient breakdown processes.

The relationships between the breakdown time, the breakdown field, the gas number density and the inter-electrode gap for air, N_2 and CO_2 have been investigated in the present work. The obtained experimental breakdown characteristics have been compared with the simulated breakdown characteristics and the data from the literature. The following characteristics have been investigated for all tested gases: the field-distance characteristics (E_{tip}/N as a function of Nd), the time-field characteristics (Nt_{br} as a function of E_{tip}/N), and the time-field characteristics (Nt_{br} as a function of E_{tip}/N).

It has been found that the values of Nt_{br} obtained in the impulsive experimental tests in the field range from $\sim 2 \cdot 10^3$ Td to $\sim 2 \cdot 10^4$ Td are significantly higher than the analytical Nt_{br} values obtained from the kinetic model as indicated in Figures 5.21-5.23. This discrepancy can be attributed to the fact that the total breakdown time is significantly longer than the nominal formative time, which is provided by both analytical models.

The results obtained in the present experimental work can be used in future research on the fast breakdown processes in gases. They will help to develop different gas-insulated components for the HV pulsed power systems, such as fast plasma closing switches filled with environmentally friendly gases and gas-insulated systems for the power industry, such as GIS (Gas Insulated Switchgear).

7.3 Novelty and contribution to the field of study

The findings from this research make several contributions:

- For the first time, accurate analytical expressions for the effective ionization coefficient for air, N_2, CO_2, and SF_6 have been obtained in a wide range of electric fields, up to $\sim 10^4$ Td.

- The values of the critical electrical field for different gasses, dry air, N_2, CO_2, and SF_6, have been obtained.

- Accurate analytical description of the electron mobility in dry air, N_2, CO_2, and SF_6 have been obtained for the electric field up to ~ 10^3 Td.

- The development of fast ionization fronts was modelled using the drift-diffusion model, underpinned by the obtained analytical expressions for the swarm parameters.

- The breakdown criterion has been introduced in the drift-diffusion model. This criterion is based on the electron density distribution behind the ionization front. Thus, the field-time breakdown characteristics for air, N_2, CO_2, and SF_6 have been obtained using the drift-diffusion model.

- The time-field breakdown characteristics of air, N_2, CO_2 and SF_6 have been obtained using the kinetic model, based on the accurate analytical representation of the transport and ionization parameters.

- In the present study, the impulsive time-field breakdown characteristics of air, N_2 and CO_2 have been obtained in the pressure range from 6.5 kPa to 405 kPa using the needle-plane electrode topology with a gap of 100 μm; HV impulses with a rise time of ~50 ns were used in this study.

- Analytical investigation of the breakdown characteristics of air with different relative humidity levels have been conducted based on the streamer breakdown criterion.

- Allometric functions have been used to obtain the scaling relationships $E/N(Nd)$ for air, N_2 and CO_2 in the range of particle densities from ~ 10^{20} 1/m^2 to ~ 10^{22}

$1/m^2$. It has been found that this scaling is also valid in a wider range of *Nd*, up to ~ 10^{24} $1/m^2$, which is supported by previous studies.

- It is envisaged that the results obtained in this work can be used in the modelling of partial discharges in different dielectrics. The developed drift-diffusion model can be used for the detailed analysis of the charge transfer during partial discharge(s) in gas-filled voids in solid and liquid insulation, and will help to estimate the timescale of such processes, which in turn will help to understand the bandwidth of the emitted electromagnetic impulses .

7.4 Future work

The breakdown characteristics in the uniform field for air with different levels of relative humidity at room temperature and atmospheric pressure based on the streamer breakdown criterion have been obtained in Chapter 6.

However, the obtained results show that the breakdown voltage obtained by the proposed approach changes slightly with an increase in the humidity level in air. That may be due to the fact that the streamer breakdown criterion, Equation 6.12, includes only the basic swarm parameters, (the effective ionization coefficient) and does not include other swarm parameters, such as the mobility and the diffusion coefficient.

Therefore, the accuracy in analysis of the breakdown characteristics of humid air may be improved if additional swarm parameters may be used in the drift-diffusion model to obtain more accurate results on the breakdown characteristics of humid air.

With regards to the impulsive breakdown experiments, further work may focus on changing the gap length between the electrodes to obtain the breakdown characteristics in a wide range of inter-electrode distances for different gases.

The reliability of insulation systems is a critical factor in the safe operation of high voltage systems. When fast transients occur, the electrical insulation components and elements of high voltage power systems may experience significant electrical stresses, which will cause acceleration of the degradation in the electrical insulation systems. Transmission cables, for example, are exposed to high harmonics leading to lifetime degradation caused by electrical tree growth and partial discharge.

The drift-diffusion models can be used in future research to investigate the breakdown characteristics and partial discharge processes in power cables in order to predict insulation faults.

References

[Aschwanden, 1984] T. Aschwanden, “Swarm Parameters in SF_6/N_2 Mixtures Determined from a Time Resolved Discharge Study.” *Gaseous Dielectrics,* pp.24-33, 1984.

[Atrazhev, 2012] V. M. Atrazhev, V. S. Vorob'ev, I. V. Timoshkin, S. J. MacGregor, M. J. Given, M. P. Wilson, and T. Wang, “Breakdown processes in gas micro-bubbles in liquids under electric stress.” *IEEE Transactions on Dielectrics and Electrical Insulation,* 19(5), pp.1552-1558, 2012.

[Babich, 2016] L. Babich and T. V. Loiko, “Generalized Paschen’s law for overvoltage conditions.” *IEEE Trans. Plasma Sci.,* 44(12), pp. 3243-3248, 2016.

[Becker, 2006] K.H. Becker, K.H. Schoenbach, J.G. Eden, “Microplasmas and applications.” *J. Phys. D Appl. Phys*., 39, R55–R70, 2006.

[Bagheri, 2018] B. Bagheri, J. Teunissen, U. Ebert, M.M. Becker, S. Chen, O. Ducasse, O. Eichwald, D. Loffhagen, A. Luque, D. Mihailova, and J.M. Plewa, “Comparison of six simulation codes for positive streamers in air.” *Plasma Sources Science and Technology*, *27*(9), p.095002, 2018.

[Bell, 2001] S. Bell, “The beginner’s guide to uncertainty of measurement.” National Physical Laboratory, UK, 2001.

[Beloplotov, 2018] D. Beloplotov, M. Lomaev, D. Sorokin, V. Tarasenko, “Displacement current during the formation of positive streamers in atmospheric pressure air with a highly inhomogeneous electric field.” *Phys. Plasmas* 25, p.083511, 2018.

[Bevington, 1993] P. Bevington, D. K. Robinson, J. M. Blair, A. J. Mallinckrodt, and S. McKay. "Data reduction and error analysis for the physical sciences." Computers in Physics 7, no. 4, pp. 415-416, 1993.

[Bolsig+, 2022] Available online: BOLSIG+ solver ver. 03/2016, Morgan database, www.lxcat.net, accessed on August 11, 2022.

[Bourdon, 2010] A. Bourdon, Z. Bonaventura, and S. Celestin, "Influence of the pre-ionization background and simulation of the optical emission of a streamer discharge in preheated air at atmospheric pressure between two point electrodes." *Plasma Sources Science and Technology*, *19*(3), pp.034012, 2010.

[Bowls, 1938] W.E. Bowls, "The effect of cathode material on the second Townsend coefficient for ionization by collision in pure and contaminated N_2 gas." *Physical Review*, *53*(4), pp.293, 1938.

[Byrne, 2014] T. Byrne, "Humidity effects in substations," *2014 Petroleum and Chemical Industry Conference Europe*, Amsterdam, Netherlands, pp. 1-10, 2014.

[Cai, 2010] X. Cai, X. Zou, X. Wang, L. Wang, Z. Guan, W. Jiang, "Over-volted breakdown and recovery of short nitrogen spark gaps." *Laser and Particle Beams*, 28(3), pp.443-450. 2010.

[Carbone, 2021] E. Carbone, W. Graef, G. Hagelaar, D. Boer, M.M. Hopkins, J.C. Stephens, B.T. Yee, S. Pancheshnyi, J. van Dijk and L. Pitchford, "Data needs for modeling low-temperature non-equilibrium plasmas: the LXCat project, history, perspectives and a tutorial." *Atoms*, 9(1), p.16, 2021.

[Carboni, 2001] V. Carboni, H. Lackner, D. Giri and J. Lehr, "The breakdown fields and risetimes of select gases under the conditions of fast charging (~20 ns and less) and high pressures (20-100 atmospheres)."m Report, AFRL-DE-TR-2001-1077, TITAN Systems Corporation, Pulse Sciences Division, San Leandro, CA, 2001.

[Chen, 2017] X. Chen, L. Lan, H. Lu, Y. Wang, X. Wen, X. Du, and W. He, "Numerical simulation of Trichel pulses of negative DC corona discharge based on a plasma chemical model." *Journal of Physics D: Applied Physics*, *50*(39), p.395202, 2017.

[Chen, 2018] X. Chen, W. He, X. Du, X. Yuan, L. Lan, X. Wen, B. Wan, "Electron swarm parameters and Townsend coefficients of atmospheric corona discharge plasmas by considering humidity." *Phys. Plasmas*, 25(6), pp. 063525, 2018.

[Christophorou, 2000] L.G. Christophorou, and J.K. Olthoff, "Electron interactions with SF_6." *Journal of Physical and Chemical Reference Data*, *29*(3), pp.267-330, 2000.

[Dakin,1974] T. Dakin, W. Luxa, G. Oppermann, G. Vigreux, J., G. Wind, and H. Winkelnkemper, "Breakdown of Gases in Uniform Fields—Paschen Curves for Nitrogen, Air, and Sulfur Hexafluoride." *Electra (CIGRE, Paris)*, 32, pp. 61-82, 1974.

[Davies, 1966] P.G. Davies, J. Dutton, and F.L. Jones, "The motion of slow positive ions in gases-Mobilities of potassium and nitrogen ions in nitrogen." *Philosophical Transactions of the Royal Society of London. Series A, Mathematical and Physical Sciences*, *259*(1100), pp.321-330, 1966.

[Davies, 1971] A.J. Davies, C.S. Davies, and C.J. Evans, "Computer simulation of rapidly developing gaseous discharges." In *Proceedings of the Institution of electrical engineers,* IET Digital Library, 118(6), pp. 816-823, 1971,

[Davies, 1978] D.K. Davies, "Ionization and attachment coefficients in CO_2: N_2: He and pure CO_2." *Journal of Applied Physics*, *49*(1), pp.127-131, 1978.

[Dhali,, 1987] Dhali, S. K., and P. F. Williams. "Two-dimensional studies of streamers in gases." Journal of applied physics 62(12), pp.4696-4707, 1987.

[Dick, 2000] A.R. Dick, S.J. MacGregor, M.T. Buttram, R.C. Pate, L.F. Rinehart, K.R. Prestwich, “Breakdown Phenomena in Ultra-Fast Plasma Closing Switches.” *IEEE Trans. Plasma Sci*. 28, pp.1456. 2000.

[Dick, 2009] E. Dick, “Introduction to finite element methods in computational fluid dynamics.” In Computational fluid dynamics, Springer, Berlin, Heidelberg. pp. 235-274, 2009.

[Dorf, 1993] R. Dorf, “The Electrical Engineering Handbook.” FL, Boca Raton:CRC, 1993.

[Douglas, 1973] H. Douglas, “Recombination rate measurements in nitrogen.” *The Journal of Chemical Physics*, *58*(11), pp.4820-4823, 1973.

[Dubinova, 2016] A.A. Dubinova, “Modelling of streamer discharges near dielectrics.” PhD Thesis, TU Eindhoven, 2016.

[Ducasse, 2007] O. Ducasse, L. Papageorghiou, O. Eichwald, N. Spyrou, and M. Yousfi, “Critical analysis on two-dimensional point-to-plane streamer simulations using the finite element and finite volume methods.” *IEEE Transactions on Plasma Science*, *35*(5), pp.1287-1300, 2007.

[Dutton database, 2022] Dutton database, www.lxcat.net, accessed on February 24, 2022.

[Dutton, 1975] J. Dutton, “A survey of electron swarm data.” *Journal of Physical and Chemical Reference Data*, *4*(3), pp.577-856. 1975.

[Eichwald, 2018] O. Eichwald, M. Yousfi, O. Ducasse, “Breakdown criteria in air: an overview supported by predictive simulations”, *11ème Conférence de la Société Française d’Electrostatique,* Grenoble, France, 2018.

[Eves, 2018] M. Eves, D. Kilpatrick, P. Edwards and J. Berry, “A Literature review on SF_6 gas alternatives for use on the distribution network.” *Western Power Distribution*, Wales, UK, 2018.

[Faircloth, 2014] D.C. Faircloth, “Technological aspects: High voltage.” arXiv preprint arXiv:1404.0952, 2014.

[Farish, 2004] O. Farish, M. D. Judd, B F. Hampton and J. S. Pearson, “SF_6 insulation systems and their monitoring.” *Advances in High Voltage Engineering*, Ed. by A. Haddad and D. Warne (London: IEEE) pp. 37–76, 2004.

[Felsenthal, 1965] P. Felsenthal, and J.M. Proud, “Nanosecond-pulse breakdown in gases.” *Physical Review, 139*(6A), p.A1796, 1965.

[Fletcher, 1949] R.C. Fletcher, “Impulse breakdown in the 10^{-9}sec range of air at atmospheric pressure.” *Physical Review, 76*(10), p.1501, 1949.

[Gallagher, 1983] J.W. Gallagher, E.C. Beaty, J. Dutton, and L.C. Pitchford, “An annotated compilation and appraisal of electron swarm data in electronegative gases.” *Journal of Physical and Chemical Reference Data, 12*(1), pp.109-152. 1983.

[Georghiou, 2000] G.E. Georghiou, “Gas discharge modelling using the finite-element flux-corrected transport method.” PhD Thesis, University of Cambridge, 2000.

[Georghiou, 2001] G.E. Georghiou, R. Morrow, and A.C. Metaxas, “The effect of photoemission on the streamer development and propagation in short uniform gaps.” *Journal of Physics D: Applied Physics, 34*(2), pp.200, 2001.

[Georghiou, 2005] G.E. Georghiou, A.P. Papadakis, R. Morrow, and A.C. Metaxas, “Numerical modelling of atmospheric pressure gas discharges leading to plasma production.” *Journal of Physics D: Applied Physics, 38*(20), pp.R303, 2005.

[Glasoe, 1948] G.N. Glasoe, and J. V. Lebacqz, Eds, “Pulse generators.” McGraw-Hill, New York, 1948.

[Go, 2018] D.B. Go, “Ionization and Ion Transport. A Primer for the Study of Non-Equilibrium, Low-Temperature Gas Discharges and Plasmas.” Morgan and Claypool Publishers, San Rafael, 2018.

[Gould, 1956] L. Gould, and L.W. Roberts, “Breakdown of air at microwave frequencies.” *Journal of Applied Physics*, *27*(10), pp.1162-1170, 1956.

[Grover, 1946] F. W. Grover, “Inductance Calculations: Working Formulas and Tables.” *Dover Publications, Inc.*, New York, 1946.

[Gupta, 2000] D.K. Gupta, S. Mahajan, and P.I. John, “Theory of step on leading edge of negative corona current pulse.” *Journal of Physics D: Applied Physics*, *33*(6), p.681, 2000.

[Haddad, 2004] A. Haddad, M. Haddad, D.F. Warne, and D. Warne, “Advances in high voltage engineering.” IEE Press, London, p. 56, 2004.

[Haefliger, 2018] P. Haefliger and C.M. Franck, “Detailed precision and accuracy analysis of swarm parameters from a pulsed Townsend experiment.” *Review of Scientific instruments*, *89*(2), pp.023114, 2018.

[Hagelaar, 2005] G. J. Hagelaar and L. C. Pitchford, “Solving the Boltzmann equation to obtain electron transport coefficients and rate coefficients for fluid models.” *Plasma Sources Sci. Technol.* 14, pp.722-733, 2005.

[Hake, 1967] R.D. Hake Jr and A.V. Phelps, “Momentum-Transfer and Inelastic-Collision Cross Sections for Electrons in O_2, CO, and CO_2.” *Physical Review*, *158*(1), pp.70, 1967.

[Hallac, 2003] A. Hallac, G.E. Georghiou, and A.C. Metaxas, “Secondary emission effects on streamer branching in transient non-uniform short-gap discharges.” *Journal of Physics D: Applied Physics*, *36*(20), pp.2498, 2003.

[Hasegawa, 1996] H. Hasegawa, H. Date, M. Shimozuma, K. Yoshida, H. Tagashira, “The Drift Velocity and Longitudinal Diffusion Coefficient of Electrons in Nitrogen and Carbon Dioxide from 20 to 1000 Td.” *J. Phys. D: Appl. Phys.*,29, pp. 2664-2667, 1996.

[Hasegawa, 2007] Hasegawa, H., H. Date, and M. Shimozuma, “Electron swarm parameters in water vapour.” *Journal of Physics D: Applied Physics*, 40(8), 2495, 2007.

[Hernandez-Avila, 2003] J.L.Hernandez-Avila, and J. De Urquijo, “Pulsed Townsend measurement of electron transport and ionization in SF_6-N_2 mixtures.” *Journal of Physics D: Applied Physics*, *36*(12), p.L51, 2003.

[Itoh, 1979] H. Itoh, M. Shimozuma, H Tagashira, and S. Sakamoto, “Measurement of the effective ionization coefficient and the static breakdown voltage in SF_6 and nitrogen mixtures.” *Journal of Physics D: Applied Physics*, *12*(12), p.2167, 1979.

[Itoh, 1988] Itoh, H., Miura, Y., Ikuta, N., Nakao, Y. and Tagashira, H., “Electron swarm development in SF_6. I. Boltzmann equation analysis.” *Journal of Physics D: Applied Physics*, *21*(6), p.922, 1988.

[Ivanov, 2016] S. N. Ivanov and K. A. Sharypov, “Switching characteristics of nitrogen in the pulsed mode in a subnanosecond time interval.” *Technical Physics Letters*, 42(3), pp. 274-277, 2016.

[Joffrion, 2017] J.B. Joffrion, D. Mills, W. Clower, C.G. Wilson, “On-Chip Microplasmas for the Detection of Radioactive Cesium Contamination in Seawater.” *Micromachines*, 8, pp. 259, 2017.

[Jovović, 2014] J. Jovović, N. Konjević, “Spectroscopic and electric characterization of an atmospheric pressure segmented gas discharge with micro hollow electrodes.” *Eur. Phys. J. D,* 68, pp. 60, 2014.

[Jungblut, 1989] H. Jungblut, D. Hansen, and W.F. Schmidt, “Ion-ion recombination in electronegative gases.” *IEEE Transactions on Electrical Insulation*, *24*(2), pp.343-348, 1989.

[Kang, 2003] W.S. Kang, J.M. Park, Y. Kim, and S.H. Hong, “Numerical study on influences of barrier arrangements on dielectric barrier

discharge characteristics." *IEEE Transactions on Plasma Science*, *31*(4), pp.504-510, 2003.

[Kawada, 1988] Y. Kawada, S. Shamoto, and T. Hosokawa, "Nanosecond-pulse breakdown of gas-insulated gaps." *Journal of applied physics*, 63(6), pp.1877-1881. 1988.

[Kline, 1979] L.E. Kline, D.K. Davies, C.L. Chen and P.J. Chantry, "Dielectric properties for SF_6 and SF_6 mixtures predicted from basic data." *Journal of Applied Physics*, *50*(11), pp.6789-6796, 1979.

[Krile, 2005] J. Krile, A. Neuber, J. Dickens, H. Krompholz, "DC and Pulsed Dielectric Surface Flashover at Atmospheric Pressure." *IEEE Trans. Plasma Sci.* 33, pp.1149–1154, 2005.

[Krile, 2006] J.T. Krile, A.A. Neuber, H.G. Krompholz, and T.L. Gibson, "Monte Carlo simulation of high-power microwave window breakdown at atmospheric conditions." *Applied Physics Letters*, 89(20), pp.201501, 2006.

[Kulikovsky, 1994] A.A. Kulikovsky, "The structure of streamers in N_2. II. Two-dimensional simulation." *Journal of Physics D: Applied Physics*, *27*(12), pp.2564, 1994.

[Kulikovsky, 1997] A. A. Kulikovsky, "Positive streamer between parallel plate electrodes in atmospheric pressure air." *Journal of physics D: Applied physics* 30, pp. 441, 1997.

[Kumar, 2021] S. Kumar, T. Huiskamp, A. J. M. Pemen, M. Seeger, J. Pachin and C. M. Franck, "Electrical Breakdown Study in CO2 and CO_2-O_2 Mixtures in AC, DC and Pulsed Electric Fields at 0.1–1 MPa Pressure." in *IEEE Transactions on Dielectrics and Electrical Insulation*, 28(1), pp.158-166, 2021.

[Laity, 2011] G. Laity, A. Neuber, A. Fierro, J. Dickens, L. Hatfield, "Phenomenology of streamer propagation during pulsed dielectric surface flashover." *IEEE Trans. Dielectr. Electr.Insul.* 18, pp.946–953, 2011.

[Laroussi, 2012] M. Laroussi, M. G. Kong, G. Morfill, W. Stolz, “Plasma Medicine: Applications of Low-Temperature Gas Plasmas in Medicine and Biology”, Cambridge University Press, 2012.

[Levatter, 1980] J. Levatter, S. Lin, “Necessary conditions for the homogeneous formation of pulsed avalanche discharges at high gas pressures.” *J. Appl.Phys.* 51, pp.210–222, 1980.

[Levko, 2019] D. Levko, R.R. Arslanbekov, and V.I. Kolobov, “Modified Paschen curves for pulsed breakdown.” *Physics of Plasmas*, *26*(6), pp.064502, 2019.

[Liu, 2020] T. Liu, I. V. Timoshkin, S. J. MacGregor, M. P. Wilson, M. J. Given, N. Bonifaci, and R. Hanna, “Field-Time Breakdown Characteristics of Air, N_2, CO_2, and SF_6.” *IEEE Trans. Plasma Sci.*, 48(10), pp.3321-3331, 2020.

[Liu, 2021] T. Liu, I. Timoshkin, M.P. Wilson, M.J.Given, S.J. MacGregor, “The Nanosecond Impulsive Breakdown Characteristics of Air, N_2 and CO_2 in a Sub-mm Gap.” *Plasma*, 5, pp.12-29, 2021.

[Lowke, 1995] J.J. Lowke and R. Morrow. "Theoretical analysis of removal of oxides of sulphur and nitrogen in pulsed operation of electrostatic precipitators." *IEEE Transactions on Plasma Science* 23 (4), pp 661-671, 1995.

[Lowke, 2003] J.J. Lowke, and F. D’Alessandro, “Onset corona fields and electrical breakdown criteria.” *Journal of physics D: applied physics*, *36*(21), pp.2673, 2003.

[Luo, 2012] D. Luo, Y. Duan, “Microplasmas for analytical applications of lab-on-a-chip.” TrAC Trends Anal. Chem., 39, pp. 254–266, 2012.

[Luque, 2008] A. Luque, V. Ratushnaya, and U. Ebert, “Positive and negative streamers in ambient air: modelling evolution and velocities.” *Journal of Physics D: Applied Physics*, *41*(23), pp.234005, 2008.

[Mankowski, 1998] J. Mankowski, J. Dickens and M. Kristiansen, “High voltage subnanosecond breakdown.” *IEEE Trans. Plasma Sci.*, 26, pp. 874-881. 1998.

[Martin, 1991] T. H. Martin, “An empirical formula for gas switch breakdown delay.” *Res. Sci. Pulsed Power*, pp.73-79. 1991.

[Masch, 1932] K. Masch, “Über Elektronenionisierung von Stickstoff, Sauerstoff und Luft bei geringen und hohen Drucken.” *Electrical Engineering (Archiv fur Elektrotechnik), 26*(8), pp.587-596. 1932.

[McDaniel, 1973] E.W. McDaniel, and E.A. Mason, “Mobility and diffusion of ions in gases.” John Wiley: New York, 1973.

[Meek, 1940] J.M. Meek, “A theory of spark discharge.” *Physical review*, 57(8), pp.722, 1940.

[Meek, 1953] J. M. Meek and J. D. Craggs, “Electrical breakdown of gases.” Clarendon Press, Oxford, 1953.

[Merciris, 2020] T. Merciris, Valensi, F. and Hamdan, “A. Determination of the Electrical Circuit Equivalent to a Pulsed Discharge in Water: Assessment of the Temporal Evolution of Electron Density and Temperature.” *IEEE Trans. Plasma Sci.* 48(9), pp. 3193-3202, 2020.

[Mesyats, 2005] G. A. Mesyats, *Pulsed Power*, Kluwer Academic/Plenum, New York, 2005.

[Morrow, 1986] R. Morrow, “A survey of the electron and ion transport properties of SF_6.” *IEEE transactions on plasma science*, *14*(3), pp.234-239, 1986.

[Morrow, 1997] R. Morrow, and J.J. Lowke, “Streamer propagation in air.” *Journal of Physics D: Applied Physics*, *30*(4), pp.614. 1997.

[Nakamura, 1987] Y. Nakamura, "Drift velocity and longitudinal diffusion coefficient of electrons in nitrogen and carbon monoxide", *J. Phys. D: Appl. Phys.*, 20, pp. 933-938, 1987.

[Nikonov, 2001] V. Nikonov, R. Bartnikas, and M.R. Wertheimer, “Surface charge and photoionization effects in short air gaps undergoing discharges at atmospheric pressure.” *Journal of physics D: applied physics*, *34*(19), pp.2979, 2001.

[Niu, 2020] G. Niu, A. Knodel, S. Burhenn, S. Brandt, J. Franzke, “Review: Miniature dielectric barrier discharge (DBD) in analytical atomic spectrometry.” *Anal. Chim. Acta,* , 1147, pp. 211–239, 2020.

[Novak, 1988] J.P. Novak, and R. Bartnikas, “Density profiles, electric field and energy dissipation in a short gap breakdown: a two-dimensional model.” *Journal of Physics D: Applied Physics*, *21*(6), pp.896. 1988.

[Ollegott, 2020] K., Ollegott, P. Wirth, C. Oberste-Beulmann, P. Awakowicz and M. Muhler, “Fundamental Properties and Applications of Dielectric Barrier Discharges in Plasma-Catalytic Processes at Atmospheric Pressure.” Chemie Ingenieur Technik, 92(10), pp.1542-1558, 2020.

[Originlab, 2022] Available online (2022): https://www.originlab.com/doc/en/Origin-Help/Interpret-Regression-Result#Goodness_of_Fit

[Paschen, 1889] F. Paschen, “ *Ueber die zum funkenübergang in luft: wasserstoff und kohlensäure bei verschiedenen drucken erforderliche potentialdifferenz.*” JA Barth, 1889.

[Pedersen, 1967] A. Pedersen, “Calculation of Spark Breakdown or Corona Starting Voltages in Nonuniform Fields.” *IEEE transactions on power apparatus and systems*, (2), pp.200-206, 1967.

[Petcharaks, 1999] K. Petcharaks, “A contribution to the streamer breakdown criterion.” *Eleventh International Symposium on High Voltage Engineering,*Vol. 3, pp. 19-22. IET, 1999.

[Ponduri, 2016] S. Ponduri, “Understanding CO_2 containing non-equilibrium plasmas: modeling and experiments.” PhD Thesis, Technische Universiteit Eindhoven, 2016.

[Prasad, 1960] A.N. Prasad and J.D. Craggs, “Measurement of ionization and attachment coefficients in humid air in uniform fields and the mechanism of breakdown.” *Proceedings of the Physical Society*, *76*(2), pp.223, 1960.

[Radmilovic, 2014] M. Radmilovic-Radjenovic, M., B. Radjenović, Š. Matejčík and M. Klas. “The Breakdown Phenomena in Micrometer Scale Direct-Current Gas Discharges.” *Plasma Chemistry and Plasma Processing* 34, pp.55-64, 2014.

[Raizer, 1991] Y. P. Raizer, “Gas Discharge Physics.” Springer-Verlag, Germany, Berlin, 1991.

[Rep’ev, 2006] A. Rep’ev, P. Repin, “Dynamics of the Optical Emission from a High-Voltage Diffuse Discharge in a Rod–Plane Electrode System in Atmospheric-Pressure Air.” *Plasma Physics Reports,* 32, pp.72–78, 2006.

[Risbud, 1979] A.Risbud and M. S. Naidu,” Ionization and attachment in water vapour and ammonia.” *J. Phys. (France) Colloq*. 40, pp.77,1979.

[Roznerski, 1984] W. Roznerski, and K. Leja, “Electron drift velocity in hydrogen, nitrogen, oxygen, carbon monoxide, carbon dioxide and air at moderate *E/N*.” *Journal of Physics D: Applied Physics*, *17*(2), pp.279, 1984.

[Ryzko, 1965] H. Ryzko, “Drift velocity of electrons and ions in dry and humid air and in water vapour.” *Proceedings of the physical society*, 85(6), pp.1283, 1965.

[Saelee, 1977] H. T. Saelee, J. Lucas, and J. W. Limbeek. "Time-of-flight measurement of electron drift velocity and longitudinal diffusion coefficient in nitrogen, carbon monoxide, carbon dioxide and hydrogen." *IEE Journal on Solid-State and Electron Devices*, 1(4), pp. 111-116. 1977

[Sanders, 1933] F.H. Sanders, “Measurement of the Townsend coefficients for ionization by collision.” *Physical Review*, 44(12), p.1020, 1933.

[Sandia, 2003] L. K. Warne, R. E. Jorgenson, S. D. Nicolaysen, “Ionization coefficient approach to modelling breakdown in nonuniform geometries.” SANDIA Report No. SAND2003-4078, 2003.

[Satoh, 1988] K. Satoh, H. Itoh, Y. Nakao, and H. Takjashira, “Electron swarm development in SF_6. II. Monte Carlo simulation.” *Journal of Physics D: Applied Physics*, *21*(6), pp.931, 1988.

[Schaefer, 1990] G. Schaefer, M. Kristiansen, and A. Guenther, “Gas Discharge Closing Switches.” New York, NY, USA: Springer, 1990.

[Schlumbohm, 1965a] H. Schlumbohm, “Stoßionisierungskoeffizient α, mittlere Elektronenenergien und die Beweglichkeit von Elektronen in Gasen.” *Zeitschrift für Physik, 184*(5), pp.492-505, 1965.

[Schlumbohm, 1965b] H. Schlumbohm, “Messung der Driftgeschwindigkeiten von Elektronen und positiven Ionen in Gasen.” *Zeitschrift für Physik, 182*(3), pp.317-327, 1965.

[Schumann, 1923] W.O. Schumann, “Elektrische Durchbruchfeldstärke von Gasen” J. Springer, p. 25, Berlin, 1923.

[Seeger, 2017] M. Seeger, J. Avaheden, S. Pancheshnyi, T. Votteler, “Streamer parameters and breakdown in CO_2,” *J. Phys. D: Appl. Phys.*, 50, p.015207, 2017.

[Serdyuk, 2013] Y. Serdyuk, “Propagation of cathode-directed streamer discharges in air.” In Proc. COMSOL Conf., Rotterdam, The Netherlands, 2013.

[Shao, 2006] T. Shao, G. Sun and P. Yan, “An experimental investigation of repetitive nanosecond-pulse breakdown in air.” *J. Phys. D Appl. Phys.*, 39(10), pp. 2192-2197, 2006.

[Sivoš, 2015] J. Sivoš, N. Škoro, D. Marić, G. Malović, and Z. Lj Petrović, “Breakdown and dc discharge in low-pressure water vapour.” *Journal of Physics D: Applied Physics*, 48(42), pp.424011, 2015.

[Snider, 1986] Snider, Eric H,” Ideal Gas Law, Enthalpy, Heat Capacity, Heats of Solution and Mixing.” New York: American Institute of Chemical Engineers, 1986.

[Stout, 1978] R.R. Stout and G.A. Dawson, “Primary ionization coefficients for dry and humid air; secondary ionization coefficients for a water surface.” *Pure and applied geophysics*, *116*(1), pp.159-166, 1978.

[Tezuka, 2011] A. Tezuka, “Finite Element and Finite Difference Methods. In Springer Handbook of Metrology and Testing.” Springer, Berlin, Heidelberg, pp. 1033-1060, 2011.

[Townsend, 1897] J. S., Townsend, "On electricity in gases and the formation of clouds in charged gases." *In Proceedings of the Cambridge Philosophical Society*, vol. 9, pp. 244-258, 1897.

[Townsend, 1901] J.S., Townsend, “ XVII. The Conductivity produced in gases by the motion of negatively charged ions.” The London, Edinburgh, and Dublin Philosophical Magazine and Journal of Science. 1(2), pp198-227. 1901.

[Irvine, 1984] T.F. Irvine, P. Liley, " Steam and gas tables with computer equations." Academic Press: Orlando, FL, 1984.

[Tran, 2010a] T.N. Tran, “Surface discharge dynamics: theory, experiment and simulation.” PhD Thesis, University of Southampton, 2010.

[Tran, 2010b] T.N. Tran, I.O. Golosnoy, P.L. Lewin, and G.E. Georghiou, “Numerical modelling of negative discharges in air with experimental validation.” *Journal of Physics D: Applied Physics*, *44*(1), pp.015203, 2010.

[UKAS, 2012] UKAS, M3003, “The Expression of Uncertainty and Confidence in Measurement.” Edition 3, United Kingdom, Accreditation Service, Feltham, Middlesex, UK, 2012.

[UNAM database, 2022] UNAM database, www.lxcat.net, accessed on March 28, 2022

[van Veldhuizen, 2003] E. M. van Veldhuizen, W. R. Rutgers, “Inception behaviour of pulsed positive corona in several gases.” *J. Phys. D: Appl. Phys.*, 36(21), pp. 2692-2696, 2003.

[Verhaart, 1984] H.F.A. Verhaart and P.C.T. Van der Laan, “The influence of water vapor on avalanches in air.” *Journal of applied physics*, *55*(9), pp.3286-3292, 1984.

[Viehland, 1995] L. A. Viehland and C. C. Kirkpatrick. “Relating ion/neutral reaction rate coefficients and cross-sections by accessing a database for ion transport properties*.” International Journal of Mass Spectrometry and Ion Processes*, 149, pp.555-571,1995.

[Vitello, 1994] P.A. Vitello, B.M. Penetrante, and J.N. Bardsley, “Simulation of negative-streamer dynamics in nitrogen.” *Physical Review E*, *49*(6), p.5574, 1994.

[Wang, 2016] W. Wang, and A. Bogaerts, “Effective ionization coefficients and critical breakdown electric field of CO_2 at elevated temperature: effect of excited states and ion kinetics.” *Plasma Sources Science and Technology*, *25*(5), pp.055025, 2016.

[Wilson, 2011] M. P. Wilson, “Impulse Breakdown of Liquid-Solid Interfaces.” PhD thesis, University of Strathclyde, Glasgow, 2011.

[Won, 2002] J. Won, P. F. Williams, “Experimental study of streamers in pure N_2 and N_2/O_2 mixtures and a ≈13 cm gap.” *J. Phys. D: Appl. Phys.*, 35(3), pp. 205-218, 2002.

[Yurgelenas, 2006] Y.V. Yurgelenas, and H.E. Wagner, “A computational model of a barrier discharge in air at atmospheric pressure: the role of residual surface charges in micro discharge formation.” *Journal of Physics D: Applied Physics*, *39*(18), pp.4031, 2006.

Appendix A: Swarm parameters

Appendix A presents the swarm parameters used in both hydrodynamic and kinetic models. The reduced effective ionization coefficient α_{eff} = (α - η)/N (m^2) is given as a function of the reduced electric field E/N (Td, 1Td=10^{21} V·m^2) for different ranges of E/N for all investigated gases. The gas pressure used in all parameters in the present work is equal to 10^5 Pa, which provides the corresponding value of the particle number density of $N = 2.5 \cdot 10^{25} (1/m^3)$ at room temperature. Tables I – IV provide all transport and ionization coefficients used in the present paper for all investigated gases.

TABLE I

Swarm parameters of air in present model

Parameter	Value/function used in the present paper	References
$D(\frac{\mathrm{m}^2}{\mathrm{s}})$	0.18	[Kulikovsky, 1997] [Kang, 2003]
$\mu_e\ (\frac{\mathrm{m}^2}{\mathrm{V}\cdot\mathrm{s}})$	$3.361\cdot 10^{24}(E/N)^{-0.222}/N$ $10\mathrm{Td} \le E/N \le 1000\mathrm{Td}$	Obtained in the present paper
$\mu_p\ (\frac{\mathrm{m}^2}{\mathrm{V}\cdot\mathrm{s}})$	$2.34\cdot 10^{-4}$	[Morrow, 1997] [Chen, 2017]
$\mu_n\ (\frac{\mathrm{m}^2}{\mathrm{V}\cdot\mathrm{s}})$	$2.7\cdot 10^{-4}$ $E/N > 50\mathrm{Td}$ $1.86\cdot 10^{-4}$ $E/N < 50\mathrm{Td}$	[Morrow, 1997] [Chen, 2017]
$\beta\ (\frac{\mathrm{m}^3}{\mathrm{s}})$	$2\cdot 10^{-13}$	[Morrow, 1997] [Georghiou, 2005] [Hallac, 2003]
$\frac{\alpha_{eff}}{N}(\mathrm{m}^2)$	$4\cdot 10^{-20}\cdot exp^{-985/((\frac{E}{N})+43)} - (30\cdot 10^{-24})$ $94\mathrm{Td} < E/N < 1500\mathrm{Td}$	Obtained in the present work

Models without taking into account D_i: [Hallac, 2003], [Morrow, 1997], [Georghiou, 2005], [Ducasse, 2007]

TABLE II

Swarm parameters for N_2 used in the present model

Parameter	Value/function used in the present paper	References
$D(\frac{\mathrm{m}^2}{\mathrm{s}})$	0.18	[Vitello, 1994]
$\mu_e\ (\frac{\mathrm{m}^2}{\mathrm{V}\cdot\mathrm{s}})$	$1.7\cdot 10^{24}(E/N)^{-0.09}/N$ $50\mathrm{Td} \le E/N \le 1000\mathrm{Td}$	Obtained in the present paper
$\mu_p\ (\frac{\mathrm{m}^2}{\mathrm{V}\cdot\mathrm{s}})$	$2.5\cdot 10^{-4}$	[Davies, 1966], [McDaniel, 1973]
$\beta\ (\frac{\mathrm{m}^3}{\mathrm{s}})$	$\sim 1\cdot 10^{-13}$	[Douglas, 1973]
$\frac{\alpha_{eff}}{N}(\mathrm{m}^2)$ $=\frac{\alpha}{N}$	$1.7\cdot 10^{-20}\cdot e^{-800/((\frac{E}{N})-3)}$ $60\mathrm{Td} < E/N < 350\mathrm{Td}$ $3\cdot 10^{-20}\cdot exp^{-1000/(\frac{E}{N})}$ $350\mathrm{Td} < E/N < 5000\mathrm{Td}$	Obtained in the present work

Present model for N_2, η=0 [Vitello, 1994], [Davies, 1971], [Kulikovsky, 1994]

TABLE III

Swarm parameters for SF_6 used in the present model

Parameter	Value/function used in the present paper	References
$D(\frac{\mathrm{m}^2}{\mathrm{s}})$	$3.553 \cdot 10^{-2} \cdot (E/N)^{0.2424}$ $E/N < 650\mathrm{Td}$	[Morrow, 1986]
$\mu_e\ (\frac{\mathrm{m}^2}{\mathrm{V} \cdot \mathrm{s}})$	$3.085 \cdot 10^{24} \cdot (E/N)^{-0.284}/N$ $25\mathrm{Td} \leq E/N \leq 4000\mathrm{Td}$	Obtained in the present paper
$\mu_p\ (\frac{\mathrm{m}^2}{\mathrm{V} \cdot \mathrm{s}})$	$6.0 \cdot 10^{-5}$ $E/N < 120\mathrm{Td}$ $1.216 \cdot 10^{-5} \ln\left(\frac{E}{N}\right) + 0.01 \cdot 10^{-4}$ $120\mathrm{Td} < E/N < 350\mathrm{Td}$ $-1.897 \cdot 10^{-5} \ln\left(\frac{E}{N}\right) + 1.83 \cdot 10^{-4}$ $E/N > 335\mathrm{Td}$	[Morrow, 1986]
$\mu_n\ (\frac{\mathrm{m}^2}{\mathrm{V} \cdot \mathrm{s}})$	$1.69 \cdot 10^{-10}\ (E/N)^2 + 0.53 \cdot 10^{-4}$ $E/N < 500\mathrm{Td}$	[Morrow, 1986]
$\beta\ (\frac{\mathrm{m}^3}{\mathrm{s}})$	$\sim 10 \cdot 10^{-13}$	[Jungblut, 1989]
$\frac{\alpha_{eff}}{N}(\mathrm{m}^2)$	$-9.06 \cdot 10^{-20} \cdot e^{-(\frac{E}{N})/2875} + (8 \cdot 10^{-20})$ $360 < E/N < 5000\mathrm{Td}$	Obtained in the present work

Models without taking into account D_i: [Dahli, 1987]

TABLE IV

Swarm parameters for CO_2 used in the present model

Parameter	Value/function used in the present paper	References
$D(\frac{\mathrm{m}^2}{\mathrm{s}})$	~ 0.1	[Schlumbohm, 1965a]
$\mu_e\ (\frac{\mathrm{m}^2}{\mathrm{V}\cdot\mathrm{s}})$	$8.68 \cdot 10^{24} \cdot (E/N)^{-0.416}/N$ $151\mathrm{Td} \leq E/N \leq 6062\mathrm{Td}$	Obtained in the present paper
$\mu_p\ (\frac{\mathrm{m}^2}{\mathrm{V}\cdot\mathrm{s}})$	$6.52 \cdot 10^{-5} \cdot e^{(-(\frac{E}{N})/399)} + (6.96 \cdot 10^{-5})$ $50\mathrm{Td} \leq E/N \leq 1200\mathrm{Td}$	Data from [Viehland, 1995], Fitting equation from the present work
$\mu_n\ (\frac{\mathrm{m}^2}{\mathrm{V}\cdot\mathrm{s}})$	$6.47 \cdot 10^{-6} \cdot exp^{((\frac{E}{N})-7.4)/86.7)} + (1.22 \cdot 10^{-4})$ $5\mathrm{Td} \leq E/N \leq 150\mathrm{Td}$	Data from [Viehland, 1995], Fitting equation from the present work
$\beta\ (\frac{\mathrm{m}^3}{\mathrm{s}})$	$\sim 1 \cdot 10^{-13}$	[Ponduri, 2016]
$\frac{\alpha_{eff}}{N}(\mathrm{m}^2)$	$4.3 \cdot 10^{-20} \cdot exp^{-986/((E/N)+49)} - (30 \cdot 10^{-24})$ $86\mathrm{Td} < E/N < 1100\mathrm{Td}$ $6.07 \cdot 10^{-20} \cdot e^{-1414/(E/N)}$ $1100\mathrm{Td} < E/N < 10000\mathrm{Td}$	Obtained in the present work

Appendix B: List of figures and tables

Appendix B summarises the list of figures and tables in this thesis.

B.1 List of figures

Figure 3.1.1 α_{eff}/N as a function of E/N in air. Experimental data: □, [Sanders, 1933]; × [Masch, 1932]. Fitting curves: dashed line, [Eichwald, 2018]; short, dashed line, [Kulikovsky, 1997]; grey short, dotted line, [Morrow, 1997]; dashed dotted line, [Nikonov, 2001]; solid grey line, [Sandia, 2003]; black short dotted line, [Widger, 2014]. Fitting curve: solid blue line, the present work. E_s/N represents the transition between different fitting curves from [Sandia, 2003] and [Nikonov, 2001]; E_{max}/N represents maximum value of E/N for fitting curves [Kulikovsky, 1997] and [Eichwald, 2018].

Figure 3.1.2 A zoomed view of Figure 3.1.1 in the range of the normalized electric field E/N from ~300 Td to ~1500 Td.

Figure 3.2.1 The effective ionization $(\alpha)/N$ in m^2 as a function of reduced electric field E/N in Td for N_2. ◅: experimental data from [Bowls, 1938], ○: experimental data from [UNAM database, 2022], Dash: fitting curve from [Sandia, 2003], Dot: fitting curve from [Davies, 1978], [Dhali, 1987], [Vitello, 1994], Solid blue line: fitting curve obtained in the present work ($60\mathrm{Td} < \mathrm{E/N} < 5000\mathrm{Td}$).

Figure 3.2.2 A zoomed view of Figure 3.2.1

Figure 3.3.1 α_{eff}/N as a function of E/N in CO_2. Experimental data points: × [UNAM database, 2022], □, ○, ▽, △ and ◇, [Dutton database, 2022]. Fitting curves: bold solid line, [Raizer, 1991]; solid line, the present work.

Figure 3.3.2 A zoomed view of a section of Figure 3.3.1

Figure 3.4.1 α_{eff}/N as a function of E/N in SF_6. Experimental data: ○ [Christophorou, 2000]. Fitting curves: dashed line, [Morrow, 1986]; solid blue line,

the present work. E_s/N represents the transition between different fitting curves from [Morrow, 1986].

Figure 3.4.2 A zoomed view of the part of Figure 3.4.1

Figure 3.5 $\mu_e N$ as a function of E/N for air. Simulation data from literature: ○ [Chen, 2018]. Fitting curves for the present work (Table 3.6): dark line, air.

Figure 3.6 $\mu_e N$ as a function of E/N for N_2. Experimental data from literature: △, [Hasegawa, 1996]. Fitting curves for the present work (Table 3.7): dark line, N_2.

Figure 3.7 $\mu_e N$ as a function of E/N for CO_2. Experimental data from literature: ◇, [Schlumbohm, 1965b]. Fitting curves for the present work (Table 3.8): dark line, CO_2.

Figure 3.8 $\mu_e N$ as a function of E/N for SF_6. Simulation data from literature: □ [Christophorou, 2000]. Fitting curves for the present work (Table 3.9): dark line, SF_6.

Figure 4.1 Computational domain of the drift-diffusion model

Figure 4.2 Calculation procedure for the breakdown voltage U_{br} and time to breakdown t_{br}.

Figure 4.3 Distribution of electron density in Air (E=115kV/cm, 1atm)

Figure 4.4 Distribution of electron density of drift-diffusion model in Air (E=60 kV/cm).

Figure 4.5 Nt_{br} as function of E/N for Air obtained by Equation 4.19. Dark line, Air.

Figure 4.6 Nt_{br} as function of E/N for N_2 obtained by Equation 4.19. Dark line, N_2.

Figure 4.7 Nt_{br} as function of E/N for CO_2 obtained by Equation 4.19. Dark line, CO_2.

Figure 4.8 Nt_{br} as function of E/N for SF_6 obtained by Equation 4.19. Dark line, SF_6.

Figure 4.9 Nt_{br} as function of $(E/N)_{br}$, obtained by equation 4.19. Dotted line: air; solid dark line: N_2; solid grey line: CO_2; dashed line: SF_6.

Figure 4.10 Avalanche boundary condition and streamer boundary condition of Nt in air, N_2, CO_2 and SF_6.

Figure 4.11 Comparison of the experimental and analytical data from the literature. ☐ air, rising time of 0.5 ns [Babich, 2016]; △ air negative polarity (monocone) [Carboni, 2001]; ▽ air positive polarity (monocone) [Carboni, 2001]; ◁ N_2 negative polarity (monocone) [Carboni, 2001]; ▷ N_2 positive polarity (monocone) [Carboni, 2001]; ◇ air, rising time of 1μs [Babich, 2016]; ○ air [Kawada, 1988]; * air [Shao, 2006].

Figure 4.12 Nominal average velocity of the ionization front, $\bar{v}_{front}$, as a function of E/N. ● air; ☐ N_2; ▽ CO_2; ▲ SF_6. Connecting lines are given for visual guidance only.

Figure 4.13 Nt_{br} as a function of $(E/N)_{br}$ in air. • Experimental data, □ [Felsenthal, 1965]; △ negative polarity (monocone) [Carboni, 2001]; ▽ positive polarity (monocone) [Carboni, 2001]; ● Drift-diffusion model, Equation 4.2 - 4.6; — Kinetic approach, Equation 4.19.

Figure 4.14 Nt_{br} as a function of $(E/N)_{br}$ in N_2. Experimental data: □ [Felsenthal, 1965]; △negative polarity (pointplane),▽ negative polarity (monocone) [Carboni, 2001]; ◇positive polarity (pointplane), ○ positive polarity (monocone) [Carboni, 2001]; ● Drift-diffusion model, Equations 4.2 - 4.6; — Kinetic approach, Equation 4.19.

Figure 4.15 Nt_{br} as a function of $(E/N)_{br}$ in CO_2. Experimental data: △negative polarity [Kumar, 2021]; ▽positive polarity [Kumar, 2021]; ● Drift-diffusion model, Equations 4.2 - 4.6; — Kinetic approach, Equation 4.19.

Figure 4.16 Nt_{br} as a function of $(E/N)_{br}$ in SF_6. Experimental data, □ [Felsenthal, 1965]; △ [Carboni, 2001]. ● Drift-diffusion model, Equations 4.2 - 4.6; — Kinetic approach, Equation 4.19.

Figure 4.17 $(E/N)_{br}$ for investigated gases for specific values of Nt_{br}. △$2 \cdot 10^{17}$ (s/m^3); ▲ $5 \cdot 10^{16}$ (s/m^3); □ $1 \cdot 10^{16}$ (s/m^3); ■ $3 \cdot 10^{15}$ (s/m^3).

Figure 5.1 Schematic diagram of the test cell (not in scale) with the needle-plane electrode configuration

Figure 5.2 Photograph of the gramophone needle tip with ~80μm radius under microscope

Figure 5.3 Size of needle and plane

Figure 5.4 Photograph of the needle plane test cell

Figure 5.5 Gas control and distribution board and botted gasses

breakdown voltage for air. (c) Positive polarity - breakdown voltage for N_2. (d) Negative polarity - breakdown voltage for N_2. (e) Positive polarity- breakdown voltage for CO_2. (f) Negative polarity- breakdown voltage for CO_2.

Figure 5.16 The breakdown voltage, $U_{br\text{-}ch}$, as function of t_{br}, positive polarity: ■ air; ● N_2; ▲ CO_2. Solid lines show fitting curves for each gas obtained by Equation 5.10. The error bars show the 95% confidence interval in the breakdown voltage and time to breakdown.

Figure 5.17 The breakdown voltage, $U_{br\text{-}ch}$, as function of t_{br}, negative polarity: □ air; ○ N_2; △ CO_2. Dashed lines show fitting curves for each gas obtained by Equation 5.10. The error bars show the 95% confidence interval in the breakdown voltage and time to breakdown.

Figure 5.18 E_{tip}/N as a function of Nd in air. Experimental data: ○, negative polarity (the present work); ●, positive polarity (the present work); △, negative polarity (monocone) [Carboni, 2001]; ▲, positive polarity (monocone) [Carboni, 2001]; □, [Shao, 2006]. Solid line, fitting curve, Equation 5.11.

Figure 5.19 E_{tip}/N as a function of Nd in N_2. Experimental data: ○, negative polarity (the present work); ●, positive polarity (the present work); △, negative polarity (pointplane) [Carboni, 2001]; ▲, positive polarity (point-plane) [Carboni, 2001]; ■, [Cai, 2010]; □, [Dick, 2000]. Solid line, fitting curve Equation 5.11.

Figure 5.20 E_{tip}/N as a function of Nd in CO_2. Experimental data, the present work: ○, negative polarity; ● positive polarity. Experimental data [Kumar, 2021]: △, negative polarity; ▲, positive polarity. Solid line, fitting curve Equation 5.11.

Figure 5.21 Field-time breakdown characteristic for different gases. Kinetic model, Equation 4.19, Nt_f as a function of E/N: air, dotted line; N_2, solid dark line; CO_2, solid

gray line; SF_6, dashed line. Experimental results obtained in the present work, Nt_{br} as a function of E_{tip}/N: air, □negative polarity, ■positive polarity; N_2, ○negative polarity, ●positive polarity; CO_2, △negative polarity; ▲positive polarity.

Figure 5.22 Field-time breakdown characteristic for air. Experimental data from the present work, Nt_{br} as a function of E_{tip}/N: ○ negative polarity; ● positive polarity. Fitting curves obtained in the present work: dash dotted line, fitting curve Equation 5.13. Experimental data and analytical data from the literature: △ negative polarity (monocone) [Carboni, 2001]; ▲positive polarity (monocone) [Carboni, 2001]; × [Shao, 2006]; ◇ [Mankowski, 1998]; □, [Felsenthal, 1965]; dashed line [Martin, 1991]; ■Drift-diffusion model; solid dark line, Kinetic model Equation 4.19, Nt_f as a function of E/N.

Figure 5.23 Field-time breakdown characteristic for N_2. Experimental data from the present work, Nt_{br} as a function of E_{tip}/N: ○ negative polarity; ● positive polarity. Fitting curves for the present work: dash dotted line, fitting curves from the Equation 5.13. Experimental data and analytical data from literature: △, negative polarity (point-plane) [Carboni, 2001]; ▽, negative polarity (monocone) [Carboni, 2001]; +, positive polarity (point-plane) [Carboni, 2001]; ▼, positive polarity (monocone) [Carboni, 2001]; × [Shao, 2006]; ◇ [Mankowski, 1998]; □ [Felsenthal, 1965]; dashed line [Martin, 1991]; ■ Drift-diffusion model; solid dark line, Kinetic model Equation 4.19, Nt_f as a function of E/N .

Figure 5.24 Field-time breakdown characteristic for CO_2. Experimental data from the present work, Nt_{br} as a function of E_{tip}/N: ○ negative polarity; ● positive polarity. Fitting curves for the present work: dash dotted line, fitting curves from the Equation 5.13. Experimental and analytical data from literature: △negative polarity (rod-plane) [Kumar, 2021]; ▽positive polarity (rod-plane) [Kumar, 2021]; dashed line [Marin, 1991]; ■ Drift-diffusion model; solid dark line, Kinetic model Equation 4.19, Nt_f as a function of E/N.

Figure 6.1 $(\alpha-\eta)/N$ as a function of E/N in air with relative humidity of 0% at 300K, 101.3kPa. Data from BOLSIG+ solver [Bolsig+, 2022].

Figure 6.2 $(\alpha-\eta)/N$ as a function of E/N in air with relative humidity of 50% at 300K, 101.3kPa. Data from BOLSIG+ solver [Morgan database].

Figure 6.3 $(\alpha-\eta)/N$ as a function of E/N in air with relative humidity of 100% at 300K, 101.3kPa. Data from BOLSIG+ solver [Morgan database].

Figure. 6.4 Breakdown voltage U_{br} as a function of pd for the air with 0%RH. Paschen curve for air [Dakin,1974]: solid red line.

Figure 6.5 U_{br} as a function of pd for air with 50% RH. solid red line: the Paschen curve for air from [Dakin,1974].

Figure 6.6 U_{br} as a function of pd for 100% RH air. Solid red line: the Paschen breakdown curve, [Dakin,1974].

Figure 6.7 U_{br} as a function of pd for dry air. Paschen curves for air [Dakin,1974]: solid red line. Points were obtained by Equation 6.11 and 6.12 for K^*=8, K^*=10, K^*=12, K^*=18.

B.2 List of tables

B.3 List of abbreviations

2D	Two-dimensional
3D	Three-dimensional
AWG	American Wire Gauge
BTE	Boltzmann Transport Equation
FCT	FD Flux Corrected Transport
FD	Finite-Difference
FEM	Finite Element Method
FDM	Finite volume method
FVM	Finite Volume Method
GWP	Global Warming Potential
HV	High Voltage
MUSCL	Monotonic Upwind-centered Scheme for Conservation Law
PDEs	Partial differential equations
PFL	Pulse forming line
ppt	Parts per thousand
RH	Relative humidity
UV	Ultraviolet

B.4 List of symbols

α	First Townsend ionization coefficient
β	Recombination coefficient
γ	Secondary ionization coefficient
η	Attachment coefficient
α_{eff}	Effective ionization coefficient
U_{br}	Breakdown voltage
$U_{br\text{-}ch}$	Breakdown voltage (in present experimental work)
t_{br}	Total time to breakdown
t_f	Formative time
t_s	Statistical time
E	Electric field
E_{tip}	Electric field of needle tip
E/N	Reduced breakdown field
$(E/N)_{cr}$	Critical field
d	Distance from the cathode to the anode
Ne	Density of electron
φ	Electric potential
e	Elementary charge
ε_0	Vacuum permittivity
ε_r	Relative permittivity
ρ	Density of total space charge
v_e	Drift velocity of electrons
v_p	Drift velocity of positive ions
p	Pressure
P_w	Partial pressure of water vapour

P_{tol}	Total pressure
P_{da}	Partial pressure of the dry air
P_{sat}	Saturation pressure of water vapour
χ_{da}	Molar fraction of dry air
χ_{w}	Molar fraction of water vapour
μ	Mobility
D	Diffusion
v_{Front}	Average velocity of the ionization front
v_{ionis}	Ionization frequency
t_{rise}	Rise time
$f_{Bandwidth}$	Bandwidth
R_{gas}	Specific gas constant
N	Neutral gas number density
$(Nt)_{\text{avalanche}}$	Avalanche boundary condition for *Nt*
$(Nt)_{\text{streamer}}$	Streamer boundary condition for *Nt*
K^*	Changeable constant parameters (in the present work, K^*=8, K^*=12, K^*=18 was used separately)
k_{B}	Boltzmann constant
k	Coverage factor
u_r	Standard repeatability uncertainty
s	Standard deviation
u_c	Combined standard uncertainty
u_i	Individual standard uncertainty

Appendix C List of publications

T. Liu, I. Timoshkin, S.J. MacGregor, Wilson, M.P. Wilson, M.J.Given, N. Bonifaci, R. Hanna, "Field-Time Breakdown Characteristics of Air, N_2, CO_2 and SF_6" *IEEE Trans. Plasma Sci.*, 48(10), pp. 3321-3331, 2020.

T. Liu, I. Timoshkin, M.P. Wilson, M.J.Given, S.J. MacGregor, "The Nanosecond Impulsive Breakdown Characteristics of Air, N_2 and CO_2 in a Sub-mm Gap." *Plasma* 5, pp.12-29. 2021.

T. Liu, I. Timoshkin, S.J. MacGregor, Wilson, M.P. Wilson, M.J.Given, "Modelling of Negative Breakdown Streamer in Topologies with Air/dielectric Interfaces." in *11ème Conférence de la Société Française d'Electrostatique*, Grenoble, France, 2018.

T. Liu, I. Timoshkin, M.P. Wilson, M.J.Given, S.J. MacGregor, "Transient Non-uniform Breakdown Processes in Atmospheric Air" in *13th Universities' High Voltage Network (UHVNet)*, Glasgow, UK, Poster presentation, 2020,

T. Liu, I. Timoshkin, M. J. Given, M.P. Wilson, S J. MacGregor, N. Bonifaci, R. Hannah, "Impulsive breakdown of CO_2 and air in overvolted gaps." *Submitted to the 23rd International Symposium on High Voltage Engineering (ISH2023)*, Glasgow, UK, 2023.

I. Timoshkin, T. Liu, Z. Wang, Y. Yao, M. Wilson, M. Given, S. MacGregor, "Impulsive breakdown behaviour of gases and gas-solid interfaces." *The 9th Plasma Science & Entrepreneurship Workshop*, York, UK. 21 - 22, November 2022.